Technische Universität München
Max-Planck-Institut für Quantenoptik

Enhancing the Emission and Coherence of Erbium Dopants

Benjamin Merkel

Vollständiger Abdruck der von der

Fakultät für Physik der Technischen Universität München

zur Erlangung des akademischen Grades eines

Doktors der Naturwissenschaften (Dr. rer. nat.)

genehmigten Dissertation.

Vorsitzender: Prof. Dr. Michael Knap

Prüfer der Dissertation:

1. Hon.-Prof. Dr. Gerhard Rempe
2. Prof. Dr. Kai Müller

Die Dissertation wurde am 18.02.2021 bei der Technischen Universität München eingereicht und durch die Fakultät für Physik am 04.08.2021 angenommen.

Abstract

Quantum networks gain increasing attention because they enable quantum secure communication and also provide technology to connect individual quantum computers and enhance their processing power. As a building block for quantum networks, individual erbium dopants are highly attractive because they promise long-lived spin quantum memories with an optical interface at a telecom wavelength, where loss in optical fibers is minimized.

In this thesis, I investigate erbium dopants in yttrium orthosilicate, which is a system with well-known material parameters and good coherence. By performing spectral hole-burning spectroscopy, I characterize spin relaxation processes and spectral diffusion due to interactions with the crystal environment. To measure the spin coherence of an erbium spin ensemble, I implement optical spin initialization and readout techniques and build a microwave resonator that enables homogeneous and coherent spin control. Strikingly, the coherence of spin ensembles is limited by dipolar interactions in the form of instantaneous spectral diffusion. To overcome this limit, I follow two approaches: decoupling the interactions by suited control sequences, and reducing the dopant concentration to unprecedented values.

In the first approach, I conduct an analytical and experimental study of dynamical decoupling in ensembles of erbium spins, with a focus on the rarely discussed case of ensembles with strongly anisotropic magnetic interactions. I find that conventional decoupling sequences can alleviate but never fully eliminate instantaneous diffusion due to dipolar interactions.

In the second approach, I reduce the spin concentration to a minimum and work with a nominally undoped crystal with trace impurities of erbium of $\sim 0.3\,\text{ppm}$. To still enable spectroscopy, I increase the optical depth by embedding the crystal in a Fabry-Perot cavity. By combining passive vibration isolation techniques with active feedback, I achieve stabilization of a cryogenic resonator with an unprecedented finesse of 10^5. In fluorescence measurements, the inhomogeneous Purcell enhancement of the ensemble is in excellent agreement with a detailed modeling of the cavity modes and their coupling to erbium dopants. For optimally coupled emitters, a Purcell factor of 58 is obtained, while the optical coherence of erbium dopants is well preserved, approaching the lifetime limit. At the end of this work, the full potential of cavity-enhanced spectroscopy is demonstrated by resolving spectral lines of single and few emitters.

Publications

- *Dynamical Decoupling of Spin Ensembles with Strong Anisotropic Interactions*
  B. Merkel*, P. Cova Fariña*, A. Reiserer
  Physical Review Letters 127, 030501 (2021)

- *Coherent Control in the Ground and Optically Excited States of an Ensemble of Erbium Dopants*
  P. Cova Fariña*, B. Merkel*, N. Herrera Valencia, P. Yu, A. Ulanowski, A. Reiserer
  Physical Review Applied **15**, 064028 (2021)

- *Erbium dopants in nanophotonic silicon waveguides*
  L. Weiss*, A. Gritsch*, B. Merkel, A. Reiserer
  Optica **8**, 40-41 (2021)

- *Laser stabilization to a cryogenic fiber ring resonator*
  B. Merkel, D. Repp, A. Reiserer
  Optics Letters **46**, 444-447 (2021)

- *Coherent and Purcell-enhanced emission from erbium dopants in a cryogenic high-Q resonator*
  B. Merkel, A. Ulanowski, A. Reiserer
  Physical Review X **10**, 041025 (2020)

Contents

x

1 Introduction

In the past decades, remarkable progress has been made in the control of quantum systems, enabling the development of first prototypical applications in quantum computation [DiVincenzo2000, Harty2014, Bruzewicz2019], quantum simulation [Bloch2012], quantum sensing [Degen2017, Schmitt2017] and quantum communication [Gisin2007, Krenn2016].

A common challenge in all platforms is the scaling to a higher number of controllable qubits in a single device. In this respect, solid-state solutions like color centers and quantum dots are attractive because they require no complex laser control for trapping and cooling of isolated quantum systems [Awschalom2018, Gao2015]. Among all quantum emitters in solids, rare-earth dopants stand out for several reasons [Macfarlane2002, Thiel2011, Zhong2019b]: first, due to their electronic structure, they exhibit transitions which are effectively shielded from the crystal environment like in a Faraday cage, leading to good preservation of their atomic properties and rather weak coupling to lattice phonons. Second, they exhibit the narrowest homogeneous optical linewidths known today (down to $73\,\mathrm{Hz}$ [Böttger2003]), while static disorder causes a distribution of optical frequencies over typically $\sim 1\,\mathrm{GHz}$ [Thiel2011]. Therefore, rare-earth dopants offer a huge potential for frequency multiplexing, i.e. an increase of the number of addressable qubits within a single optical mode. Finally, many rare-earth dopants have large magnetic moments (up to $7\,\mu_B$), which shows their potential for quantum sensing and makes them an attractive platform for microwave-to-optical conversion [Williamson2014, Fernandez-Gonzalvo2015, Bartholomew2020].

Of all color centers and rare-earth impurities in solids, erbium dopants have the unique property of a coherent optical transition at $1.5\,\mu\mathrm{m}$, as shown in this thesis [Merkel2020]. At this wavelength, optical attenuation in silica fibers is minimized (fig. 1.1). Because of the exponential scaling, the difference to shorter wavelengths is dramatic: while a $50\,\mathrm{km}$ long fiber transmits about $10\,\%$ of all photons at $1.5\,\mu\mathrm{m}$, the transmission drops to less than 10^{-6} for wavelengths $< 1\,\mu\mathrm{m}$. Consequently, all classical fiber-optic communication already operates in the telecom band around $1.5\,\mu\mathrm{m}$, and a variety of fiber-coupled technologies have been developed for these wavelengths, including erbium-based lasers and amplifiers, as well as modulators. Therefore, erbium dopants are not only expedient as optical interface for long-distance quantum communication; their use for quantum information processing also promises good integration into existing fiber network infrastructure.

In this work, we investigate erbium dopants in an yttrium orthosilicate host crystal, whose properties are described in chapter 2. After characterizing the material system in optical spectroscopy experiments (chapter 4) using a novel experiment setup (chapter 3) built in the course of this thesis, we probe its spin coherence with microwave pulses (chapter 5). Here, we analytically and experimentally study the effectiveness of dynamical decoupling in systems with highly anisotropic magnetic interactions and find that the coherence time of erbium spins is limited by their dipolar coupling to similar spins.

To suppress dipolar interactions in the ensemble of erbium dopants, we then turn to very low spin concentrations. Since this results in a very weak interaction with light, we embed the crystal in a Fabry-Perot cavity and study the Purcell-enhanced fluorescence and the coherence of the optical transition (chapter 6).
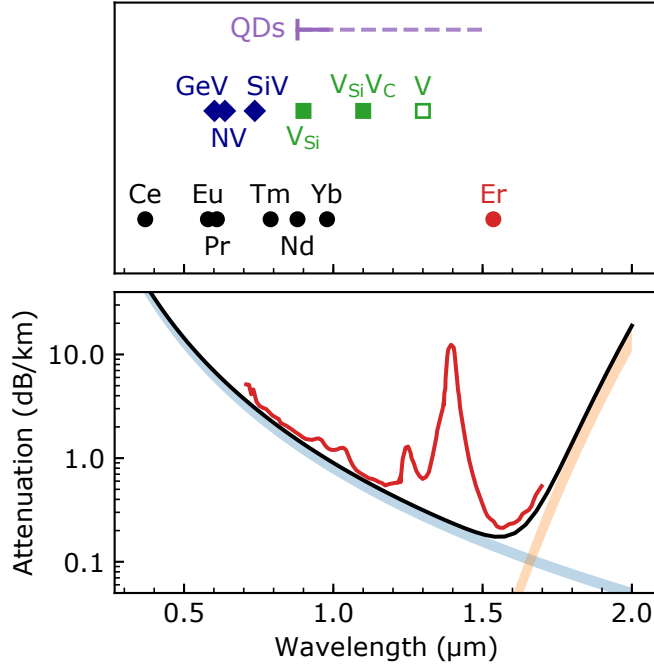
Figure 1.1: **Bottom panel: Wavelength-dependent attenuation of a silica fiber.** Typical loss in optical fibers is dominated by Rayleigh scattering at short wavelengths (blue) and infrared multi-photon absorption at long wavelengths (orange); the shaded areas reflect possible variations with fabrication technique [Guenot2003]. The resulting theoretical limit (black curve) has minimum attenuation in the telecom window around 1.55 µm, which is well approached by commercial optical fibers (red curve, data from [Agrawal2010]), except for additional absorption peaks, caused by indiffusion of water during the fiber drawing process and vibrational resonances of the OH-group [Thomas2000].

Top panel: Emission wavelengths of commonly studied solid-state emitters: InAs/GaAs quantum dots (purple line), color centers in diamond (blue diamonds), defects in silicon carbide (green squares) such as vacancies (filled) and vanadium dopants (open squares) [Atatüre2018, Wolfowicz2020], as well as commonly studied rare-earth dopants (black circles) [Thiel2011, Ortu2018]. Erbium dopants (red circle) emit in the center of the telecom window at 1.55 µm.

2 Material system Er:YSO

Before we turn to the experimental investigation of erbium-doped crystals, we first discuss the key properties of the material system in this chapter. On the one hand, erbium dopants can be represented by an effective four-level system – the simplest realization of a non-zero spin ground level and the corresponding optically excited states. On the other hand, all properties of such four-level system are highly anisotropic, as a consequence of the underlying low crystal lattice symmetry. We show how anisotropic magnetic coupling can be treated analytically and also discuss possible extensions of the simple four-level scheme that include coupling to nuclear spins in the host crystal or hyperfine interaction in erbium isotopes with non-zero nuclear spin.

2.1 Crystal field level structure

An optical transition at the telecom wavelength of $\sim 1.5\,\mu m$ is characteristic for trivalent erbium, Er^{3+}, its most common and stable oxidation state found in solid-state environments [Morss1976]. Its electron configuration $[Xe]\,4f^{11}$ exhibits some properties typical for rare-earth elements: electrons in the partly filled $4f$ shell are located much closer to the nucleus than the fully occupied $5s$ and $5p$ orbitals, which shield them from the environment like a Faraday cage [Freeman1962]. The large orbital angular momentum associated with $4f$ electrons gives rise not only to large magnetic moments but also to a rich variety of electronic levels. In a free atom, most angular momentum states would be degenerate because of rotational symmetry. In a solid-state environment, however, interactions with other crystal constituents lead to a splitting of the electronic levels, depending on the remaining symmetry at the crystallographic site. Their impact can be modeled as an effective crystal field.

2.1.1 Choosing a host crystal for erbium dopants

In order to optically drive the $1.5\,\mu m$ transition between $4f$ electronic states in Er^{3+} ions, breaking the symmetry via the crystal field is favorable, because otherwise the intra-shell transition would be electric-dipole-forbidden [Reid2005]. In addition, a lower symmetry lifts the degeneracy, reduces undesired scattering into dispensable states close-by, and removes an additional degree of freedom that otherwise could obstruct clean qubit control. In other respects, symmetry can also be beneficial to qubit properties: the absence of a first-order Stark shift due to a vanishing permanent electric dipole in inversion symmetric systems makes qubits more robust against slowly fluctuating electric fields. Such symmetry was confirmed for Yb:YVO$_4$ [Kindem2018] and Nd:YVO$_4$ [Bartholomew2018], for example, but the large induced electric dipoles in these materials could still be perturbed by local fields.

Two more aspects should be considered when assessing the capability of a material to host erbium dopants for application in quantum technology: first, is it feasible to incorporate erbium ions into the host crystal at well defined sites without inducing lattice defects or too large strain? And second, which possible interactions would be expected between erbium dopants and other crystal constituents?

The first question addresses the concern that fluctuating spins and charges occupy lattice defect states and cause decoherence in the erbium qubits [Thiel2011, Zhong2019b]. Also, a well-defined crystal environment improves the homogeneity of dopants in the ensemble [Kunkel2016,

Welinski2017, Jang1995], which increases reproducibility and lowers the ion concentration required to accumulate a certain number of similar dopants. While particular inhomogeneities are a resource that can be used, for example, to increase the potential bandwidth of the system [Maniloff1999, Afzelius2009, Chen2020], in general one desires control over that degree of freedom.

In this regard, materials that can incorporate erbium during the growth process are typically preferred over crystals to which erbium was added by ion implantation, because such process would damage the lattice. Historically, different erbium doped materials have been studied in the context of laser design, including yttrium aluminum garnet (YAG) because of its thermal properties [Moncorgé2005], or $LiNbO_3$ because of its electro-optical and acousto-optical tuning capabilities [Baumann1996]. Among those crystals, yttrium compounds turned out to be a good fit: because the ionic radii of both elements are comparable and they have the same charge configuration [Shannon1976], erbium can substitute for yttrium and occupy its well-defined lattice sites.

The second question refers to any interactions with other atomic magnets in the sample, even in absence of magnetic impurities. In $LiNbO_3$, for example, both lithium and niobium have large nuclear magnetic moments of $3 - 6\,\mu_N$, with the nuclear magneton μ_N [Stone2005]. Due to dipole-dipole interactions, these nuclear magnets would couple to erbium spins and potentially limit their performance in qubit storage applications [Askarani2019, Thiel2010]. Similarly, YAG crystals are not optimal because of significant nuclear magnetic moments of aluminum.

Yttrium, on the other hand, with its nuclear spin of 1/2, has a nuclear magnetic moment of only $0.137\,\mu_N$, 45 times smaller than that of niobium. Of particular interest are yttrium compounds with oxygen and silicon, whose most abundant isotopes, ^{16}O and ^{28}Si, have no nuclear spin. Overall, the remaining low magnetic noise caused by nuclear spins in yttrium oxides and yttrium silicates seems to be a small price to pay for the convenience of its growth and doping capabilities. Indeed, the first coherence measurements on yttrium orthosilicate (Y_2SiO_5, YSO) were promising [Macfarlane1997], and soon more systematic studies on that material system confirmed its potential, when a record-narrow homogeneous linewidth of $73\,Hz$ was observed [Böttger2003, Böttger2006b, Böttger2009].

Because of its wide band gap of $\sim 6\,eV$ and the large transparency window down to a wavelength of $200\,nm$ [Pang2005, Upadhyay2019], YSO is an attractive host material for a variety of other rare-earths with emission in the near-infrared, such as Nd [Zhong2015b], Yb [Ortu2018] and Tm [Venet2019], or in the visible spectrum, such as Eu [Zhong2015a], Pr [Utikal2014] and Ce [Kornher2020, Suzuki1992].

2.1.2 Y_2SiO_5 crystal properties and lattice structure

Yttrium orthosilicate grows as a monoclinic crystal with lattice parameters $a = 10.41\,\text{Å}$, $b = 6.721\,\text{Å}$, $c = 12.49\,\text{Å}$, and an angle $\beta = 102.65°$ between a and c axis (see figure 2.1a) [Maksimov1970]. In each unit cell, there are in total 16 yttrium atoms: two distinct crystallographic sites (1 and 2) with different coordination numbers to oxygen [Becerro2004], each of which appears eight times, according to the $I\,2/a$ (C_{2h}^6) space group. For each site there are two orientations (classes I and II), which are related by a C_2 inversion on the b-axis and thus are magnetically inequivalent.

Optical experiments provide no means to determine the orientation of the crystal axes a,b,c directly. Instead, a different, orthogonal set of coordinate axes D_1,D_2,b can be defined by the crystal's polarization eigenaxes: YSO is birefringent, and the polarization of light passing through the crystal will change if it is not aligned with one of its eigenaxes [Beach1990, Sabooni2016]. Because of the low lattice symmetry, b is the only crystal axis that is also a

polarization eigenaxis, while D_1 and D_2 lie in the a-c plane but do not coincide with one of both crystal axes. Since the refractive index for a polarization vector $\vec{E}$ is the same as for its opposite orientation, $-\vec{E}$, it is unfortunately not possible to infer the crystal axes unambiguously from optical measurements alone; instead, measurements of the magnetic properties are required.
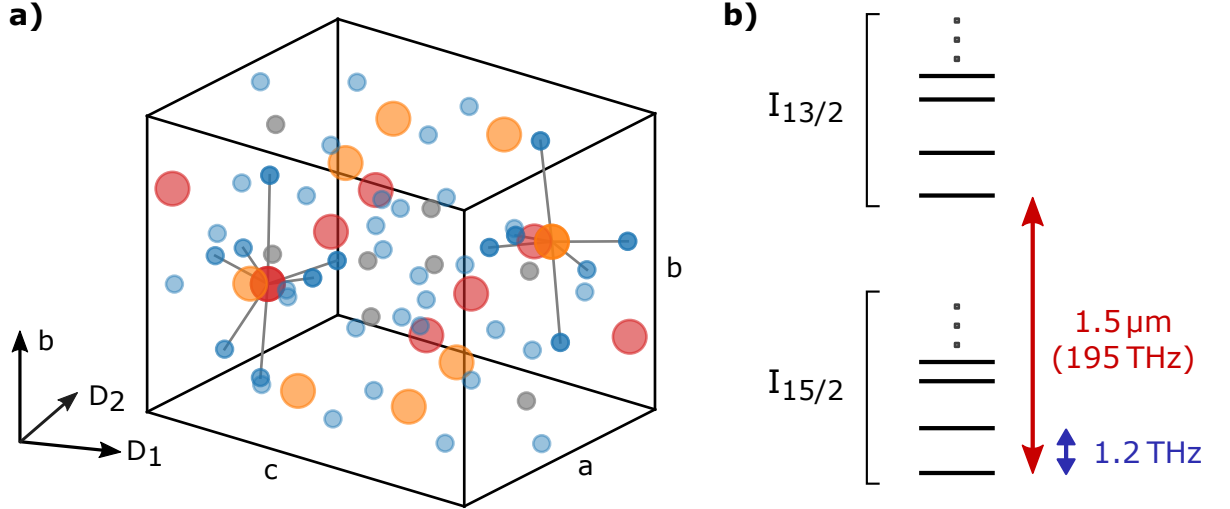
Figure 2.1: **a) Unit cell of yttrium orthosilicate (YSO).** While the crystal orientation is typically described relative to the polarization eigenaxes D_1, D_2, and b, the lattice axes a and c are not aligned with them. In each unit cell, there are 8 silicon atoms (grey), 40 oxygen atoms (blue), and 16 yttrium atoms, which are classified as site 1 (orange) or site 2 (red) depending on their coordination number to oxygen. **b) Sketch of crystal field levels of Er^{3+}:Y_2SiO_5.** The optical transition between the lowest levels of the $^4I_{15/2}$ and $^4I_{13/2}$ manifolds occurs at a telecom wavelength of 1.5 μm. Within each manifold, different crystal field levels are separated by ~ 1 THz, each of which is a Kramers doublet that will split into two states in an external magnetic field.

2.1.3 Erbium in YSO: crystal field levels

Er^{3+} dopants can substitute for yttrium ions and occupy any of their sites, with equal probability for site 1 and 2 [Böttger2006a]. Since yttrium ions in YSO are trivalent as well, no additional charge compensation is required.

In agreement with Hund's rule, the lowest energy level of erbium ions with [Xe] $4f^{11}$ electron configuration is $^4I_{15/2}$, with a total number of $2J+1 = 16$ individual states [Abragam2012]. Because of the low C_1-symmetry of each erbium site, the crystal field level lifts all but one angular momentum degeneracies, which is – according to Kramers' theorem – the maximum impact of interactions with purely electric fields. Lifting the remaining degeneracy is only possible by applying magnetic fields. As a result, the $^4I_{15/2}$ 'ground state' and the $^4I_{13/2}$ 'excited state' manifolds consist of 8 and 7 crystal field doublets. The telecom transition at 1.5 μm occurs between the lowest doublets of each manifold (see figure 2.1b).

Because the splitting between different crystal fields within each manifold is on the order of ~ 1 THz [Doualan1995] and therefore much larger than thermal energy at cryogenic temperature (~ 40 GHz at 2 K) or inhomogeneous broadening (~ 1 GHz), the erbium ion is typically modeled as effective spin-1/2 system with just a single doublet in ground and excited state (see figure 2.2a) [Abragam2012]. This approximation, however, loses validity if strong magnetic fields $\gtrsim 2$ T are applied, as then the Zeeman splitting becomes comparably

large. Then, the full crystal field Hamiltonian has to be used to calculate energy levels and transitions between them [Horvath2019].

In the following section we will review the level structure of Er^{3+}:YSO in the effective spin-1/2 model.

2.2 The Zeeman Hamiltonian in the effective spin-1/2 model

Energy and time evolution of qubit states are defined by the system Hamiltonian. An accurate knowledge of this operator helps us understand dynamics and spectra observed in experiments and make predictions about outcomes for other laboratory conditions.

While in general the interactions of $4f$-electrons with the crystal field and among themselves need to be known, the effective spin-1/2 model assumes a single electron, whose properties are modified such that its behavior reflects that of the full system. For example, the Zeeman Hamiltonian of an electron in a magnetic field $\vec{B}$ is given by its Landé factor g and total angular momentum $\vec{J}$, and with the Bohr magneton μ_B it reads

$$\mathcal{H}_Z = \frac{\mu_B g}{\hbar} \vec{B} \cdot \vec{J}. \tag{2.1}$$

In an isolated atom, the angular momentum is a good quantum number, and the Landé g-factor a scalar value. The crystal field levels of erbium ions in YSO, however, are superpositions of states with different angular momentum – thus, there is no simple expression for the Zeeman energy E_Z. Still, it scales linearly with the magnetic field amplitude $B = |\vec{B}|$, and it can be modeled as interaction of an effective spin-1/2 with an effective g-factor, g_{eff}, that condenses all crystal field effects into a single number:

$$E_Z = \pm \tfrac{1}{2} \mu_B g_{\text{eff}} B \tag{2.2}$$

2.2.1 g-tensor and effective magnetic field

A more general approach takes into account the low symmetry of the crystal field, which makes the effective g-factor depend on the direction of the magnetic field. As a result, the scalar g-value needs to be replaced with a three-dimensional, symmetric tensor $\mathbf{g}$, and the Zeeman Hamiltonian for a spin vector $\vec{S}$ now reads

$$\mathcal{H}_Z = \frac{\mu_B}{\hbar} \vec{B} \cdot \mathbf{g} \cdot \vec{S}. \tag{2.3}$$

This Hamiltonian describes the precession of the spin vector in an effective magnetic field $\vec{B}_{\text{eff}} = B\,\vec{b}_{\text{eff}}$, implicitly defined by $\vec{B} \cdot \mathbf{g} = \vec{B}_{\text{eff}}\,g_{\text{eff}}$ and $g_{\text{eff}} = |\vec{B} \cdot \mathbf{g}|/B$.

An explicit expression for $\vec{b}_{\text{eff}}$ and g_{eff} can be derived in the g-tensor eigenbasis, where $\mathbf{g}$ is diagonal with eigenvalues g_x, g_y, g_z. Let b_x, b_y, b_z be the components of the magnetic field unit vector along the g-tensor eigenaxes. Then we can write

$$\frac{\vec{B}}{B} \cdot \mathbf{g} = \begin{pmatrix} b_x \\ b_y \\ b_z \end{pmatrix} \cdot \begin{pmatrix} g_x & 0 & 0 \\ 0 & g_y & 0 \\ 0 & 0 & g_z \end{pmatrix} = \begin{pmatrix} b_x\,g_x \\ b_y\,g_y \\ b_z\,g_z \end{pmatrix} = \vec{b}_{\text{eff}}\,g_{\text{eff}}, \tag{2.4}$$

which yields the effective g-value given by

$$g_{\text{eff}} = \sqrt{(b_x g_x)^2 + (b_y g_y)^2 + (b_z g_z)^2}. \tag{2.5}$$

Clearly, if the g-tensor is anisotropic, $g_x \neq g_y \neq g_z$, the precession axis is not aligned with the external magnetic field, $\vec{b}_{\text{eff}} \nparallel \vec{B}$, and the effective g-value depends on the field direction.

a)

$|\downarrow\rangle_e$ $|\uparrow\rangle_e$ $\mu_B\, g_{e,\mathrm{eff}}\, B$

$|\uparrow\rangle_g$ $\mu_B\, g_{g,\mathrm{eff}}\, B$

$|\downarrow\rangle_g$

b)
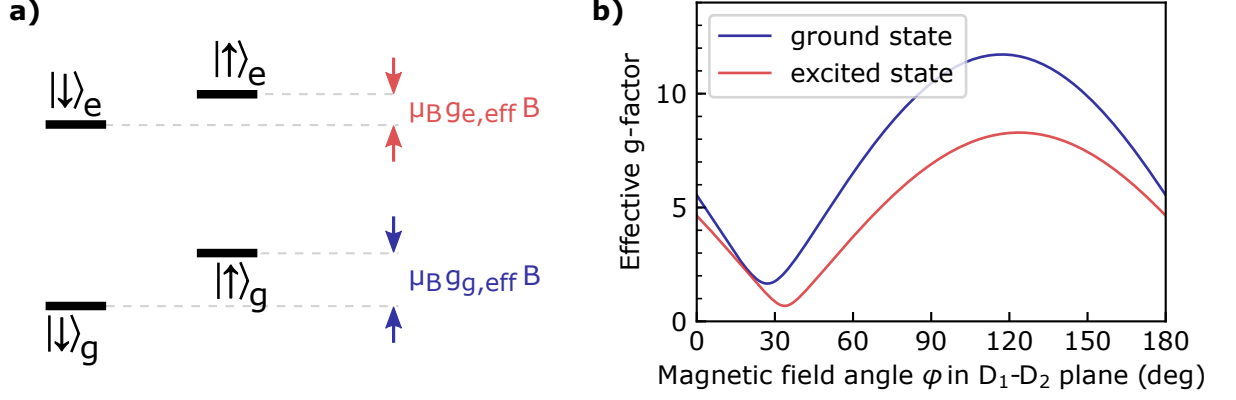
Figure 2.2: **a) Level scheme in the effective spin-1/2 model.** For magnetic fields below a few tesla, higher crystal field levels of Er:YSO can be ignored, and the lowest Zeeman doublets of ground and excited states can be treated as effective spin-1/2 system, with effective g-values $g_{g,\mathrm{eff}}$ and $g_{e,\mathrm{eff}}$, respectively. **b) Effective g-values for ground and excited state.** Because of a high g-tensor anisotropy, the effective g-values vary strongly with the magnetic field orientation, here for site 1 dopants. If the magnetic field is applied in the D_1-D_2 plane, the ground state splitting is always larger than the excited state splitting.

2.2.2 Diagonalizing the Zeeman Hamiltonian

To calculate the eigenstates of the Zeeman Hamiltonian, we express the effective magnetic field unit vector $\vec{b}_{\mathrm{eff}}$ and the spin vector $\vec{S}$ by their components along the eigenaxes of the g-tensor. We choose spherical coordinates Θ and Φ to represent the direction of the effective magnetic field, and express the spin operators by Pauli matrices acting on the two-dimensional spin Hilbert space $\{\, |+\frac{1}{2}\rangle,\ |-\frac{1}{2}\rangle\,\}$:

$$\mathcal{H}_Z = \frac{\mu_B g_{\mathrm{eff}} B}{\hbar} \begin{pmatrix} \sin\Theta\cos\Phi \\ \sin\Theta\sin\Phi \\ \cos\Theta \end{pmatrix} \cdot \begin{pmatrix} \hat{S}_x \\ \hat{S}_y \\ \hat{S}_z \end{pmatrix} \tag{2.6a}$$

$$= \frac{1}{2}\mu_B g_{\mathrm{eff}} B \begin{pmatrix} \cos\Theta & \sin\Theta(\cos\Phi - i\sin\Phi) \\ \sin\Theta(\cos\Phi + i\sin\Phi) & -\cos\Theta \end{pmatrix} \tag{2.6b}$$

Diagonalizing equation 2.6b gives the two Zeeman eigenstates

$$|\uparrow\rangle = \qquad\ \cos\tfrac{\Theta}{2}\,|+\tfrac{1}{2}\rangle + e^{i\Phi}\sin\tfrac{\Theta}{2}\,|-\tfrac{1}{2}\rangle \tag{2.7a}$$

$$|\downarrow\rangle = -e^{-i\Phi}\sin\tfrac{\Theta}{2}\,|+\tfrac{1}{2}\rangle \quad + \cos\tfrac{\Theta}{2}\,|-\tfrac{1}{2}\rangle \tag{2.7b}$$

with the Zeeman energies $E_Z = \pm\frac{1}{2}\mu_B g_{\mathrm{eff}} B$.

2.2.3 g-tensor anisotropy of Er:YSO

For erbium ions in YSO the g-tensor is highly anisotropic, and there is no intrinsic connection between the eigenaxes of the g-tensor and the crystal axes. Furthermore, ground and excited state have different g-tensors, which have not even the same eigenaxes.

For site 1, investigated throughout this thesis, the g-tensor components in the D_1-D_2-b coordinate system are for the ground state [Sun2008]

$$\mathbf{g}_g = \begin{pmatrix} 3.070 & -3.124 & \pm3.396 \\ -3.124 & 8.156 & \mp5.756 \\ \pm3.396 & \mp5.756 & 5.787 \end{pmatrix}, \tag{2.8}$$

with eigenvalues $g_x = 0.560$, $g_y = 1.798$, $g_z = 14.654$. Here, the different signs belong to the two magnetically inequivalent classes I and II.

The g-tensor components for the excited state are

$$\mathbf{g}_e = \begin{pmatrix} 1.950 & -2.212 & \pm 3.584 \\ -2.212 & 4.232 & \mp 4.986 \\ \pm 3.584 & \mp 4.986 & 7.888 \end{pmatrix} \tag{2.9}$$

with eigenvalues $g_x = 0.247$, $g_y = 0.848$, $g_z = 12.974$.

As a result of the low lattice symmetry, the effective g values of both magnetic classes are the same only if the external magnetic field is applied along the b-axis or in the D_1-D_2 plane. Most experiments in this work were conducted in one of these settings. The exact magnetic field orientation in the D_1-D_2-b coordinate system is typically denoted by the polar angle ϑ, measured from the b-axis, and the azimuthal angle φ, measured from the D_1-axis. The effective g-values for a field in the D_1-D_2 plane ($\vartheta = 90°$) are exemplarily shown in figure 2.2b.

2.3   Optical transitions in the four-level scheme

In a free ion, optical transitions between states of the $I_{15/2}$ and $I_{13/2}$ manifold would be electric-dipole-forbidden because their wavefunctions have the same parity, leaving magnetic-dipole transitions or higher-order multipoles as main coupling mechanisms to radiation. Ions doped into a solid, however, have reduced symmetry due to interactions with the crystal field, resulting in significant electric-dipole contributions for optical transitions between ground state doublet and excited state doublet [Li1992, Reid2005].

The exact transition strength depends both on direction and polarization of the incident light, and is represented by an absorption tensor, similar to magnetic interactions being described by the g-tensor [Petit2020]. Unfortunately, the eigenaxes of the absorption tensor do not coincide with the lattice axes or the g-tensor eigenaxes. If the laser beam is propagating along the b-axis, as it was the case for most experiments in this work, the absorption coefficient for light polarized as $\vec{E} \parallel D_2$ is twice as high as for $\vec{E} \parallel D_1$ [Böttger2006a].

The center wavelength of the transitions between states in ground and excited Zeeman doublet is 1536.48 nm for site 1 and 1538.90 nm for site 2 [Böttger2006a], but can also be slightly altered by strain in the crystal [Zhang2020, Böttger2008, Welinski2017]. The large splitting between the transition wavelengths of both sites allows us to perform site-selective experiments. In the following, we focus only on site 1 erbium dopants.

Although the Zeeman Hamiltonians of ground and excited state do not commute and therefore their spin precession axes are always different, we still call $|\downarrow\rangle_g \to |\downarrow\rangle_e$ and $|\uparrow\rangle_g \to |\uparrow\rangle_e$ *spin-preserving transitions*, and $|\downarrow\rangle_g \to |\uparrow\rangle_e$ and $|\uparrow\rangle_g \to |\downarrow\rangle_e$ *spin-flip transitions*. Their relative strengths depend on the misalignment of the magnetic moments in ground and excited state and thus on the magnetic field orientation. While for most configurations the spin-preserving transition is about 9 times stronger than the spin-flip transition [Hastings-Simon2008], for certain other orientations of the external field both transitions are equally probable (see chapter 4.3.1).

The decay of the excited state back to the ground state is not only caused by the transitions within the four-level scheme of the effective spin-1/2, but also by other decay paths via higher crystal field levels of the $I_{15/2}$ manifold. By comparing the transition strengths in the four-level scheme with the measured excited state lifetime of about 11 ms, one can derive the branching ratio β: typically, only a fraction $\beta = 0.21$ of all decay events happen via the spin-preserving transition without participation of higher crystal field levels [Böttger2006a]. This particular value was derived for a single optical mode ($\vec{E} \parallel D_2$) that was close but not

exactly aligned with the maximum absorption; in general the transition strengths and thus the branching ratio depend on the polarization of the considered mode.

Note that these ratios were calculated with respect to the total decay rate, including any non-radiative decay or emission into phonon-sidebands. For rare-earth elements doped into YSO, however, coupling to phonons is expected to be small [Rebane2002, Reed1973]; the crystal field branching ratio is equivalent to the decay probability into the zero-phonon mode at $\sim 1536\,\mathrm{nm}$. For comparison: in NV centers in diamond, for example, only $\sim 3\,\%$ of all excitations decay into the zero-phonon mode. [Gao2015]

2.4 Magnetic interaction in the Zeeman eigenbasis

Interpreting the g-tensor anisotropy as tilt of the effective magnetic field axis, around which the spins precede, turns out to be not helpful when interacting spins are considered. The reason is that not spins but their magnetic moments are the origin of Zeeman energy and dipolar interactions. In systems with an anisotropic g-tensor, the spins are aligned with the effective, tilted magnetic field axis, but their magnetic moments are not: they still precede perpendicular to the untilted magnetic field axis as expected for any classical dipole. [Maryasov2013, Maryasov2020]

A similar argument questions the meaning of spin operators in the context of qubit eigenstates $|\uparrow\rangle$ and $|\downarrow\rangle$: since Zeeman Hamiltonian and $\hat{S}_z$ operator do not commute, the spin z-component will continuously change, even though the system is in an eigenstate. To discuss processes like spin-flips and qubit rotations, it is therefore not beneficial to use the spin operators $\hat{S}_x$, $\hat{S}_y$, $\hat{S}_z$ as it was done above.

Instead, by a more elegant choice of basis operators we could write all interactions as rotations of the effective qubit, not the spin. Such a set of qubit operators is still provided by the Pauli matrices $\hat{\sigma}_x$, $\hat{\sigma}_y$, $\hat{\sigma}_z$, similar to the spin operators, only that they are now defined in the qubit basis: [Maryasov2012, Baibekov2014]

$$\hat{\sigma}_x = \ |\downarrow\rangle\langle\uparrow| + |\uparrow\rangle\langle\downarrow| \tag{2.10a}$$

$$\hat{\sigma}_y = i\,|\downarrow\rangle\langle\uparrow| - i|\uparrow\rangle\langle\downarrow| \tag{2.10b}$$

$$\hat{\sigma}_z = \ |\uparrow\rangle\langle\uparrow| - |\downarrow\rangle\langle\downarrow| \tag{2.10c}$$

Since these operators, together with the identity matrix, form a complete basis of operators in the two-dimensional Hilbert space, it is possible to write any magnetic moment as a linear combination of them:

$$\vec{m} = -\frac{\mu_B}{\hbar}\mathbf{g}\cdot\vec{S} = -\frac{\mu_B}{2}\left[\vec{u}^x\hat{\sigma}_x + \vec{u}^y\hat{\sigma}_y + \vec{u}^z\hat{\sigma}_z\right] \tag{2.11}$$

A representation of the directional vectors $\vec{u}^x$, $\vec{u}^y$, $\vec{u}^z$ in the g-tensor eigenbasis can be found by calculating $\mathbf{g}\cdot\vec{S}$ first in the $\hat{S}_z$-basis and then making a basis transformation to the Zeeman eigenbasis via eq. 2.7. One arrives at

$$\vec{m} = -\frac{\mu_B}{2}\left[\begin{pmatrix} g_x(\cos^2\frac{\Theta}{2} - \sin^2\frac{\Theta}{2}\cos 2\Phi) \\ -g_y\sin^2\frac{\Theta}{2}\sin 2\Phi \\ -g_z\sin\Theta\cos\Phi \end{pmatrix}\hat{\sigma}_x + \begin{pmatrix} -g_x\sin^2\frac{\Theta}{2}\sin 2\Phi \\ g_y(\cos^2\frac{\Theta}{2} + \sin^2\frac{\Theta}{2}\cos 2\Phi) \\ -g_z\sin\Theta\sin\Phi \end{pmatrix}\hat{\sigma}_y \right.$$
$$\left. + \begin{pmatrix} g_x\sin\Theta\cos\Phi \\ g_y\sin\Theta\sin\Phi \\ g_z\cos\Theta \end{pmatrix}\hat{\sigma}_z \right] \tag{2.12}$$

Note that because of the g-tensor anisotropy the directional vectors are not orthogonal to each other. But since they were constructed via the Zeeman eigenstates, they still fulfill $\vec{B} \cdot \vec{u}^{x,y} = 0$ and $\vec{B} \cdot \vec{u}^z = g_{\text{eff}} B$, and therefore simplify the Zeeman Hamiltonian to

$$\mathcal{H}_Z = -\vec{B} \cdot \vec{m} = \tfrac{1}{2} \mu_B g_{\text{eff}} B \, \hat{\sigma}_z \tag{2.13}$$

2.4.1 Dipolar coupling Hamiltonian between similar erbium ions

The large magnetic moments of erbium ions induce magnetic fields, which in turn couple to other magnetic moments. In its most general form, the resulting interaction between two magnetic dipoles $\vec{m}_1$ and $\vec{m}_2$ is given by [Abragam2012, Smith1992]

$$\mathcal{H}_{\text{dd}} = \frac{\mu_0}{4\pi \, r^3} \left[\vec{m}_1 \cdot \vec{m}_2 - 3(\vec{m}_1 \cdot \hat{r})(\vec{m}_2 \cdot \hat{r}) \right], \tag{2.14}$$

where μ_0 is the magnetic constant, $\hat{r}$ the unit vector connecting the dipoles, and r their distance.

In this section, we will focus on the dipolar coupling Hamiltonian $\mathcal{H}_{\text{dd}}$ for similar erbium dopants, i.e. ions with the same Zeeman energy. In systems whose eigenenergies are dominated by the Zeeman Hamiltonian, one can make a secular approximation and ignore terms that could cause transitions between Zeeman eigenlevels of different energy [Edén2014]. By rewriting the expression for the magnetic moment (eq. 2.11) using ladder operators $\hat{\sigma}_\pm = (\hat{\sigma}_x \pm i\hat{\sigma}_y)/2$, we can easily identify those non-secular terms like $\hat{\sigma}_+\hat{\sigma}_z$, $\hat{\sigma}_+\hat{\sigma}_+$, etc. and discard them. We arrive at

$$\mathcal{H}_{\text{dd}} = \frac{\mu_0}{4\pi \, r^3} \left(\frac{\mu_B}{2} \right)^2 \Big[(\vec{u}^x \cdot \vec{u}^x + \vec{u}^y \cdot \vec{u}^y) (\hat{\sigma}_+\hat{\sigma}_- + \hat{\sigma}_-\hat{\sigma}_+) + (\vec{u}^z \cdot \vec{u}^z) \, \hat{\sigma}_z\hat{\sigma}_z$$
$$- 3 \left((\vec{u}^x \cdot \hat{r})^2 + (\vec{u}^y \cdot \hat{r})^2 \right) (\hat{\sigma}_+\hat{\sigma}_- + \hat{\sigma}_-\hat{\sigma}_+) - 3(\vec{u}^z \cdot \hat{r})^2 \, \hat{\sigma}_z\hat{\sigma}_z \Big]. \tag{2.15}$$

In the context of pairwise interactions, the product of two spin operators always denotes the tensor product in this work, e.g. $\hat{\sigma}_z\hat{\sigma}_z = \hat{\sigma}_z \otimes \hat{\sigma}_z$.

Thus, the Hamiltonian has the form

$$\mathcal{H}_{\text{dd}} = 2J_S (\hat{\sigma}_+\hat{\sigma}_- + \hat{\sigma}_-\hat{\sigma}_+) + J_I \, \hat{\sigma}_z\hat{\sigma}_z. \tag{2.16}$$

The first term couples anti-parallel spin-pairs with their opposite orientations, $|\uparrow\downarrow\rangle \leftrightarrow |\downarrow\uparrow\rangle$, a process that we call flip-flop and discuss in chapter 4.4.3. In contrast, the second term induces an energy shift depending on the spin state of the interaction partner, which will eventually lead to dipolar broadening and spectral diffusion (see section 4.2.3). Therefore, we will refer to J_S and J_I as the flip-flop and spectral diffusion coupling coefficients.

We can derive a more compact expression for J_I by introducing the angle $\alpha = \angle \left(\vec{u}_z, \hat{r} \right)$, and writing $\vec{u}_z = \mathbf{g} \cdot \vec{b}_{\text{eff}}$ (cf. equations 2.12, 2.4 and 2.6):

$$\langle \uparrow\uparrow | \mathcal{H}_{\text{dd}} | \uparrow\uparrow \rangle = J_I = \frac{\mu_0}{4\pi \, r^3} \left(\frac{\mu_B}{2} \right)^2 \left[\vec{u}^z \cdot \vec{u}^z - 3 \left(\vec{u}^z \cdot \hat{r} \right)^2 \right] \tag{2.17}$$

$$= \frac{\mu_0}{4\pi \, r^3} \frac{h^2 \gamma_{\text{eff}}^2}{4} \left[1 - 3\cos^2 \alpha \right] \tag{2.18}$$

with the effective gyromagnetic ratio γ_{eff}, expressed in the components of the magnetic field unit vector $\vec{b} = \vec{B}/B$:

$$\gamma_{\text{eff}} = \frac{\mu_B}{h} |\vec{u}^z| = \frac{\mu_B}{h} \sqrt{\frac{\sum g_i^4 \, b_i^2}{\sum g_i^2 \, b_i^2}} \tag{2.19}$$

Similarly, an analytical expression for J_S could be obtained as well [Car2019], but it is more lengthy because of its dependence on two angles, $\angle(\vec{u}^x, \hat{r})$ and $\angle(\vec{u}^y, \hat{r})$, and not necessary for this work.

As we will discuss in more detail in section 5.2.3, the spectral diffusion mechanism sets an upper bound to the achievable coherence time of interacting spin ensembles. The effect corresponds to an inhomogeneous emission linewidth $\Delta\nu_{\text{fwhm}}$ that can be calculated by averaging eq. 2.18 over random spin configurations of neighboring dopants (see appendix A.1):

$$\Delta\nu_{\text{fwhm}} = \frac{2\pi}{9\sqrt{3}} \, \mu_0 h \gamma_{\text{eff}}^2 \, n \tag{2.20}$$

Dipolar interaction between dissimilar erbium ions

If the Zeeman energies of both spins are not the same, e.g. because they belong to different crystallographic sites, the secular approximation disallows flip-flop processes and the coupling Hamiltonian reduces to a pure $\hat{\sigma}_z \hat{\sigma}_z$ term. The coefficient J_I, however, looks more complex than in eq. 2.17, because in general the two spins have different g-tensors and thus their directional vectors $\vec{u}_1^z$ and $\vec{u}_2^z$ are not aligned.

The resulting dipolar broadening due to dissimilar spins can be calculated by [Lim2018]

$$\Delta\nu_{\text{fwhm}} = \frac{2\pi}{9\sqrt{3}} \, \mu_0 h \gamma_{\text{eff},1} \gamma_{\text{eff},2} \, n, \tag{2.21}$$

as we will numerically validate in section 4.2.3. Here, $\gamma_{\text{eff},1}$ and $\gamma_{\text{eff},2}$ are the effective gyromagnetic ratios of site 1 and site 2, and n is the density of just the perturbing spins.

2.5 Superhyperfine structure

To fully understand the dynamics and energy spectrum of Er^{3+}:YSO, we also need to take interactions between erbium dopants and the magnetic moments of other crystal constituents into account, most prominently due to yttrium nuclear spins. To distinguish such coupling from the hyperfine interaction between electron and nuclear spin of the same ion, the interaction between erbium electron and yttrium nuclear spin is called 'superhyperfine interaction'. It can be modeled as dipole-dipole coupling and with no significant contribution from contact interaction, since erbium $4f$ states are confined to their own nucleus and have negligible overlap with neighboring nuclei [Macfarlane1998, Car2018].

Yttrium has a magnetic g-factor of $g_n = -0.274$ and a spin of $I = 1/2$, resulting in a magnetic moment of about $h \cdot 1\,\text{MHz/T}$ [Stone2005]. Although this value is four to five orders of magnitude smaller than a typical magnetic moment of an erbium electron spin, coupling to yttrium nuclear spins can be significant because they are in close proximity to each erbium dopant. Still, the coupling is extremely asymmetric: while the average magnetic field induced by an erbium electron spin at the nearest-neighbor yttrium site can be more than $100\,\text{mT}$, the reciprocal magnetic field induced by the yttrium nuclear spin at the erbium ion is only on the order of $\sim 5\,\text{μT}$. Therefore, a perturbative treatment seems reasonable.

We can assume that the precession axis of erbium magnetic moments is solely determined by the external magnetic field $\vec{B}$, while the precession axis of yttrium spins also depends on the magnetic field induced by the nearest erbium ion, $\vec{B}_{\text{Er}\to\text{Y}}$. Because the Larmor frequency of the erbium electron is much higher than that of the nuclear spin, the induced magnetic field only depends on the expectation value of the erbium magnetic moment, $\langle \vec{m} \rangle$. In a system with isotropic g-tensor, this would be the projection of the magnetic moment on the $\vec{B}$-axis,

but in general the expectation value is not aligned with the field, and we find (eq. 2.11): $\langle\vec{m}\rangle = \mp\mu_B\,\vec{u}^z/2$. As a result, the induced field is

$$\vec{B}_{\text{Er}\to\text{Y}} = \pm\frac{\mu_0}{4\pi\,r^3}\frac{\mu_B}{2}\left(\vec{u}^z - 3\left(\vec{u}^z\cdot\hat{r}\right)\hat{r}\right) \tag{2.22}$$

and the perturbation Hamiltonian then reads

$$\mathcal{H}_{\text{shf}} = -g_n\mu_N\vec{I}\cdot\left(\vec{B} + \vec{B}_{\text{Er}\to\text{Y}}\right), \tag{2.23}$$

where μ_N is the nuclear magneton and $\vec{I}$ the nuclear spin vector of yttrium.

If there was only a single yttrium site coupled to the erbium ion, the four electron spin states in ground and excited level would each split into two (see figure 2.3). The magnitude of such superhyperfine splitting depends on the particular yttrium site and its distance and orientation relative to the erbium magnetic moment, with maximum values of a few 100 kHz.

Furthermore, not only the amplitude but also the orientation of the induced magnetic field $\vec{B}_{\text{Er}\to\text{Y}}$ changes between ground and excited state of the erbium electron, because their g-tensors are different. As consequence, optical excitation of the erbium dopants can stimulate transitions between yttrium nuclear spin states, which we will discuss in more detail in chapter 4.3.3. As we will show, such optical superhyperfine transitions can be suppressed by applying a high external magnetic field.

Although a level scheme consisting of four doublets can be used to describe the coupling between the erbium ion and a specific yttrium site, the combined frequency shift due to interaction with all neighboring nuclear spins will rather appear as inhomogeneous broadening, which we will discuss in more detail in section 4.2.4.

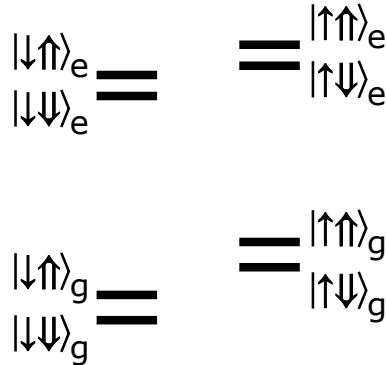Figure 2.3: **Superhyperfine states for a single dipole-coupled Er-Y pair.** Because the yttrium nuclear spin ($\Uparrow$ or $\Downarrow$) interacts with the magnetic field induced by the erbium electron spin ($\uparrow$ or $\downarrow$), all states split into superhyperfine doublets. In general, the superhyperfine splittings in ground and excited state are different because they depend on the electron g-tensor.

2.6 Hyperfine structure of ^{167}Er

Of all stable erbium isotopes, ^{167}Er is the only one with a nuclear spin ($I = 7/2$); its natural isotope abundance is about 23% [Stone2005, Meija2016]. Because of the additional nuclear spin degree of freedom, ^{167}Er has in total 16 hyperfine states in place of each ground and excited state doublet. While at high magnetic fields they can be clearly separated into electron-like and nuclear-like states, the presence of a non-zero hyperfine tensor, **A**, leads to a hybridization at low magnetic fields. Together with a quadrupole interaction tensor, **Q**, we can write the full hyperfine Hamiltonian for ^{167}Er in the effective spin-1/2 model as [Horvath2019, Abragam2012]

$$\mathcal{H}_{\mathrm{hf}} = \mu_B \vec{B} \cdot \mathbf{g} \cdot \vec{S} - \mu_N g_n \vec{B} \cdot \vec{I} + \vec{I} \cdot \mathbf{A} \cdot \vec{S} + \vec{I} \cdot \mathbf{Q} \cdot \vec{I} \tag{2.24}$$

Since now the Hilbert space is 16-dimensional, the spin components of $\vec{S}$ and $\vec{I}$ along the coordinate axes need to be expressed in the product space spanned by both operators:

$$\vec{S} = \sum_{i \in \{x,y,z\}} \vec{e}_i \, \hat{S}_i \otimes \hat{\mathbb{1}} \,, \quad \text{and} \quad \vec{I} = \sum_{i \in \{x,y,z\}} \vec{e}_i \, \hat{\mathbb{1}} \otimes \hat{I}_i, \tag{2.25}$$

where $\vec{e}_i$ are the basis vectors of the coordinate system and $\otimes$ denotes the outer product.

Because the dopants have an electron spin of $S = 1/2$, we can still write the spin operators as multiples of the Pauli matrices, $\hat{S}_i = \hbar \hat{\sigma}_i / 2$. For the nuclear spin with $I = 7/2$, however, we have to use generalized spin matrices that can be derived from the properties of the angular momentum and the ladder operators $I_{\pm} = I_x \pm i\, I_y$. For an arbitrary angular momentum I, the corresponding matrix elements are as follows: [Weil2006]

$$(I_x)_{mn} = \frac{\hbar}{2} \left(\delta_{m,n+1} + \delta_{m+1,n} \right) \sqrt{(I+1)(m+n-1) - mn} \tag{2.26}$$

$$(I_y)_{mn} = \frac{i\,\hbar}{2} \left(\delta_{m,n+1} - \delta_{m+1,n} \right) \sqrt{(I+1)(m+n-1) - mn} \tag{2.27}$$

$$(I_z)_{mn} = \hbar \, \delta_{m,n} \left(I + 1 - m \right) \tag{2.28}$$

Here, m and n are the matrix row and column, with $1 \leq m, n \leq (2I+1)$, and $\delta_{m,n}$ is the Kronecker delta.

These expressions allow us to write the hyperfine Hamiltonian in eq. 2.24 as 16-dimensional matrix. By diagonalizing it numerically, we can calculate the expected level structure, as shown in figure 2.4. The typical splitting between nuclear-like hyperfine states is about $\sim 765\,\mathrm{MHz}$.

Due to their smaller magnetic moments, nuclear spins of ^{167}Er provide a qubit resource even at high magnetic fields, where all paramagnetic impurities occupy their electronic ground states. In combination with their weaker coupling to magnetic noise from other nuclear magnetic moments in the crystal, the coherence time of ^{167}Er nuclear spins can extend to more than a second. [Rančić2018]

While we present an absorption spectrum for an isotope-enriched ^{167}Er-doped crystal in section 4.3.4, the focus of this work is on zero-nuclear-spin isotopes ^{164}Er, ^{166}Er, ^{168}Er and ^{170}Er, as found in erbium-doped crystals with natural isotopic composition.
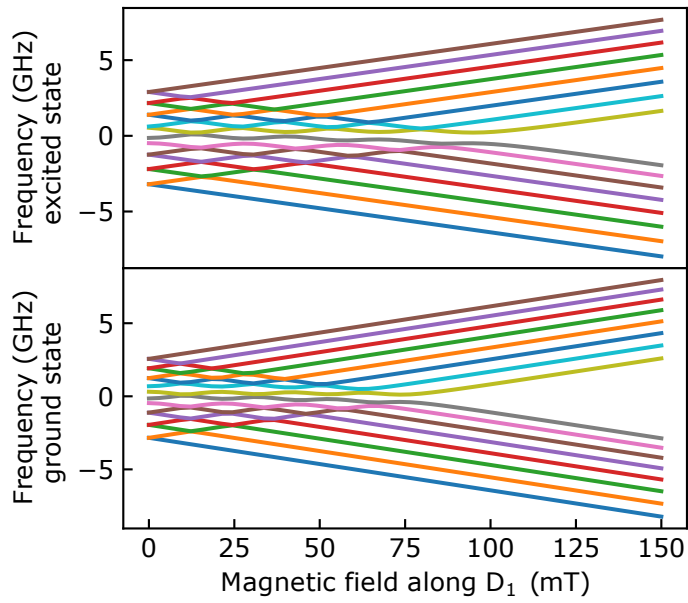
Figure 2.4: **Hyperfine levels of ^{167}Er:YSO.** About 23 % of all erbium ions have a nuclear spin of $I = 7/2$, and the resulting hyperfine interaction splits ground and excited level into 16 hyperfine states, each. Here, the states were calculated from eq. 2.24 for a magnetic field along the D_1 axis, with parameters (for site 1) taken from [Horvath2019].

3 Experimental setup and lab equipment

Before we turn to the actual spectroscopy experiments in the next and following chapters, we give an overview over the hardware used in this work and provide details on some technical aspects. In this chapter, we focus on the crystals, the cryostat geometry and the laser system. Spectroscopy of single dopants also requires sufficient laser stability. To this end, we develop and characterize a fiber ring-resonator as potential alternative for an optical frequency reference.

3.1 Transmission measurements of Er:YSO at cryogenic temperature

In order to resolve the $1.5\,\mu$m zero-phonon line and manipulate and study the spin of erbium dopants in YSO, their coupling to phonons needs to be suppressed by operating at cryogenic temperature. In this work, we work with different cryostats, crystals and magnetic field orientations, and the actual measurement geometry depends on all three of them. In the following, we first specify which crystals we investigate, then we show different measurement geometries, and in the end we list all hardware that we use in a typical experiment.

3.1.1 YSO crystals

In this work, we use YSO crystals grown by *Scientific Materials.* For holeburning spectroscopy in chapters 4 and 5, the crystals are doped with 10 ppm of erbium (relative to the total concentration of yttrium sites), while the cavity experiments in chapter 6 are performed on nominally undoped crystals with a residual erbium contamination of about 0.2 ppm (see section 6.3.3).

All samples are thin slabs that are cut along the D_1-D_2 plane; with thicknesses along the b-axis of 2 mm for holeburning experiments in chapter 4, 0.5 mm for microwave experiments in chapter 5, and 0.02 mm for cavity experiments in chapter 6. In order to apply magnetic fields along specific directions relative to the crystal axes, we use different measurement geometries as described in the following.

3.1.2 Cryostat setups

In most of our experiments we use a helium closed-cycle cryostat 'Attodry2100' with a base temperature of $\sim 1.8\,$K and optical access through a top window. By mounting the sample at the bottom of a $\sim 1\,$m long sample stick that is suspended at the top of the cryostat, it is – to some extent – isolated from vibrations generated by the cryostat pulse tube, while thermalization occurs via helium exchange gas.

In the simplest geometry for a transmission measurement, the erbium-doped crystal slab is placed horizontally on a mirror. A laser beam incident from the top is reflected at the mirror and passes the sample twice before leaving the cryostat through the top window again (see figure 3.1a). Because the superconducting solenoid in the cryostat can only generate vertical magnetic fields, however, such configuration only allows for measurements with the magnetic field $\vec{B}$ oriented along the crystal b-axis.

By placing the crystal upright in a rotation mount, the magnetic field is applied in the D_1-D_2 plane, such that the two crystallographic subclasses I and II are also equivalent. Now

we implement a measurement geometry where the excitation beam and the transmitted beam propagate separately along the sample stick (see figure 3.1b). Optical elements along the beam path ensure robust coupling and can be altered to shape the beam at the crystal position, e.g. by creating a focus point with additional lenses.
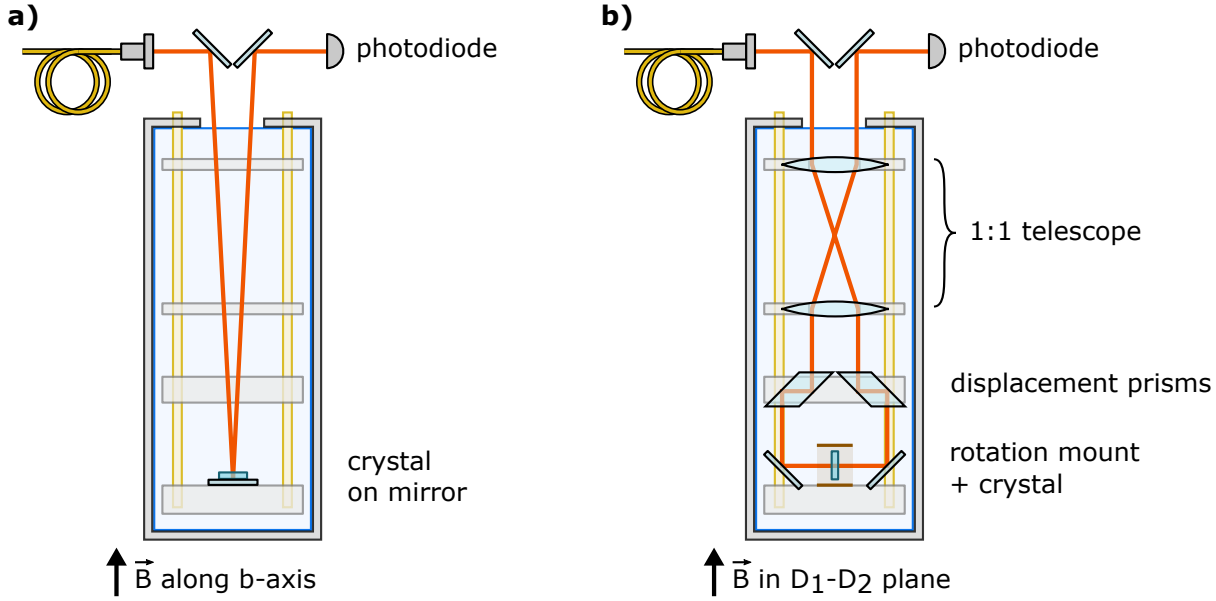
Figure 3.1: **a) Beam path in the cryostat sample stick for $\vec{B} \parallel$ b.** For low-temperature transmission measurements, the crystal is mounted at the bottom end of a sample stick inside a closed-cycle cryostat, with a vertical magnetic field provided by a superconducting solenoid. Since crystals used in this work are slabs parallel to the D_1-D_2 plane, the sample is oriented horizontally in order to apply the magnetic field along the crystal b-axis. **b) Beam path in the cryostat sample stick for $\vec{B} \perp$ b.** In order to study different magnetic field orientations in the D_1-D_2 plane, the crystal is mounted vertically in a rotation mount. 45°-mirrors deflect the output of a fiber collimator into the cryostat, through the crystal, and back along the sample stick onto a photodiode. Since the optical access is restricted to a 1-inch window while the vacuum tube diameter is 5 cm, a pair of prisms displaces the transmitted beam closer to the sample stick axis. To reduce beam pointing sensitivity, a pair of lenses form an inverting, non-magnifying telescope. All components are mounted on aluminum plates connected by fiber glass rods.

Setup with permanent magnets

For experiments on coherent spin control with microwaves and dynamical decoupling in chapter 5 we use a different closed-cycle cryostat, the 'PhotonSpot' helium sorption fridge with a base temperature of 0.8 K. Instead of thermalization via exchange gas, the sample is connected to a copper cold finger, so that a long sample stick is obsolete and a compact construction is possible. Because this cryostat does not include superconducting coils, we use a pair of neodymium disk magnets with 7 cm diameter (Maqna) that are placed on opposite sides outside of the sample space (see figure 3.2). By moving them horizontally around the cryostat, we can change the magnetic field orientation and strength, up to a maximum amplitude of ~ 30 mT.
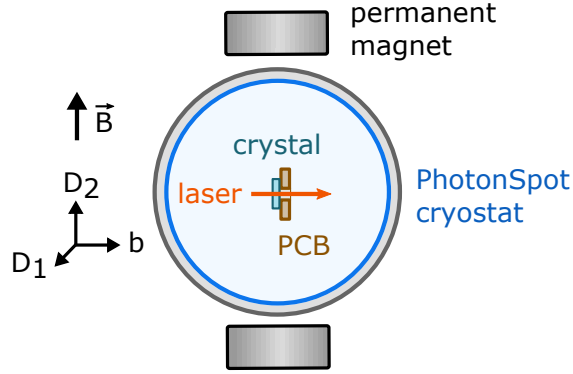
Figure 3.2: **Measurement geometry in the PhotonSpot cryostat (top view).** Because there is no superconducting solenoid inside the PhotonSpot cryostat, we place two permanent magnets outside to generate a magnetic field, here for $\vec{B} \parallel D_2$. We mount the crystal on a printed circuit board (PCB) to apply microwaves (see section 5.1.3), with a hole for optical access. In early experiments, the laser beam is collimated and fiber-coupled with anti-reflection coated gradient-refractive-index lenses next to the crystal; in later experiments, windows were added to the cryostat for free-space optical access.

3.1.3 Laser system and experiment control

For optical excitation of the erbium ions at $\sim 1536\,\mathrm{nm}$, we use commercial narrow-band laser systems: the NKT Photonics BASIK X15 laser 'Koheras', the OEwaves Gen 3, and a Toptica DL pro. Because of its inferior short-term stability, the latter one is only used for microwave experiments in chapter 5, where all spectral features have widths of several megahertz. In order to achieve excellent long-term stability, we establish phase-locks for all lasers to a frequency comb (Menlo Systems FC1500-250-ULN) that in turn is locked to a frequency reference. In the beginning of this project, a radio-frequency reference with stability of 10^{-14} was used, but over the course of the experiment it was upgraded to an optical resonator (Menlo Systems ORS1500) with sub-hertz stability.

Gating of the laser beams is implemented using Gooch & Housego acousto-optical modulators operating at modulation frequencies of 100, 200 or 300 MHz, provided by a direct digital synthesis (DDS) radio-frequency source that also allows for fast frequency sweeps. The detection of optical excitation and transmission signals is done either with conventional InGaAs photodiodes (Thorlabs PDA10) or with an avalanche photodiode (Thorlabs APD430C or PDB570C). A field-programmable gate array (FPGA) from National Instruments (cRIO-9035) with 50 ns time resolution triggers the DDS rf source and records the photodiode voltages.

Note that the laser setup for cavity experiments is more complex, because an additional laser is required to stabilize the cavity length and the erbium fluorescence is detected with a single photon counter that needs to be protected by a series of filter elements. More details will be provided in section 6.2.5.

3.2 Laser stabilization to a fiber ring resonator at cryogenic temperature

While the frequency comb setup, to which we lock our lasers, can provide an optical reference with sub-Hz linewidth and stability of 10^{-15}, such an ultra-stable optical frequency reference is expensive and requires professional maintenance, and it became only available to our group after we had started this project. Here, we explore the potential of a cryogenic fiber ring-resonator as an alternative frequency-stable reference. Such an approach is particularly attractive, because its cryogenic operation at a temperature-insensitive point promises lower thermal noise, which otherwise limits the short-term stability of state-of-the-art optical resonators.

In this section, we first review current technologies and how they motivate the development of a cryogenic fiber-based frequency reference. We explain in more detail the competing mechanisms that give rise to a temperature-insensitive point around 3.5 K and describe the technical details of our resonator. Then, we characterize its sensitivity to vibrations and fluctuations in temperature and pressure. In the end, we extrapolate the stability observed in our proof-of-concept experiment to the controlled environments that are achieved in other work and compare the expected stability with already existing systems.

Overview and motivation

The construction of lasers with ultra-high frequency stability is a key enabling technology for optical atomic clocks [Ludlow2015] and a large variety of precision measurements [Krohn2014, Ghelfi2014, Derevianko2014, Hogan2016, Canuel2018, Karr2019]. In spite of recent alternative approaches [Norcia2018], the best results have been obtained with lasers locked to ultra-stable external frequency references. Well-studied examples for such system include spectral holes in rare-earth doped crystals [Thorpe2011, Cook2015], fiber-optical delay lines [Kéfélian2009, Dong2015, Dong2016], as well as whispering-gallery-mode [Lim2017] and Fabry-Perot resonators [Salomon1988, Webster2008, Kessler2012]. The latter have demonstrated an impressive performance down to a relative frequency stability of $4 \cdot 10^{-17}$ [Matei2017]. In that experiment, the detrimental effect of temperature fluctuations has been minimized by operating a crystalline silicon resonator at a zero-crossing of its thermal expansion coefficient around 124 K. The achieved frequency stability has then been limited by thermal noise of the mirror coatings [Numata2004]. While this noise can be reduced by cooling to even lower temperature [Zhang2017, Robinson2019], this comes at the prize of a larger sensitivity to temperature drifts, as the system is then operated below the zero-crossing of the thermal expansion coefficient of silicon.

Therefore, in this section we explore a cryogenic fiber-based resonator as an alternative design for a frequency-stable reference. This has two advantages: First, such resonator is easier to implement as it only requires off-the-shelf components. Second, we show that our fiber resonator exhibits a temperature-insensitive point around 3.55 K, 35-fold lower than that of crystalline silicon studied previously [Zhang2017].

Fiber delay lines have been investigated at room temperature, mainly because of their lower cost and complexity [Kéfélian2009] as compared to Fabry-Perot resonators. Recent experiments have demonstrated sub-Hz short-term stability [Dong2015]. However, both temperature fluctuations and thermal noise have been limiting the performance [Dong2016]. Here we show that both of these limitations can be alleviated when operating at cryogenic temperature.

Our experiment is intended as a proof-of-concept. We thus do not target or achieve the ultra-high precision of other cryogenic experiments with Fabry-Perot resonators [Zhang2017] or rare-earth doped crystals [Thorpe2011, Cook2015]. Still, we perform a detailed characterization

of our device with respect to vibrations as well as temperature and pressure instability. The observed low sensitivity and in particular the existence of a temperature-insensitive point make our approach promising for future precision experiments.

3.2.1 Expected temperature dependence

In our experiment we use a fiber ring resonator which exhibits a ladder of equidistant resonances with free spectral range $f_{\mathrm{FSR}} = c/(nL)$. Here, n is the refractive index, L the length of the fiber, and c the speed of light. In most Fabry-Perot frequency references investigated to date [Matei2016, Webster2008] the cavity field is in vacuum with constant $n = 1$. Thus, a temperature-insensitive point is observed when the thermal expansion coefficient $\alpha = L^{-1}(\partial L/\partial T)$ exhibits a zero-crossing. In contrast, in our experiment the light is guided in a silica fiber, whose refractive index changes with temperature T, as described by the normalized thermo-optic coefficient $\beta_{\mathrm{TO}} = n^{-1}(\partial n/\partial T)$. In our setting, both the thermal expansion [White1975] and the thermo-optic coefficient [Arcizet2009] change with temperature. The combined sensitivity $\alpha + \beta_{\mathrm{TO}}$ of fused silica exhibits a zero-crossing around $13\,\mathrm{K}$ [Arcizet2009], making it a promising material for cryogenic frequency references.

Instead of pure glass, we use a commercial fiber, which gives an additional contribution to the total temperature sensitivity. The fiber cladding will exert a radial pressure on the core if their thermal expansion coefficients are not the same, which changes both the refractive index and fiber length. The effect on phase stability has been studied recently down to temperatures below $100\,\mathrm{K}$ [Zhu2020], finding that acrylate coatings transition to a stiff, glass-like state with thermal expansion converging to zero at $0\,\mathrm{K}$. In our modeling, we include the effect of thermal strain as coefficient β_{TS}, getting the total temperature sensitivity:

$$\frac{1}{f}\frac{\mathrm{d}f}{\mathrm{d}T} = -(\alpha + \beta_{\mathrm{TO}} + \beta_{\mathrm{TS}}). \tag{3.1}$$

The existence, temperature and curvature of a temperature-insensitive point, which corresponds to a zero-crossing of eq. 3.1, will thus depend on the used fiber. In particular the material and diameter of the core, cladding, and acrylate coating will determine the thermal strain coefficient. While we use a standard commercial product for our initial experiments, this gives access to a large parameter space for future optimization.

3.2.2 Setup

In our experiment, we fabricate a fiber ring resonator by splicing the ends of a 95:5 fused fiber beam-splitter to a $\sim 120\,\mathrm{m}$ long fiber. The latter is coiled to an aluminum cylinder of $4\,\mathrm{cm}$ outer diameter that fits into the sample space of our closed-cycle cryostat. To avoid bend-induced loss that would limit the finesse, both the beam-splitter and fiber are made from Corning® ClearCurve® bend-insensitive fiber. We do not expect that the properties of the fused coupler (Evanescent Optics Inc., type 954) significantly influence our measurements.

We first determine the resonator properties at cryogenic temperature by measuring its transmission at $1535\,\mathrm{nm}$ through the two open ports of the beam-splitter, cf. figure 3.3. After adjusting the input polarization to match one of the resonator eigenmodes, we observe a free spectral range of $1.71(4)\,\mathrm{MHz}$ and a fwhm linewidth of $87(7)\,\mathrm{kHz}$. This corresponds to a finesse of $20(1)$ and a round-trip transmission of about $70\,\%$. This value is limited by the splice-, bend- and absorption loss of the fiber and the excess loss of the beam splitter, and might be further increased in future devices. The sample is thermalized to its cryogenic environment via helium exchange gas, whose pressure is monitored with a Pirani pressure gauge at ambient temperature. To characterize the sensitivity of the device to perturbations, we attach a cryogenic vibration sensor and a resistive thermometer in close proximity to the ring resonator.
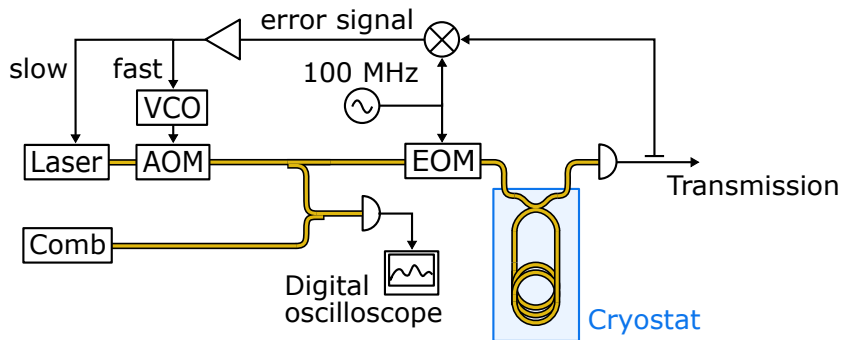
Figure 3.3: **Experimental setup.** A cryogenic fiber ring resonator serves as a frequency reference for stabilizing a laser at $1535\,\mathrm{nm}$. To this end, the transmission is measured by a fast photodiode. An error signal is generated using the Pound-Drever-Hall technique with the help of a radio-frequency source at $100\,\mathrm{MHz}$, an electro-optical modulator (EOM) and a mixer. The feedback signal is applied to a voltage-controlled oscillator (VCO) that drives an acousto-optical modulator (AOM). In addition, slow drifts of the laser frequency are compensated via its tuning port. To characterize the frequency stability, the beating signal of the laser light with an ultra-stable frequency comb is recorded.

3.2.3   Vibration sensitivity

We now study the stability of the resonator against external perturbations. To investigate its short-term stability, we lock the laser (Koheras BASIK X15) to the frequency comb. We then tune the laser to the side of the fiber resonator transmission dip. Fluctuations of the resonator frequency will lead to a fluctuation of the transmitted power, which we transfer to frequency deviations using the independently measured spectral response. The resulting time trace is shown in figure 3.4a.

A fast-Fourier-transform gives the spectral properties of the frequency shift (3.4b), which exhibits a number of peaks at different frequencies (black). The reason for the peaked structure is acoustic resonances that are excited by the broadband noise of our pulse tube cryocooler. The position and width of the resonances shows large similarities with the vibration spectrum measured by the attached piezo-electric sensor (blue).

Deviations in the amplitude of the peaks can be explained by the sensor being only sensitive to vibrations along the axis parallel to the coil center, while the resonator will be sensitive to vibrations along all axes. By comparing the peaks in the spectra of sensor and resonator between 0.3 and 4 kHz, we can estimate that the vibration sensitivity of our resonator is about $< 5 \cdot 10^{-11} \, (\mathrm{m/s^2})^{-1}$ in that frequency range.
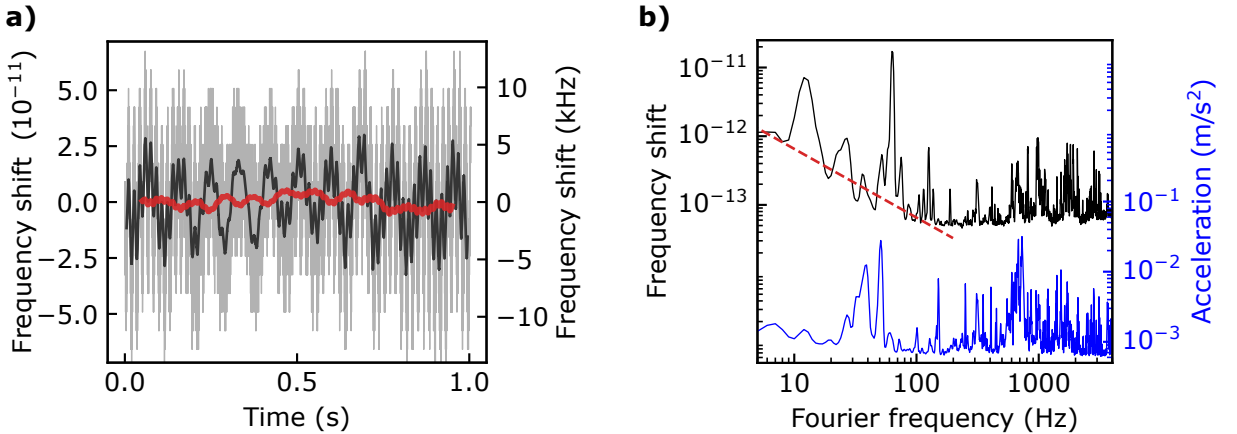
Figure 3.4: **Short-term stability.** (a) Frequency shift of the resonance as a function of time (grey), with running averages over 10 ms (black) and 100 ms (red). (b) Transmission spectrum (black) of the fiber ring resonator obtained from the data in (a), compared to the sample stage vibrations (blue) measured by a cryogenic acceleration sensor. The red dashed line indicates the calculated noise floor caused by measured temperature drifts of about 1 mK/s.

3.2.4   Characterization of temperature and pressure sensitivity

As a next step, we investigate the sensitivity with respect to temperature and pressure changes by locking the laser to the resonator using the Pound-Drever-Hall technique [Black2001], with an input power of ~ 0.1 mW. We use a modulation frequency that is much larger than the free-spectral range and tuned such that the sidebands are halfway between higher-order resonances and thus not phase-shifted upon transmission. We then record the frequency difference between the laser and frequency comb after changing the sample space temperature and waiting a few seconds until full thermalization.

The obtained temperature dependence (with a constant amount of helium in the sample space) is shown in figure 3.5a. We observe a first-order temperature-insensitive point around 3.55 K. The data is well-fit by a third-order polynomial (red curve), from which we extract the curvature at the turning point, $-22(1) \cdot 10^{-9} \, \mathrm{K}^{-2}$. We repeat this procedure for different
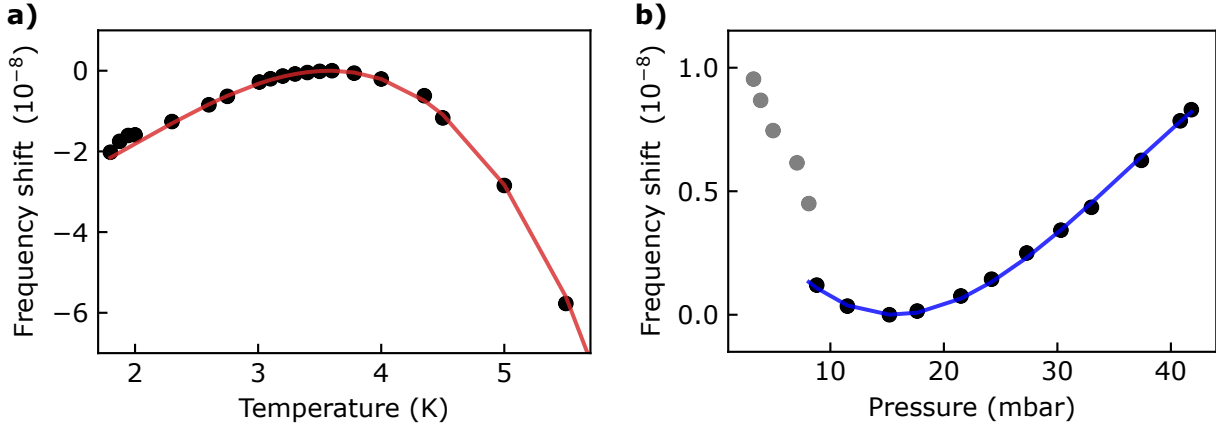
Figure 3.5: **Temperature and pressure sensitivity. a)** The frequency shift of the fiber ring resonances with temperature shows a turning point around $3.55\,\mathrm{K}$, shown for an exchange gas pressure of $18\,\mathrm{mbar}$. The measured data (black dots) are fit by a third-order polynomial (red line) to extract a curvature of $-22(1) \cdot 10^{-9}\,\mathrm{K}^{-2}$ at the turning point. **b)** Shift of the resonance frequency with pressure at a temperature of $3.55\,\mathrm{K}$. At low pressure (grey dots) the resonator thermalization may be impaired. A fit to a third-order polynomial (blue line) gives a pressure-insensitive point around $15\,\mathrm{mbar}$, with a remaining pressure dependence of $4.2(2) \cdot 10^{-11}\,\mathrm{mbar}^{-2}$.

amounts of helium gas in the sample space and thus different pressures. We find that the temperature of the turning point and its curvature do not change significantly (not shown).

To directly investigate the pressure sensitivity, we evacuate the sample space and then repeatedly add small amounts of helium while the temperature of the sample space is kept at the insensitive point, $\sim 3.55\,\mathrm{K}$. The observed frequency shift (figure 3.5b) corresponds to a sensitivity of $\lesssim 5 \cdot 10^{-10}\,\mathrm{mbar}^{-1}$ over a large pressure range, with a first-order insensitive point around $15\,\mathrm{mbar}$.

Measurements at lower pressure (grey) are less reliable as the thermalization of the fiber resonator with the surroundings is impaired when the pressure is too low. Similarly, we cannot exclude that changing temperature gradients contribute to the measured pressure dependence. Thus, the above value should be considered as an upper bound.

Still, we note that the observed low pressure sensitivity justifies that our temperature scans have been performed at constant helium filling level instead of constant gas pressure. The reason is that in the investigated regime, the pressure changes at $\lesssim 2.5\,\mathrm{mbar/K}$. Thus, its impact on the temperature sensitivity is only $\lesssim 1.25 \cdot 10^{-9}\,\mathrm{K}^{-1}$, i.e. small compared to the observed temperature dependence. For the same reason, compensating temperature changes by connecting the sample space to a room-temperature helium reservoir, as pioneered in [Cook2015], does not seem promising in our fiber-based ring resonator unless the temperature sensitivity can be further reduced by materials engineering.

3.2.5 Long-term stability

After characterizing the sensitivity to external perturbations, we measured the stability over a period of sixteen hours, see figure 3.6. The inset shows the raw data with a slow linear drift by about $5 \cdot 10^{-11}\,\mathrm{h}^{-1}$, similar to the isothermal creep reported for other amorphous materials such as ultra-low expansion glass commonly used in reference cavities [Webster2008]. As it may originate from the thermal stress exerted by the fiber cladding, different fiber types may show a different linear drift. Still, after subtracting a linear fit, our resonator exhibits a long-term stability around $20\,\mathrm{kHz}$, or 10^{-10}, limited by the moderate temperature stability of $\pm 100\,\mathrm{mK}$ obtained in our cryostat.
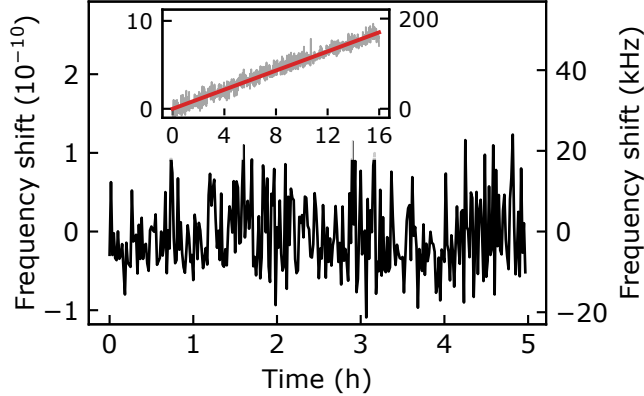
Figure 3.6: **Long-term stability.** Shift of the laser frequency when locked to the fiber ring resonator (with $60\,\mathrm{s}$ averaging intervals to eliminate the influence of vibrations). The temperature is kept within $100\,\mathrm{mK}$ around the temperature-insensitive point of $3.55\,\mathrm{K}$. The inset shows the raw data, while the main graph has been obtained by subtracting a linear fit.

3.2.6 Discussion and outlook

Our implementation does not achieve a stability that exceeds previous experiments, neither those with fiber interferometers at room temperature ($5 \cdot 10^{-15}$) [Dong2015], nor that of cryogenic silicon resonators ($4 \cdot 10^{-17}$) [Matei2017]. The reason is that our setup does not include any thermal shields or vibration-damping enclosures. Instead, it constitutes a proof-of-concept experiment to determine the sensitivity to pressure, temperature and vibrations, which we discuss in the following.

Vibration sensitivity

The extracted vibration sensitivity of our fiber coil, $< 5 \cdot 10^{-11}\,(\mathrm{m/s^2})^{-1}$, is only about tenfold larger than that of specially optimized, unitary aspect ratio ultra-low expansion glass cavities at room temperature [Webster2008, Leibrandt2011] and that of crystalline silicon resonators [Matei2017]. Operating our resonator in a closed-cycle cryocooler with decoupled vibrations down to a level of $\lesssim 10^{-3}\,\mathrm{m/s^2}$ [Zhang2017], we expect that our fiber ring resonator would perform around 10^{-14} short-term stability.

Even better short-term stability can be achieved with improvements of our resonator design. First, additional vibration damping material may be inserted between the aluminum cylinder and the fiber coil. Second, increasing the fiber length while reducing the finesse may be advantageous. Third, an optimized geometric arrangement of the fiber may reduce the vibration sensitivity, with a fifty-fold lower value demonstrated at room temperature [Huang2019]. Finally, our setup does not require coupling of a free-space optical beam into

a micro-sized resonator mode. Thus, it should be possible to build an effective cryogenic vibration isolation stage. As the thermalization is done by exchange gas, one could e.g. simply use a large mass on a soft spring to hold the fiber resonator while damping out all high-frequency vibrations. Alternatively, active damping and magnetic levitation could be implemented in cryostats with larger sample space, offering the potential for unprecedented short-term stability.

Temperature and pressure sensitivity

In this context, also the upper bound of the pressure sensitivity, $4.2(2) \cdot 10^{-11} \, \text{mbar}^{-2}$, is important. It is much smaller than the linear change of $\sim 3 \cdot 10^{-7} \, \text{mbar}$ observed with Fabry-Perot cavities at room temperature and atmospheric pressure [Egan2015]. Getting the stability to the 10^{-16} level would require pressure stabilization to 10^{-4}, which should be straightforward in a closed cryogenic volume. Alternatively, placing the system in cryogenic vacuum with typical pressures $\ll 10^{-9} \, \text{mbar}$ will eliminate the influence of pressure and its fluctuations.

Next, we compare the observed temperature sensitivity of $22(1) \cdot 10^{-9} \, \text{K}^{-2}$ to other experiments. It is about an order of magnitude worse than ultra-low expansion glass cavities at room temperature, $1.5 \cdot 10^{-9} \, \text{K}^{-2}$ [Webster2008], but close to that of Fabry-Perot cavities made from crystalline silicon and operated at their temperature-insensitive point, $17 \cdot 10^{-9} \, \text{K}^{-2}$ at $124 \, \text{K}$ [Kessler2012].

Therefore, to estimate the potential of our cryogenic fiber ring resonator, we make an explicit comparison with the most stable sub-10 K resonator to date: a silicon cavity operated around $4 \, \text{K}$ [Zhang2017, Robinson2019]. To achieve the same linear sensitivity ($0.02 \, \text{ppb/K}$), we would need to stabilize the fiber within $1 \, \text{mK}$ proximity to the turning point, which is directly feasible in most commercial cryocoolers. With additional passive and active heat shields, temperature fluctuations below $10 \, \mu\text{K}$ have been demonstrated [Zhang2017]. For our resonator, this would lead to an expected stability below $2 \cdot 10^{-18}$. Optimization of the fiber coating thickness and material may allow for even lower temperature sensitivity at the turning point.

Noise analysis

Still, the question whether such setup would allow for unprecedented frequency stability requires a careful analysis of thermal noise in the fiber. There are two main mechanisms predicted from theory [Wanser1992, Duan2010] and confirmed experimentally [Dong2015, Dong2016]:

At high frequencies, thermodynamic noise (thermoelastic and thermorefractive) dominates the spectrum in room temperature experiments [Wanser1992]. This contribution scales with $T^2 \frac{\text{d}f}{\text{d}T}$. When operating at cryogenic temperature, and in particular at the temperature insensitive point, it should therefore be negligible.

The second cause of thermal noise can be derived from the fluctuation-dissipation theorem, where the spectral density of spontaneous fiber length fluctuations reads [Duan2010]:

$$S_l(f) = \frac{2kTL\Phi_0}{3\pi E_0 A f}. \tag{3.2}$$

Here, k is Boltzmann's constant, L the fiber length and A its cross section, f the frequency, E_0 the value of Young's modulus without loss and Φ_0 its loss angle.

The T-scaling in the above formula suggests that cooling a fiber to cryogenic temperature may lead to an improved stability – comparing to measurements at room temperature [Dong2015] even linewidths of a few mHz seem feasible. However, care has to be taken in this

extrapolation, as the loss angle of the fiber assembly will also change when lowering the temperature. While that of the fiber will likely increase [Arcizet2009], that of the acrylate coating may be reduced when it transitions to a stiff, glass-like state [Zhu2020]. Therefore, additional measurements are required to give a reliable estimation about the ultimately achievable stability of a cryogenic fiber-based setup.

Summary

In summary, we have characterized the sensitivity of a fiber-ring resonator to environmental fluctuations at cryogenic temperature. Our approach may find direct application in laboratories that operate cryogenic setups and have moderately high requirements on laser stability. As an example, our setup is intended for spectroscopy of rare-earth doped crystals, as described in chapters 4, 5 and 6.

In addition, the robustness and light-weight design of our resonator makes it promising for laser stabilization in space [McRae2013]. Finally, when operated in an optimized closed-cycle cryostat [Zhang2017], our system may also be considered for laser stabilization to an unprecedented accuracy, depending on the yet unknown contribution of thermal noise at cryogenic temperature. If this contribution is too large, however, further reduction by two orders of magnitude seems feasible by operating our setup in a dilution refrigerator.

4 Spectral holeburning and lifetime analysis

A simple method to study the level splitting of dopants in a solid is absorption spectroscopy: when the transmission of a laser beam through the sample is detected while the excitation frequency is scanned, a drop in transmission can be observed whenever the laser is resonant with a transition.

In a moderate magnetic field, the splitting between different transitions in the effective four-level system will be larger than the ensemble broadening due to strain inhomogeneities, and individual absorption peaks can be resolved (see figure 4.1). By measuring the full absorption spectrum, it is possible to reconstruct the complete level structure. Initially, this method was used to determine the g-tensor of Er:YSO from absorption spectra at different crystal orientations in the external magnetic field [Sun2008]. Since we already know the g-tensor, we can use absorption spectra to identify the orientation of the crystal in our experiment. Furthermore, the relative peak amplitudes reflect the thermal distribution of spins in the ground states and can be used to extract the crystal temperature.

a)   **b)**
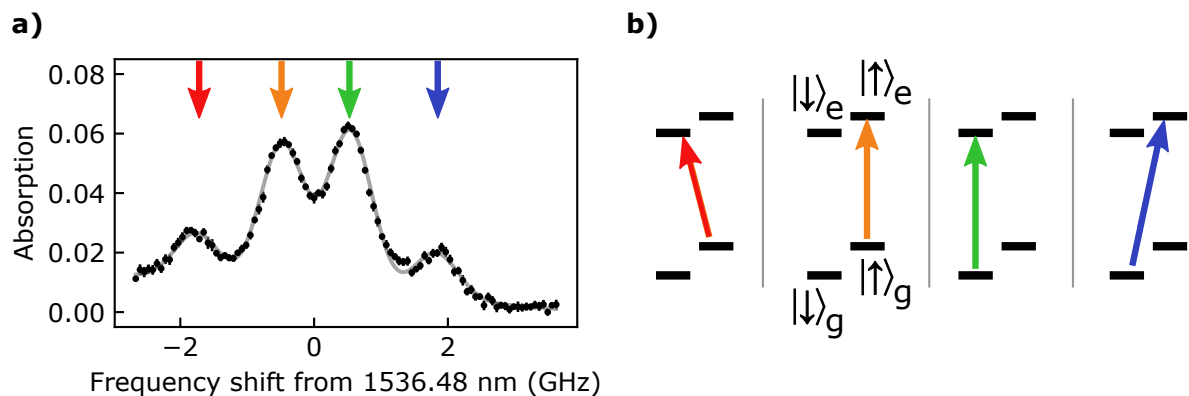
Figure 4.1: **Absorption scan (a) and level schemes (b).** From transmission measurements, we obtain the absorption spectrum of erbium dopants in YSO, which can be fit with a sum of four Lorentzians (solid grey curve). At a magnetic field of $100\,\mathrm{mT}$ along $\varphi = 28°$ in the D_1-D_2 plane, we can resolve all four absorption lines of the ensemble, with inhomogeneous widths of $0.77\,\mathrm{GHz}$. The spin-flip transitions (blue and red arrows) are significantly weaker than the spin-preserving ones (orange, green).

A simple absorption scan, however, can not resolve the level fine structure caused by interactions, because the splittings are smaller than the inhomogeneous broadening. Without controlled preparation of non-equilibrium states, an absorption spectrum does not reveal spin dynamics, either. In order to measure characteristic time scales in our system, for example the lifetime of ground state spins, and to investigate the dipolar coupling of erbium dopants in the ensemble and to other magnetic sites, we choose an advanced technique, known as holeburning spectroscopy.

In the next sections, we will first explain the basic measurement principle and how we can use holeburning spectroscopy to study inhomogeneous line broadening and spectral diffusion. Then, we discuss optical pumping, which creates non-equilibrium states and reveals the associated relaxation time constants as well as the level splittings. We demonstrate the great potential of this spectroscopy method by applying it not only to the erbium electron spin but also to the superhyperfine structure due to yttrium nuclear spins and to the hyperfine states

in ^{167}Er isotopes with nuclear spin. In the end, we focus on the erbium electron spin lifetime and discuss its dependence on temperature and magnetic field. We find lifetimes of 450 ms at low magnetic fields, which are limited by flip-flop processes caused by dipolar interactions.

4.1   Holeburning spectroscopy

At sufficiently high laser power, the $^4I_{15/2} \leftrightarrow \, ^4I_{13/2}$ transition will be saturated: then, on average half of the dopants will be in the excited state, where an incident laser photon can stimulate emission of a second photon, while the other half would be in the ground state and could absorb an incoming photon. In total, the number of transmitted photons would be the same as in the incident laser beam; there is no net absorption.

This effect can be demonstrated by a pump-probe experiment: first, an intense laser pulse strongly drives a transition at one particular frequency, then a much weaker second pulse probes the transmission while the laser frequency is swept. Dopants whose optical transition was not resonant with the first pulse were not excited and still contribute to the absorption spectrum. Only where pump and probe frequency match, the ions resonant with both lasers were saturated and now appear transparent. Because of the frequency selection by the first laser pulse, the absorption spectrum now shows narrow features called spectral holes (see figure 4.2).

Spectral holeburning is a powerful tool for several reasons: first, because of the swept probe frequency the signal is now the contrast between hole and baseline, which is more robust against fluctuations in coupling and detection efficiency. Second, the burn pulse effectively selects a small subset of ions resonant with the laser, and the spectral hole features provide a frequency resolution that is no longer limited by the ensemble inhomogeneous linewidth of the optical transition. And third, the first pulse ('burn') prepares a non-equilibrium state in the crystal, and by varying time delay between burn and probe pulse, one can study the dynamics of relaxation and spectral diffusion processes. In the following sections, we will look into these aspects in more detail.
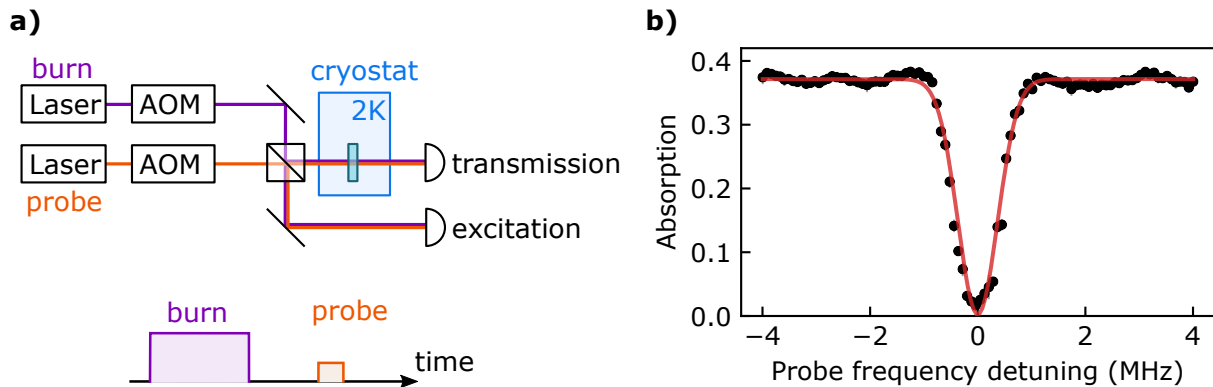
Figure 4.2:   **a) Setup and sequence for holeburning experiments.** A strong laser pulse ('burn') resonant with a transition modifies the absorption spectrum, which is probed by a second, weaker pulse ('probe'). Both pulses are generated with acousto-optical modulators (AOMs), and by varying pulse amplitudes, lengths, frequencies and delays, a variety of information about the excited dopants can be extracted from these measurements. **b) Frequency scan over the spectral hole.** After the burn pulse has saturated an optical transition, the reduced absorption will appear as 'spectral hole' in a frequency sweep of the probe laser. The data were taken for a magnetic field of 10 mT along the b-axis and fitted by a Lorentzian.

4.2 Hole broadening and spectral diffusion

By selecting only a subset of ions with the burn pulse frequency, holeburning creates spectral features much narrower than the inhomogeneous absorption line of the entire ensemble. The width of such a spectral hole, however, does not only depend on the length, power and frequency stability of the burn laser pulse, but can also increase over time due to interactions with the crystal environment, which is known as spectral diffusion. Understanding all contributing mechanisms helps us to create narrow holes and suppress spectral diffusion.

Pursuing narrow spectral holes is motivated by some protocols for storing quantum states, known as atomic frequency comb (AFC) memories, which shape the ensemble absorption line into a comb-like periodic pattern by means of holeburning. Any photon absorption creates a superposition of excitations at fixed detunings, set by the constant frequency spacing $\Delta\nu$ of the created AFC. In contrast to the random dephasing of excitations in a broad absorption line, the periodic frequency structure of an AFC rephases automatically after a storage time $T = 1/\Delta\nu$, leading to collective emission of the input photon state.

While the AFC protocol provides multi-mode capability for storing qubits at the single photon level [Riedmatten2008] and its memory time can be extended by mapping the optical excitation onto ground-level spins [Afzelius2010], its fidelity is largely dominated by the finesse of the atomic frequency comb [Afzelius2009], which is limited by the spectral width of its teeth. Therefore, the creation of narrow spectral holes and the suppression of broadening by spectral diffusion is essential for high-fidelity ensemble-based storage protocols. But even research on single dopants requires knowledge and control of spectral diffusion, as it will be seen as random jumps of the optical transition frequency over the course of an experiment.

In this section we first explain how properties of the burn laser pulse set the excitation bandwidth. Then, we discuss the dominant spectral diffusion mechanisms, namely dipolar coupling to other erbium spins in the ensemble and to yttrium nuclear spins. In the end, we compare the time scales of such diffusion processes.

4.2.1 Pulse-dependent hole width

Some of the mechanisms contributing to the total width of a spectral hole are solely set by properties of the burn laser pulse. First, the spectral shape of a laser pulse is determined by its Fourier transform. Rectangular pulses, which have been used throughout this entire work, are known to have a sinc-shaped spectrum with strong side lobes. By shaping the temporal envelope, one could achieve pulses with narrower spectral widths, with the steepest side lobe suppression provided by Gaussian pulses [Freeman1998]. Because of the non-linear response of the ions, however, the excitation bandwidth of a laser pulse can significantly deviate from its Fourier transform [McDonald1991].

For longer pulses, the excitation bandwidth is no longer dominated by the temporal envelope but by fluctuations of the laser frequency over the duration of the pulse. In this work, we used lasers with good stability on timescales shorter than $1\,\mathrm{ms}$ and locked them to an optical frequency comb as stable long-term frequency reference (see section 3.1.3 for details). Although the achieved stability varied, depending on wavelength, laser and lock parameters, typical fluctuations were on the order of a few kilohertz.

A second contribution of the laser pulse to the spectral hole width stems from broadening of the ion transition in case of high laser intensity. For a single ion, such power broadening leads to an effective line shape given by [Citron1977]

$$A(\widetilde{\Delta}) \sim \frac{\widetilde{P}}{\widetilde{\Delta}^2 + 1 + \widetilde{P}}.\tag{4.1}$$

Here, we use dimensionless parameters that are obtained by normalizing the excitation power P to the saturation power P_{sat}, $(\widetilde{P} = P/P_{\mathrm{sat}})$, and the detuning Δ to half of the transition fwhm $\Delta_{\mathrm{fwhm,0}}$ without power broadening, $(\widetilde{\Delta} = 2\Delta/\Delta_{\mathrm{fwhm,0}})$.

In our experiments, however, we observe a deviation of this saturation behavior (see figure 4.3), because we illuminate the erbium-doped crystal with a Gaussian beam, and when the peak intensity is high enough to saturate ions in the beam center, there will be still ions further away from the beam axis that are not saturated. To reflect this aspect in the model, we integrate over the Gaussian intensity profile, with a dimensionless distance $\widetilde{r} = \sqrt{2}r/w$ from the beam axis, where w is the beam radius and r the distance from the center:

$$A(\widetilde{\Delta}) \sim \int_0^\infty \mathrm{d}\widetilde{r}\, \widetilde{r}\, \frac{\widetilde{P}\, \exp\left(-\widetilde{r}^2\right)}{\widetilde{\Delta}^2 + 1 + \widetilde{P}\, \exp\left(-\widetilde{r}^2\right)} \sim \ln\left(1 + \frac{\widetilde{P}}{\widetilde{\Delta}^2 + 1}\right) \qquad (4.2)$$

Small deviations from this model are expected if outer parts of the beam profile are clipped.
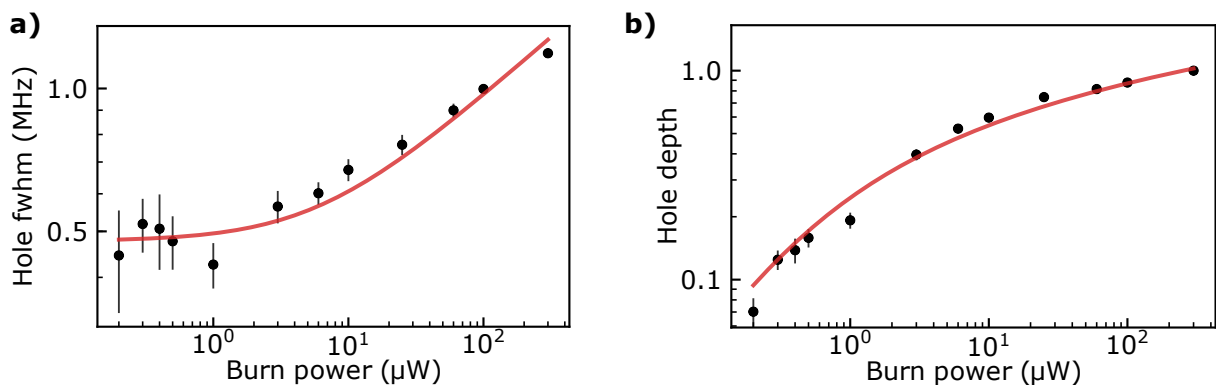
Figure 4.3: **Power broadening.** The width (a) and depth (b) of a spectral hole are measured for burn pulses of 1 ms length and different power levels. Below a saturation power of about 1 µW, the width stays constant, while the hole depth scales linearly with power. Above saturation level, the hole broadens, while the increase of the depth is slowed down. Both curves can be fit by a model that integrates over ions in the radial intensity distribution of a Gaussian beam (solid curves are fits to eq. 4.2). The data were taken at a magnetic field of 100 mT applied along $\varphi = 20°$ in the D_1-D_2 plane.

4.2.2 Spectral diffusion of Er:YSO

While the laser pulse parameters determine the excitation bandwidth, the width of a spectral hole can also grow over time due to interactions with a dynamically changing local environment, shifting the transition frequencies of individual ions in a random and uncorrelated way. Such spectral diffusion is a common phenomenon in solid-state systems, where other magnetic impurities and charged defect states can alter the local electric and magnetic fields at the dopants significantly. [Ambrose1991, Kuhlmann2013, Tyryshkin2012, Acosta2012, Bartholomew2017]

Charge fluctuations in YSO have a comparably little impact on spectral diffusion because the optical transitions of erbium have small Stark coefficients of $\lesssim 10\,\mathrm{kHz/(V/cm)}$ [Minář2009, Macfarlane2007], more than one order of magnitude smaller than those of NV centers in diamond [Tamarat2006]. In addition, the large band gap of YSO ($\sim 6\,\mathrm{eV}$, about $1500\,\mathrm{THz}$ [Pang2005, Upadhyay2019]) suppresses free charge carrier generation by multi-photon absorption processes, so that the only relevant charge fluctuations are due to surface states or charged defects. In this work, we studied only properties of bulk crystals, but in nanocrystals and

micro-structured devices the close proximity to interfaces makes dopants more susceptible to fluctuations from charged surface states.

In YSO, the major share of spectral diffusion stems from magnetic interactions with other spins in the host crystal. These interacting spins can be either paramagnetic impurities or nuclear spins. While paramagnetic impurities, such as erbium or other rare-earth dopants and charge traps, typically appear in low density but with large magnetic moments, nuclear spins of the host crystal (mainly of yttrium ions in YSO) have smaller moments but are more abundant. In the following, we first calculate the spectral diffusion linewidth due to dipolar erbium-erbium interactions; then we estimate the impact of yttrium nuclear spins.

4.2.3   Dipolar broadening due to Er-Er interactions

In chapter 2.4.1 we have discussed the dipolar coupling Hamiltonian between the magnetic moments of two erbium ions and its contribution to a state-dependent energy shift: depending on the spin orientation of the interaction partner, the energy of a single erbium electron spin is shifted either up- or downwards. By summing over all possible interaction partners in the ensemble of dopants, one can find the total energy shift, which then depends on the distances, angular positions and spin orientations of all other dopants. Averaging the total energy shift over random ensemble configurations yields a Lorentzian distribution, which accounts for a broadening of the corresponding optical and spin transitions.

For similar erbium ions (i.e. dopants with the same g-tensor) at low dopant concentration n, one can integrate the individual energy shifts (eq. 2.18) analytically and derive the dipolar transition linewidth (see appendix A.1)

$$\Delta\nu_{\text{fwhm}} = \frac{2\pi}{9\sqrt{3}}\,\mu_0 h \gamma_{\text{eff}}^2\, n, \tag{4.3}$$

where γ_{eff} is the effective gyromagnetic ratio as defined in eq. 2.19 (see figure 4.4, red curves).

For dissimilar spins, however, analytical treatment of eq. 2.17 is more difficult since the magnetic moments of site-1- and site-2-dopants are not aligned because of their different g-tensors. Instead, we adopt the proposed expression from [Lim2018],

$$\Delta\nu_{\text{fwhm}} = \frac{2\pi}{9\sqrt{3}}\,\mu_0 h \gamma_{\text{eff},1}\gamma_{\text{eff},2}\, n, \tag{4.4}$$

where $\gamma_{\text{eff},1}$ and $\gamma_{\text{eff},2}$ are the effective gyromagnetic ratios of site 1 and site 2, and n is the density of just the perturbing spins. To validate this ansatz, we run a Monte Carlo simulation of the total frequency shifts, each one calculated by numerically evaluating eq. 2.17 and summing over 100 interaction partners. We find good agreement between equation 4.4 and the simulation results (see figure 4.4, blue curves and error bars). The total linewidth can then be calculated by summing over the individual contributions from both sites.

Note that the spin transition linewidth stays constant over a large range of magnetic field orientations. This is a peculiarity of the high g-tensor anisotropy: in contrast to spins of isolated atoms, the magnetic moments of erbium in YSO tend to align not with the external magnetic field but with the g-tensor principal axis of the largest eigenvalue. At $\varphi = 25°$, the magnetic moment of site 1 is small and therefore less sensitive to magnetic field fluctuations, and at $\varphi = 80°$, magnetic moments of site 2 are small and contribute only little to local magnetic fields.
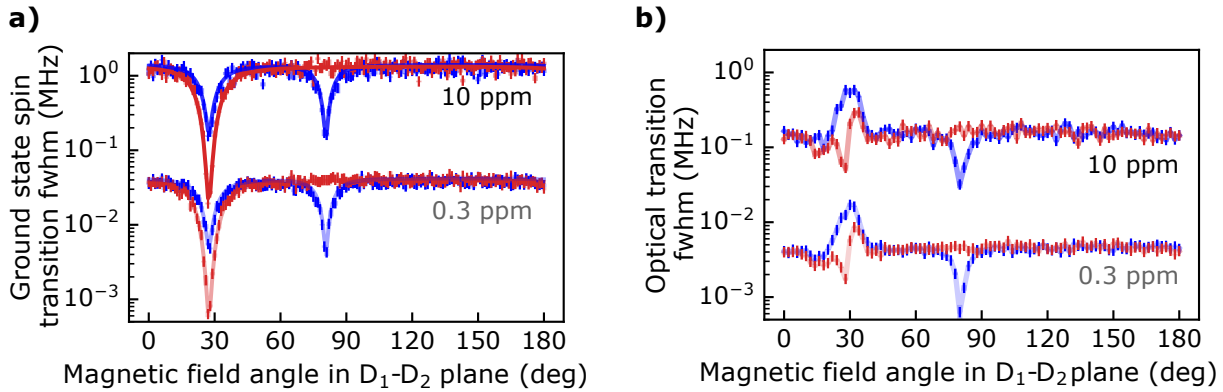
Figure 4.4: **Spectral diffusion linewidth for spin (a) and optical transition (b) due to interactions among erbium dopants.** Energy shifts of site-1-dopants due to dipolar interactions with site-1- (red) and site-2-dopants (blue) produce Lorentzian broadening of the ensemble-averaged optical and spin transition. Their widths are calculated by 2000 runs of a Monte Carlo simulation for an ensemble of 100 interacting ions (error bars). The results for the spin transition broadening are compared with the analytical solution by eq. 4.3 and 4.4 (solid curves), finding good agreement. We show the results for a total erbium concentration of 10 ppm (5 ppm per site), as it was used for holeburning and spin decoupling experiments (full color), and for 0.3 ppm, as found in undoped crystals used in the cavity experiments (light color).

Spectral diffusion linewidth of the optical transition

While the transition frequencies between the Zeeman ground states follow a Lorentzian distribution with a linewidth determined by eq. 4.3 and 4.4, and an equivalent broadening occurs in the excited levels as well, the distribution of the spin-preserving optical transition frequencies as probed in holeburning experiments typically is narrower. For each optically active ion, the effective local magnetic field induced by surrounding spins affects ground and excited state in similar ways, and the resulting energy shifts are typically correlated.

For a full analysis, we extend the Monte Carlo simulation and first calculate the exact optical transition frequency from the total energy shifts of ground and excited state for the same spin configuration, before we average over different local environments (see figure 4.4b). We observe again an almost constant inhomogeneous linewidth when changing the magnetic field angle. Notably, for orientations around $\varphi = 25°$, one would naively expect narrower lines because the effective g-values for ground and excited state are the same. However, because of the different g-tensors, the corresponding magnetic moments are not aligned, such that an even stronger shift of the optical transition frequency originates from the local magnetic field components perpendicular to the external field.

4.2.4 Er-Y interactions

Now we turn to the coupling of the optically active erbium dopants to their neighboring yttrium nuclear spins. Such superhyperfine interaction causes shifts of the level energies just like the dipolar coupling between erbium ions (see section 2.5). There are, however, few major differences: the nuclear magnetic moment of yttrium is about four orders of magnitude smaller than the typical erbium electron magnetic moment, and only yttrium atoms very close to the erbium dopant contribute significantly to its spectral diffusion because of the $1/r^3$-dependence of the dipolar interaction on the distance. On the other hand, *all* yttrium atoms in the crystal have a magnetic moment, not just a fraction, and they occupy well-defined sites in the crystal lattice.

Instead of integrating over a spherically distributed dilute ensemble of interacting partners, we now have to sum over all yttrium sites (at distances r_i, with connecting unit vectors $\hat{r}_i$) and sum up their induced magnetic fields at the erbium dopant. For simplicity, we consider the high-field case, in which the external magnetic field B_0 dominates over the field induced by erbium dopants ($B_0 \gtrsim 200\,\text{mT}$, cf. figure 4.5b). Thus, the yttrium nuclear magnetic moments are aligned with the external magnetic field axis (unit vector $\vec{b}$).

$$\vec{B}_{\text{Y}\rightarrow\text{Er}} = \frac{\mu_0}{4\pi}\frac{\mu_N g_n}{2}\sum_i \frac{\vec{b} - 3(\vec{b}\cdot\hat{r}_i)\hat{r}_i}{r_i^3} \tag{4.5}$$

Then, we can calculate the expected energy level frequency shift by multiplication with the erbium magnetic moment (see figure 4.5a). We observe that the linewidth broadening due to varying yttrium spin configurations can be as large as the spectral diffusion linewidth due to erbium-erbium interactions in a 10 ppm crystal (compare figures 4.4 and 4.5a).

Around $\varphi = 30°$, we observe only little broadening of the spin transition, because the effective electron g-factor is small and thus the transition is less sensitive to perturbations of the magnetic field. At the same orientation, the broadening of the optical transition is increased, because the magnetic moments in ground and excited state are almost perpendicular to each other and therefore the energy shifts in the excited state are not at all correlated with the superhyperfine energy shifts of the ground state. As a consequence, the spectral diffusion of the optical transition is not reduced to the difference of the individual linewidths in ground and excited state, but instead increased to their sum.
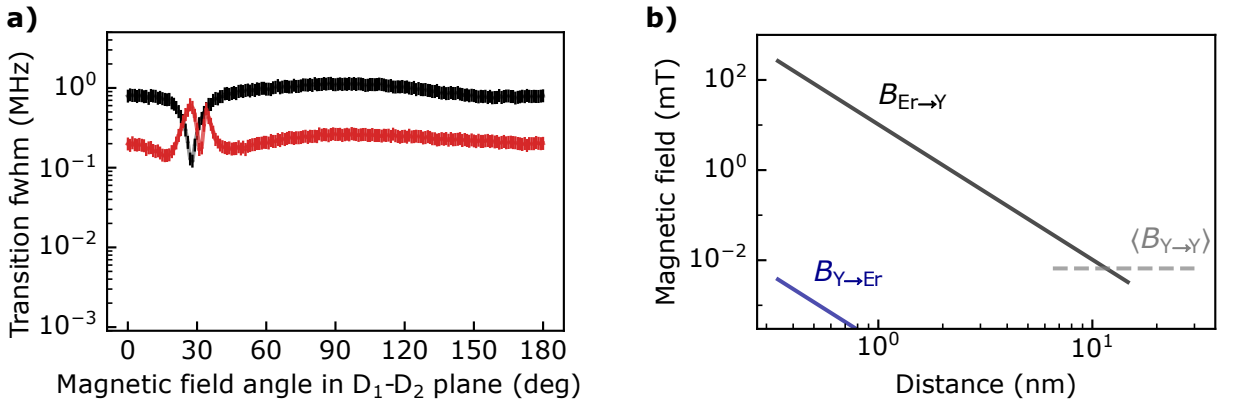
Figure 4.5: **a) Spectral diffusion linewidth due to the yttrium nuclear spin bath.** Random orientations of the yttrium nuclear spins cause a Lorentzian frequency distribution for the spin (black) and the optical transition (red) of site 1 erbium dopants. Their widths are calculated by 2000 runs of a Monte Carlo simulation for the 550 closest yttrium sites, assuming the external magnetic field is higher than the field induced by erbium dopants, $B_0 > B_{\text{Er}\rightarrow\text{Y}}$.
b) Frozen core field distribution. The magnetic field at an yttrium site induced by an erbium spin, $B_{\text{Er}\rightarrow\text{Y}}$, decays with distance r as $1/r^3$ (black line). For distances $< 10\,\text{nm}$, it dominates over the average magnetic field fluctuations by yttrium spins, $\langle B_{\text{Y}\rightarrow\text{Y}}\rangle$ (grey dashed line) and suppresses resonant flip-flops (frozen core effect). For comparison, the magnetic field at the erbium site induced by yttrium spins, $B_{\text{Y}\rightarrow\text{Er}}$, is five orders of magnitude smaller because of the small nuclear magnetic moments (blue line).

4.2.5 Timescale of spectral diffusion processes

In the previous sections, we have calculated the spectral diffusion linewidth as fluctuation in transition frequency for varying local configurations of erbium and yttrium spins. While the spectral diffusion linewidth only tells the magnitude of typical fluctuations in transition frequency, the diffusion rate sets the timescale on which they take place and needs to be considered as well. If the width of a spectral hole is probed quicker than the diffusion rate, it will appear as narrow as the excitation bandwidth, while broadening of the hole will be observed only for longer burn-probe delays.

In general, the diffusion rate is given by the correlation time of the surrounding spins, which is bound above by their lifetime. While the flip-rate of erbium electron spins can be fairly high and is typically dominated by spin-lattice relaxation processes (see section 4.4), yttrium nuclear spins are more long-lived because phonons can not efficiently couple to their small level splitting.

Frozen core effect

Instead of phonon-assisted relaxation, the flip-rate of yttrium spins is dominated by nuclear spin flip-flops among nearest neighbor sites, which are mutual flips of anti-parallel spin pairs [Böttger2006b]. Because flip-flops are resonant processes, they can only occur between yttrium neighbors with comparable level splittings, which restricts the flip-flop partners to sites whose local magnetic fields differ by less than typical field fluctuations induced by the yttrium spin bath, $B_{Y \rightarrow Y}$. In proximity to the large magnetic moment of an erbium electron spin, however, the local magnetic field is heavily distorted and yttrium nuclear spins are no longer resonant (see figure 4.5b). As a consequence, yttrium flip-flops are suppressed in a region around each erbium ion, called 'frozen core', and nuclear spins within that region have even longer lifetimes [Zhong2015a, Rančić2018].

Instantaneous diffusion

In addition to the randomization of spin configurations on a timescale set by their lifetime, they can also be altered by optical or microwave pulses. As a simple example, the optical excitation of erbium dopants changes their magnetic moments because of different g-tensors in ground and excited state, which shifts the energy levels of all other ions in their proximity. As consequence, any control pulse that addresses not only the central spin but also other dopants close by will have an immediate affect on their transition frequency distribution.

Such 'instantaneous spectral diffusion' is less severe for optical laser pulses, as the narrow excitation bandwidth typically addresses only $\lesssim 1\%$ of the entire erbium ensemble. In experiments with microwave control pulses, however, we observe that instantaneous diffusion poses a significant limit to achievable coherence times (see section 5.2.3).

In addition to instantaneous diffusion, optical excitation of erbium dopants also induces spectral diffusion due to superhyperfine coupling. Although yttrium nuclear spins by themselves are not resonant with the laser pulses, they still respond to the modification of their local magnetic fields. In particular, yttrium spins in the previously 'frozen core' will readjust their axis of precession, which changes the magnetic field that they induce at the erbium site. Furthermore, the hybridization of erbium electron and yttrium nuclear spin states effectively stimulates yttrium spin flips when an erbium transition is driven (see section 4.3.3). Both of these coupling mechanisms to yttrium spins, however, are suppressed when operating at high magnetic fields ($\gtrsim 1\,\mathrm{T}$).

In holeburning experiments we can compare the impact of optically induced spectral diffusion with the broadening due to the finite lifetime of spin configurations by varying burn pulse parameters and burn-probe delay (see figure 4.6). As the hole width does not change significantly with the burn-probe delay while it increases with the burn pulse length, we can conclude that optically induced diffusion dominates the linewidth broadening. Note that for this particular magnetic field orientation the superhyperfine coupling is significantly enhanced, and efficient flipping of yttrium spins by optical excitation of the erbium ion is possible (see section 4.3.3).

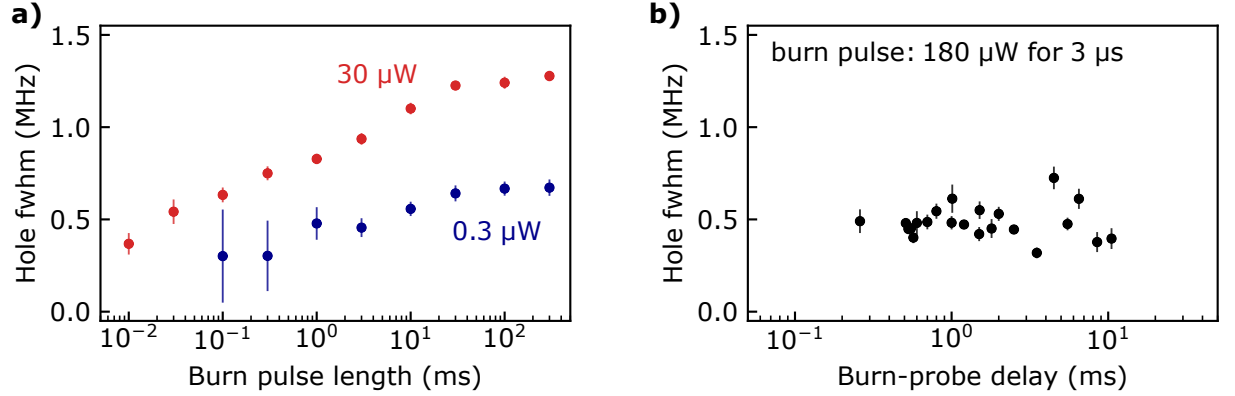Figure 4.6: **Spectral diffusion timescale.** While the width of the spectral hole increases with the burn pulse length even for excitation levels below saturation (a), it stays constant when the delay before the probe measurement is increased (b), indicating that optically induced diffusion is the dominant process. The data were taken at a magnetic field of $100\,\text{mT}$ applied along $\varphi = 22°$ in the D_1-D_2 plane.

4.3 Spin pumping

While the previous section dealt with the width of a spectral hole and its broadening over time, now we turn to the time evolution of its depth, and how it decays.

After saturating the optical transition during the first burn pulse, the population will decay from the excited state back into the ground state, and the initial spectral hole disappears on a timescale governed by the excited state lifetime. In systems where the excited state can also decay to other, meta-stable states, the population in the initial ground state might be reduced even when no dopants are left in the excited state (see figure 4.7a). As a consequence, a lower absorption on the burn pulse transition can be measured for probe delays longer than the excited state lifetime. Such a 'persistent' spectral hole is an indication for spin pumping into other ground level states, and its decay time constant reflects the life time of the participating spin state.

In Er:YSO the decay via an optical spin-flip transition back to the ground level occurs with a typical probability of $\lesssim 10\,\%$ [Hastings-Simon2008]. Therefore, it is possible to pump a small but significant fraction of electrons into the other ground level spin state. In holeburning experiments with varying burn-probe delays, the different relaxation processes will contribute with exponential decays at their respective timescales to the total signal. The combination of a decay from the excited state on a 11 ms timescale and relaxation from the other spin state with a ~ 100 ms lifetime is a bi-exponential function [Hastings-Simon2008] (figure 4.7b). Since the optical lifetime is well known and does not change significantly with experimental parameters like dopant concentration, magnetic field or temperature, probing the spin hole decay allows us to measure the ground level spin lifetime.
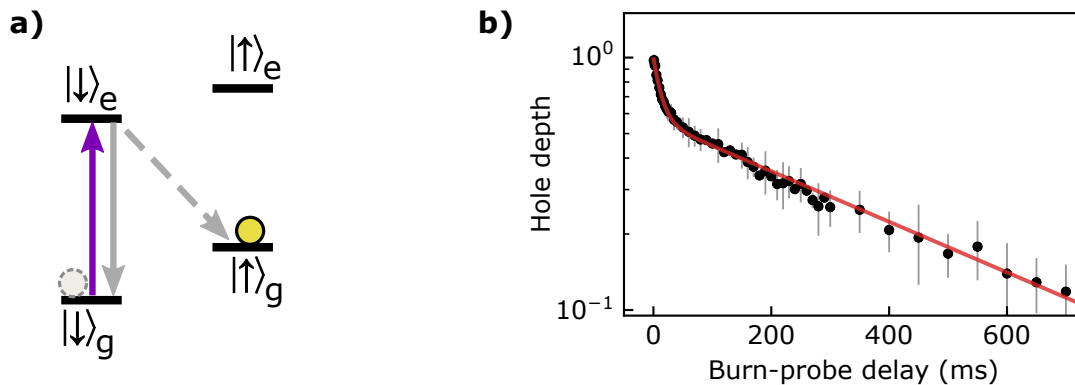
Figure 4.7: **a) Optical spin pumping.** After optically exciting an erbium ion (purple arrow), it can decay into the ground level either by a spin-preserving transition (solid grey arrow) or by an optical spin-flip transition (dashed grey arrow). As a result, spin population can be pumped from the initial ground state (grey dashed circle) into the other spin state (yellow circle).
b) Decay of the central hole. After burning a spectral hole on the spin-preserving transition of Er:YSO, the measured hole depth decays with increasing burn-probe delay on a fast timescale set by the excited state lifetime of about 11 ms. Due to significant optical spin pumping, a population difference in the ground state is built up during the burn pulse and decays on a slower timescale set by the spin lifetime, 430(20) ms. The data were taken for a magnetic field of 50 mT along the b-axis, and it was fit by a bi-exponential decay function (red curve).

In the following sections, we first explain how the optical spin pumping efficiency and its dependence on the magnetic field orientation can be calculated. Then, we discuss how the absorption spectrum changes as a result of spin pumping. In the end, we show that optical excitation can not only pump the electron spin of erbium dopants but also nuclear spins of yttrium ions in their proximity or of ^{167}Er-dopants.

4.3.1 Optical spin-flip transition probability

The excited state can decay either via one of the optical zero-phonon transitions in the effective spin-1/2 system or via higher crystal field levels and subsequent phonon relaxation into the ground state. Because latter decay path is a higher-order process and was found to be predominantly spin-preserving [Lauritzen2008], for optical spin pumping only the decay probability via a spin-flip transition in the effective four-level scheme is relevant, which we calculate in the following.

Since the g-tensors in ground and excited state are different, the respective Zeeman Hamiltonians do not commute, and they do not share the same eigenstates – on the contrary, the magnetic moments of ground and excited state are aligned along different precession axes. Although the induced electric dipole transition does not couple to magnetic moments, it still projects the excited state magnetic moment onto the ground state precession axis. Consequently, when we neglect other decay paths via higher crystal field levels, we can calculate the probability to decay via a spin-flip transition as

$$p_{\text{flip}} = |{}_g\langle\downarrow|\uparrow\rangle_e|^2, \tag{4.6}$$

where the individual eigenstates, $|\uparrow\rangle_e$ and $|\downarrow\rangle_e$ in the excited state and $|\uparrow\rangle_g$ and $|\downarrow\rangle_g$ in the ground state, are obtained by diagonalizing the Zeeman Hamiltonians, according to eq. 2.7.

This number, p_{flip}, does not only describe the probability of the excited state to decay via an optical spin-flip transition, it also is a measure of the transition strength when exciting the dopants. By providing sufficient laser power, however, efficient excitation is possible even on a weak optical transition. Once the population has been transferred into the excited state, the branching of its decay into a spin-preserving and a spin-flip optical transition determines the resulting ground state spin polarization: while the cases $p_{\text{flip}} = 0$ and $p_{\text{flip}} = 1$ allow for perfect preparation of a pure spin state in a single optical cycle, the spin pumping efficiency for $p_{\text{flip}} = 0.5$ would be minimal.

Therefore, a different measure is often used to characterize spin pumping capabilities: the branching contrast ϱ_{flip} is defined such that it equals 1 in case of an equal likelihood to end in either spin ground state after a single excitation event:

$$\varrho_{\text{flip}} = 4\,p_{\text{flip}}\,(1 - p_{\text{flip}}) \tag{4.7}$$

By numerically calculating the strengths of the optical spin-flip transitions for different magnetic field orientations in the D_1-D_2 plane (see figure 4.8), we find that over a large range the branching contrast is almost constant at $11\,\%$, in agreement with [Hastings-Simon2008], whereas it peaks around $\varphi = 30°$ with a maximum contrast of $60\,\%$. This difference can be observed even in simple absorption scans: while in the absorption spectrum at $\varphi = 28°$ all four transitions are visible, in most other orientations the absorption at both spin-flip transitions will be too low, and their lines disappear. Of course, in crystals with higher dopant concentration and higher absolute signal the spin-flip transitions could be resolved again.
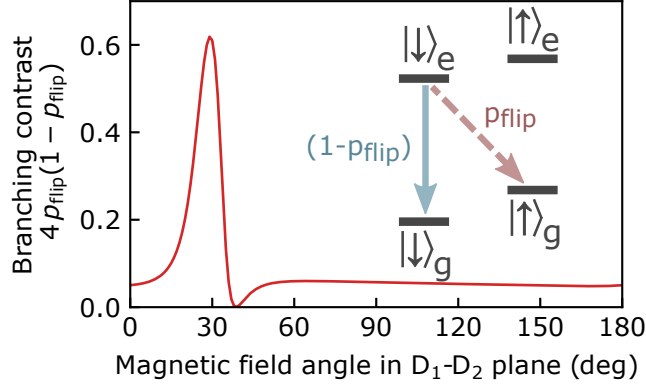
Figure 4.8: **Branching contrast for the optical spin-flip transition.** Depending on the orientation of the external magnetic field, the magnetic moments of ground and excited state are not aligned, and the excited state spin $|\!\downarrow\rangle_e$ overlaps with the opposite spin orientation in the ground state, $|\!\uparrow\rangle_g$. Therefore, the excited state can decay via a spin-flip transition (probability p_{flip}) or a spin-preserving one $(1 - p_{\text{flip}})$, and the branching contrast between both transitions can be calculated via eq. 4.6 and 4.7.

Rate equations for optical spin pumping

While the spin-flip probability and the branching contrast only set the relative strength of the spin-flip transition compared to the spin-preserving one, the actual spin-pumping efficiency after a burn pulse of certain length can be calculated with a set of rate equations [Lauritzen2008, Hastings-Simon2008].

Let $P_g(t)$, $P_e(t)$, $P_s(t)$ be the probabilities to find an ion in the states $|\!\downarrow\rangle_g$, $|\!\downarrow\rangle_e$, and $|\!\uparrow\rangle_g$. Driving the transition $|\!\downarrow\rangle_g \leftrightarrow |\!\downarrow\rangle_e$ with the pump rate γ_p leads to the rate equations

$$\frac{\mathrm{d}}{\mathrm{d}t}P_g(t) = -(\gamma_p + \gamma_s)P_g(t) + \left(\gamma_p + (1 - p_{\text{flip}})\gamma_{\text{opt}}\right)P_e(t) + \gamma_s\,P_s(t) \tag{4.8a}$$

$$\frac{\mathrm{d}}{\mathrm{d}t}P_e(t) = \quad\quad + \gamma_p\;P_g(t) \quad\quad\quad\quad - (\gamma_p + \gamma_{\text{opt}})\,P_e(t) \tag{4.8b}$$

$$\frac{\mathrm{d}}{\mathrm{d}t}P_s(t) = \quad\quad + \gamma_s\;P_g(t) \quad\quad\quad\quad + p_{\text{flip}}\gamma_{\text{opt}}\;P_e(t) - \gamma_s\,P_s(t), \tag{4.8c}$$

where $\gamma_{\text{opt}} = 1/T_{\text{opt}}$ is the inverse of the excited state lifetime, T_{opt}, and $\gamma_s = 1/(2T_{\text{spin}})$ is the spin relaxation rate, normalized such that the polarization $P_s(t) - P_g(t)$ decays with a characteristic time T_{spin}.

Coherent effects are neglected because inhomogeneities predominate on the relevant time-scale of spin-flip dynamics, and we assume a low magnetic field, so that the spin relaxation rates in both directions are equal (otherwise, they had to be weighted with the respective Boltzmann factors). Also, spin-flips in the excited state are then suppressed because the small level splitting slows down spin-lattice relaxation, and there are no opposite spins for flip-flops in the excited state.

These equations can be solved numerically to simulate the population before, during, and after the illumination with a resonant burn laser pulse (figure 4.9a). Alternatively, one can also derive an analytical expression for the maximum spin transfer into the opposite ground state, $P_s(\infty)$. In the limit of strong driving, it reads

$$P_s(\infty) = \frac{\gamma_s + p_{\text{flip}}\gamma_{\text{opt}}}{3\gamma_s + p_{\text{flip}}\gamma_{\text{opt}}} \tag{4.9}$$

and is approached at a rate $(3\gamma_s + p_{\text{flip}}\gamma_{\text{opt}})/2$.

For most magnetic field orientations, the probability of a decay via a spin-flip transition is small, $p_{\text{flip}} < 10\%$, and the asymptotic spin transfer probability remains below 50%. An easy way to overcome this limit requires optical excitation resonant with the spin-flip transition instead of the spin-preserving one. In order to drive the weak optical spin-flip transition, higher laser power is required; but once the population is in the excited state, the high probability to decay via a spin-preserving transition is then in our favor.

The population transfer can be simulated with rate equations similar to eq. 4.8, but with p_{flip} and $1 - p_{\text{flip}}$ interchanged. As a result, for the same parameters, a higher maximum spin pumping efficiency can be achieved, approaching $P_s(\infty) \approx 1$ (see figure 4.9b).
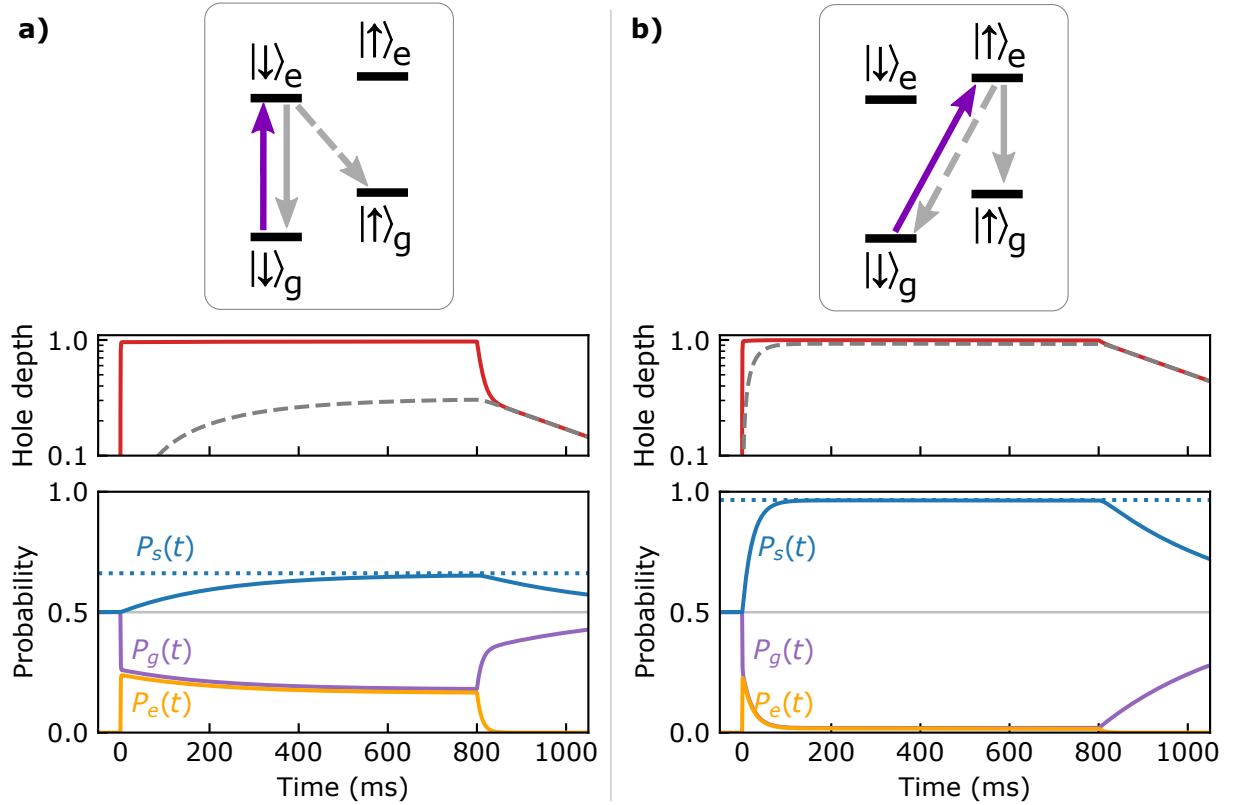
Figure 4.9: **Spin population dynamics for optical pumping on the spin-preserving transition (a) or the spin-flip transition (b).** Starting with a mixed state in thermal equilibrium, the burn laser drives the optical transition from $t = 0\,\text{ms}$ to $t = 800\,\text{ms}$. The bottom panel shows the probabilities to find the system in the ground state resonant with the laser, $P_g(t)$ (purple), the opposite spin ground state, $P_s(t)$ (blue), and the excited state, $P_e(t)$ (orange), which were calculated by numerically solving the rate equations 4.8, as well as the analytical limit for the spin pumping efficiency, $P_s(\infty)$ (dotted blue line). Upon optical excitation of the spin-preserving transition (a), population pumped into the excited state makes up a great share of the measurable hole depth (center panel, red line), but it decays quickly once the laser is turned off. Population transfer into the other spin ground state (dashed grey line) happens on a longer time scale, but its contribution to the hole depth also decays slower. The rates for this plot were chosen to match with figure 4.7b, but would depend on magnetic field orientation and burn pulse intensity. If instead the spin-flip transition is excited (b), a larger fraction decays into the opposite spin ground state, and a higher spin pumping efficiency can be achieved.

4.3.2 Sideholes and antiholes: fine structure

We can witness spin pumping not only by looking at the decay of the hole at the burn laser frequency, but also by probing another optical transition, involving the other spin state directly. For example, any transition from the other spin ground state will show higher absorption, seen as antiholes, because optical pumping has created excess population in that state (see figure 4.10) [Hastings-Simon2008].

Because the burn pulse selects only a subset of dopants that share at least one common transition frequency, all holes and antiholes are much narrower than the ensemble inhomogeneous linewidth, and their splittings can be measured on a megahertz scale. This allows precise measurements of the level structure even at small magnetic fields, when the ensemble absorption lines still overlap. Note, though, that then the sidehole spectrum complexity increases because the burn pulse addresses two different subsets of dopants: those whose $|\uparrow\rangle_g \to |\uparrow\rangle_e$ transition is resonant, and those whose $|\downarrow\rangle_g \to |\downarrow\rangle_e$ is. [Hastings-Simon2008]

In contrast to a slow decay of the central hole (i.e. at the burn laser frequency), the observation of antiholes is an unambiguous indication of spin pumping and allows for an independent measurement of the spin lifetime: while optical pumping into any other long-lived state would be seen as slow decay timescale of the central hole, the side- and antiholes reflect the dynamics only of those states at a certain detuning from the initial state. An example will be discussed later in section 5.1.4.

Note that typically the width of the antihole at the other spin-preserving transition is as narrow as the central hole ($\lesssim 1\,\mathrm{MHz}$), whereas the features at the spin-flip transitions appear broader ($\sim 10\,\mathrm{MHz}$). Apparently, there is an inhomogeneity in the level splittings of ground and excited state, which causes this broadening; and while the splittings of ground and excited state are correlated, the absolute optical transition frequency is not.
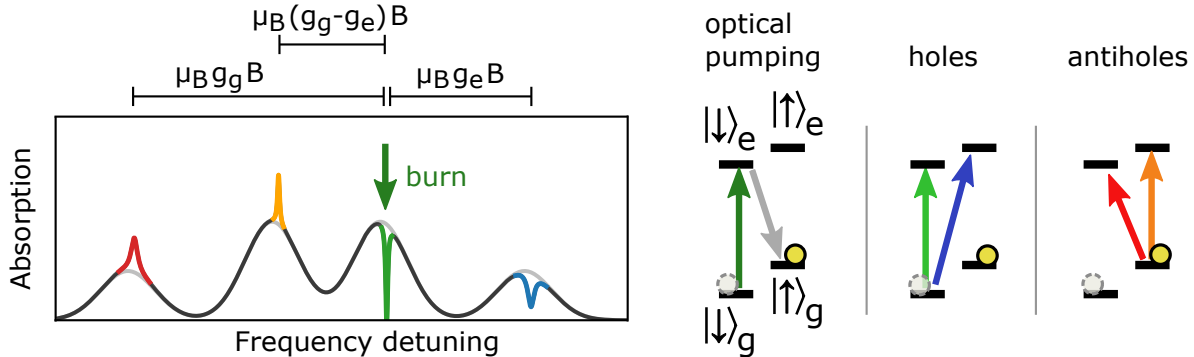
Figure 4.10: **Illustration of a sidehole spectrum (left) and level schemes (right) after optical pumping.** A burn pulse on the spin-preserving transition (dark green arrow) induces spin pumping by decay via a spin-flip transition (grey arrow). This creates spectral holes on transitions that share the same ground state (green, blue), while transitions from the other spin ground state have increased absorption and show an antihole (red, yellow). The detunings of sideholes and antiholes from the burn laser are determined by the magnetic field and the effective g-factors of the ground and excited states, g_g and g_e, respectively. The shown widths of the ensemble absorption line and the spectral hole features are not to scale.

4.3.3 Superhyperfine hole spectrum

Similar to optical pumping of erbium electron spins into a different ground level spin state, it is also possible to pump surrounding yttrium nuclear spins via the erbium optical transitions. Since the electron magnetic moments of ground and excited state are not aligned because of their different g-tensors, also the precession axes of the surrounding nuclear spins will change upon optical (de-)excitation [Car2018, Terblanche2001]. In the same way as we calculated the probability of an electron spin-flip on the optical transition in sec. 4.3.1, we can now write down the probability of a nuclear spin-flip, $p_{\text{Y-flip}}$, and derive the branching contrast $\varrho_{\text{Y-flip}}$ from it:

$$p_{\text{Y-flip}} = \left| {}_g\langle \uparrow\Uparrow | \uparrow\Downarrow \rangle_e \right|^2 \tag{4.10}$$

$$\varrho_{\text{Y-flip}} = 4\, p_{\text{Y-flip}} \left(1 - p_{\text{Y-flip}}\right), \tag{4.11}$$

To find the eigenstates, we first diagonalize the electron spin Zeeman Hamiltonian for the external field and neglect any field induced by nuclear spins, since it can reach at most a few μT, even for nearest neighbors (cf. figure 4.5b). Then, we calculate the total magnetic field vector at the yttrium site by adding the field induced by the erbium spin, $\vec{B}_{\text{Er}\rightarrow\text{Y}}$, to the external field $\vec{B}_0$ (see section 2.5). The result will not only depend on the external magnetic field orientation and strength but also differ between ground and excited state of the electron spin:

$$\vec{B}_{\text{Y}}^{(\text{g})} = \vec{B}_0 + \vec{B}_{\text{Er}^{(\text{g})}\rightarrow\text{Y}} \tag{4.12}$$

$$\vec{B}_{\text{Y}}^{(\text{e})} = \vec{B}_0 + \vec{B}_{\text{Er}^{(\text{e})}\rightarrow\text{Y}} \tag{4.13}$$

Since these magnetic fields define the axes of precession (cf. Hamiltonian in eq. 2.23), the branching contrast as defined in eq. 4.10 can also be expressed geometrically by the angle $\beta = \angle(\vec{B}_{\text{Y}}^{(\text{g})}, \vec{B}_{\text{Y}}^{(\text{e})})$ between these total fields, reaching its maximum when the field vectors are perpendicular to each other [Car2018]:

$$\varrho_{\text{Y-flip}} = \sin^2(\beta) \tag{4.14}$$

Note that the branching contrast still depends on the yttrium site and its relative position with respect to the erbium ion, and so does the energy splitting between the superhyperfine levels. Therefore, in holeburning experiments in magnetic field configurations where nuclear spin pumping is possible at multiple Y sites, many sideholes will appear at different detunings and amplitudes (figure 4.11).

When we calculate the superhyperfine splitting of the excited state for the five yttrium spins with the highest optical branching contrast (indicated by vertical bars), we find indeed good agreement with the observed sidehole positions. Note that the deepest sidehole can be attributed to several yttrium sites with similar frequency splittings. In fact, all bulk yttrium spins whose local magnetic field is dominated by the external field B_0 rather than the erbium magnetic moment have the same level splitting of $\gamma_{\text{Y}} B_0$, with the gyromagnetic ratio for yttrium, $\gamma_{\text{Y}} = 2.1\,\text{MHz/T}$.

The exact shape of the spectrum, however, is more complex: for example, the optically pumped yttrium spins also cause stronger absorption at other superhyperfine transitions, which would be visible as antiholes [Askarani2019, Thiel2010]. In addition, the interactions with many yttrium spins can no longer be described by the four transitions of a single erbium-yttrium pair and lead to spectral diffusion and a broadening of the lines. Furthermore, calculations suggest that in this particular configuration the individual branching contrasts depend very sensitively on the exact magnetic field orientation and amplitude (cf. figure 4.12).
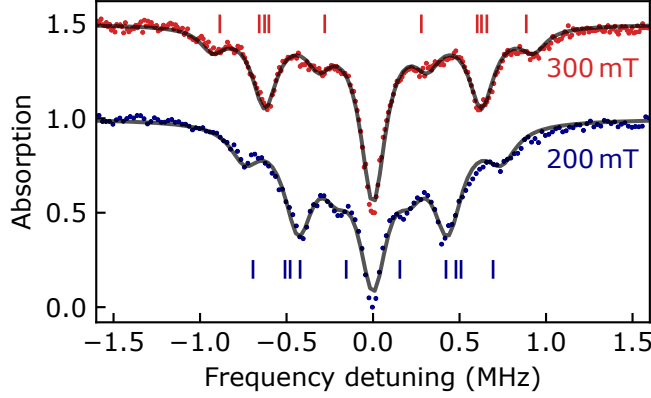
Figure 4.11:   **Sidehole spectrum after optical pumping of Y nuclear spins.** For a magnetic field of 200 mT (blue) and 300 mT (red) applied along $\varphi = 21.8°$ in the D_1-D_2 plane, the branching contrast of optical superhyperfine transitions is extraordinarily high, and efficient pumping of the yttrium nuclear spins via the erbium dopants is possible. The curves were measured for a burn pulse length of 100 ms and are plotted offset along the y-axis. We can fit each obtained sidehole spectrum with a sum of multiple Lorentzians (solid black lines) and compare it with calculations of the predicted superhyperfine level splittings in the excited state for the five yttrium spins with the highest branching contrast (vertical bars), finding good agreement.

Consequences of optical superhyerfine coupling for quantum information processing

The observed superhyperfine spectrum in holeburning experiments clearly demonstrates that optical addressing of nuclear spins via their coupling to the erbium dopants is possible. In section 6.4.3 we can even show coupling to an individual yttrium site, seen as modulation in photon echo experiments.

On the one hand, such coupling makes it possible to create entanglement between the erbium electron spin and a neighboring yttrium nuclear spin, or to transfer quantum states from the erbium dopant to a remote nuclear spin coherently. This could facilitate the use of yttrium nuclear spins as long-term quantum memories that are interfaced optically via the erbium ion, similar to the use of carbon nuclear spins as quantum register coupled to NV defects in diamond [Jelezko2004, Dutt2007, Bradley2019].

On the other hand, the superhyperfine coupling can be undesired if long coherence of the optical erbium transition is required. As soon as multiple yttrium sites couple to the erbium electron spin at different rates, the optical coherence will quickly drop [Car2020]; the changes in the nuclear spin bath induced by optical excitation accelerate spectral diffusion.

In order to identify configurations that allow for long coherence times on the erbium optical transition, we calculate the individual branching contrast for the 36 nearest yttrium spins depending on the orientation and strength of the external magnetic field. Then, we subsume the overall effect in the cumulative branching contrast

$$\varrho_{\text{Y-flip}}^{(\text{cum})} = 1 - \prod_i \left(1 - \varrho_{\text{Y-flip}}^{(\text{i})}\right). \tag{4.15}$$

This number represents the probability that any optical branching occurs for at least one yttrium neighbor. Since the superhyperfine coupling strength decreases with increasing distance from the erbium dopant, the cumulative branching contrast converges as the number of considered yttrium sites approaches 36.

As shown in figure 4.12, branching of superhyperfine optical transitions occurs predominantly for magnetic field orientations between $\varphi = 20°$ and $\varphi = 40°$ in the D_1-D_2 plane,

because then the change in orientation of the erbium magnetic moments between ground and excited state is maximal. Unfortunately, this is the same range, for which the differential g value $|g_g - g_e|$, which reflects the magnetic field sensitivity of the optical spin-preserving transition, is minimal. Therefore, it is not possible to simultaneously minimize superhyperfine branching of yttrium spins and magnetic field sensitivity of the optical transition.
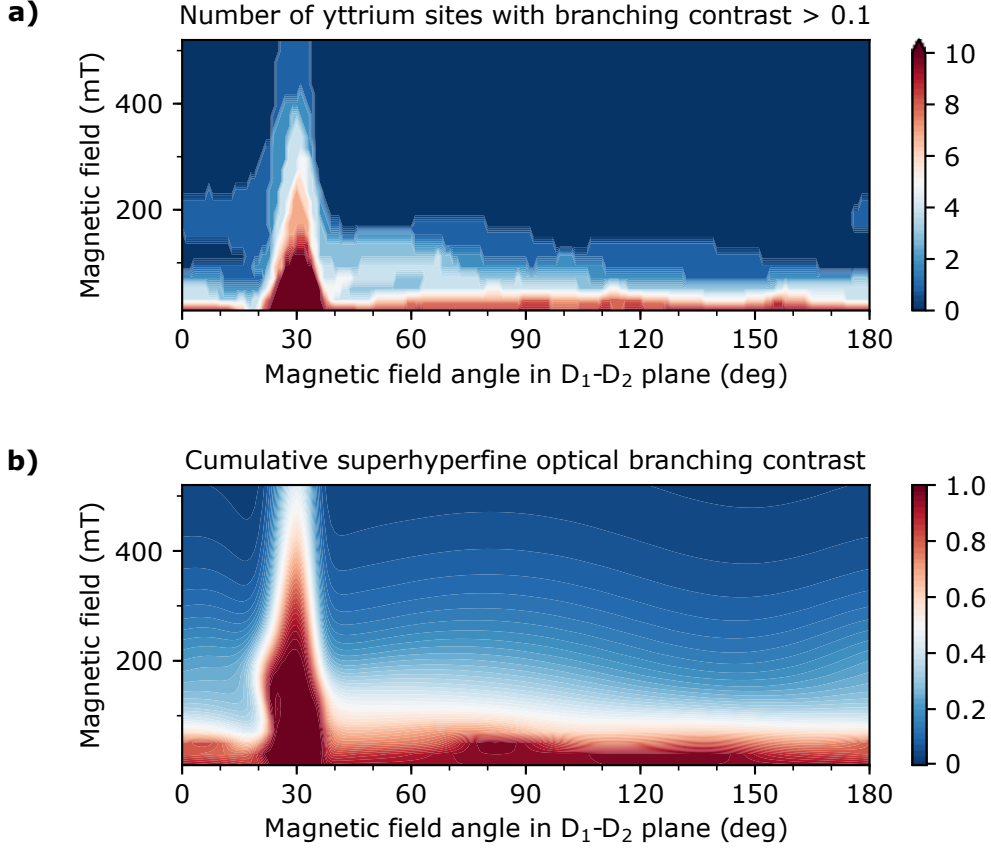
Figure 4.12: **a) Number of yttrium sites with significant branching contrast of their optical superhyperfine transitions.** For a given external magnetic field orientation and amplitude, we can calculate the branching contrast of optical superhyperfine transitions via eq. 4.14 for the 36 nearest yttrium neighbors. Because the coupling strength drops with distance, in most cases only a handful of ions shows significant branching. **b) Cumulative branching contrast of optical superhyperfine transitions.** To represent the overall effect of individual superhyperfine couplings, we calculate the cumulative branching contrast via eq. 4.15. For a magnetic field orientation around $\varphi = 30°$, many yttrium sites show significant branching, and optical coherence would quickly diffuse into different superhyperfine states. High magnetic fields, however, suppress nuclear spin flips caused by superhyperfine coupling efficiently.

4.3.4 ^{167}Er hyperfine spectrum

Optical pumping can not only transfer the erbium electron into its other spin state or flip the nuclear spin of neighboring yttrium sites; it can also involve hyperfine states of the ^{167}Er isotope with its nuclear spin of $7/2$. While driving optical transitions between hyperfine states and polarizing the nuclear spin is not fundamentally different from electron or superhyperfine spin pumping, there are some peculiarities, which we will discuss in the following.

First, in crystals with natural isotopic composition only 23% of all erbium ions have nuclear spin, and at low magnetic fields and a temperature of $1.7\,\mathrm{K}$ all ground states will

be populated equally, which lowers the effective concentration in each hyperfine states by another factor of 16.

And second, the splitting of ground and excited levels into a large number of states results in complex sidehole and antihole spectra (see figure 4.13a) [Baldit2010]. Preparation of a hyperfine state with specific magnetic quantum number m_I can not be achieved by a single laser pulse anymore but requires the repeated sweeping of the burn laser across the $\Delta m_I = \pm 1$ optical hyperfine sidebands [Rančić2018].
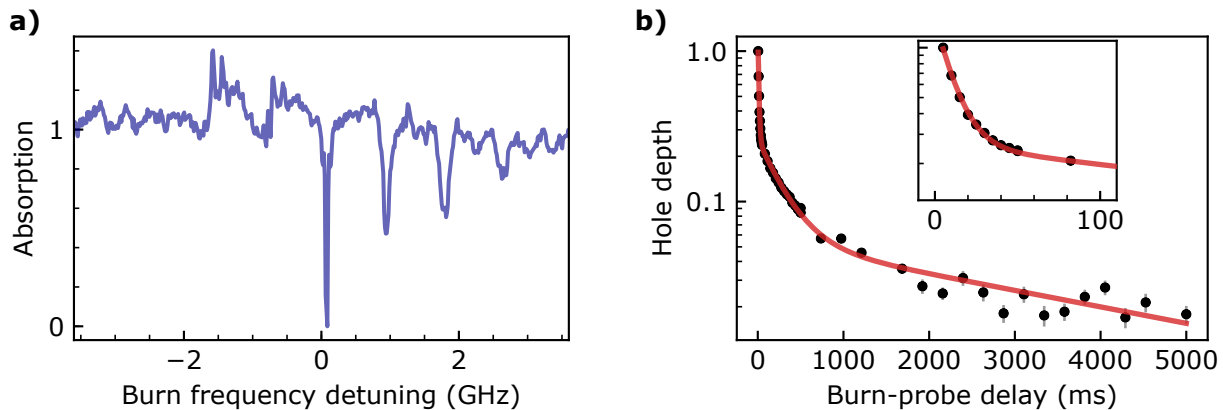
Figure 4.13: **a) Sidehole spectrum of ^{167}Er.** At low magnetic field, the complex hyperfine structure of ^{167}Er isotopes leads to a rich spectrum of sideholes and antiholes, here measured for a field of $57\,\text{mT}$ applied along $\varphi = 10°$ in the D_1-D_2 plane, in an isotope-enriched crystal (erbium concentration of $50\,\text{ppm}$, of which $93\,\%$ is ^{167}Er). In this experiment, burn pulses of $50\,\text{ms}$ length were applied and scanned in frequency, while the probe pulse frequency was kept constant. **b) Second-long lifetime of hyperfine holes.** After burning a spectral hole in the ^{167}Er-enriched crystal, its decay shows three distinct timescales, with the fastest (about $10\,\text{ms}$) accounting for decay of the optical excitation (see inset for zoom-in). On an intermediate timescale ($\sim 100\,\text{ms}$) the decay of the electron spin component is visible, and the longest timescale of several seconds indicates the lifetime of nuclear spin states of ^{167}Er. The data were taken for the same magnetic field configuration as in (a) and fitted with the sum of three exponentials.

Measurements in isotope-enriched crystals show a spectral hole lifetime of more than a second (figure 4.13b), which is likely limited by comparably fast flipping of the electron spin component at low magnetic field. At higher fields, the electron spin freezes out, and the nuclear spin states can exhibit long lifetimes of several $100\,\text{s}$, while their coherence time can exceed one second [Rančić2018, McAuslan2012].

While the prospect of long storage and coherence times makes erbium nuclear spins very attractive for quantum information processing, the complex level structure and long lifetimes can pose a challenge for spectroscopic studies. Furthermore, in chapter 6 we will investigate erbium dopants coupled to an optical cavity with only $\sim 20\,\text{MHz}$ linewidth, which is orders of magnitude smaller than typical hyperfine level splittings and prevents repumping and full-optical control of ^{167}Er dopants. Therefore, we will focus only on even erbium isotopes without nuclear spin in the following.

4.4 Spin lifetime

Eventually, the goal of this thesis is to explore if Er:YSO can be used for quantum information processing – either by storing quantum states in the electronic spin of erbium ions themselves, or by utilizing their optical interface and potential coupling to nuclear spins, which then could serve as long-term quantum memories. In any case, there is a great desire to extend the electron spin lifetime and understand which processes set a limit.

In this section, we first give an overview over all common spin relaxation processes and discuss their temperature dependence, before we focus on flip-flop processes, which commonly limit the spin lifetime at low magnetic fields.

4.4.1 Spin relaxation processes and their temperature dependence

In general, the electron spin-flip rate Γ is the sum of the flip-flop rate Γ_{FF} and spin-lattice relaxation rates, which include the one-phonon direct-flip process (coefficient α_D) as well as the two-phonon Raman (α_R) and Orbach processes (α_O) [Böttger2006b, Cruzeiro2017]. The latter involve scattering of phonons between ground state and second-to-lowest crystal field, with energy splitting $\Delta = h \cdot 1.2\,\mathrm{THz}$ [Doualan1995]. These processes depend on the magnetic field and temperature:

$$\Gamma = \Gamma_{\mathrm{FF}} \operatorname{sech}^2\left(\frac{\mu_B g_g B}{2k_B T}\right) + \alpha_D\, g_g^3 B^5 \coth\left(\frac{\mu_B g_g B}{2k_B T}\right) + \alpha_R\, T^9 + \alpha_O\, e^{-\Delta/k_B T} \qquad (4.16)$$

Since flip-flops occur among dopant pairs with anti-parallel spins, $\uparrow\downarrow$ and $\downarrow\uparrow$, their rate scales with the product of the Boltzmann occupation probabilities, $p_\uparrow p_\downarrow \sim \operatorname{sech}^2\left(\epsilon/2k_B T\right)$, which is ≈ 1 for small Zeeman level splittings ϵ.

Spin-lattice relaxation processes, on the other hand, scale with the thermal occupation of phonon modes and show a strong temperature dependence (figure 4.14). At temperatures below $2\,\mathrm{K}$, the two-phonon relaxation processes can be neglected, and for small Zeeman level splittings the temperature dependence of the one-phonon flip rate is approximately linear, $\coth\left(\epsilon/2k_B T\right) \sim T$.
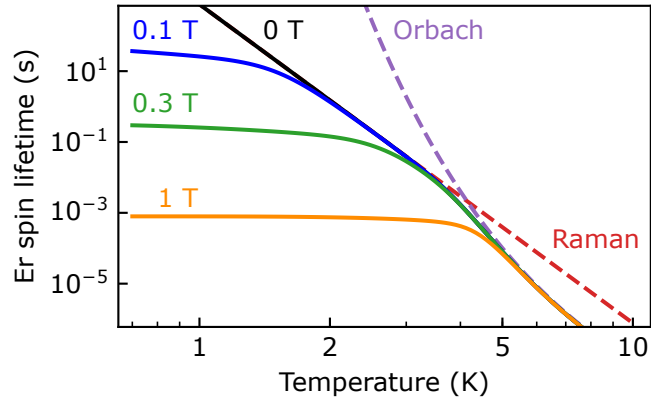
Figure 4.14: **Spin-lattice relaxation times.** At low temperature, the one-phonon direct-flip process dominates and scales as $\sim B^5$ with the magnetic field, while two-phonon relaxation by Raman and Orbach processes kick in at higher temperature. Here, flip-flop processes are not included, and the curves were calculated for typical coefficients: $g_g = 10$ ($\vec{B} \parallel D_2$), $\alpha_D = 1.1\,\mathrm{s}^{-1}\mathrm{T}^{-5}$ [Böttger2006b], $\alpha_R = 1.3 \times 10^{-3}\,\mathrm{s}^{-1}\mathrm{K}^{-9}$ and $\alpha_O = 2.5 \times 10^{10}\,\mathrm{s}^{-1}$ [Kurkin1980].

One-phonon spin-lattice relaxation

The direct spin-flip rate due to a one-phonon process is the sum of phonon absorption and phonon emission rates, Γ_{abs} and Γ_{em}. Because of the bosonic nature of phonons, absorption and emission rate have different dependencies on the phonon occupation number n [Norambuena2018]:

$$\Gamma_{\mathrm{abs}} = 2\pi\hbar^{-2}\, \rho(\epsilon)\, J^2\, n \tag{4.17}$$

$$\Gamma_{\mathrm{em}} = 2\pi\hbar^{-2}\, \rho(\epsilon)\, J^2\, (n+1) \tag{4.18}$$

Here we applied Fermi's Golden Rule, with the density of states $\rho(\epsilon) \sim \epsilon^3$ and the transition matrix element J. For Kramers ions, this matrix element is only non-zero because of admixtures of higher crystal field levels in the presence of a magnetic field [Shrivastava1983]. The lowest order magnetic field dependence is $J \sim \mathcal{O}(B)$, and combined with $\epsilon \sim g_g B$ we find

$$\Gamma_{\mathrm{abs}} = \alpha_D\, g_g^3 B^5 \left[\exp(\epsilon/k_B T) - 1\right]^{-1} \tag{4.19}$$

$$\Gamma_{\mathrm{em}} = \alpha_D\, g_g^3 B^5 \left[1 - \exp(-\epsilon/k_B T)\right]^{-1}. \tag{4.20}$$

Because it originates from higher crystal field level contributions in presence of a magnetic field, the coefficient α_D is likely anisotropic and depends on the orientation of the external magnetic field. For other rare-earth dopants in YSO, like neodymium and ytterbium, such anisotropy has already been extracted from measurements, with a maximum change in α_D by a factor of 5 [Lim2018, Cruzeiro2017]. Similarly, a different scaling with magnetic field is expected above 1 T, where the effective spin-1/2-model starts to break down and admixtures of higher crystal field levels become more significant.

For many processes, only the sum of absorption and emission is relevant: after spin pumping in holeburning experiments, for example, the population deviation from thermal equilibrium will decay with $\Gamma_{\mathrm{abs}} + \Gamma_{\mathrm{em}}$. Similarly, the redistribution of spins among the dopants happens at that rate, causing spectral diffusion, and it also describes the decay of an equal superposition, $\frac{1}{\sqrt{2}}\left(|\uparrow\rangle + |\downarrow\rangle\right)$. On the other hand, if we are operating with one particular spin ground state only, the lifetime only depends on either Γ_{abs} or Γ_{em}, which has to be used in eq. 4.16 instead. Possible scenarios could be experiments at high magnetic fields, for example a study on (super-)hyperfine states or on the optical coherence.

4.4.2 Spin lifetime dependence on the magnetic field strength

Because flip-flop process and one-phonon spin-lattice relaxation have different dependencies on the magnetic field amplitude, we can separate their contributions to the decay rate at low fields (see fig. 4.15). At low temperature, the only free parameters in eq. 4.16 are the flip-flop rate Γ_{FF} and the direct-flip coefficient α_D, whose dependence on the magnetic field orientation is unknown.

As becomes clear: at low magnetic fields and low temperature, any spin-lattice relaxation is highly suppressed, and the ultimate electron spin lifetime is set by flip-flop processes. In the next section, we will explain in more detail how the flip-flop rate can be calculated, and discuss approaches how to reduce it.
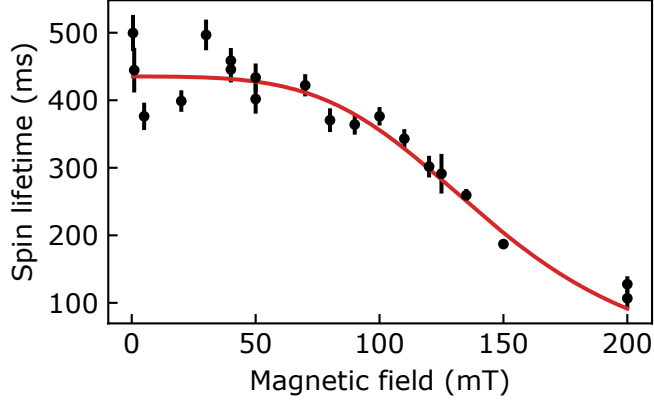
Figure 4.15: **Ground state spin lifetime vs. magnetic field.** While spin-lattice relaxation causes a drop of the spin lifetime at high magnetic fields, the plateau at low fields is determined by flip-flops. Fitting the data to eq. 4.16 (solid curve) yields a flip-flop time of $\Gamma_{\mathrm{FF}}^{-1} = 440(10)\,\mathrm{ms}$, in agreement with the prediction (eq. 4.22) for a 10 ppm crystal and a 12 MHz inhomogeneous spin transition linewidth. The obtained direct-flip coefficient $\alpha_D = 18\,\mathrm{s}^{-1}\mathrm{T}^{-5}$ is higher than the value of $1.1\,\mathrm{s}^{-1}\mathrm{T}^{-5}$ measured for a magnetic field along the D_1-axis [Böttger2006b].

4.4.3 Electron spin flip-flops

In contrast to Raman, Orbach and direct flip processes, the flip-flop mechanism is not related to spin-lattice relaxation. Instead, it is a cross-relaxation process of anti-parallel pairs of spins, governed by the $\hat{\sigma}_+\hat{\sigma}_-$ terms of the dipolar coupling Hamiltonian between similar spins (eq. 2.16).

In order to derive an analytical expression for the flip-flop rate, one can start with Fermi's Golden Rule [Car2019, Cruzeiro2017]:

$$\Gamma_{\mathrm{FF}} = \frac{2\pi}{\hbar}\,\rho\,\left\langle\,|\langle\uparrow\downarrow|\mathcal{H}_{\mathrm{dd}}|\downarrow\uparrow\rangle|^2\,\right\rangle_{\mathrm{avg}}. \tag{4.21}$$

Here, ρ is the density of final states $|\downarrow\uparrow\rangle$, and $\langle\cdot\rangle_{\mathrm{avg}}$ denotes taking the average over all possible spin pair configurations. With our short-hand notation of the dipole-dipole Hamiltonian (eq. 2.16), the matrix element for a single pair of spins evaluates to $\langle\uparrow\downarrow|\mathcal{H}_{\mathrm{dd}}|\downarrow\uparrow\rangle = 2J_S$.

Car et al. provide an analytical solution to the averaging integral over solid angles and express the effective density of states by the inhomogeneous spin transition linewidth Γ_s, $\rho \sim 1/(\hbar\Gamma_s)$:

$$\Gamma_{\mathrm{FF}} = \frac{1}{12\,\hbar^2}\,\mu_0^2\,\mu_B^4\,\Xi\big(\mathbf{g}_g,\vec{B}\big)\,\frac{n^2}{\alpha_0\Gamma_s}, \tag{4.22}$$

where $\alpha_0 \approx 1$ is a dimensionless parameter introduced to define a cut-off interaction radius for convergence reason, and we separate the dependence on the magnetic moment directional vectors $\vec{u}^x,\vec{u}^y$ (cf. eq. 2.15) and the averaging over all solid angles into

$$\Xi\big(\mathbf{g}_g,\vec{B}\big) = \frac{1}{4\pi}\int \mathrm{d}\Omega\,\left|\tfrac{1}{4}\left(\vec{u}^x\!\cdot\vec{u}^x + \vec{u}^y\!\cdot\vec{u}^y\right) - \tfrac{3}{4}\left((\vec{u}^x\cdot\hat{r})^2 + (\vec{u}^y\cdot\hat{r})^2\right)\right|^2. \tag{4.23}$$

In figure 4.16 we perform the averaging numerically and calculate the electron spin lifetime limit by flip-flops. Later, in chapter 5.2.5, we will apply the same approach to different coupling coefficients J_S that change under the influence of microwave pulse sequences.
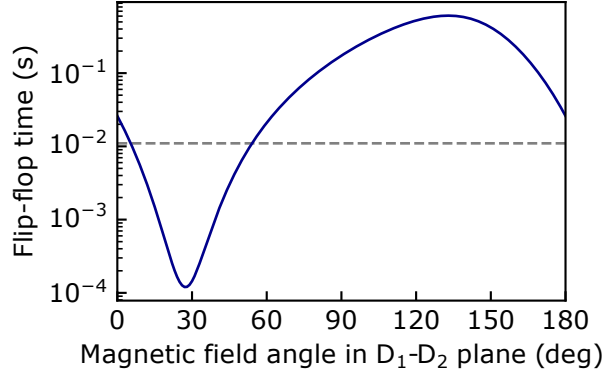
47

Figure 4.16: **Flip-flop time constant.** By numerically averaging over the solid angle, we can calculate the flip-flop time constant Γ_{FF}^{-1} from eq. 4.22, for a total dopant concentration of 10 ppm (5 ppm per site). When the magnetic field is rotated in the D_1-D_2 plane, the predicted flip-flop time varies by several orders of magnitude.

Concentration dependence

An important result of the Golden Rule approach is the expected scaling of the flip-flop rate with dopant concentration, $\Gamma_{FF} \sim n^2$. Here, n is the concentration of similar erbium ions with the same g-factor, which is significantly lower than the total erbium concentration in the crystal: 50 % of all ions occupy site 2 and can not participate in flip-flops with site-1-dopants. Likewise, 50 % of ions on site 1 belong to magnetic class II and are resonant with class-I-dopants only for certain magnetic field orientations. And lastly, ^{167}Er makes up 23 % of all ions, and because of its different hyperfine level structure it probably contributes less to cross-relaxation processes with zero-nuclear-spin isotopes, if at all [Car2019].

It is even possible to reduce the number of potential flip-flop partners over the course of an experiment by broadband optical pumping of all spins into one particular state [Welinski2020, Cruzeiro2017]. Unfortunately, this comes at the price of increased cross-relaxation for the opposite spin state. Alternatively, a magnetic field gradient should as well suppress flip-flop interactions but might be undesired for other reasons.

While the spin lifetimes predicted by eq. 4.22 for a 10 ppm doped crystal were in good agreement with their measurements, [Car2019] observed deviations from the model by up to one order of magnitude for a higher-doped crystal with 50 ppm, which could be explained by the role of inhomogeneous broadening. Since only spins with the same Zeeman splitting can participate in flip-flops, the number of potential flip-partners is reduced by the inhomogeneous width. This, however, is only true as long as spin transition frequencies show no correlation with the dopant position in the crystal. With increasing dopant concentration, the mean distance between two interacting spins can become smaller than the correlation length of disorder in the crystal [Welinski2017], and adjustment of the formula is necessary. Another effect could be an increase in the inhomogeneous linewidth broadening due to dipolar interactions, as already discussed in the context of spectral diffusion (section 4.2.3): the dipolar linewidth is expected to scale linearly with concentration [Cruzeiro2017, Abragam2012].

Nevertheless, it is clear that in the low-concentration limit the flip-flop rates will quickly drop below the direct-flip rate of the one-phonon process. This regime can be explored by using nominally undoped YSO crystals and studying the remaining dopants due to contamination with various rare-earth elements [Siyushev2014, Cruzeiro2017]. Efficient optical control and readout, however, usually require coupling to optical resonators [Dibos2018, Kindem2020], an approach that we will follow in chapter 6.

48

5 Coherent spin control and dynamical decoupling

In the previous chapter, we have used optical spectroscopy to study the lifetime of the electron spin of erbium dopants. To continue and now look into its coherence properties, we need tools to rotate the Zeeman qubit state on the Bloch sphere. To this end, we build a microwave resonator that provides us with homogeneous control over the ensemble of investigated spins. Using different dynamical decoupling sequences, we can extend the observable coherence time and show that it is limited by dipolar interactions between similar spins. A theoretical model supports these findings and suggests modified decoupling sequences tailored to the anisotropic erbium g-tensor in order to reach the ultimate coherence time limit set by dipole-dipole interactions.

5.1 Qubit control using microwave pulses

Probing the coherence of erbium spins is possible either optically by driving Raman transitions [Rančić2018, Serrano2018, Hartmann1968] or via oscillating magnetic fields at microwave frequencies [Probst2015, Guillot-Noël2007]. In order to study the effect of dynamical decoupling sequences on the entire spin ensemble, we choose microwave fields as coherent control, because the required homogeneity and peak power are easier to establish in the microwave domain than with laser beams. Still, achieving a sufficient pulse fidelity and control bandwidth remains challenging and makes high demands on the technical implementation.

In this section, we first review the effect of microwave pulses on the Zeeman qubit states. Then, we discuss all requirements for homogeneous coherent control and how they are met with the microwave resonator designed for this work. In the end, we demonstrate efficient spin initialization via holeburning and a high microwave pulse fidelity in Rabi flops, which form the basis for later decoupling experiments.

5.1.1 Effect of microwave pulses on the Zeeman qubit

The qubit eigenstates $|\uparrow\rangle$ and $|\downarrow\rangle$ are defined by the Zeeman Hamiltonian of the erbium electron spin, which reflects the energy of its magnetic moment $\vec{m}$ in the external field $\vec{B}_0$. By applying a microwave pulse, an oscillating component $\vec{B}_{\mathrm{mw}}$ is added to the magnetic field, and the former eigenstates start to undergo rotations, governed by the perturbation Hamiltonian $\mathcal{H}_{\mathrm{mw}} = -\vec{B}_{\mathrm{mw}} \cdot \vec{m}$. Because of the g-tensor anisotropy, the magnetic moment is *not* aligned with the static field (see section 2.4), so even if the microwave field is perpendicular to it, $\vec{B}_{\mathrm{mw}} \perp \vec{B}_0$, the resulting microwave interaction Hamiltonian is a linear combination of *all* rotations $\hat{\sigma}_x$, $\hat{\sigma}_y$, $\hat{\sigma}_z$ on the Bloch sphere:

$$\mathcal{H}_{\mathrm{mw}} = \tfrac{1}{2}\,\mu_B B_{\mathrm{mw}} \left(g_{\mathrm{mw,x}}\hat{\sigma}_x + g_{\mathrm{mw,y}}\hat{\sigma}_y + g_{\mathrm{mw,z}}\hat{\sigma}_z \right), \qquad (5.1)$$

where the effective microwave g-factors $g_{\mathrm{mw,i}}$ can be calculated from the directional vectors $\vec{u}^i$ of the magnetic moment (see eq. 2.11) by [Probst2013, Abragam2012]

$$g_{\mathrm{mw,i}} = \vec{u}^i \cdot \frac{\vec{B}_{\mathrm{mw}}}{B_{\mathrm{mw}}}. \qquad (5.2)$$

The effect of the microwave Hamiltonian $\mathcal{H}_{\mathrm{mw}}$ with a time-dependent magnetic field amplitude $B_{\mathrm{mw}} = B_{\mathrm{mw,max}} \cos(\omega t)$ can be discussed in the rotating frame, and much like in systems with isotropic g-tensor, the components $\hat{\sigma}_x$, $\hat{\sigma}_y$ of the microwave Hamiltonian directly translate into rotations in the rotating frame. [Vandersypen2005, Abragam2012]

Note that in general the microwave Hamiltonian also has a term $\sim \hat{\sigma}_z$, even though the microwave field is perpendicular to the static field axis (see figure 5.1). Because this term can not induce spin flips, it is widely ignored in literature, although it might appear in higher-order corrections as shift of the transition frequency for the duration of a pulse [Maryasov2012].
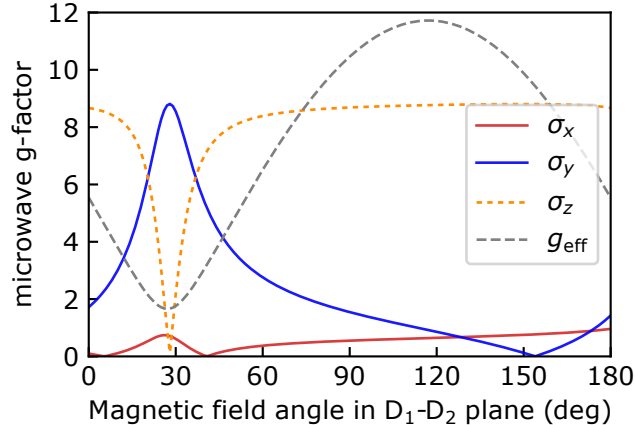

Figure 5.1: **Microwave g-factors.** Because of the anisotropic erbium g-tensor, a microwave field $\vec{B}_{\mathrm{mw}} \parallel$ b induces always a combination of rotations $\hat{\sigma}_x$, $\hat{\sigma}_y$, $\hat{\sigma}_z$ even if it is perpendicular to the external field $\vec{B}_0$ in the D_1-D_2 plane. Their relative strengths are given by the microwave g-factors according to eq. 5.2, here compared with the effective g-factor g_{eff} from the static field.

5.1.2 Technical requirements for microwave control

In our experiments with bulk crystals, the signal originates from the individual contributions of many erbium ions in an ensemble that is distributed in space and over different Zeeman transition frequencies. In order to measure the coherence time and identify the effect of decoupling sequences reliably, it is important that all ions behave similarly when microwave pulses are applied.

In holeburning experiments, we measured a distribution of spin transition frequencies over a width of $\sim 10\,\mathrm{MHz}$, which now defines the minimum excitation bandwidth that must be covered by each microwave pulse. As a consequence, the pulses need to be intense, but as short as possible – not only to ensure a wide Fourier transform and excitation bandwidth [Freeman1998, McDonald1991], but also because short pulses can be applied at higher rates, which increases the bandwidth at which interactions can be dynamically decoupled. In addition, a very homogeneous microwave field is required to make sure the spatial position of each individual ion does not play a role.

Because of the required high field amplitudes we choose to work with a microwave resonator and place the sample in its near-field. The resonator must meet two more requirements: first, its resonance frequency must match the electron spin-flip transition for typical static magnetic fields of $\sim 25\,\mathrm{mT}$. And second, the resonator bandwidth must be high enough, not only to cover the full inhomogeneous transition linewidth, but also to accommodate pulses of the desired duration. For example, a resonator bandwidth of $\Delta\nu = 10\,\mathrm{MHz}$ would set the minimum pulse length to $\sim 1/(2\pi\Delta\nu) \approx 16\,\mathrm{ns}$.

Which resonator design can be used and which microwave power can be deployed also depends on the transition frequency itself: while low-frequency circuitry tends to allow for simpler design techniques, resonant structures for frequencies below $1\,\mathrm{GHz}$ quickly require large dimensions that do not fit into our cryostat. On the other hand, transition frequencies above $9\,\mathrm{GHz}$ require expensive microwave equipment and can only be realized at considerable static magnetic fields, which would let spin-lattice relaxation dominate over dipolar interactions and eventually preclude any coherence time extension by dynamical decoupling.

Certain orientations of the static magnetic field offer large microwave g-factors, which reduces the required power significantly. Unfortunately, at those orientations also the flip-flop rates get very high and even exceed the excited state decay rate, which renders any ground spin initialization by optical pumping impossible (compare figures 5.1 and 4.16).

Altogether, an absolute transition frequency of about $3\,\mathrm{GHz}$ seems reasonable, which can be realized with our setup for effective g-factors > 6. In the following experiments, we achieve this by applying the external field along the D_2-axis of YSO ($\varphi = 90°$). In this configuration, the typical inhomogeneous linewidth is about $10\,\mathrm{MHz}$, which we could pre-characterize in holeburning experiments (cf. section 4.3.2; measurements will be shown later in figures 5.3b and 5.4b).

5.1.3 Low-Q microwave resonator

Our microwave resonator is based on a design for a double split-ring resonator that is fabricated as a printed circuit board (PCB) and which was shown to generate a very uniform field [Bayat2014]. In contrast to a single split-ring resonator, which would form the most simple resonant LC circuit, the nested arrangement of two split-rings with their gaps on opposite sides greatly improves homogeneity of the microwave field inside (see figure 5.2a). Additionally, we use a thin crystal slab of only $500\,\mathrm{\mu m}$ thickness, in direct proximity to the copper traces in order to reduce the field inhomogeneity perpendicular to the PCB plane.

For an intuitive understanding of the design parameters, one can look at a single split-ring LC circuit made out of thin wire, with a resonance frequency $\omega_0 = 1/\sqrt{LC}$. In a coarse approximation, the inductance L scales linearly with the wire length while the capacitance C is proportional to the inverse of the gap. Since a large gap degrades the field homogeneity inside the split-ring, the resonance frequency can be tuned most effectively with the wire length and thus the split-ring radius. In this simple picture it becomes clear that a finite-width split-ring combines the resonance frequencies of rings at different radii, and we can increase the design bandwidth by increasing the split-ring width.

By optimizing the parameters using a finite-difference time-domain solver (CST Microwave Studio 2018), we finalize the resonator design with a resonance frequency at $3\,\mathrm{GHz}$ and a bandwidth of $50\,\mathrm{MHz}$ (see figure 5.2b-d).
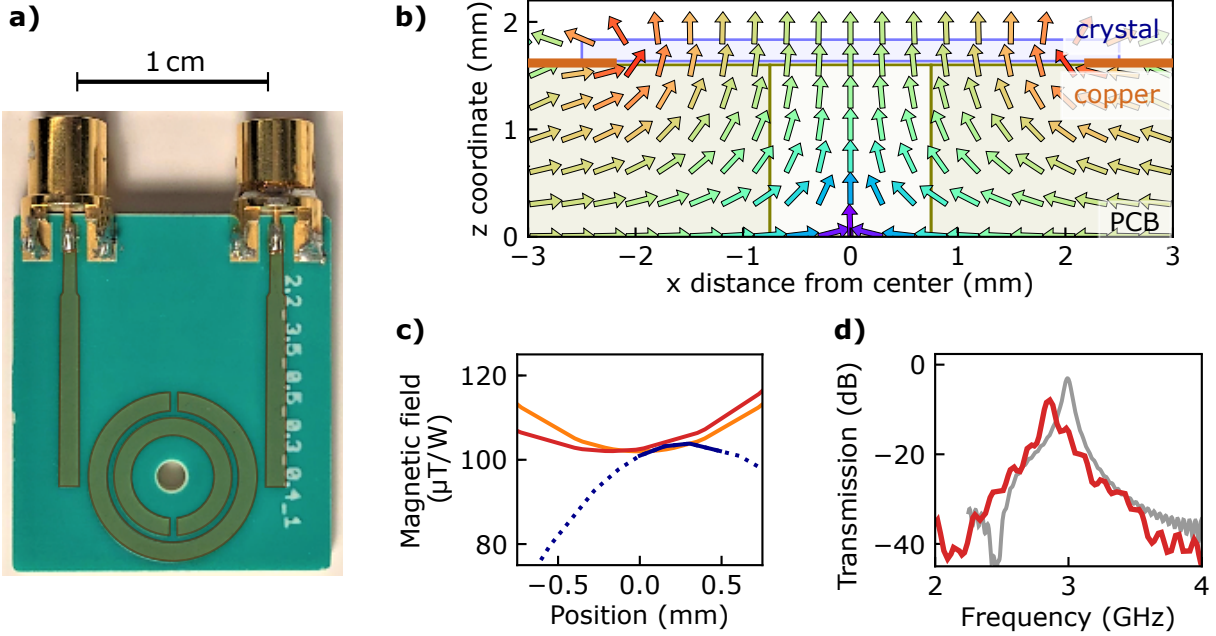
Figure 5.2: **Microwave double split-ring resonator. a) Photograph.** Copper traces on a PCB form two concentric split-ring resonators, into which microwaves are coupled via single strip lines. The traces are highlighted for better visibility; the crystal (not shown) is placed on top of the split-rings such that it covers the through-hole that provides optical access. **b) Magnetic field mode plot.** The magnetic field vectors (arrows) and amplitudes (increasing from blue to red) are plotted for a cross section through the PCB with the through-hole, the inner ring copper trace and the crystal. **c) Magnetic field profile.** Line cuts of the mode profile along the beam axis (blue) and perpendicular to it (red and orange) reveal an excellent field inhomogeneity of $\lesssim 2\%$ over the typical beam width of $\lesssim 0.2\,\text{mm}$, and $\lesssim 5\%$ over the crystal thickness of $0.5\,\text{mm}$ (solid blue line inside the crystal; dotted in air). **d) Resonator transmission.** The measured resonance frequency and bandwidth (red curve) are close to the simulated values of $3\,\text{GHz}$ and $50\,\text{MHz}$, respectively (grey curve), but small shifts are observed upon assembly of the resonator in a cryostat and cooldown to cryogenic temperature.

Pulse generation and amplification

Microwave pulses are coupled into the resonator via strip-lines that connect to coaxial cables. To generate the pulses, we use a DDS source (Rhode & Schwarz SGS100A) as input for an arbitrary waveform generator (Zurich Instruments HDAWG) that shapes the sine wave into reproducible short pulses with controllable relative phases. These pulses are then amplified to a maximum peak power of $100\,\text{W}$ (Mini Circuits ZHL-100W-352+) before they are fed via the cryostat coaxial cables into the resonator. While optimized pulse shapes or composite pulses could increase the pulse fidelity over the entire inhomogeneous linewidth, they would also require higher peak power or longer pulses [McDonald1991, Genov2020], which would then reduce the achievable decoupling bandwidth. Therefore, we decide to solely use rectangular pulses in this work.

5.1.4 Spin initialization and readout

After discussing the technical requirements of coherent spin control in the previous section, we now turn to its implementation in measurement sequences. Since all our experiments in this chapter were performed at low magnetic fields with a thermally distributed spin ground state population in the ensemble, all measurements on the electron spin start with a state preparation step, which we explain in the following.

Optical pumping as introduced in section 4.3 can be used to initialize the spin in one particular ground state. To overcome the spin pumping efficiency limit set by the small branching ratio (see section 4.3.1), we do not drive the spin-preserving but the spin-flip transition with the burn laser (see figure 5.3a). Because the subsequent relaxation via the spin-preserving transition is highly probable, an efficient population transfer into the opposite spin ground state is possible, if sufficient laser power is available ($\sim 1\,\mathrm{mW}$ in our experiments).

To read out the ground state polarization and quantify the spin initialization efficiency, we probe the antihole on the spin-preserving transition of the final spin state. By analyzing its decay over time, we obtain a ground state spin lifetime of $53(5)\,\mathrm{ms}$, limited by flip-flops (cf. figure 4.16). For this spin lifetime and the expected branching contrast, we can calculate the maximum spin initialization efficiency from rate equations (eq. 4.8) and find a state preparation efficiency of $0.9(1)$, in agreement with the measured antihole area relative to the hole on the spin-preserving transition of the original spin state (see figure 5.3b).
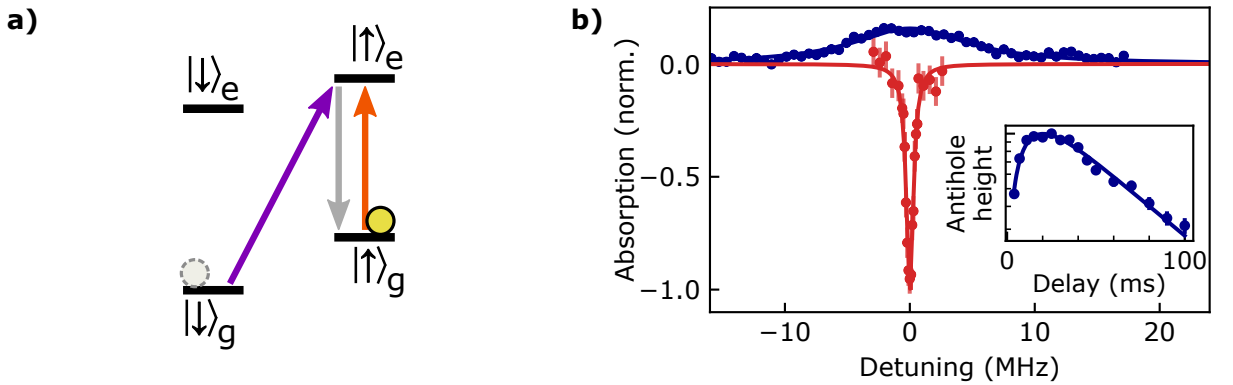
Figure 5.3: **a) Schematics of spin initialization and readout.** For spin initialization, the burn laser drives the spin-flip transition to the excited state with opposite spin (purple arrow), from where the spontaneous decay via a spin-preserving transition is favored (grey arrow), so that spin population is transferred from one ground state (grey circle) to the other (yellow circle). The ground state spin polarization is probed on the spin-preserving transition of the final spin (orange arrow). **b) Probing the spin polarization.** After successful spin initialization, the increase in absorption on the probe transition is seen as antihole (blue curve), which decays for increasing burn-probe delays with the spin lifetime of $53(5)\,\mathrm{ms}$ (inset). By comparing its initial area with the spectral hole obtained when burning on the probe transition (red curve), a spin initialization efficiency of $0.9(1)$ can be estimated.

Because erbium spins are only pumped if their optical transitions are addressed by the burn laser, only a fraction of the entire ensemble is initialized. However, we do not observe a correlation between the exact spin transition frequency of dopants and their spectral position in the optical absorption line of the ensemble. Therefore, we expect the optically addressed subset of ions to represent the coherence properties of the entire ensemble in the following experiments.

Furthermore, we decide to deliberately introduce a small tilt of the magnetic field vector perpendicular to the D_1-D_2 plane, so the spin transitions of both magnetic classes are sepa-

rated and potential inhomogeneities are further reduced. The effective dopant concentration addressed by microwave pulses is therefore reduced from initially $10\,\mathrm{ppm}$ (both sites, both classes) only $n \approx 2\,\mathrm{ppm}$, taking into account that $^{167}\mathrm{Er}$ isotopes have different level splittings.

5.1.5 Rabi oscillations

By applying a sequence of microwave pulses between spin initialization and readout, we can observe its effect on the spin polarization as a change in the probed antihole area.

In a first experiment, we demonstrate coherent population transfer between the two ground spin states by applying a single microwave pulse and varying its length t_p (figure 5.4). Depending on the pulse area $\Omega\,t_p$ we see population transfer into the other spin state (at odd multiples of π) and back into the initial ground state (at multiples of 2π). These Rabi oscillations $P_\downarrow(t_p) = \sin^2(\Omega\,t_p/2)$ are evidence of coherent spin manipulation and prerequisite for decoupling measurements discussed in the next section.

We observe an exponential decay of the envelope function, which is caused not only by pulse imperfections but also by a loss of coherence, partly due to dipolar interactions [Baibekov2014]. Also, we see that the Rabi oscillation slows down with increasing pulse length. A possible reason is heating of wires by the microwave pulse, which leads to increased resistance and lower incoupling into the resonator.
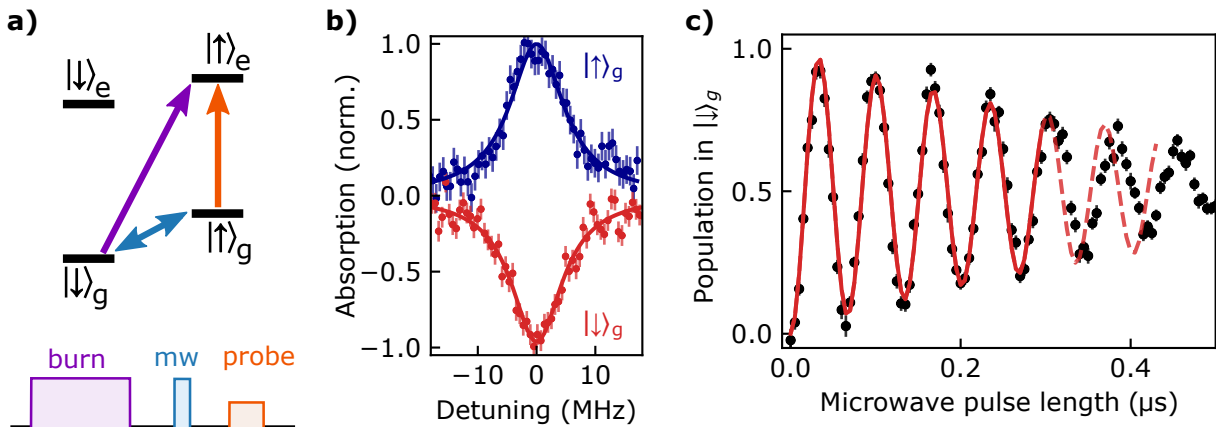
Figure 5.4: **a) Measurement sequence with microwave control.** After spin initialization by burning on the spin-flip transition (purple arrow and pulse), a microwave pulse is applied on the ground state spin transition (blue). The resulting spin polarization is read out optically on the spin-preserving probe transition (orange). **b) Readout before and after inversion.** On the probe transition, the antihole as obtained after spin initialization (blue curve) is inverted after applying a microwave π pulse on the ground state spin transition (red curve), with a typical pulse fidelity of $98\,\%$ at the line center. **c) Rabi oscillations.** By varying the length of the microwave pulse between spin initialization and readout, oscillations of the ground state spin polarization are observed with a Rabi frequency of $2\pi \cdot 14.9(1)\,\mathrm{MHz}$. By fitting only the first $0.3\,\mathrm{\mu s}$ to a decaying sine function (solid red curve) and extrapolating it to longer pulse lengths (dashed), a slowing down of the Rabi oscillation becomes apparent possibly due to heating of cables and higher ohmic losses.

While the measured spin-flip fidelity at the center of the transition reaches 0.98 (see figure 5.4b), the average value for spins in the ensemble is lower because the flip efficiency decays with detuning $\delta\nu$ from the microwave frequency: [Agnello2001]

$$\langle \sin^2\theta \rangle = \int_{-\infty}^{\infty} d\delta\nu \, \frac{1}{\pi} \frac{(\Delta\nu/2)}{(\delta\nu)^2 + (\Delta\nu/2)^2} \frac{\Omega^2}{\Omega^2 + (2\pi\delta\nu)^2} \sin^2\left(\frac{\sqrt{\Omega^2 + (2\pi\delta\nu)^2}\, t_p}{2}\right) \quad (5.3)$$

For the Rabi frequency $\Omega = 2\pi \cdot 14.9(1)\,\text{MHz}$ measured on resonance, and the ensemble linewidth of the spin transition extracted from holeburning experiments, $\Delta\nu \approx 10\,\text{MHz}$, we calculate an average π-pulse fidelity of $\langle \sin^2\theta \rangle \approx 0.78$ for a π-pulse length of $33\,\text{ns}$. Such a π pulse is a key building block of dynamical decoupling sequences that will be discussed in the next section, together with $\pi/2$ rotations. To make sure that both pulses have the same bandwidth and manipulate all ions in the same way, we use $\pi/2$ pulses of the same length as for π rotations but with reduced microwave power.

5.1.6 Ramsey and spin-echo measurements

While Rabi oscillations are already a proof of coherent evolution, their exponential envelope is not a good measure for the system's coherence time because of the disturbance by continuous microwave irradiation. A better approach is a Ramsey experiment, in which an equal superposition state is prepared by a short pulse with area $\pi/2$, followed by a free-evolution period. If the coherence is preserved, a second and final $\pi/2$ pulse will complete a full population inversion, while any dephasing reduces the readout contrast. If all pulses are much shorter than the typical free-evolution periods, their impact on the state evolution can be assumed to be instantaneous, and the readout signal directly reveals the coherence during a free-evolution period.

Since the coherence time obtained in Ramsey experiments is limited by static disorder and the inhomogeneous transition linewidth, we also employ spin-echo experiments, which can correct for ensemble dephasing due to static frequency shifts, as shown in the following.

Ramsey experiments

A Ramsey experiment measures the phase coherence of the prepared superposition state during a free-evolution period without any decoupling. But because the spin transition frequencies in the investigated ensemble are not all exactly the same, different relative phases will be acquired. Thus, the ensemble average over these superposition states decays over time into a mixed state, which will appear as loss of coherence over time. The shape of the signal decay depends on the temporal correlation of the relative detunings in the spin ensemble. It is exponential for static disorder frequency shifts, while fast spectral diffusion could distort the decay curve to a more Gaussian shape [Sousa2009, Bauch2020]. The observed characteristic time $T_2^* = 0.04(1)\,\mu\text{s}$ (see figure 5.5a) corresponds to an inhomogeneous linewidth of $1/(\pi\,T_2^*) = 8(2)\,\text{MHz}$, which is in coarse agreement with the observed spectral hole width of $6(1)\,\text{MHz}$ in these particular experiments. The hole width is narrower compared to fig. 5.4b, likely because of a lower magnetic field inhomogeneity across the probed sample volume due to a smaller beam diameter.
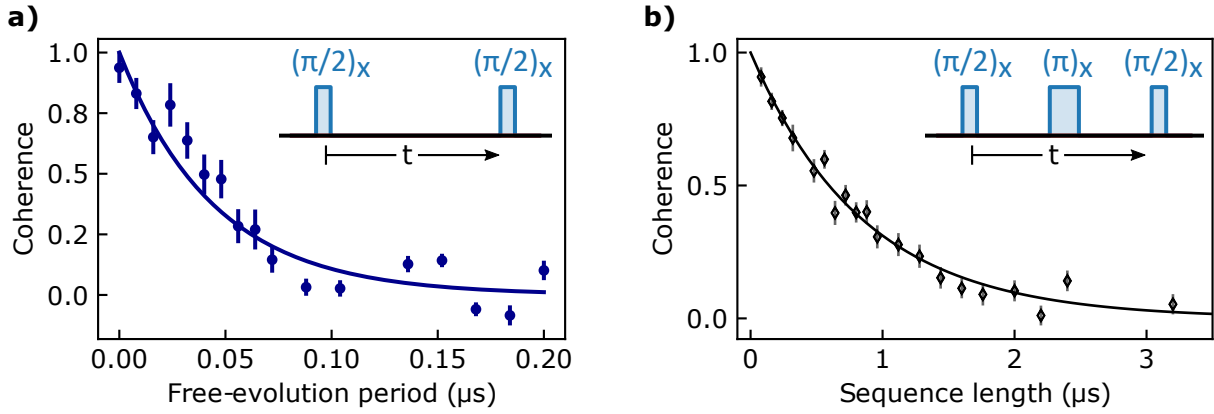
Figure 5.5: **a) Ramsey experiment.** Because of different transition frequencies in the ensemble, the ground state spin coherence as measured with a Ramsey sequence decays on a timescale $T_2^* = 0.04(1)\,\mu s$ set by the inhomogeneous linewidth (data points fitted by an exponential decay). **b) Spin-echo measurement.** By applying a π pulse halfway through the sequence, the dephasing due to static frequency shifts is corrected, and the resulting spin-echo coherence time extended to $T_2 = 0.86(9)\,\mu s$.

Spin-echo coherence time

Dephasing due to different transition frequencies in an ensemble of many ions does not reflect the coherence of each individual spin and can be reverted. To this end, a spin-echo sequence applies a π pulse halfway through the free-evolution period, which inverts the phases that were acquired during the first half. After the second half of the free-evolution period all superposition states in the ensemble refocus into the same state again, because the phases acquired before and after the π pulse cancel out. Similarly to the Ramsey sequence, a final $\pi/2$ pulse rotates the superposition back into one of the eigenstates again to prevent further dephasing until readout.

In our measurements, we obtain a spin echo coherence time of $T_2 = 0.86(9)\,\mu s$ (see figure 5.5b), which is still far from the fundamental limit $T_2 = 2\,T_1$ set by the ground state spin lifetime $T_1 \approx 50\,ms$ as measured in holeburning scans (cf. inset of figure 5.3b). The reason is that the refocusing effect from the single π pulse in a spin-echo sequence can cancel out only dephasing due to static disorder, i.e. frequency shifts which stay constant over the entire sequence length. In contrast, the interaction among spins in the ensemble or with a fluctuating environment can change over time and thus still induces decoherence.

5.2 Dynamical decoupling theory

In the previous section, we found that the coherence time as obtained by spin-echo measurements is orders of magnitude smaller than the fundamental limit set by the spin lifetime. This excess dephasing originates from coupling to a fluctuating nuclear spin bath and from dipolar interactions with other erbium spins in the ensemble, governed by the respective Hamiltonian.

A common technique to reduce excess dephasing is dynamical decoupling: by applying quasi-instantaneous microwave pulses and rotating the spins, their effective time evolution can be modified and shaped. Then, the interaction Hamiltonian for a free-evolution period is replaced by an average Hamiltonian that describes the effective evolution of the prepared superposition, and that can be designed to a great extent by the applied pulse sequence. [Brinkmann2016]

In this section, we first present the formal framework of the Average Hamiltonian Theory and apply it to the decoupling of erbium spins from the nuclear spin bath by π-pulse trains. Then, we review the dipolar interaction Hamiltonian and discuss how it requires decoupling techniques that differ from a simple π-pulse train. We derive that commonly used pulse sequences that decouple isotropic interactions provide only a moderate coherence time extension in systems with highly anisotropic g-tensors, such as in Er:YSO. In the end, we study modified decoupling sequences that are optimized for systems with anisotropic g-tensors and investigate the theoretical coherence time limit set by dipolar interactions.

5.2.1 Constructing an Average Hamiltonian

A formal method to study the effect of a pulse sequence on the potential decoupling effects is provided by the Average Hamiltonian Theory [Brinkmann2016, Choi2020]. Assuming instantaneous microwave pulses and an otherwise time-independent Hamiltonian, the sequence can be split up into time intervals τ_k of free evolution, but each with a modified Hamiltonian $\mathcal{H}_k$ that takes into account the current spin orientation due to the preceding rotations. Then, the phase evolution of the whole sequence can be described by an average Hamiltonian $\bar{\mathcal{H}}$, which reads to the zeroth order as

$$\bar{\mathcal{H}} = \frac{\sum_k \tau_k \mathcal{H}_k}{\sum_k \tau_k} \tag{5.4}$$

To find the free-evolution Hamiltonians in between the pulses, it is common to write them in the interaction frame of the microwave field, also referred to as 'toggling frame'. The effect of microwave pulses in this frame are rotations of the spins.

For example, a simple π pulse maps the spin z-component $\hat{\sigma}_z$ onto $-\hat{\sigma}_z$ so that the phase evolution by any Zeeman-like perturbation of the form $\mathcal{H}_0 = \epsilon\,\hat{\sigma}_z$ will be reversed after the pulse, $\mathcal{H}_1 = \epsilon\,(-\hat{\sigma}_z)$. As a consequence, in a spin-echo sequence, where the system spends equal periods of time in either orientation, the Zeeman Hamiltonians before and after the pulse cancel out, and the phase evolution is independent of static disorder as caused by inhomogeneous magnetic fields. Thus, the system is – to first order – decoupled from Zeeman interactions, and longer coherence times can be achieved.

In general, decoupling sequences aim to construct an average Hamiltonian that does not contain certain interaction terms or even equals zero; the required sequence depends on the type of interaction.

Free-evolution Hamiltonians for rotated spins

For more complex pulse sequences, we need to understand how the free-evolution Hamiltonian after some $\pi/2$ rotations around the x- and y-axis of the toggling frame depends on the initial spin components. To this end, we need to find out which component of the initial spin state is aligned with the coordinate axes of the toggling frame. In general, we can express every spin component $\hat{\sigma}_i$ by the projection of the spin vector $\hat{\vec{\sigma}}$ on the respective basis vector $\vec{e}_i$ of the toggling frame, $\hat{\sigma}_i = \vec{e}_i \cdot \hat{\vec{\sigma}}$.

To account for the effect of a $\pi/2$ pulse, the spin vector $\hat{\vec{\sigma}}$ in the subsequent Hamiltonian needs to be replaced with the rotated vector $\mathbf{R} \cdot \hat{\vec{\sigma}}$, where the matrices for $\pi/2$ rotations around the x- and y-axis of the toggling frame are defined as follows (see figure 5.6):

$$\mathbf{R}_x = \begin{pmatrix} 1 & 0 & 0 \\ 0 & 0 & -1 \\ 0 & 1 & 0 \end{pmatrix} \quad , \quad \mathbf{R}_y = \begin{pmatrix} 0 & 0 & 1 \\ 0 & 1 & 0 \\ -1 & 0 & 0 \end{pmatrix} \tag{5.5}$$

$$\mathcal{H}_0 = \epsilon\,\hat{\sigma}_z \qquad \mathcal{H}_1 = \epsilon\,(\vec{e}_z \cdot \mathbf{R}_y \cdot \hat{\vec{\sigma}}) \qquad \mathcal{H}_2 = \epsilon\,(\vec{e}_z \cdot \mathbf{R}_x \mathbf{R}_y \cdot \hat{\vec{\sigma}})$$
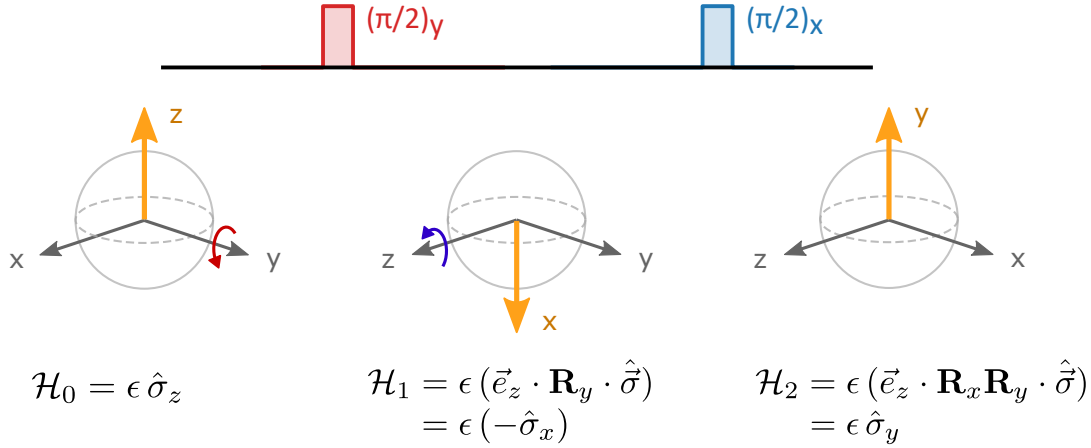$$= \epsilon\,(-\hat{\sigma}_x) \qquad\qquad = \epsilon\,\hat{\sigma}_y$$

Figure 5.6: **Example of average Hamiltonian contributions after rotation pulses.** A Zeeman-like Hamiltonian $\mathcal{H}_0 = \epsilon\,\hat{\sigma}_z$ will depend on the projection of the rotated spin vector $\mathbf{R} \cdot \hat{\vec{\sigma}}$ on the z-axis basis vector $\vec{e}_z$ after the application of microwave pulses. Concatenated pulses will appear as multiplication of their rotation matrices, here depicted for a sequence of a $\pi/2$ rotation around the y-axis of the toggling frame, $\mathbf{R}_y$, followed by a rotation around the x-axis, $\mathbf{R}_x$. The bottom row depicts the orientation of spin vector components $\hat{\sigma}_x$, $\hat{\sigma}_y$, $\hat{\sigma}_z$ in the toggling frame, in which microwave pulses are applied. The spin vector projection onto the z-axis is highlighted as it determines the effective contribution to the Zeeman-like Hamiltonian.

Pulse imperfections, robustness of decoupling sequences, and higher-order corrections

In real experiments, the average Hamiltonian alone can not explain all observations. For example, a large variety of π-pulse trains shares the same average Hamiltonian but yield different coherence decays [Gullion1990]. The reason are imperfections in the experimental realization of the decoupling sequence, leading to different error sources: the finite pulse length and possible deviations in the rotation angle and axis [Choi2020].

First, the finite length t_p of a microwave pulse does not only modify the effective time spent in each free-evolution interval. By breaking each π pulse into two finite-length $\pi/2$ pulses, one can see that the spins also spend some time in an intermediate orientation with

its own energy shifts and interaction matrix elements. Furthermore, for each pair of spins, a cross-interaction error can occur, which describes the interaction of one spin before the pulse with the other spin after it.

Second, any imperfection in the pulses leads to rotation errors: a deviation in microwave power results in an over- or under-rotation (i.e., a rotation angle not equal to π or $\pi/2$), while a detuned microwave frequency causes a tilt of the rotation axis. To make decoupling sequences robust against such imperfections, the relative phases and rotation axes in a train of π pulses should follow certain order [Souza2012].

In [Choi2020], an algebraic set of robustness conditions was derived that takes all the above imperfections into account. As a rule of thumb, a higher symmetry of the pulse pattern increases its robustness [Mansfield1971, Souza2012], for example, because an error introduced by one particular pulse can later be reversed by another pulse with opposite phase.

These symmetrization techniques can also reduce the impact of higher-order terms in the designed decoupling sequence. The simple expression for the average Hamiltonian in eq. 5.4 is only the first term of a series representation for the propagation operator. Higher-order terms of this so-called Magnus expansion include commutators of the Hamiltonians for all free-evolution intervals. The first-order correction, for example, reads [Choi2020, Brinkmann2016]

$$\bar{\mathcal{H}}^{(1)} = \frac{-i}{2\hbar T} \sum_{k}^{n} \sum_{l}^{k} \left[\tau_l \mathcal{H}_l, \tau_k \mathcal{H}_k \right], \tag{5.6}$$

where the sums iterate over a total number of n free-evolution intervals with Hamiltonians $\mathcal{H}_k$ and lengths τ_k, and $T = \sum_{k}^{n} \tau_k$ is again the total sequence length.

5.2.2 Decoupling interactions with off-resonant spin baths

One of the major sources of excess dephasing of erbium spins in YSO is their coupling to a bath of yttrium nuclear spins, which produce fluctuating local magnetic fields at the erbium sites. Since this coupling is a Zeeman-like perturbation, it can be canceled out by π pulses that invert the erbium spins, as outlined in the beginning of section 5.2.1.

A single π pulse, however, can only decouple static disorder, i.e. frequency shifts that do not change over the entire sequence length, but it can not correct for fluctuating frequency shifts induced by dynamics in the nuclear spin bath. In a common approach towards a higher decoupling bandwidth, multiple refocusing sequences are concatenated, and π pulses are applied at a faster rate. [Biercuk2011, Bar-Gill2012]

Such a train of decoupling pulses also allows for varying the rotation axes in order to make the sequence more robust against pulse imperfections. Instead of applying only $(\pi)_x$-pulses, for example, one could alternate between $(\pi)_x$- and $(\pi)_y$-pulses, so that the decoupling effect does not depend on the initialization axis of the input state. Two such universal decoupling sequences that consist only of π pulses are XY-4 and XY-8 (see figure 5.7) [Kawakami2016, Souza2012, Gullion1990], which we will also use in our experiments in section 5.3.

For optimal decoupling, the spacing between the π pulses needs to be shorter than the correlation time of the the magnetic environment, whose upper bound is the lifetime of the nuclear spins. In addition, stronger correlation is expected on a much shorter time scale determined by the nuclear spin precession frequencies [Childress2006]. For Er:YSO, the yttrium gyromagnetic ratio of $\approx 2\,\mathrm{MHz/T}$ and the magnetic field of several $100\,\mathrm{mT}$ induced by the erbium spins (cf. figure 4.5b) let us expect a characteristic time scale of the order of $\sim 1\,\mu\mathrm{s}$ for the nuclear spin bath dynamics at low magnetic fields (in agreement with [Car2020]).

In general, such decoupling of a fluctuating spin bath is not restricted to nuclear spins but also applies to dissimilar paramagnetic impurities, such as erbium spins on site 2 or
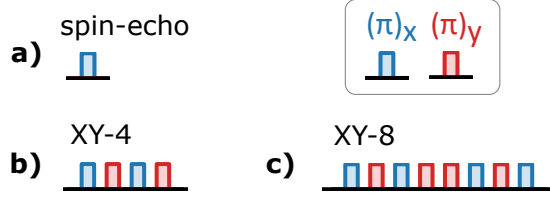
Figure 5.7: **Pulse sequences for decoupling from a fluctuating spin bath.** While a simple spin-echo sequence uses only a single refocusing π pulse (a), a higher decoupling bandwidth can be achieved by a train of π pulses, as in XY-4 (b) and XY-8 (c). Because these two sequences combine rotations around x- and y-axis, they are universal, i.e. they work equally well for any input state. By concatenating XY-4 with its phase-shifted variant, the XY-8 sequence gains more robustness against pulse imperfections.

site-1-dopants of magnetic class II, as well as other rare-earth impurities and charge traps with $g \approx 2$. All these electron spins that are not resonant with the microwave pulses have fast precession frequencies in the interaction frame of the optically addressed erbium ions, and their coupling averages out to a perturbation that is equivalent to an effective magnetic field. Therefore, the interaction with any off-resonant spins can be expressed as Zeeman-like perturbation $\sim \epsilon \hat{\sigma}_z$ and decoupled by a train of π pulses.

For similar erbium spins, however, such treatment as effective magnetic field perturbation is no longer possible in the context of decoupling, because both dopants of an interacting spin-pair are affected by microwave pulses in the same way.

5.2.3 Dipolar interactions with resonant erbium spins

When we apply the refocusing π pulse in a spin-echo experiment, we do not only invert the spin polarization of the optically addressed dopants but also flip all resonant erbium spins that they are interacting with. Consequently, every microwave pulse alters the local spin configuration and redistributes the transition frequencies in the ensemble, thus causing instantaneous spectral diffusion (see figure 5.8). The inhomogeneous linewidth $\Delta\nu_{\text{fwhm}}$ associated with this effect limits the coherence time to $T_2 = (\pi \Delta\nu_{\text{fwhm}})^{-1}$.

We can calculate the instantaneous diffusion linewidth with the formula for dipolar broadening derived from integration over all interacting spin pairs (cf. section 4.2.3 and A.1):

$$\Delta\nu_{\text{fwhm}} = \frac{2\pi}{9\sqrt{3}}\, \mu_0 h \gamma_{\text{eff}}^2\, n_{\text{eff}} \tag{5.7}$$

Here, the dopant concentration n is replaced by an effective concentration $n_{\text{eff}} = n \langle \sin^2 \theta \rangle$, because due to pulse imperfections and inhomogeneities only a fraction $\langle \sin^2 \theta \rangle$ of all similar erbium spins is inverted by the π pulse. Because the spin transitions of site-1-dopants of class II, site-2-dopants, and ^{167}Er isotopes are far detuned, the concentration of similar erbium spins is reduced to $n = 2\,\text{ppm}$. Assuming that the inhomogeneous linewidth as derived from the spin-echo coherence time of $0.86(9)\,\mu\text{s}$ (fig. 5.5b) is solely determined by instantaneous spectral diffusion, we find that $\langle \sin^2 \theta \rangle \approx 0.73$, in agreement with the value 0.78 independently deduced from the Rabi frequency and the ensemble linewidth (section 5.1.5).

Clearly, a smaller rotation angle would lower the pulse fidelity and reduce the dipolar broadening, thus enabling longer coherence times [Lim2018, Petersen2018]. For quantum memories or sensing, however, the entire ensemble of optically addressed spins needs to be decoupled.

In the following, we investigate to which extent the coherence limitation set by instantaneous diffusion can be alleviated by dynamical decoupling with tailored sequences. To this
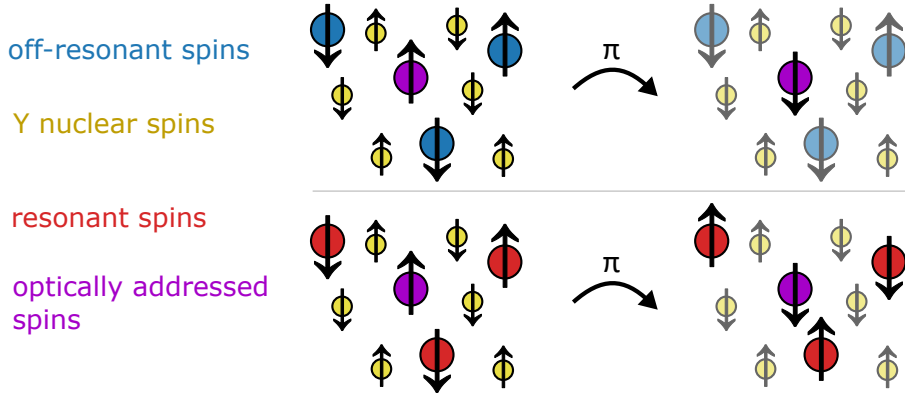
Figure 5.8: **Effect of a microwave π pulse on resonant and off-resonant spins.** The effective magnetic field generated by nuclear spins and off-resonant paramagnetic impurities remains unaffected when a π pulse is applied (top panel). Thus, the inversion of an optically addressed spin decouples it efficiently from the off-resonant spin bath. In contrast, similar erbium spins that are resonant with the microwave will be inverted, too (bottom panel). As a result, the local magnetic environment of optically addressed spins is changed by each π pulse, which precludes efficient decoupling.

end, we recall the dipolar Hamiltonian and discuss the effect of microwave pulses more formally in the framework of the Average Hamiltonian Theory, before we analyze their potential for dynamical decoupling.

Dipolar coupling Hamiltonian

The coupling between two erbium electron spins with magnetic moments $\vec{m}_1$ and $\vec{m}_2$ is governed by the magnetic dipole-dipole interaction Hamiltonian

$$\mathcal{H}_{\mathrm{dd}} = \frac{\mu_0}{4\pi\, r^3} \left[\vec{m}_1 \cdot \vec{m}_2 - 3(\vec{m}_1 \cdot \hat{r})(\vec{m}_2 \cdot \hat{r}) \right], \tag{5.8}$$

where $\hat{r}$ is the unit vector connecting the spins and r is the distance.

In section 2.4.1 we have derived an expression of this coupling Hamiltonian in the Zeeman eigenbasis with

$$\mathcal{H}_{\mathrm{dd}} = J_S \left(\hat{\sigma}_x \hat{\sigma}_x + \hat{\sigma}_y \hat{\sigma}_y \right) + J_I\, \hat{\sigma}_z \hat{\sigma}_z, \tag{5.9}$$

where J_S and J_I contain all dependencies on orientation and position of the dopants relative to the external magnetic field.

By their action on the eigenstates, we identified J_S as flip-flop coefficient and J_I as spectral diffusion coefficient that induces state-dependent frequency shifts, because

$$\langle \uparrow\uparrow | \mathcal{H}_{\mathrm{dd}} | \uparrow\uparrow \rangle = J_I \tag{5.10}$$

$$\text{and} \qquad \langle \uparrow\downarrow | \mathcal{H}_{\mathrm{dd}} | \downarrow\uparrow \rangle = 2\, J_S. \tag{5.11}$$

From these matrix elements, we can derive the dipolar transition linewidth $\Delta\nu_{\mathrm{fwhm}}$ and the flip-flop rate Γ_{FF} by summing over all interacting spin pairs and averaging over random distributions, as done in sections 4.2.3 and 4.4.3. While the flip-flop rate sets a limit to the spin lifetime, $T_1 \leq \Gamma_{\mathrm{FF}}^{-1}$, the inhomogeneous linewidth due to dipolar broadening limits the maximum achievable coherence time, $T_2 \leq (\pi\Delta\nu_{\mathrm{fwhm}})^{-1}$, because of instantaneous spectral diffusion. Therfore, the task is to find a sequence that not only decouples a Zeeman term $\epsilon\,\hat{\sigma}_z$ but also the spectral diffusion term $J_I\,\hat{\sigma}_z\hat{\sigma}_z$.

Dipolar interaction Hamiltonian under global rotations

In contrast to the Zeeman-like interaction with an off-resonant spin bath, the dipolar coupling with similar erbium spins is not governed by a single-qubit operator $\hat{\sigma}_z$, but by the two-qubit operator $\hat{\sigma}_z\hat{\sigma}_z$.

In a typical experiment, all spins at certain transition frequency will be addressed by the microwave pulses, so we can apply only global rotations that affect both spins in the same way. Therefore, while a π pulse maps $\hat{\sigma}_z$ onto $-\hat{\sigma}_z$, it will leave $\hat{\sigma}_z\hat{\sigma}_z$ unchanged. Still, rotations by $\pi/2$ will map $\hat{\sigma}_z\hat{\sigma}_z$ onto $\hat{\sigma}_x\hat{\sigma}_x$ or $\hat{\sigma}_y\hat{\sigma}_y$ and vice versa, but they can never invert the sign. Formally, this can be derived by substituting both spin components with the projections of the rotated spin vectors on the coordinate axes, as shown in section 5.2.1, for example $\hat{\sigma}_x\hat{\sigma}_x \to (\vec{e}_x \cdot \mathbf{R} \cdot \hat{\vec{\sigma}}) \otimes (\vec{e}_x \cdot \mathbf{R} \cdot \hat{\vec{\sigma}})$.

As a consequence, it is not possible to eliminate an individual interaction term, like $\hat{\sigma}_x\hat{\sigma}_x$, in the average Hamiltonian. More generally, it can be shown that the isotropic interaction term $\hat{\vec{\sigma}} \cdot \hat{\vec{\sigma}}$ remains invariant under any global rotations [BenAttar2020, Choi2017]. In our case, the isotropic Hamiltonian reads

$$\mathcal{H}_{\mathrm{dd,iso}} = \frac{2J_S + J_I}{3} \left(\hat{\sigma}_x\hat{\sigma}_x + \hat{\sigma}_y\hat{\sigma}_y + \hat{\sigma}_z\hat{\sigma}_z \right) \tag{5.12}$$

$$= \frac{\mu_0}{12\pi\, r^3} \frac{\mu_B^2}{4} \sum_{i\in\{\,x,y,z\,\}} g_i^2 \left(1 - 3\, r_i^2 \right)\ \hat{\vec{\sigma}} \cdot \hat{\vec{\sigma}}, \tag{5.13}$$

where g_i and r_i are the g-tensor eigenvalues and the components of the unit vector connecting the spins, $\hat{r}$, in the g-tensor eigenbasis.

Apparently, for systems with isotropic g-tensor ($g_x = g_y = g_z$) this isotropic Hamiltonian equals zero, because $\sum_i \left(1 - 3\, r_i^2 \right) = 3 \left(1 - |\hat{r}|^2 \right) = 0$, and full decoupling is possible. This is not the case, however, for erbium dopants in YSO with their highly anisotropic g-tensor. Here, full decoupling of dipolar interactions is not possible, because the isotropic part of the coupling Hamiltonian will stay non-zero for *any* average Hamiltonian.

5.2.4 Decoupling dipolar interactions: symmetric sequences

There exist plenty of pulse sequences that were designed to decouple interactions in spin ensembles with isotropic g-tensors [Haeberlen1968, Mansfield1981, Waeber2019]; the earliest of which, known as WAHUHA sequence, however lacks of robustness against pulse errors and does not achieve decoupling from static disorder. Recently, a more complex variant, 'DROID-60' ('Disorder-RObust Interaction-Decoupling'), was designed to meet both needs (figure 5.9): a robust sequence that can decouple not only disorder from static shifts or slowly fluctuating nuclear spin baths but also dipolar interactions [Choi2020].

Since global rotations by π do not induce any change in the interaction Hamiltonian, DROID-60 and similar sequences also consist of several $\pi/2$ pulses. Their action on the spins can be seen as a tilt of the effective precession axis, and in this sense it is similar to the decoupling achieved by fast rotation of the entire sample, also known as magic-angle-spinning [Laws2002, Hennel2005]. Interaction components perpendicular to the effective precession axis will average out, and if the axis orientation relative to the external magnetic field is chosen adequately, the dipolar frequency shift will be zero. According to the angle dependence of J_I (eq. 2.18), this would be the case if $(1 - 3\cos^2 \alpha_{\mathrm{eff}}) = 0$, i.e. for the magic angle $\alpha_{\mathrm{eff}} = 54.74°$ between the effective precession axis and the magnetic field.

Unfortunately, full decoupling by magic-angle-spinning is not feasible in our work, because the spinning frequency would need to exceed the interaction strength of $\sim 1\,\mathrm{MHz}$ in our sample and a macroscopic rotation of the sample is hardly compatible with optical spectroscopy
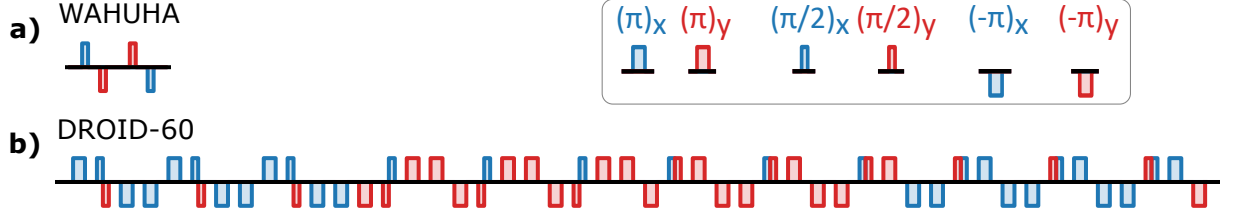
Figure 5.9: **Symmetric pulse sequences for decoupling of interactions.** WAHUHA (a) is the simplest decoupling sequence that yields an isotropic average Hamiltonian and consists only of $\pi/2$ pulses. The DROID-60 sequence (b) combines $\pi/2$ and π pulses for additional decoupling from the spin bath, and because it concatenates all possible phase-shifted variants, it is very robust against any pulse imperfections. Since all pulse spacings between its $\pi/2$ pulses are symmetric, it produces an isotropic average Hamiltonian.

that requires a dedicated optical mode. Therefore, we investigate more closely the decoupling potential of microwave pulse sequences.

DROID-60 in its original form, like many other pulse sequences designed to decouple interactions, consists of symmetric pulse spacings between the $\pi/2$ rotations, so that the average Hamiltonian reduces to the isotropic term of the interaction, $\mathcal{H}_{\text{dd,iso}}$ [Farfurnik2018, Choi2020]. Although this is not sufficient for full decoupling in our system with an anisotropic g-tensor, we first analyze its effect on dipolar broadening, before we discuss how it can be tailored to our material.

Coherence time limit for an isotropic average Hamiltonian

In the isotropic Hamiltonian, the coefficient of the $\hat{\sigma}_z \hat{\sigma}_z$ diffusion term is changed from J_I to $(2J_S + J_I)/3$. It is not clear, however, if or under which circumstances such change actually reduces the dipolar linewidth. Such analysis requires knowledge about the relative magnitudes of both coefficients J_S and J_I.

Because both coefficients depend on the relative orientation of the connecting vector $\hat{r}$ to the directional vectors $\vec{u}^i$ of the magnetic moments, an exact analytical comparison is difficult. For a qualitative understanding, we neglect the angle dependencies for now and only compare the magnitudes of the directional vectors (figure 5.10a).

Because of the high g-tensor anisotropy and the non-linear dependence of the gyromagnetic ratio (see eq. 2.19), we find that for almost all orientations of the external magnetic field, the magnetic moment is well aligned with its precession axis $\vec{u}^z$, which is mostly determined by the g-tensor principal axis with the largest eigenvalue, g_z. While such alignment close to the precession axis protects effectively against spin-flips (indicated by a small J_S coefficient), it also means that by intermixing J_S and J_I, the dipolar broadening term can be reduced for almost all magnetic field orientations.

For an exact comparison of the dipolar broadening for an isotropic Hamiltonian produced by a DROID-60 sequence (fig. 5.10b), we again sum over the frequency shifts of all interacting spin pairs, now governed by the new coefficient $(2J_S + J_I)/3$, and evaluate its solid angle dependence numerically along the lines of the derivation in the appendix A.1.

5.2.5 Decoupling limit for dipolar interactions: asymmetric sequences

In the last section, we have shown why traditional decoupling sequences like WAHUHA or DROID-60 work well for systems with isotropic g-tensors but fail to fully decouple interactions between dopants with anisotropic g-tensors. Now we discuss how such symmetric decoupling
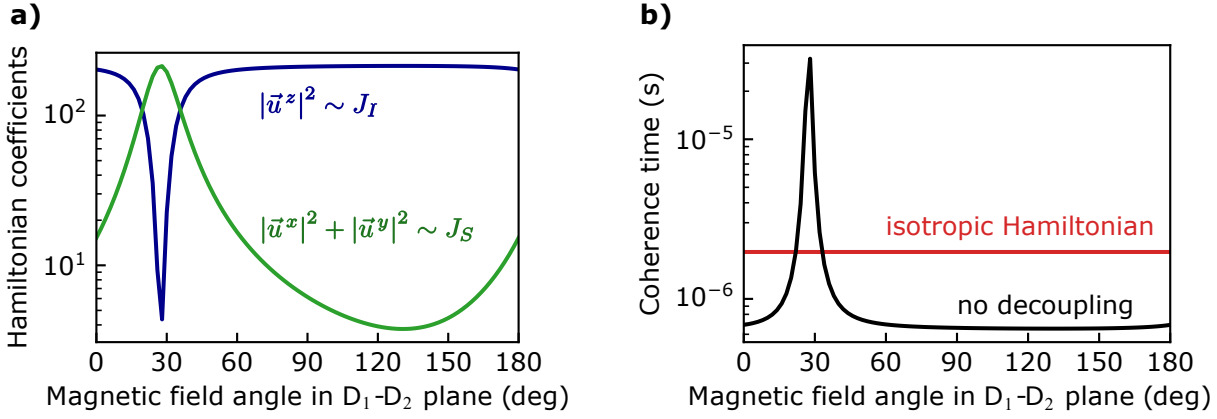
Figure 5.10: **a) Relative magnitude of dipolar coupling coefficients.** The spectral diffusion coefficient J_I is related (via the effective gyromagnetic ratio) to the magnitude of the magnetic moment along its precession axis, $|\vec{u}^z|^2$, while the flip-flop coefficient J_S scales with the magnitude of the magnetic moment perpendicular to its precession axis, $|\vec{u}^x|^2 + |\vec{u}^y|^2$. **b) Coherence time limit by instantaneous diffusion.** Decoupling sequences like WAHUHA or DROID-60 produce an isotropic average Hamiltonian by intermixing the coefficients J_S and J_I. As a consequence, the impact of instantaneous diffusion is reduced where $J_S < J_I$. The coherence times were calculated from the dipolar linewidth (eq. 5.7 and A.1) for an effective concentration of resonant spins of $2\,\text{ppm}$.

sequences could be modified in order to maximize their efficiency to suppress instantaneous diffusion in our system.

Since dipolar broadening, which leads to instantaneous diffusion, is only caused by $\hat{\sigma}_z\hat{\sigma}_z$ terms of the average Hamiltonian, these contributions should be reduced as much as possible, which could be achieved by intermixing J_I and J_S contributions (cf. figure 5.10). Because global rotations can not eliminate individual terms and leave the isotropic Hamiltonian invariant, a suppression of the $\hat{\sigma}_z\hat{\sigma}_z$ terms comes at the price of increasing the weight of the flip-flop terms $\hat{\sigma}_x\hat{\sigma}_x + \hat{\sigma}_y\hat{\sigma}_y$.

Redistributing interaction terms by modified pulse spacings

Engineering the average Hamiltonian in order to enhance or suppress certain interaction terms can be achieved by modifying the pulse spacings of a sequence like WAHUHA or DROID-60 [Farfurnik2018, Mohammady2018, Choi2020]; the resulting pulse train will inherit most robustness properties from the original decoupling sequence. For our purpose, we want to substitute the large $J_I\,\hat{\sigma}_z\hat{\sigma}_z$ terms with smaller $J_S\,\hat{\sigma}_z\hat{\sigma}_z$ ones that appear for rotated spins. To this end, we need to shorten the time intervals during which the $\hat{\sigma}_z$ component is aligned with the z-axis of the toggling frame.

[Choi2020] already suggest a modified WAHUHA+echo sequence in which the $\hat{\sigma}_z$ component spends only a fractional time $c\tau$ aligned with the z-axis, compared with a time interval $(1 - c)\tau/2$ spent along x and y, each. Similar modification can be made to the DROID-60 sequence; the resulting average Hamiltonian has the same form as eq. 5.9 but with new coefficients $\widetilde{J}_S$ and $\widetilde{J}_I$ in place of J_S and J_I [Choi2020]:

$$\mathcal{H}_{\text{dd}} = \widetilde{J}_S\left(\hat{\sigma}_x\hat{\sigma}_x + \hat{\sigma}_y\hat{\sigma}_y\right) + \widetilde{J}_I\,\hat{\sigma}_z\hat{\sigma}_z, \tag{5.14}$$

with

$$\widetilde{J}_S = \frac{1+c}{2}\,J_S + \frac{1-c}{2}\,J_I \quad , \qquad \widetilde{J}_I = (1-c)J_S + c\,J_I. \tag{5.15}$$

Here, the parameter c determines how the dipolar interaction is distributed on the spectral diffusion and the flip-flop term. For $c = 1$ we retrieve the original Hamiltonian without decoupling, and for $c = 1/3$ we reproduce the conventional DROID-60 sequence and the results for an isotropic Hamiltonian. Any other value of c will distort the original pulse spacings and requires a more asymmetric pulse pattern (see figure 5.11b for a maximally asymmetric sequence, $c = 0$).

Although the construction of such sequence might look arbitrary at first sight, it can be shown that any decoupling sequence built from rotations of the Clifford group ($\pi/2$ rotations around the x- or y-axis) will have this form [BenAttar2020, Choi2017, Frydrych2015]. Note, though, that the effect of non-Clifford rotations in decoupling sequences is rarely studied, but [BenAttar2020] suggest that the use of rotations of the icosahedral group (with pulse areas of $2\pi/5$) could introduce other terms, for example by interchanging $(\hat{\sigma}_x\hat{\sigma}_x - \hat{\sigma}_z\hat{\sigma}_z)$ with $(\hat{\sigma}_x\hat{\sigma}_z + \hat{\sigma}_z\hat{\sigma}_x)$.

Optimum decoupling sequence for Er:YSO

As we have seen in figure 5.10, for most magnetic field orientations the dipolar broadening could be reduced by substituting J_I completely by J_S, which can be realized for a value of $c = 0$. The resulting sequence would be quite asymmetric as several pulse spacings would be contracted to zero, resulting in an average Hamiltonian

$$\mathcal{H}_{\text{dd,c=0}} = \frac{J_S + J_I}{2} \left(\hat{\sigma}_x\hat{\sigma}_x + \hat{\sigma}_y\hat{\sigma}_y\right) + J_S\,\hat{\sigma}_z\hat{\sigma}_z. \tag{5.16}$$

For this average Hamiltonian, we again calculate the expected linewidth broadening and the corresponding maximum coherence time, and also the respective flip-flop rate (see figure 5.11). Because now the large coefficient J_I has been shifted to the flip-flop terms $(\hat{\sigma}_x\hat{\sigma}_x + \hat{\sigma}_y\hat{\sigma}_y)$, the spin lifetime has been decreased, and for an orientation of the external magnetic field between $\varphi = 90°$ and $160°$ the coherence time is no longer limited by instantaneous diffusion but by the spin lifetime, which is set by flip-flops.

However, we will not observe a significant coherence time extension for asymmetric decoupling sequences in our experiments, because for realistic conditions the asymmetry parameter is limited to $c \gtrsim 0.2$. This lower bound can be calculated by taking into account the finite pulse widths of $33\,\text{ns}$, which is not negligible compared with a typical pulse spacing of about $100\,\text{ns}$.

In addition, by calculating the commutators between the Hamiltonians for the individual free-evolution periods, the first higher-order correction to the average Hamiltonian can be estimated (see eq. 5.6). While the quantitative analysis is difficult because the coefficients of the $\hat{\sigma}_i\hat{\sigma}_i$ terms are now products of J_S and J_I and the correct order of averaging over time and over pairs of interacting spins is not trivial, one finds that the higher-order correction favors an isotropic Hamiltonian.

Unfortunately, the maximum coherence time extension by two orders of magnitude can only be achieved for an optimal asymmetric decoupling sequence with $c = 0$, and the realistic value of $c = 0.2$ limits the best possible coherence time already to a value only 1.5 times longer than for an isotropic Hamiltonian. The reason for this extreme sensitivity is again the high anisotropy of the g-tensor for erbium in YSO. While the interaction coefficients J_S and J_I are orders of magnitude apart, their mixing in the average Hamiltonian occurs only linearly, and the large J_I term dominates for a wide range of parameters.
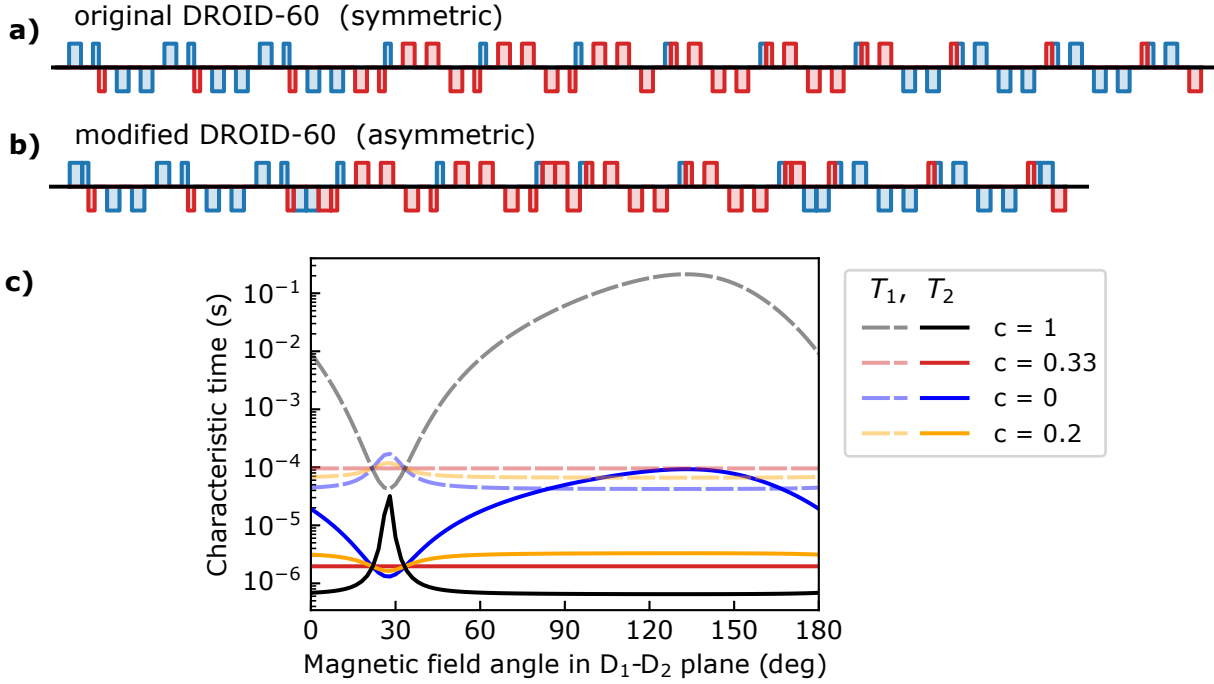
Figure 5.11: **Symmetric (a) and asymmetric (b) DROID-60 decoupling sequence.** For systems with highly anisotropic g-tensors like Er:YSO, the longest coherence times would be excepted for a modified DROID-60 sequence with asymmetric pulse spacings, realizing $c = 0$ in the limit of infinitesimally short pulses, where c is the asymmetry parameter (see eq. 5.15). **c) Effect of decoupling sequences on lifetime and coherence time limits set by dipolar interactions.** By numerical integration over all interacting spin-pairs, we calculate the coherence time from the dipolar linewidth broadening (solid curves) and the lifetime from the average flip-flop rate (dashed curves), without decoupling ($c = 1$, black), for an isotropic Hamiltonian as obtained for a DROID-60 sequence ($c = 1/3$, red), the maximum effect for a completely asymmetric sequence ($c = 0$) and a realistic sequence with finite pulse widths ($c = 0.2$, yellow).

Decoupling limit for other host materials

The findings of our analysis can be extended to other host materials as well (see figure 5.12).

In general, in systems with a highly prolate g-tensor, $g_z \gg g_x, g_y$ (like for Er:YSO or Er:LiNbO$_3$), for a large range of orientations a very asymmetric decoupling sequence ($c = 0$) could extend the interaction-limited coherence time by up to two orders of magnitude, while an isotropic Hamiltonian ($c = 0.33$) obtained for realistic sequence parameters only allows for a moderate decoupling.

In material systems with a very oblate g-tensor, $g_x, g_y \gg g_z$ (like for Er:CaWO$_4$), symmetric decoupling sequences typically perform better than asymmetric ones. However, all decoupling sequences lead only to a moderate increase of the coherence time by at most a factor of 3. Intuitively, this is clear, because two of three magnetic moment directional vectors $\vec{u}^i$ have large magnitudes; consequently there is no huge difference between the interaction coefficients J_S and J_I, and intermixing them does not change the resulting dynamics significantly.
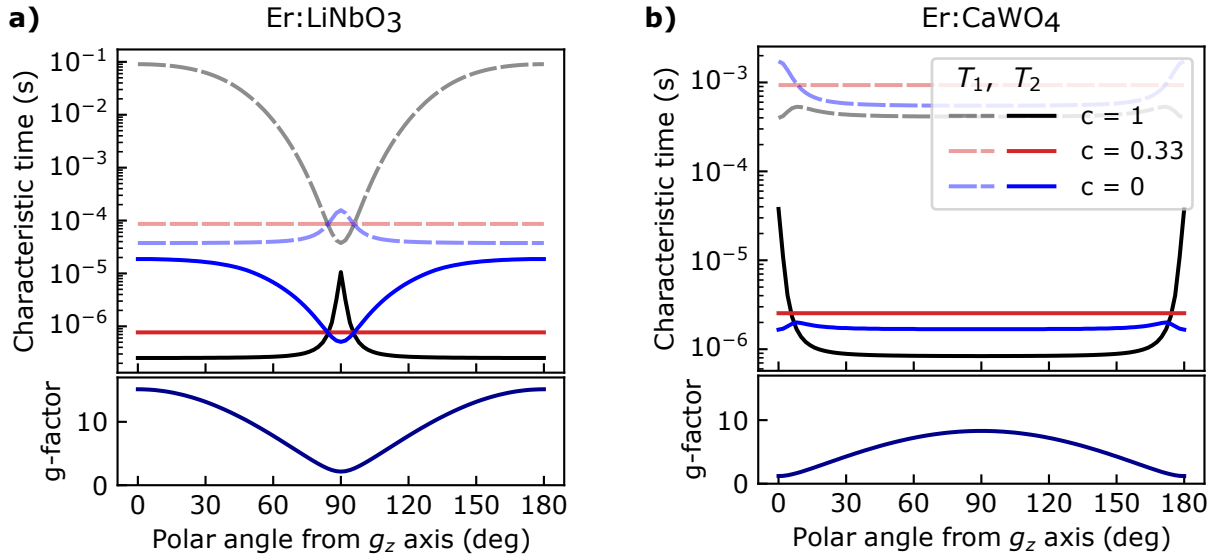
Figure 5.12: **Effect of decoupling sequences on lifetime and coherence time limits set by dipolar interactions in Er:LiNbO$_3$ (a) and Er:CaWO$_4$ (b).** We calculate the coherence time limit from the dipolar linewidth (solid curves) and the lifetime from the flip-flop rate (dashed curves) for other host crystals with the same optical depth (2 ppm of resonant spins): (a) LiNbO$_3$ as another material system with a highly prolate g-tensor [Thiel2012b], and (b) CaWO$_4$ with a very oblate g-tensor [Bertaina2007]. The results depend on the asymmetry parameter of the decoupling sequence, c: starting from the original Hamiltonian without decoupling ($c = 1$, black), an isotropic average Hamiltonian ($c = 0.33$, red) extends the coherence time for most magnetic field orientations in all systems. With very asymmetric sequences ($c = 0$, blue), a further reduction of instantaneous diffusion is possible only for prolate g-tensors (a) but not for oblate ones (b).

5.3 Dynamical decoupling experiments

In the spin-echo measurements on the ground-state spin transition we obtained a coherence time of $0.86(9)\,\mu$s. By comparing it with the expected instantaneous diffusion based on the concentration of addressed dopants and the effective π-pulse fidelity, we found good agreement, indicating a coherence time limit set by dipolar interactions. For coupling to the fluctuating nuclear spin bath, however, we expect a characteristic time of a similar order of magnitude.

In this section, we separate the impact of the fluctuating off-resonant spin bath and the instantaneous diffusion from resonant spins by performing decoupling experiments not only on the ground-state spin transition but also between excited states. Because optical excitation selects only a small subset of erbium ions ($\sim 1\,\%$), the concentration of resonant spins in the excited state is greatly reduced and instantaneous diffusion is minimized (see figure 5.13).
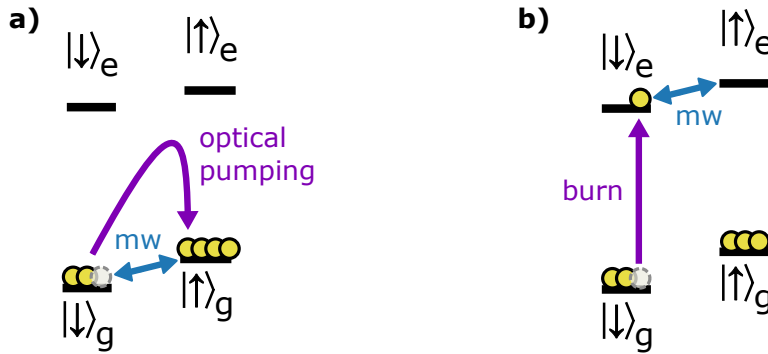

Figure 5.13: **Comparison of dynamical decoupling in ground state (a) and excited state (b).** For ground-state experiments (a), optical pumping (purple arrow) is required to prepare a non-equilibrium spin polarization (population depicted as yellow circles). Microwave pulses (blue arrow) always address all dopants, which leads to strong instantaneous spectral diffusion. To measure the coherence in the excited state (b), a burn pulse on the spin-preserving transition is sufficient to prepare the initial state. Because only the optically selected subset is resonant with microwave pulses, instantaneous spectral diffusion is orders of magnitude smaller than in ground-state experiments.

5.3.1 Decoupling in the excited state

The experimental setup for decoupling measurements on the excited state is basically the same as for studies on the ground state, and although we apply static and microwave magnetic field along different orientations ($\vec{B}_0 \parallel b$, $\vec{B}_{\mathrm{mw}} \parallel D_2$), this particular choice does not restrict our findings. Because no ground state spin polarization is required, we apply only a short pulse on the spin-preserving transition for spin initialization in the excited state, and we also probe its population after a shorter delay time before it spontaneously decays on a 11 ms timescale. By comparing the area of the spectral hole with the entire ensemble absorption line, we estimate that the effective concentration of dopants in the excited state is only a few percent of all ions in one magnetic class.

On the excited-state spin transition, we measure a spin-echo coherence time of $1.7(1)\,\mu$s, which is already longer than what we had observed previously in the ground state but is in excellent agreement with predictions for coupling to the nuclear spin bath [Kornher2020]. In addition, we can significantly extend the coherence time by applying a train of π pulses, which indicates that it is no longer limited by instantaneous spectral diffusion (figure 5.14a). In fact,

we find a power-law scaling of the coherence time with the number of π pulses, $T_2 \sim (n_\pi)^{2/3}$ (fig. 5.14b), as predicted for decoupling from a fluctuating spin bath with Lorentzian spectral noise density [Sousa2009, Bar-Gill2012, Gong2017, Medford2012].

Intuitively, this can be understood by noting that the observed coherence decays for all measured $(XY\text{-}4)^N$ sequences collapse into a single curve when plotted against the pulse spacing τ (figure 5.14a inset). As long as the pulse spacing is shorter than the correlation time of the environmental spin bath, τ_c, the sequence can revert all dephasing, but for pulse spacings longer than τ_c the environment is randomized and the decoupling efficiency drops.

Initially, it is not clear whether the decoupled fluctuations originate from nuclear spins or from other erbium electron spins; the measurable spin-echo coherence time depends not only on the bath correlation time but also on its diffusion linewidth $\Delta\omega$. Depending on the exact model, the order of magnitude is given by $T_2 \approx (\Delta\omega\,\tau_c)^{1/2}$ [Lim2018, Zhong2015a] or rather $T_2 \approx (\Delta\omega)^{2/3}\,\tau_c^{1/3}$ [Sousa2009].

On the one hand, the contribution of neighboring yttrium ions to spectral diffusion is strongly suppressed because of the frozen-core effect (cf. section 4.2.4) [Böttger2006b, Arcangeli2014, Zhong2015a]. On the other hand, the reorientation of erbium magnetic moments upon optical excitation will significantly affect the yttrium spins, as their induced fields dominate over the external field of about $22\,\mathrm{mT}$ (cf. fig. 4.5b). In addition, we expect a correlation of nuclear spin precession on a timescale set by γB, with the gyromagnetic ratio of yttrium, $\gamma \approx 2\,\mathrm{MHz/T}$, which could explain the apparent correlation time of a few microseconds (inset of figure 5.14a).
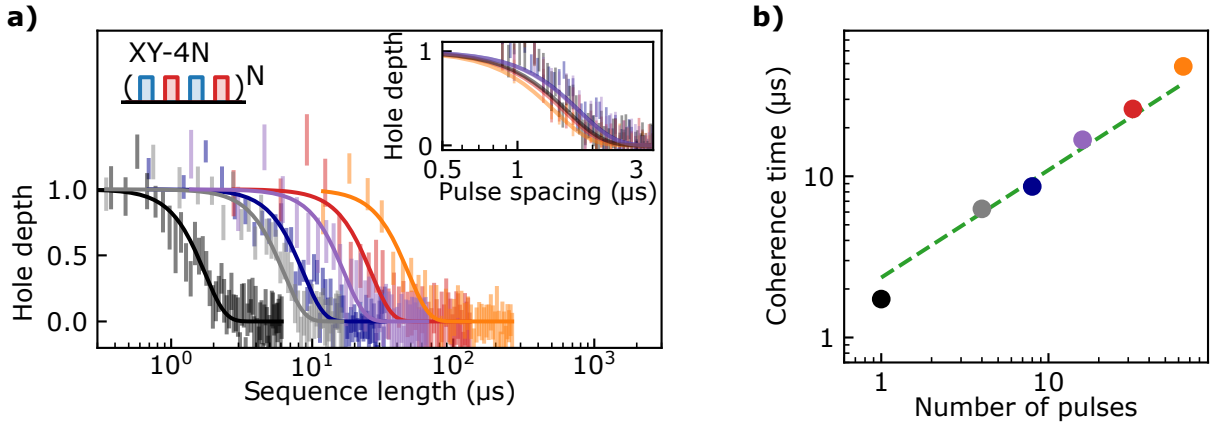
Figure 5.14: **a) XY-4 decoupling in the excited state.** Because of their lower concentration, the coherence of optically excited dopants is not limited by instantaneous diffusion but by a fluctuating spin bath, which can be decoupled using multiple XY-4 sequence blocks. The readout hole depth decays as $\exp\left[-(t/T_2)^3\right]$ (fits as solid curves), almost exclusively determined by the pulse spacing (inset). **b) Power-law for dynamical decoupling.** Up to a value of $48(3)\,\mathrm{\mu s}$ for $n_\pi = 64$ pulses, we observe a scaling of the coherence time with the number of decoupling pulses as $T_2 \sim (n_\pi)^{2/3}$ (green dashed line), as predicted for dephasing due to a fluctuating spin bath with Lorentzian spectral noise density.

5.3.2 Decoupling in the ground state

From the decoupling experiments on the excited state we know the coherence time limit set by the fluctuating spin bath. In this section, we turn to the ground-state spin again and attempt decoupling of resonant spins.

First, we apply XY-4 and XY-8 sequences, which have enabled effective decoupling of the excited state from the spin bath but are known to have no effect on dipolar interactions. As expected, we observe no significant improvement (fig. 5.15a), which supports our hypothesis of a limit set by instantaneous spectral diffusion. In this case, the magnetic environment changes with each π pulse, and the diffusion speeds up with increasing decoupling bandwidth.

In order to decouple dipolar interactions, we instead use the DROID-60 sequence [Choi2020]. On the one hand, it simultaneously achieves decoupling from the fluctuating spin bath, which would otherwise limit the coherence time for long sequence lengths. On the other hand, it is designed to be very robust against pulse imperfections, which is particularly important for sequences that consist of many pulses. Using DROID-60 decoupling, we obtain a coherence time of 2.5(4) µs, which is in perfect agreement with the theoretical prediction for an isotropic average Hamiltonian (see figure 5.15b, predicted decay as dashed red line).

We did not observe a significant increase in coherence time by a modified DROID-60 sequence with more asymmetric pulse spacings (not shown). Because the finite pulse lengths of 33 ns in our experiments severely limit the achievable asymmetry parameter and the maximum coherence time extension (as discussed in section 5.2.5), we leave a more systematic study for future work.
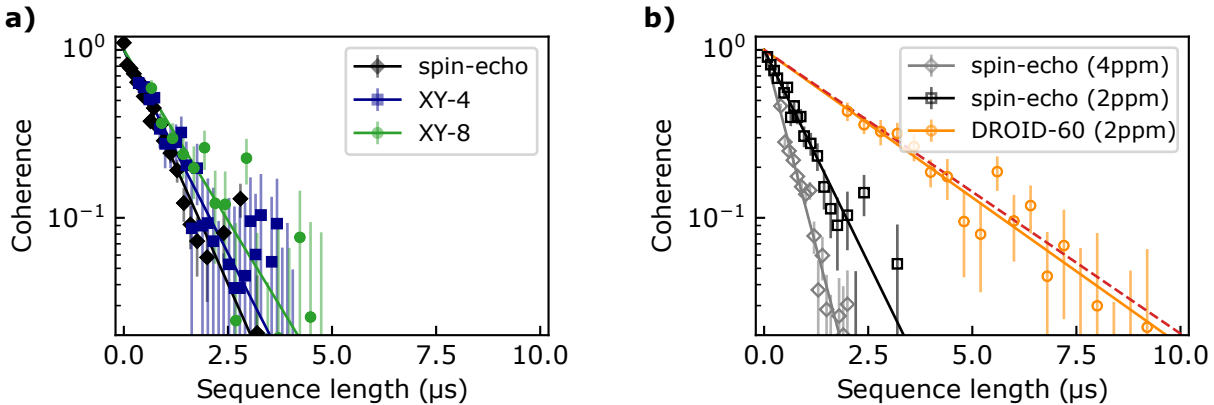
Figure 5.15: **Decoupling in the ground state.** (a) π-pulse trains like XY-4 and XY-8 do not provide significant improvement compared with a spin-echo (exponential fits as solid lines), because they can not decouple resonant spins. All three data sets were taken at a magnetic field along $\varphi = 130°$ in the D_1-D_2 plane, with the magnetic classes slightly detuned (2 ppm similar spins). (b) In contrast to π-pulse trains, the DROID-60 sequence yields a coherence time extension up to 2.5 µs, in agreement with the theoretical prediction from section 5.2.3 (dashed red line). Furthermore, we can demonstrate the scaling of instantaneous diffusion with the concentration of resonant spins: by aligning both magnetic classes we double the concentration of similar spins to 4 ppm, and observe a coherence time reduction by a factor of ~ 2, as expected for instantaneous diffusion. These curves were measured at a static magnetic field parallel to the D_2-axis.

70

6 Cavity-enhanced spectroscopy

The size of quantum networks can be increased by quantum repeaters [Briegel1998], whose implementation requires the ability to generate spin-photon entanglement with high efficiency and at a fast repetition rate. In this respect, the weak interaction of single ions with light in general and the long excited state lifetime of erbium in YSO in particular pose a serious challenge.

Although it might be tempting to increase the number of interacting dopants by raising the dopant concentration in the host crystal and creating strong ensemble absorption lines, we have seen in the previous chapter that dipole-dipole interactions between dopants impact their spin lifetime and coherence properties, and thus low dopant concentrations seem favorable. Enlarging the crystal dimensions would be possible but only to some extent, because technical constraints and inhomogeneities of crystal and control fields will limit the fidelity of operations.

Instead, the most promising approach to boost both the readout signal and the interaction strength between light and ions makes use of an optical resonator. By embedding the crystal in an optical cavity formed by two mirrors, light that is reflected back and forth will interact with the dopants effectively a few thousand times (figure 6.1). In addition, the scattered light will be emitted primarily into the well-defined cavity mode, which allows for high detection efficiencies.

In this chapter, we first briefly review the important terms and parameters that lead to the Purcell effect. Then, we describe the experimental details of the cavity design and assembly, including mirror fabrication, crystal preparation, and tuning and stabilization capabilities, before turning to the optical measurements. We perform fluorescence and photon echo experiments and demonstrate outstanding optical coherence properties. A model of the cavity geometry and the distribution of dopants at different coupling strengths to the light field supports our findings and makes predictions about the properties of optimally coupled single ions.
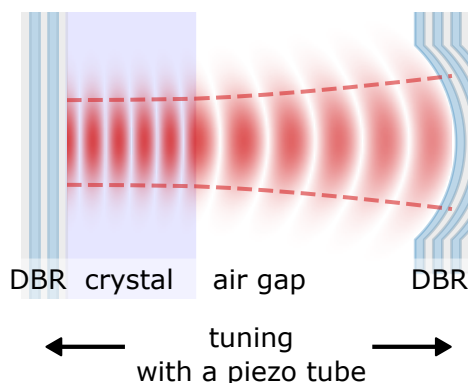

Figure 6.1: **Cross section of cavity and mode profile.** Two distributed Bragg-reflectors (DBR) form the mirrors of our cavity. The YSO crystal with erbium dopants is bonded to the planar mirror, and the air gap to the concave mirror can be tuned with a piezo tube.

6.1 Erbium-doped crystals in a cavity

Several attempts have been made to couple erbium dopants to optical resonators: the tightest confinement of light and the highest coupling strengths can be achieved in photonic crystal cavities. Such devices can be carved directly into the host crystal [Miyazono2016], but their fabrication by focused ion beam milling likely creates lattice defects and charge traps that potentially lower the coherence of erbium dopants. Alternatively, the nanophotonic cavity can be fabricated from a separate chip and made of a different material, like silicon [Dibos2018]. By bringing the Er:YSO crystal into contact with the resonator, dopants couple to its evanescent field. While this approach reduces the risk of fabrication-induced crystal damage, the addressed dopants are still close to an interface with potential charge fluctuations. Furthermore, the different thermal expansion coefficients of silicon and YSO induce strain at cryogenic temperature, which increases the ensemble inhomogeneity.

In this work, we take a different route and embed the crystal in a Fabry-Perot resonator. A similar approach has been studied in [Casabone2020], where erbium-doped Y_2O_3 nanocrystals were coupled to a Fabry-Perot fiber cavity. However, emitters in nanocrystals suffer from fluctuating electric fields induced by surface charges [Bartholomew2017], and also the stabilization of a fiber cavity at cryogenic temperature has remained challenging [Bogdanović2017, Salz2020, Ruf2020].

Here, we instead investigate erbium dopants in a YSO bulk crystal, without degrading its great coherence properties [Böttger2003, Rančić2018]. While such a design has a larger mode volume than nanophotonic structures, we achieve significantly higher quality factors, resulting in comparable coupling strengths. In order to minimize dipolar interactions between erbium ions, we use a nominally undoped crystal and probe the remaining erbium impurities.

6.1.1 Ion-cavity coupling

A Fabry-Perot cavity consisting of two mirrors facing each other is the simplest example of an optical resonator. In such an arrangement, the light field can only occupy discrete modes, as opposed to the continuous spectrum in free space, and in consequence, the decay of an excited atom is modified. The exact behavior depends on the interplay of three processes: the spontaneous decay of an atomic excitation at rate $2\gamma = 1/T_1$ (with lifetime T_1), the decay of the light field in the cavity at rate $\kappa = \pi \Delta\nu_{\text{cav}}$ (with cavity mode fwhm linewidth $\Delta\nu_{\text{cav}}$), and the coupling rate between light field and atom, g: [Vuckovic2014]

$$g = \frac{d}{n}\sqrt{\frac{\pi\nu}{\hbar\varepsilon_0 V}} \tag{6.1}$$

Here, d is the electric dipole matrix element of a specific transition at frequency ν, n is the refractive index of the material embedding the emitter, ε_0 is the electric constant, and V is the cavity mode volume, defined by the electric field amplitude $E(\vec{r})$ via

$$V = \frac{\int \mathrm{d}^3\vec{r}\, n^2(\vec{r})\,|E(\vec{r})|^2}{\max\left\{n^2(\vec{r})\,|E(\vec{r})|^2\right\}}. \tag{6.2}$$

Note that the above definition for the coupling rate assumes a perfect positioning of the emitter at a field maximum. At arbitrary position, it scales with $|E(\vec{r})|/\max\{|E(\vec{r})|\}$.

Purcell-enhanced emission

In this work, we consider the 'Purcell regime', $\kappa \gg g \gg \gamma$, in which a photon, once emitted from the atom, will quickly leave the cavity rather than interact with the same atom again [Reiserer2015, Kuhn2010]. Still, the density of photonic modes is modified by the cavity, and now the atomic polarization $c(t)$ also decays into the cavity mode at rate g^2/κ:

$$c(t) = \mathrm{e}^{-\gamma t - \frac{g^2}{\kappa}t} \tag{6.3}$$

Since our cavity covers only a small solid angle, the polarization decay rate γ remains unchanged, and the additional emission into the cavity mode accelerates the decay. This is called Purcell effect, and we can define the Purcell factor P_{TL} for a two-level system by

$$c(t) = \mathrm{e}^{-(1+P_{\mathrm{TL}})\gamma t} \quad , \qquad P_{\mathrm{TL}} = \frac{g^2}{\kappa \gamma} \tag{6.4}$$

Erbium in YSO, however, is not a two-level system, and the excited state can decay into many different crystal field levels. Because of the strong wavelength dependence of the cavity-enhanced coupling rate g, in our system only the transition to the $I_{15/2}$ ground state experiences a Purcell boost, while other decay channels remain unaffected. Therefore, the branching ratio (i.e. the fraction of decay to the $I_{15/2}$ ground state with respect to all decay channels) changes from its value β without cavity. We can write

$$c(t) = \mathrm{e}^{-(1-\beta)\gamma t - \beta(1+P_{\mathrm{TL}})\gamma t} = \mathrm{e}^{-(1+\beta P_{\mathrm{TL}})\gamma t} \tag{6.5}$$

Thus, the effective Purcell factor of Er:YSO, including the branching ratio for other decay channels, can be written as $P_{\mathrm{Er}} = \beta P_{\mathrm{TL}}$.

6.1.2 Cavity mirror fabrication

In this work, the cavity consists of one planar mirror that allows for bonding of the crystal membrane, and one concave mirror to ensure lateral confinement of the light field (see figure 6.1). For a high coupling rate to the ions and strong Purcell enhancement, we need to make the mode volume as small as possible (see eq. 6.1). Since the axial dimension is determined by the crystal thickness, the remaining tuning knob is the curvature of the concave mirror. A small radius of curvature (ROC) is required for a small mode waist and small mode volume. Since mirror fabrication by conventional, mechanical polishing only works for macroscopic mirrors with large ROC $\gtrsim 5\,cm$, we apply a micro-fabrication technique by laser-ablation [Hunger2012, Uphoff2015].

The process uses a train of laser pulses emitted by a CO_2 laser at $9.3\,\mu m$ to melt and evaporate material at the surface of a silicon dioxide substrate (figure 6.2). The shape and size of the resulting depression can be controlled by the diameter and power of the laser beam as well as the number of length of the incident pulses, and it is possible to produce Gaussian depressions with a ROC of less than $100\,\mu m$. Importantly, the creation of a liquid phase in the absorption process helps to smooth the surface of the fabricated dimple, which reduces scattering loss of the future mirror.
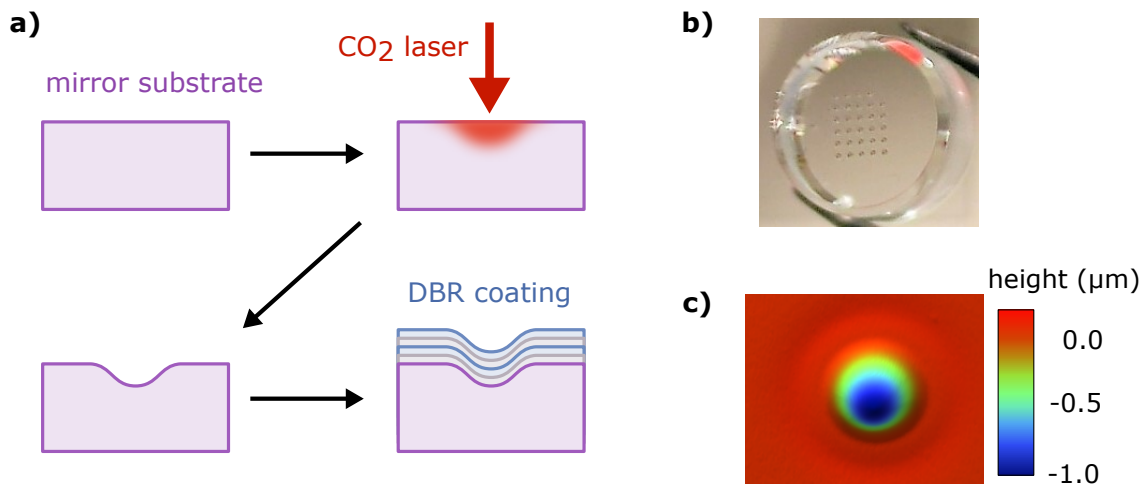

Figure 6.2: **a) Mirror fabrication by laser ablation.** Short pulses with a high-power CO_2 laser heat the mirror substrate locally and melt and evaporate some material. After cooling down, a smooth depression with a small radius of curvature remains. In a final step, a distributed Bragg-reflector is coated on top of the mirror substrate with the depression. **b) Photograph of depressions on a mirror substrate**. On a single mirror substrate with $7\,mm$ in diameter we can fabricate multiple depressions and later select one of them. **c) Surface profile of a single depression.** Analyzing the depressions with a white-light interferometer reveals their depth and radius of curvature.

After fabricating a dimple with suitable diameter and radius of curvature, the substrate is then coated with a stack of dielectric layers that form a Bragg reflector. We use in total 35 quarter-wavelength layers optimized for a wavelength $\lambda = 1536\,nm$, with Ta_2O_5 as material with high refractive index ($n_{Ta_2O_5} = 2.045(2)$) alternating with SiO_2 as low-refractive-index material ($n_{SiO_2} = 1.457(1)$) [Rodríguez-deMarcos2016]. While the concave mirror on the air side of our cavity is terminated by a low-refractive-index material, resulting in a designed transmission of $7\,ppm$, we use a high-refractive-index termination for the planar mirror on the crystal side, by leaving out the top-most SiO_2 layer. Note that the refractive index of the YSO membrane ($n \approx 1.77$ [Sabooni2016, Beach1990]) lies between the values for Ta_2O_5 and

SiO_2 and lowers the transmittance to a theoretical value of $57.5\,\text{ppm}$ for the mirror on the crystal side. Later, we confirm the transmission values in measurements (see section 6.1.5).

While it would be possible to increase the mirror reflectivities by adding more layers to the Bragg reflectors, this would lower the outcoupling efficiency of cavity photons through the mirrors, and then the relative impact of scattering and absorption loss became more significant.

6.1.3 Crystal processing and transfer

In order to minimize scattering losses, not only the mirror surfaces need to be smooth but also the crystal membrane. At the same time, its thickness L_c needs to be small enough to fulfill the stability condition $L_a + L_c/n_c \lesssim ROC$ for a given radius of curvature ROC, where L_a is the width of the air gap and n_c the crystal refractive index [vanDam2018].

While for some materials like silicon compounds or diamond there exist techniques for a bottom-up fabrication of thin crystals [Aharonovich2012, McCann2001, Chambers2000], attempts with yttrium silicates have resulted in poly-crystalline structures [Chambers2001]. Depending on the grain size, those would not only lead to higher scattering loss, but also to inhomogeneities in level structures and an increased number of charged surface states or crystal defects, which could degrade the coherence properties of incorporated erbium ions.

Instead, we take a top-down approach and start with a bulk crystal of YSO with optimum coherence properties, and remove material until we reach the desired thickness. Unfortunately, all attempts to adopt chemical etching processes to yttrium silicates have resulted either in extremely slow etch rates or a high surface roughness, and also reactive ion etching did not yield smooth surfaces. While focused-ion-beam milling does work in order to remove material, it certainly creates lattice defects close to the surface. Therefore, we choose an optimized mechanical polishing process as offered by *Optec Munich.*

First, one side of the crystal is polished down to the required smoothness. Then, this side is glued to a flat glass substrate, which provides mechanical stability for the subsequent polishing of the other side. After this procedure, we first clean the crystal surface with acetone and isopropanol. For a safe handling of the sample we cover a glass substrate with teflon tape, add a drop of acetone and flip the membrane onto it while it is glued to its substrate. The glue dissolves, and once the acetone has evaporated, the membrane is loosely lying on the teflon tape.

Now we can clean its top surface from glue residuals, using lens cleaning tissues soaked with isopropanol or acetone. We keep the membrane in place by first adding a drop of acetone at its edge, which creeps between the crystal and the teflon tape and makes it stick to it by surface tension. Once the surface quality is satisfying, we let all acetone evaporate again, before we press the flat mirror onto the membrane, which bonds to it via van-der-Waals forces. Now we can flip the mirror with the crystal and clean its other surface. In a white-light interferometer we measure the surface roughness of the crystal membrane after the cleaning procedure and also confirm its thickness (figure 6.3).

In the following section we discuss the optical properties of the assembled cavity.
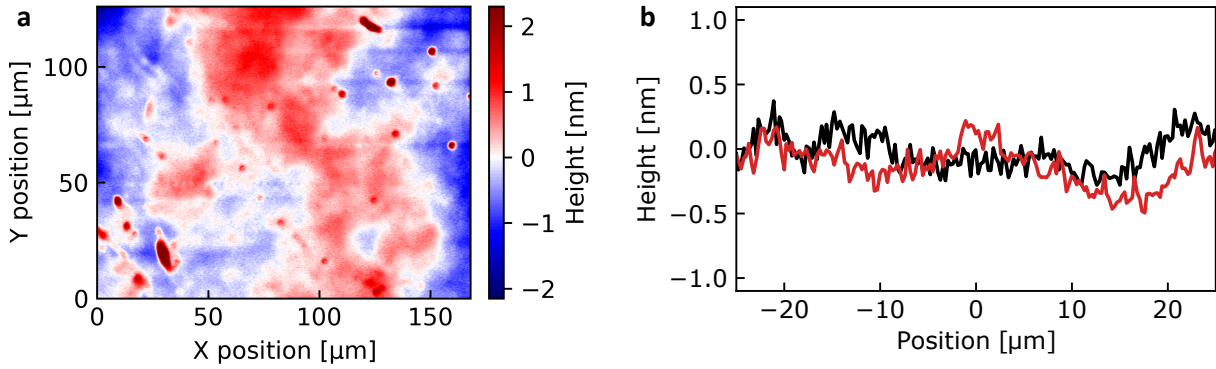
Figure 6.3: **Crystal surface roughness, measured with a white-light interferometer.** After polishing and cleaning, the crystal surface is flat except for few dust particles visible in the height map (a). Line cuts along the x- and y-axis (black and red curves in panel b) show an rms roughness of $\lesssim 0.2\,\mathrm{nm}$ on a scale of the typical mode diameter, $\simeq 10\,\mu\mathrm{m}$, likely limited by the instrument noise.

6.1.4 Mode spectrum of a cavity with crystal membrane

In a simple picture, the eigenmodes of a Fabry-Perot cavity with two spherical mirrors are standing waves along the cavity axis, with their lateral field distribution given by a Gaussian envelope function modulated by Hermite polynomials. Our system, however, includes a crystal membrane between the mirrors, whose thickness is of the same order as half the mirror separation and can not be neglected. The additional interface between the crystal and the air gap reflects some of the light and causes perturbations of the mode spectrum.

To qualitatively understand the effect, one can imagine a perfectly reflective crystal-air interface. Then, the light fields in both parts of the cavity could be treated separately, and their respective modes would each fulfill boundary conditions at the interface. The electric field on the air side has a zero at the interface, whereas on the crystal side it would take its maximum. The boundary conditions are different because there is a phase shift of π when light on the air side is reflected from the interface, which is zero when light is reflected inside the crystal. In this oversimplification the mode spectrum would therefore decompose into the 'air-modes' and the 'crystal-modes'. [Janitz2015]

In reality, the crystal-air interface is partly transmissive and the modes couple. Still, it might be possible to assign the labels 'air-like' or 'crystal-like' to the modes, but in general they hybridize (see figure 6.4). For coupled Gaussian modes, it is possible to derive a set of equations analytically that define the eigenmodes [vanDam2018], but numerical calculations provide more flexibility.

The effect of the crystal membrane on the transverse mode spectrum is typically negligible and can be treated perturbatively as coupling between transverse modes due to refraction of the curved wavefront at the crystal-air interface [Benedikter2015, Janitz2015]. Therefore, the problem reduces to a one-dimensional calculation of the correct longitudinal modes, and from there we can reconstruct the full spectrum.
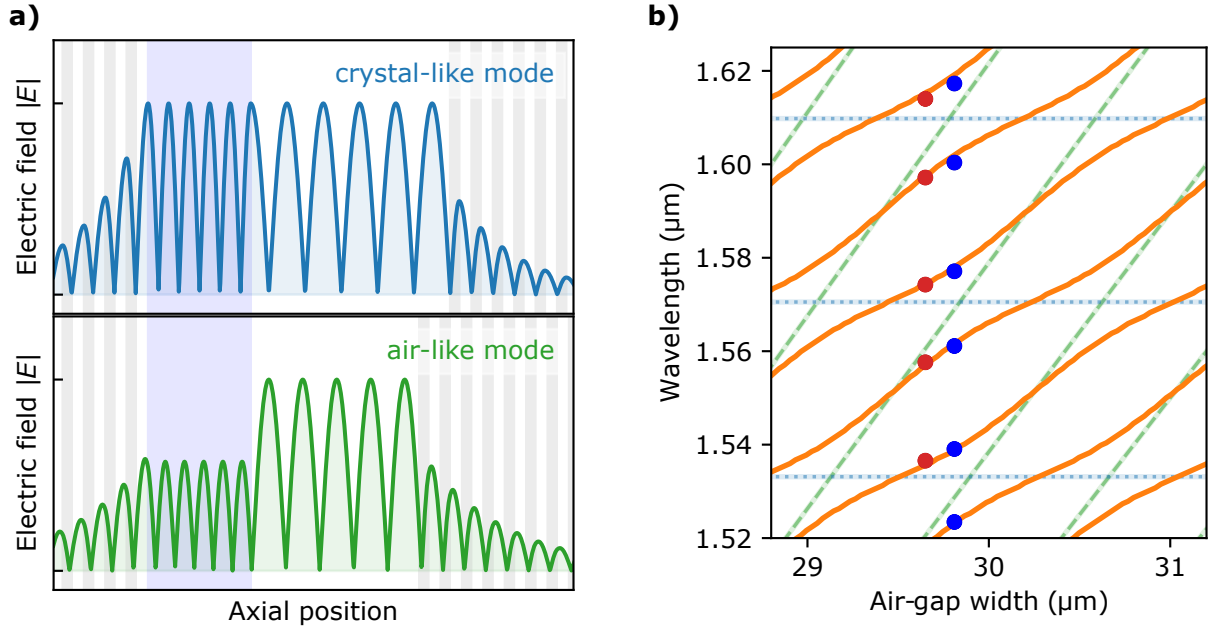
Figure 6.4: **a) Electric field profile of the axial cavity modes.** Depending on the width of the air gap, the resonant mode varies between crystal-like (top), with an anti-node at the crystal surface, or air-like (bottom), with a node. In crystal-like modes, a larger fraction of the energy density is in the crystal. **b) Axial mode spectrum.** Considering uncoupled modes on air- and crystal-side (dashed curves), the air-side mode (green dashed line) strongly depends on the air-gap width, while the crystal-side mode (blue dotted line) stays constant. Due to coupling of both sides through the crystal-air interface, the modes hybridize (orange line), and their wavelengths tuning with air-gap width becomes non-linear. The measured resonances for two differently tuned air gaps are marked by blue and red circles.

Transfer-matrix algorithm

One approach to derive the correct longitudinal modes is the construction of a transfer-matrix for the entire cavity, based on the transfer-matrices of its individual layers. A transfer-matrix $\mathbf{S}$ describes how the electric field components E_+ and E_- of a forward and a backward propagating plane wave are connected with their values E'_+, E'_- at a later point along the propagation axis:

$$\begin{pmatrix} E_+ \\ E_- \end{pmatrix} = \mathbf{S} \cdot \begin{pmatrix} E'_+ \\ E'_- \end{pmatrix} \tag{6.6}$$

In a non-absorbing medium of thickness L with homogeneous refractive index n, for example, the forward-propagating wave with wavelength λ_0 acquires a phase shift of $\varphi = 2\pi n L/\lambda_0$, while the backward-propagating wave acquires a phase shift of $-\varphi$. Since no scattering couples both waves, the transfer-matrix $\mathbf{P}$ for propagation is diagonal:

$$\mathbf{P} = \begin{pmatrix} e^{i\varphi} & 0 \\ 0 & e^{-i\varphi} \end{pmatrix} \tag{6.7}$$

On the other hand, an interface between two media causes reflection, which couples forward- and backward propagating waves, according to the Fresnel coefficients $r_{1,2}$ and $t_{1,2}$, and $r_{2,1}$ and $t_{2,1}$, respectively. Then, the resulting transfer-matrix, $\mathbf{I}_{1\to2}$, is [Katsidis2002, vanDam2018]

$$\mathbf{I}_{1\to2} = \frac{1}{t_{1,2}} \begin{pmatrix} 1 & -r_{2,1} \\ r_{1,2} & t_{1,2}t_{2,1} - r_{1,2}r_{2,1} \end{pmatrix} \tag{6.8}$$

If the interface has non-negligible roughness with rms value σ, we can use modified Fresnel coefficients $\tilde{r}_{1,2}$ and $\tilde{t}_{1,2}$ to account for that [Szczyrbowski1977]:

$$\tilde{r}_{1,2} = r_{1,2} \exp\left(-2\left(\frac{2\pi\sigma n_1}{\lambda_0}\right)^2\right) \tag{6.9}$$

$$\tilde{t}_{1,2} = t_{1,2} \exp\left(-\frac{1}{2}\left(\frac{2\pi\sigma(n_2 - n_1)}{\lambda_0}\right)^2\right) \tag{6.10}$$

Note that now the sum of reflection $R = |r_{1,2}|^2$ and transmission $T = |t_{1,2}|^2$ is lower than one because of scattering losses $\mathcal{L} = 1 - R - T$.

By multiplying all transfer matrices, one can calculate the transfer matrix $\mathbf{S}$ for the total system. For example, the matrix for propagation in medium 1, partial reflection at an interface and propagation in medium 2 reads:

$$\mathbf{S} = \mathbf{P}_1 \cdot \mathbf{I}_{1\rightarrow 2} \cdot \mathbf{P}_2 = \begin{pmatrix} S_{11} & S_{12} \\ S_{21} & S_{22} \end{pmatrix}. \tag{6.11}$$

The resulting matrix components are related to the reflection and transmission coefficients of the total system, r and t [Acquaroli2018]:

$$r = \frac{S_{21}}{S_{11}} \quad , \qquad t = \frac{1}{S_{22}} \tag{6.12}$$

The reflection $R = |r|^2$ and transmission $T = |t|^2$ calculated for the entire cavity show resonances for all longitudinal modes, where transmission is maximal and reflection minimal. Furthermore, the coefficients also contain information about the phase of the reflected and transmitted beam, $\arg(r)$ and $\arg(t)$.

Fitting the longitudinal mode spectrum

For our cavity, the total transfer-matrix does not only consist of the crystal slab, the air gap and the rough interface in between; we also include the complete layer stacks of the distributed Bragg reflectors in each mirror (see section 6.1.2), which allows us to reproduce the correct wavelength dependence of the mirror transmissions.

We can numerically calculate the total transfer-matrix and all its longitudinal resonance wavelengths for different combinations of crystal thicknesses and air-gap widths and compare them with our measurements. Because a single longitudinal mode spectrum can not distinguish between a thin crystal with large air gap and a thick crystal with small air gap, we tune the air-gap width by applying voltages to the piezo tube that clasps around the mirrors. All mode spectra measured in different settings have to agree on the crystal thickness, which then reveals the individual air-gap widths as well.

The resulting mode spectrum is shown in figure 6.4b; the experimentally achievable tuning range at cryogenic temperature is limited to $10 - 100\,\mathrm{nm}$ in air-gap width, see section 6.2.1. Note that because of the hybridization of crystal- and air-like modes, the free spectral range is not a constant.

Transverse mode spectrum

In order to calculate the beam waist and the total mode volume, we have to consider also the transverse mode spectrum, which – for a given crystal thickness and air-gap width – depends only on the mirror radius of curvature.

While the beam cross-section of higher transverse modes looks very different from the fundamental Gaussian mode, they acquire similar phases while propagating along the cavity axis. The only difference is the increasing impact of a Gouy phase shift, φ_G, for higher transverse mode numbers (n, m), which accounts for the curved wavefront.

For a Gaussian beam propagating through medium with refractive index n_c, the Gouy phase at distance z from its waist is simply $\varphi_G = -\arctan(z\lambda_0/\pi w_0^2 n_c)$, with the beam waist w_0. In a planar-concave cavity with homogeneous medium, the fundamental mode has its waist at the planar mirror. While this is still true for the mode inside the crystal slab, the beam diverges quicker on the air-side of the cavity due to a lower refractive index. Consequently, the beam on the air-side has a different apparent waist, which is also shifted inside the crystals and closer to the crystal-air interface [vanDam2018].

The resulting Gouy phase shifts $\varphi_{G,c}$ and $\varphi_{G,a}$ for propagation through the crystal and the air gap with widths L_c and L_a, respectively, are

$$\varphi_{G,c} = -(n + m + 1)\arctan\left(\frac{L_c}{\pi w_0^2}\frac{\lambda_0}{n_c}\right) \tag{6.13}$$

$$\varphi_{G,a} = -(n + m + 1)\arctan\left(\frac{L_a + L_c(1 - 1/n_c)}{\pi w_0^2}\lambda_0\right). \tag{6.14}$$

By adding these Gouy shifts to the respective propagation transfer-matrices for crystal and air gap, we can incorporate them into the one-dimensional model and calculate the corresponding transverse mode spectra for different mode numbers (n, m). The mode waist w_0 is left as a free parameter, and from a fit to the measured transverse mode spectra, we can extract the mirror radius of curvature (ROC) by an analytical expression derived for a coupled Gaussian beam model [vanDam2018]:

$$w_0^2 = \frac{\lambda_0}{\pi}\sqrt{\left(L_a + \frac{L_c}{n_c}\right)\left[ROC - \left(L_a + \frac{L_c}{n_c}\right)\right]} \tag{6.15}$$

Fitting the full mode spectrum

Using the transfer-matrix approach with the Gouy phase correction, we can calculate all cavity resonances over a large range of wavelengths for various crystal thicknesses, mirror curvatures and differently tuned air gaps. A least-square fit to the measured mode spectra converges – within some uncertainty range – to a single set of geometry parameters.

There is, however, still one degree of freedom left: the relative orientation of crystal axes and electric field polarization determines the effective refractive index of the crystal, which enters the model in many places. While we can measure and control the polarization of the incident laser beam, the orientation of the crystal is unknown. To resolve this ambiguity, we make measurements for both polarizations ($\vec{E} \parallel D_1$ and $\vec{E} \parallel D_2$) and compare the results. Since crystal thickness and air-gap width are independent of the polarization, the fits for both polarizations should agree on these parameters. As a result, we get to know the orientation of the crystal membrane inside the cavity.

Implementation of a complete fitting routine was part of a master's thesis in our group [Ulanowski2020].

For our cavity, the fit converges to a set of cavity parameters that match well with the measured data: a mirror radius of curvature of $155(3)\,\mu m$, a crystal thickness of $18.2(1)\,\mu m$, and an air gap of $29.8(1)\,\mu m$ when tuned to $1536\,nm$. At that wavelength, the fundamental mode has a waist of $w_0 = 5.7\,\mu m$ and a mode volume of $V = 750(10)\,\mu m^3$ (see eq. 6.2), and its polarization is restricted to $\vec{E} \parallel D_1$ because the limited tuning range is smaller than the splitting between orthogonal polarization modes.

6.1.5 Cavity linewidth and losses

The dynamics of excited erbium dopants in the cavity does not only depend on the coupling rate g and thus the mode volume, but also on the cavity field decay rate κ. For a simple cavity with a homogeneous medium between two mirrors, the intensity decay rate 2κ is given by the photon losses $\mathcal{L}$ per round trip time $t_{\text{round-trip}}$, with contributions from mirror transmission on the crystal- and air-side, T_c and T_a, respectively, as well as additional scattering and absorption losses, $\mathcal{L}_{\text{loss}}$:

$$2\kappa = \frac{\mathcal{L}}{t_{\text{round-trip}}} = \frac{1}{t_{\text{round-trip}}} \left(T_c + T_a + \mathcal{L}_{\text{loss}} \right) \tag{6.16}$$

Because of the partially reflective crystal-air interface, the round-trip time is not well-defined in our cavity. Instead, we introduce an effective cavity length L_{eff}, which is defined by normalizing the energy of the total light field to the average energy density in the crystal: [vanDam2018]

$$L_{\text{eff}} = \frac{\int \mathrm{d}z \, n(\vec{r})^2 |\vec{E}(\vec{r})|^2}{n_c^2 |\vec{E}_{\text{max,c}}|^2/2} \tag{6.17}$$

Here, the integration of the intensity $|\vec{E}(\vec{r})|^2$ extends along the entire cavity axis, while the normalization is done with respect to the maximum intensity in the crystal, $|\vec{E}_{\text{max,c}}|^2$.

This effective cavity length allows us to treat the cavity as if there was a homogeneous medium with the crystal refractive index n_c between two mirrors at distance L_{eff}. Consequently, the round-trip time can be written as $t_{\text{round-trip}} = 2n_c L_{\text{eff}}/c$. Similar to the normalization in the effective length definition, we now have to weight the loss term on the air-side with the intensity ratio relative to the crystal-side: [vanDam2018]

$$\kappa = \frac{c}{4n_c L_{\text{eff}}} \left(T_c + \frac{|\vec{E}_{\text{max,a}}|^2}{n_c |\vec{E}_{\text{max,c}}|^2} T_a + \mathcal{L}_{\text{loss,eff}} \right) \tag{6.18a}$$

$$= \qquad \kappa_c + \qquad \kappa_a \qquad + \quad \kappa_l \tag{6.1}$$

Here, $\vec{E}_{\text{max,a}}$ is the maximum electric field amplitude on the air-side, and κ_c, κ_a and κ_l are the fractional cavity field decay rates due to outcoupling through the mirrors on crystal- and air-side as well as scattering and absorption loss, respectively.

In general, the "true" scattering and absorption losses can be separated into contributions weighted by the electric field on the air- and crystal-side of the cavity, in addition to their dependence on the surface roughness of crystal and mirrors. Therefore, the total losses strongly change with the resonance wavelength of the cavity.

Linewidth measurements

In the following we present experiments in which we measure the cavity linewidth and its dependence on the wavelength due to the changing energy distribution between air- and crystal-side. To this end, we monitor the transmission or reflection of a laser beam through the cavity while sweeping its frequency across the resonance by applying a ramp to the laser controller. To calibrate the frequency axis, we modulate the input laser at 100 MHz with an electro-optical modulator and use the observed sideband splitting as reference (see figure 6.5a). At 1536 nm, we measure a linewidth of $\Delta\nu_{\text{fwhm}} = 22(2)$ MHz, corresponding to a total field decay rate of $\kappa = 2\pi \cdot 11(1)$ MHz.
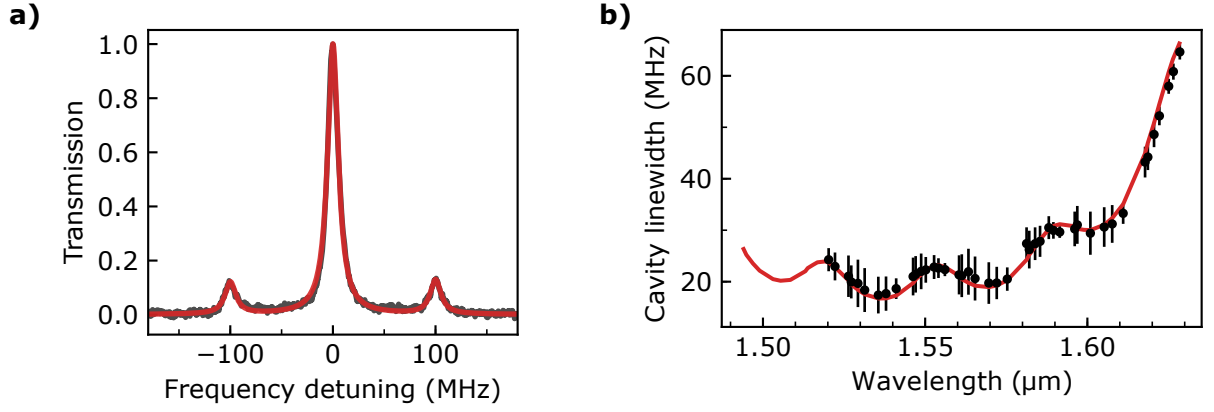
a)

b)

Figure 6.5: **a) Cavity transmission scan.** When the laser frequency is scanned across the resonance, a Lorentzian resonance is obtained. The side-peaks at $\pm 100\,\mathrm{MHz}$ result from sideband modulation of the laser and are used to calibrate the frequency axis. **b) Wavelength dependence of the cavity linewidth.** Because the electric field distribution in crystal and mirror coatings changes with wavelength, the total loss and thus the cavity linewidth is wavelength-dependent as well.

Over a large range of wavelengths, the linewidth varies by a factor of up to 3 (figure 6.5b). The strong increase for longer wavelengths can be explained by the reduced mirror reflectivity, since the distributed Bragg reflectors were optimized for 1536 nm. The additional modulation is a result of the different electric field distributions of air-like and crystal-like mode.

While for a cavity with a homogeneous medium inside we can calculate the finesse $\mathcal{F} = \Delta\nu_{\mathrm{FSR}}/\Delta\nu_{\mathrm{fwhm}}$ via the free spectral range $\Delta\nu_{\mathrm{FSR}}$, the latter is not well defined in our cavity because of the hybridization into crystal- and air-like modes (cf. figure 6.4b). Instead, we can calculate the effective cavity length L_{eff} from the axial mode profile using eq. 6.17, and then the finesse via

$$\mathcal{F} = \frac{\pi}{\kappa\, t_{\mathrm{round\text{-}trip}}} = \frac{\pi}{\kappa}\, \frac{c}{2 n_c\, L_{\mathrm{eff}}}. \tag{6.19}$$

For our cavity, we find a finesse of $1.2(2) \cdot 10^5$.

Outcoupling efficiency

In the following, we show how contributions from outcoupling through the mirrors, κ_a and κ_c, can be separated and extracted from measurements of the cavity reflection and transmission.

As can be derived from the complete transfer-matrix (cf. eq. 6.12), reflection and transmission coefficients r and t of the entire cavity take the following form, for a small detuning $\delta\nu$ from a resonance [Reiserer2015]:

$$r = 1 - \frac{2\kappa_a}{\kappa + i\, 2\pi\delta\nu} \quad , \qquad t = \frac{2\sqrt{\kappa_a \kappa_c}}{\kappa + i\, 2\pi\delta\nu} \tag{6.20}$$

On resonance, the reflection $R^{(c)}$ and transmission $T^{(c)}$ of a laser beam impinging on the crystal side are therefore

$$R^{(c)} = 1 - \eta \frac{4\kappa_c(\kappa - \kappa_c)}{\kappa^2} \quad , \qquad T^{(c)} = \eta \frac{4\kappa_a \kappa_c}{\kappa^2}, \tag{6.21}$$

where η is the mode-matching efficiency between laser beam and cavity mode.

Note that the ratio $\alpha_c = T^{(c)}/(1 - R^{(c)})$ does not depend on the mode matching efficiency anymore. Together with the measured values for a laser beam impinging on the air-side mirror (α_a), we can calculate the field decay rate for outcoupling through the crystal-side mirror, κ_c (and the air-side mirror κ_a, congruently):

$$\kappa_c = \alpha_a \, \kappa \frac{1 - \alpha_c}{1 - \alpha_a \alpha_c} \tag{6.22}$$

From our measurements, we derive $\kappa_a = 2\pi \cdot 1.5(3)\,\mathrm{MHz}$, $\kappa_c = 2\pi \cdot 5(1)\,\mathrm{MHz}$, and the resulting outcoupling efficiency $\eta_{\mathrm{out}} = (\kappa_a + \kappa_c)/\kappa = 60\,\%$.

6.1.6 Cavity parameters and expected Purcell factor

The dynamics of light-matter interaction in the cavity is determined by the coupling rate g, the polarization decay rate γ and the field decay rate κ. In the previous sections, we have extracted the mode volume and the cavity field decay rate from measurements of the mode spectrum and the cavity linewidth. Now we calculate the photon-dopant coupling rate from the mode volume and the transition dipole moment, and estimate the expected Purcell factor.

Optical transition dipole moment

The dipole moment d of an optical transition is related to its oscillator strength f and the absorption coefficient α by [McAuslan2009, Thiel1999, Moncorgé2005]

$$d^2 = \frac{3\hbar e_0^2 n_c}{4\pi m_e \nu \chi} f \quad , \qquad f = \frac{4 m_e c \varepsilon_0 n_c}{N e_0^2 \chi} \int \mathrm{d}\nu \, \alpha(\nu), \tag{6.23}$$

where e_0 is the elementary charge, m_e is the mass of the electron, ε_0 the electric constant and c the vacuum speed of light. ν is the transition frequency, N the dopant concentration (per volume), n_c the crystal refractive index, and $\chi = [(n_c^2 + 2)/3]^2 \approx 3$ a local field correction factor accounting for the polarizability of the medium.

In the same way as a local field correction is necessary in bulk crystal absorption measurements, it is also required for cavity experiments as well, since the polarizability of the crystal was not yet considered in the previous sections. Because the dimensions of our crystal membrane are larger than the wavelength, the polarizability is the same as in a bulk crystal, and we can use the same local field correction factor as in bulk absorption measurements. This is in contrast to experiments on nano-structured materials, which require different treatment [Miyazono2016, Zhong2018].

Therefore, we include the polarizability correction factor in the definition for the coupling rate (eq. 6.1) as follows:

$$g = \frac{\sqrt{\chi} d}{n} \sqrt{\frac{\pi \nu}{\hbar \varepsilon_0 V}} \tag{6.24}$$

Notably, when using the correct definition, $g^2 \sim \chi d^2 \sim f$ is independent of the correction factor and only depends on the oscillator strength. This is in agreement with the observation that also the spontaneous emission rate only depends on the product χd^2 [McAuslan2009, Moncorgé2005].

Since the absorption of erbium in YSO is strongly anisotropic and depends on the light polarization [Petit2020], we calculate the expected dipole moment for $\vec{E} \parallel D_1$ from absorption measurements in the same configuration [Böttger2006a]. The resulting oscillator strength of $f = 1.02 \cdot 10^{-7}$ is consistent with the reported value in [Miyazono2016] and gives a dipole moment of $d = 1.4 \cdot 10^{-32}\,\mathrm{Cm}$ and a coupling rate of $g = 440\,\mathrm{kHz}$.

All the above analysis only considers the enhancement of the electric-dipole optical transition, but neglects that for Er:YSO magnetic-dipole transitions contribute significantly to the absorption [Li1992, Dodson2012, Petit2020]. Thus, it could be argued that the light-atom coupling rate in the cavity needs to be modified to account for magnetic-dipole transitions [Dibos2018, Raha2020, Baranov2017]. In this work, however, we observe good agreement of the measured fluorescence curves with the predictions as calculated from the electric-dipole Purcell enhancement alone, which indicates that the magnetic-dipole transition is enhanced by the same factor as the electric-dipole transition. One reason is that the homogeneous crystal is penetrated by electric and magnetic field equally, as opposed to photonic crystal cavities with distinct transverse electric and transverse magnetic modes. Furthermore, we derived the dipole moment and the oscillator strength from the total absorption coefficient, without distinguishing contributions from electric and magnetic dipole transitions.

Cavity parameters and Purcell factor

Now we have calculated the coupling rate from the oscillator strength, and we already know the cavity field decay rate from linewidth measurements (see section 6.1.5). To fully describe the dynamics of atomic excitations in the cavity, we need to know the polarization decay rate γ. Here, we take the value $\gamma = 1/(2T_1)$ corresponding to the excited state lifetime of $T_1 = 11.4\,\text{ms}$ [Böttger2006b]. Because this lifetime already includes possible decay into other crystal field levels, which are not cavity-enhanced, no additional correction of the obtained Purcell factor is required.

The full set of cavity parameters and the corresponding Purcell factor for maximally coupled erbium dopants is:

$$g_{\text{max}} = 2\pi \cdot 67(7)\,\text{kHz} \tag{6.25a}$$

$$\kappa = 2\pi \cdot 11(1)\,\text{MHz} \tag{6.25b}$$

$$\gamma = 2\pi \cdot 7\,\text{Hz} \tag{6.25c}$$

$$P_{\text{Er,max}} = \frac{g_{\text{max}}^2}{\kappa\gamma} = 58(6) \tag{6.25d}$$

Branching ratio

Alternatively, we can also first derive the Purcell factor for an ideal two-level system resonant with the cavity, P_{TL}, and then correct for potential other decay channels by multiplication with a branching ratio β (see eq. 6.5).

The maximum Purcell factor for a two-level system is defined by the geometrical cavity properties:

$$P_{\text{TL,max}} = \frac{3}{4\pi^2} \frac{Q}{n_c^3 V} \tag{6.26}$$

Here, V is the mode volume, n_c the refractive index of the crystal, and $Q = \nu/\Delta\nu_{\text{fwhm}}$ is the quality factor of the resonance. At a frequency $\nu = 195\,\text{THz}$, we measured a linewidth $\Delta\nu_{\text{fwhm}} = 22\,\text{MHz}$, resulting in a Q-factor of $Q = 9 \cdot 10^6$ and a geometrical Purcell factor of $P_{\text{TL,max}} = 530(50)$.

The branching ratio β is the fraction of excitations that decays into the cavity mode. Because the cavity modes are linearly polarized but the absorption of erbium dopants can not be described by a vector dipole moment aligned with one of the crystal axes, the branching ratio depends on the polarization. It can be calculated as ratio of the spontaneous emission rate of photons with matching polarization, T_{spon}^{-1}, to the total decay rate T_1^{-1}: [McAuslan2009, Moncorgé2005]

$$\beta = \frac{T_{\text{spon}}^{-1}}{T_1^{-1}} = \frac{1}{T_1^{-1}} \frac{3\varepsilon_0 \hbar c^3}{8\pi^2 n_c \chi d^2 \nu^3} \tag{6.27}$$

With the values for χd^2 as calculated above from absorption measurements using eq. 6.23, we find that $\beta = 0.11$ for $\vec{E} \parallel D_1$. This is lower than the values reported for $\vec{E} \parallel D_2$ by a factor of 2, corresponding to the difference in absorption strengths [McAuslan2009, Böttger2006a, Petit2020].

The resulting Purcell factor for maximally coupled erbium dopants, including the branching ratio, is $P_{\text{Er,max}} = \beta P_{\text{TL,max}} = 58(6)$, which is the same as obtained in eq. 6.25.

For comparison, the two-level Purcell factor achieved with our Fabry-Perot resonator is by a factor $3 - 10$ higher than that of cryogenic fiber cavities [Casabone2020, Ruf2020, Jensen2020] and comparable to that reported for a nanophotonic resonator fabricated into erbium-doped YSO [Miyazono2016]. However, a 10 times higher Purcell factor has been demonstrated by coupling an YSO bulk crystal to the evanescent field of a silicon nanophotonic cavity, but came at the price of 100 times larger emitter linewidths [Dibos2018, Raha2020].

6.2 Cavity tuning and stabilization

Maximum Purcell enhancement will be experienced only by ions whose transition frequencies are close to the cavity resonance. Therefore, experiments with cavity-enhanced ion-photon coupling not only require the capability of tuning the cavity into resonance with the emitters, but also of keeping it there over the duration of each experiment.

Since the cavity resonance frequency scales as the inverse of the effective cavity length L_{eff}, any fluctuations in the mirror spacing caused by mechanical vibrations will be seen as fluctuations of the resonance frequency. This effect is even more serious because of the short absolute cavity length of about $50\,\mu\mathrm{m}$. Stabilizing the cavity frequency within one linewidth therefore requires suppression of vibrations below $L_{\mathrm{eff}}\Delta\nu_{\mathrm{fwhm}}/\nu \approx 5\,\mathrm{pm}$.

In this section, we explain the tuning mechanism and discuss different techniques that allow us to achieve the required stability.

6.2.1 Cavity tuning

In our cavity, the two mirrors are held by frames that are mounted at opposite ends of a piezo tube (figure 6.6). By applying a voltage to the piezo, we can expand the tube and increase the distance between the cavity mirrors. At the same time, the mirror frames are pushed back against the piezo by springs that apply restoring forces, so that the mirror spacing can be reduced again when the piezo voltage is lowered. The system comes at rest in a steady-state with an effective cavity length controlled by the piezo voltage, and the sign of the length change depends on the poling of the voltage applied to the piezo tube.
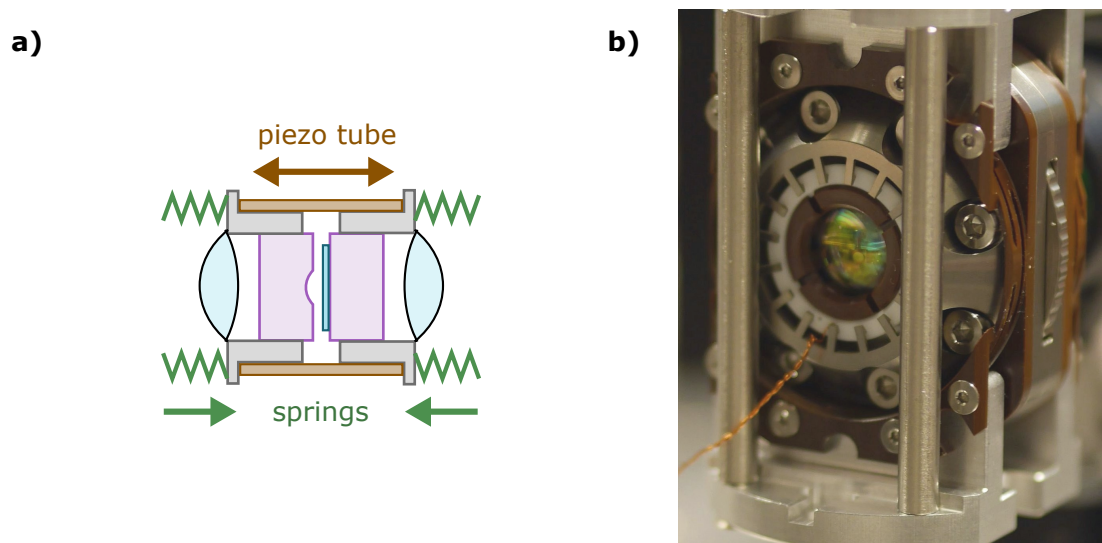

Figure 6.6: **a) Schematics of the cavity mount cross section.** By expansion and compression of the piezo tube, the effective cavity length can be tuned, while springs provide restoring forces and decouple common-mode vibrations. Lenses are included to optimize mode matching of a laser beam coupled into the cavity. **b) Photograph of the cavity mount.** Visible in brown is the spring suspension for damping of common-mode vibrations, a wire connecting to the piezo tube, and a lens in the center for optical coupling.

At cryogenic temperature, we observe an upward shift of the resonance frequencies by $60 - 100\,\mathrm{GHz}$ per $100\,\mathrm{V}$ piezo voltage, corresponding to an air-gap reduction by $20\,\mathrm{nm}$. After the initial cooldown, however, the fundamental mode closest to the erbium transition at $1536\,\mathrm{nm}$ was found at $1539\,\mathrm{nm}$. Assuming a linear response of the piezo tube, a voltage of

more than 600 V would have been required to reach the transition wavelength, which exceeded the maximum output of our instruments.

Instead, we exploit the hysteresis effect commonly observed in piezo electric materials: a repeated charging at high voltage and subsequent grounding of the piezo tube leads to a long-term change in its dimensions that is not reverted when a low voltage is applied afterwards. In our case, about 10 iterations were necessary in order to tune the cavity resonance to about 1536.5 nm, where we expect the emission of erbium ions.

In later experiments, we notice that the step-wise hysteresis tuning stops working when the mode reaches 1535.25 nm, which corresponds to a maximum tuning range of 3.75 nm in wavelength. This could possibly be increased by a factor of two by applying negative tuning voltages, which would increase the tube length and shift the cavity resonance to longer wavelengths.

Unfortunately, the maximum tuning range is smaller than the ~ 10 nm splitting between two modes of orthogonal polarization, which restricts our experiments to the configuration $\vec{E} \parallel D_1$. Although a polarization $\vec{E} \parallel D_2$ would be desirable because of the larger optical dipole moment, it was not possible in the given cavity geometry to tune the corresponding cavity mode close to the erbium transition frequency. After completing the measurements presented in sections 6.3 and 6.4, however, we observe that reassembling the cavity changes its mode spectrum sufficiently to enable tuning of the $\vec{E} \parallel D_2$ polarization mode into resonance with the erbium transitions.

6.2.2 Passive cavity stability

For cavity experiments at cryogenic temperature, we use the same cryostat and similar laser beam geometry as described in section 3.1.2 for holeburning in bulk crystals. For better mechanical decoupling of the cavity from the lab environment and the cryostat enclosure, we modify the sample stick suspension by adding compressed-air dampers that suppress high-frequency vibrations (see figure 6.7a). In addition, the new setup allows for optimization of position and tilt of the sample stick with the goal of avoiding contact with the walls of the surrounding vacuum tube insert (VTI) and keeping a safe distance from vibrating parts.

To characterize the cavity stability, we tune a laser into resonance with a cavity mode, lock it there to the frequency comb, and monitor its transmission through the cavity over time. Any mechanical vibration will lead to fluctuations in the resonance frequency and thus appear as a drop in transmission signal. Therefore, we can extract the achieved stability by analyzing the transmission time trace (fig. 6.7, panels b and c).

With just the passive vibration isolation, we observed reasonable mechanical stability, with rms length fluctuations as low as 3 pm. This value is already more than one order of magnitude smaller than typical residual vibrations of actively stabilized cryogenic fiber cavities [Casabone2020, Ruf2020]. Unfortunately, however, such a passive stability is not easily reproducible. In many configurations, the sample stick touches the walls of the VTI, and vibrations from the cryostat pulse tube and the lab environment can bypass all passive vibration damping elements.

While we do see some dependence of the cavity vibrations on the sample stick position and tilt, we do not always achieve full decoupling from the VTI vibrations. A possible reason is a bending of the sample stick when it is cooled down. This hypothesis is supported by the observation that the cavity transmission passes through the cryostat window at a different position and angle after cooldown, as compared to room temperature.
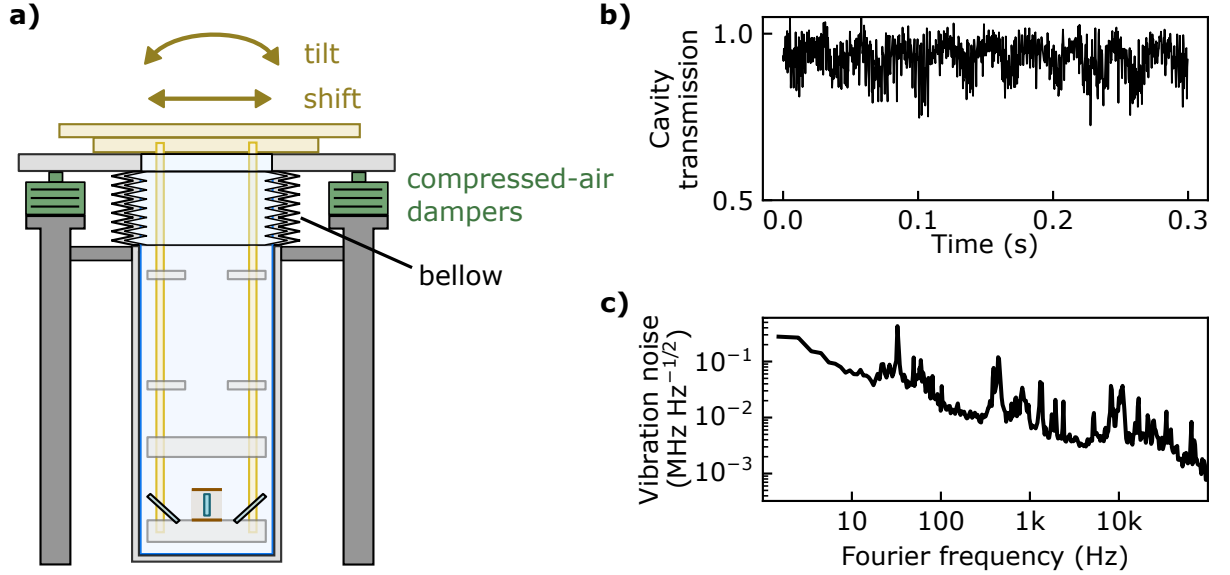
Figure 6.7: **a) Modified sample stick suspension.** Similar to holeburning experiments, the cavity is mounted at the bottom of the sample stick (yellow rods) hanging inside a vacuum tube insert (VTI, light grey), which itself is suspended at the cryostat enclosure (dark grey). In order to decouple the cavity from vibrations originating from the cryostat pulse tube or the lab environment, it is essential that the sample stick does not touch the walls of the vacuum tube insert. For optimum control, the sample space is extended to the top by a semi-flexible bellow, and the sample stick suspension is supported by compressed-air dampers (green). That way, tilting and shifting of the sample stick inside the VTI is possible for optimum positioning. **b) Passive cavity stability.** Without active stabilization, the transmission signal fluctuates because of cavity vibrations (about 3 pm rms length fluctuations). **c) Vibration spectrum.** A Fourier transform of (b) reveals the vibration spectrum of the cavity, here plotted as root-mean-square spectral density of the resonance frequency fluctuations. Overall, the vibration noise spectral density decays only as $\sim 1/f^{0.5}$, which means that high-frequency vibrations contribute as much to the rms stability as low-frequency ones.

6.2.3 Active feedback to the piezo tube

In an attempt to reduce cavity vibrations that are still omnipresent at low temperature, we implement an active feedback system that measures fluctuations in cavity length and applies appropriate voltages to the piezo tube to compensate those vibrations and keep the mirror spacing constant.

To measure fast fluctuations in the cavity resonance frequency, we adopt the Pound-Drever-Hall technique to generate an error signal based on the optical reflection from the cavity [Black2001], as shown in figure 6.8. Close to resonance, the error signal is almost linear, and its sign reflects the sign of the detuning up to a maximum detuning of the modulation frequency, 100 MHz.

Using the Pound-Drever-Hall signal as input, we generate a feedback signal with an OpalKelly FPGA ('lockbox') as first developed by [Leibrandt2015]. This programmable digital circuit can apply various filters and amplification to the input. In a typical setting, we choose a combination of proportional and integral gain, similar to the output of a lowpass-filtered amplifier circuit. In theory, the achievable bandwidth of the lockbox FPGA is 1 MHz. In reality, it is lowered for two reasons: first, because we need another circuit to add a constant high voltage offset that is required to coarse-tune the piezo tube. And second, because a
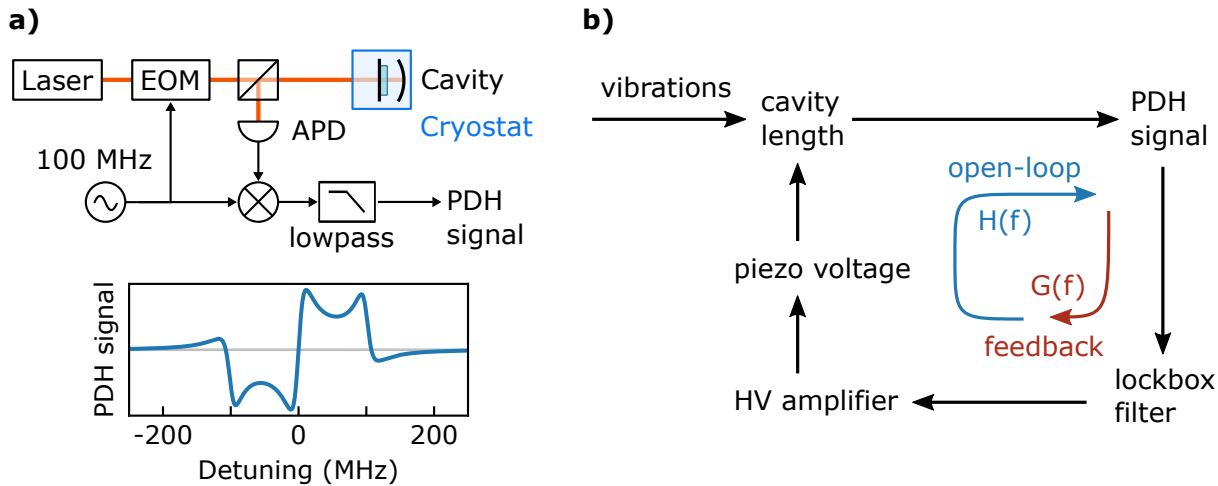
Figure 6.8: **a) Generation of a Pound-Drever-Hall (PDH) signal.** By passing the laser through an electro-optical phase modulator (EOM) we create sidebands at a splitting of $\pm 100\,\mathrm{MHz}$ from the carrier frequency. Because the sidebands have opposite phases, their interference with the carrier cancels out in a power measurement. In a beam reflected from the cavity, however, the frequency components are phase-shifted, depending on their detuning from the resonance (see eq. 6.20). As a consequence, the interference terms of carrier and sidebands do not cancel out, and the power measured with an avalanche photodiode (APD) oscillates at the modulation frequency of $100\,\mathrm{MHz}$. By mixing the APD output down with the local oscillator used to drive the EOM, one can retrieve the relative phase between sidebands and carrier, and thus generate an error signal that reflects the detuning between laser and cavity resonance (bottom panel). **b) Piezo feedback loop and transfer functions.** For small detunings, the PDH signal is proportional to changes in cavity length, which can be caused both by vibrations and tuning via the piezo voltage. In an open-loop measurement, the lockbox outputs a constant voltage that is amplified and applied to the piezo tube; the resulting effect on the PDH signal is described by the transferfunction $H(f)$ (blue). By dynamically updating the lockbox output as a function $G(f)$ of the error signal, the feedback loop is closed (red), and vibrations are counteracted.

piezoelectric material does not behave like an ohmic load with high resistance but has significant capacitive reactance, and its expansion due to charge transfer occurs at finite bandwidth [Richter2009, Fleming2008].

Adding the fast, low-voltage feedback signal from the lockbox to a quasi-constant high-voltage offset is done by a circuit for an ultra-low noise, high-voltage amplifier that drives the piezo [Pisenti2016]. This device uses a flyback converter to create a high-voltage output of up to $250\,\mathrm{V}$ that can be tuned by a low-voltage control signal and is low-pass-filtered at $\sim 10\,\mathrm{Hz}$ bandwidth. To this offset, a second low-voltage signal is added with $\sim 100\,\mathrm{kHz}$ bandwidth and DC-coupling, which will be the feedback output from the lockbox.

Transfer function and mechanical resonances

A formal analysis and optimization of the feedback loop is provided by control theory and considers the transfer functions of all components, which describe how signals and fluctuations propagate through the system.

Excluding the filter implemented on the lockbox FPGA, we can measure the system transfer function $H(f)$ by modulating the output of the FPGA at frequency f and detecting the corresponding Fourier component of the error signal. This transfer function is the combined response of the high-voltage amplifier, the reactance load of the piezo, the mechanical response of the cavity to a modulated piezo voltage, and the PDH signal generation (see figure 6.8b).

Together with the transfer function $G(f)$ implemented by the filter on the FPGA, we can construct the total open-loop transfer function $G(f)H(f)$. By closing the feedback loop, any noise at the cavity can be suppressed by a factor $1/|1 + G(f)H(f)|$. [Åström2010, Gallego2016]
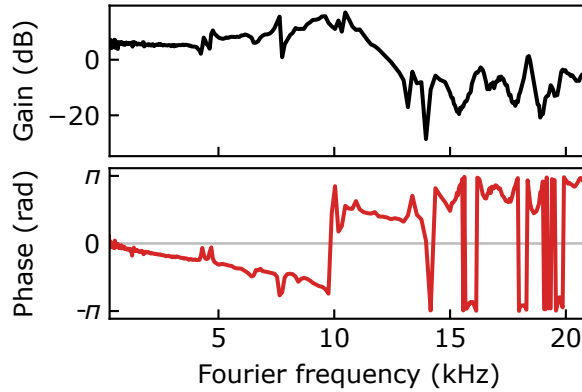
Figure 6.9: **Cavity transfer function $H(f)$.** By modulating the piezo voltage, the PDH signal oscillates with frequency dependent gain and phase. At $10\,\mathrm{kHz}$, the cavity has mechanical resonance that inverts the phase, which leads to increased oscillations if feedback is applied without phase correction.

At first glance, it seems sufficient just to apply high gain with the correct sign in order to compensate mechanical vibrations. A crucial element, however, is the phase of the total transfer function, in particular the phase response of the cavity: close to each mechanical eigenfrequency, $H(f)$ has a pole with a corresponding phase shift of π. In general, this inhibits the suppression of noise above the lowest mechanical eigenfrequency, because feedback would be applied with the wrong phase. In our cavity, we observe the limiting eigenfrequency at about $10\,\mathrm{kHz}$ (see figure 6.9).

Therefore, the cavity mount has to be designed with the aim of shifting its resonance to frequencies as high as possible, which requires stiff and light-weight material (Marcor for our cavity). In addition, one could try and gauge the exact phase response of the cavity resonances and implement a custom filter on the FPGA, which adjusts the output phases for all frequencies accordingly. This method could allow us to counteract vibrations above the lowest eigenfrequency, but the finite sampling bandwidth compared to the Q-factor of these resonances limits the achievable performance improvement.

6.2.4 Active stabilization by photo-thermal feedback

Despite applying a feedback voltage to the piezo tube, it is not always possible to keep the cavity on resonance with the laser during each experiment duration of several 100 µs. If the cavity mount touches the VTI wall and vibrations from the pulse tube reach the cavity without attenuation, oscillations at the mechanical eigenfrequencies can be observed with amplitude greater than the cavity linewidth, which could not be canceled out by feedback to the piezo tube. Therefore, we have to fall back to stabilization by thermo-optic feedback [Brachmann2016, Gallego2016], which we describe in the following.

Losses inside the cavity can be either due to scattering or due to absorption. Any absorption of light will lead to a small increase in temperature and to a distortion of the local cavity geometry, e.g. to an expansion of the crystal membrane or the Bragg reflectors. Their expansion into the air gap reduces the effective cavity length and shifts its resonance to higher frequencies, which at the same time also lowers the laser power coupled into the cavity and thus reduces the heating. Therefore, a steady-state will be reached in which the resonance shifts just far enough to keep the intra-cavity power and the heating at a value that can sustain the shift.

The resulting feedback leads to a self-stabilization of the cavity resonance if the laser is red-detuned with respect to the shifted cavity, but has the opposite effect for blue-detuned excitation. In reasonably slow scans across the resonance, this can be seen as hysteresis and asymmetric lineshape (see figure 6.10). This effect is known as photo-thermal stabilization or thermo-optic shift [Brachmann2016, Navarro-Urrios2014].

In general, the photo-thermal shift due to thermal expansion competes with an opposite shift due to changing refractive indices [Konthasinghe2017]. In contrast to experiments on silicon cavities, we do not expect a large contribution from free-carrier generation due to multi-photon absorption processes, because the band gaps of materials like YSO, SiO2 and TaO2 are more than five times larger than the photon energy [Navarro-Urrios2014].
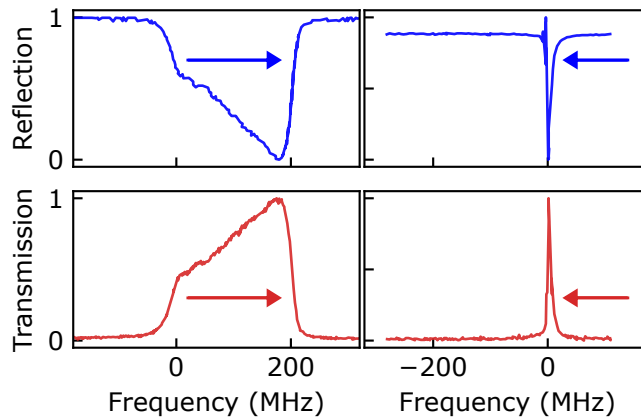
Figure 6.10: **Cavity transmission and reflection scans with photo-thermal feedback.** Absorption losses in the mirror coatings cause heating of the cavity, which shifts its resonance to a higher frequency. When the laser approaches the cavity resonance from lower frequencies, the photo-thermal feedback is self-stabilizing and the resonance is dragged along (left column). If the cavity resonance is approached with a blue-detuned laser, the thermo-optic shift is opposite to the tuning direction, and the resonance appears narrower (right column). The scan speed was about 40 MHz/ms, and the laser power a few µW.

In this work we are only interested in the self-sustaining property of the photo-thermal shift for a red-detuned excitation laser. Fluctuations of the cavity resonance frequency increase or lower the absorbed laser power, and the resulting local temperature change shifts the resonance back to its initial frequency.

Because of the high finesse of our cavity, the resonance frequency is sensitive to small variations in the geometry. As consequence, the photo-thermal effect can provide feedback at a bandwidth of up to 1 MHz and thus stabilize the cavity even above its mechanical eigenfrequencies [Brachmann2016]. In our experiments, we observe resonance frequency rms fluctuations of 8(2) MHz with piezo-feedback only, and can reduce it to $\lesssim 2$ MHz by applying photo-thermal feedback (see figure 6.11).

Unfortunately, the temperature increase associated with the heating also applies to the crystal and the erbium dopants, as we will discuss in section 6.4.1. Therefore, the laser power should be kept at a minimum.
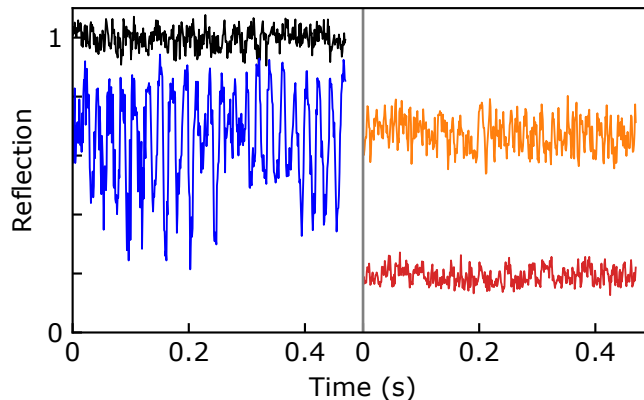
Figure 6.11: **Cavity stabilization with photo-thermal feedback.** For low laser power (left panel), the cavity reflection on resonance shows large fluctuations despite active piezo-tuning (blue); the off-resonant curve (black) is used for normalization. Simultaneous irradiation with an 8 μW laser beam resonant with a different cavity mode (right panel) allows for photo-thermal stabilization of the reflection on resonance (red) as well as detuned by half a linewidth (orange).

6.2.5 Laser setup

Similar to the holeburning experiments on bulk crystals, we use the NKT Photonics BASIK X15 laser 'Koheras' for resonant excitation of the erbium dopants at 1536 nm. In order to stabilize the cavity by feedback to the piezo-tube and by the photo-thermal effect, we use a second laser at 1564 nm, resonant with a different longitudinal mode and allowing for cavity stabilization independent of the erbium excitation (see figure 6.12).

Overall, we can detect about 5 % of all photons emitted from the cavity, considering the outcoupling probability on the crystal-side, the mode-matching with the fiber mode, transmission losses of optical elements and fibers, and the detector efficiency of about 50 %, when operated in regime with a low dark count rate of ~ 25 Hz. Unfortunately, the cavity transmission was partly clipped inside the sample stick and could not be used for experiments, which lowered the maximum detectable fluorescence signal by about 1/3.
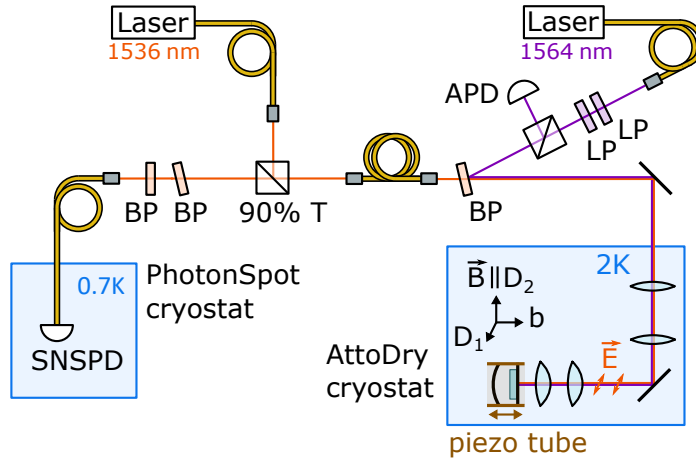

Figure 6.12: **Combined laser setups for resonant spectroscopy and cavity locking.** A laser resonant with the optical transition at 1536 nm is coupled into the cavity via a beam splitter cube, and 90 % of the reflected and emitted photons are routed to the detection setup. We use superconducting nanowire single photon detectors (SNSPD, PhotonSpot) that are protected from reflected, strong excitation pulses by an additional gating AOM (LightComm, not shown). For stabilization of the cavity independent of the resonant excitation, a second laser resonant with a cavity mode at 1564 nm is used to generate a Pound-Drever-Hall signal and apply photo-thermal feedback. A tilted bandpass (BP, Thorlabs) separates the reflected lock laser from the erbium signal at 1536 nm, which is further spectrally filtered (BP, Semrock). In addition, longpass filters (LP, Semrock) with a cut-off wavelength at 1550 nm suppress any contribution of amplified spontaneous emission at 1536 nm in the lock laser spectrum. Both lasers are independently locked to a frequency comb (Menlo Systems, not shown) and can be gated using acousto-optical modulators (Gooch & Housgeo, not shown).

6.3 Fluorescence measurements

In the following, we study the properties of cavity-coupled erbium dopants in experiments. In this section, we first measure the fluorescence decay of resonantly excited ions and compare the observed lifetime reduction with the predicted Purcell factor based on the cavity properties (cf. section 6.1.6). Since the emitters are distributed homogeneously in the crystal, however, most of them are not maximally coupled to the cavity field. We model the distribution of Purcell factors in the measured ensemble based on the mode profile and the excitation and detection probabilities. We find very good agreement and can reproduce different signal shapes when cavity vibrations are included. In the end, we measure the spectral distribution of emitters and estimate the total number of ions coupled to the cavity.

6.3.1 Decay time analysis of Purcell-enhanced fluorescence

Each fluorescence measurement consists of a short laser pulse on the spin-preserving transition and the detection of the subsequent photon emission into the cavity mode, which is tuned into resonance with the ion transition. For a single ion coupled to the cavity, the averaged fluorescence signal follows an exponential decay, according to eq. 6.5.

In our system, however, many dopants in the crystal are coupled to the cavity mode at different rates, depending on the local electric field amplitude. Consequently, the observed fluorescence signal is the sum of exponential curves with different time constants, weighted by the number of ions that experience the same Purcell factor.

In figure 6.13a we show the measured fluorescence curves after exciting the ions with a pulse of $0.5\,\mu s$ length and $54\,nW$ power. Without suppressing cavity vibrations by photo-thermal feedback, most ions spend only a fraction of the experiment time on resonance with the cavity, and the lower average Purcell factor results in a slower fluorescence decay (blue curve). By increasing the lock laser power to $8\,\mu W$, we can reduce the cavity resonance instability and boost the Purcell enhancement (red curve).

Remarkably, both curves agree very well with the prediction of a full model without free parameters, that calculates the ensemble-averaged fluorescence for the inhomogeneous distribution of Purcell factors for our cavity parameters (see the following section 6.3.2 for details). Such a model starts with the maximum Purcell factor for an optimum ion position as derived in equation 6.25, but then includes the dopant distribution at different field amplitudes of the cavity mode as well as excitation and photon collection efficiencies depending on the individual Purcell factors. The model accounts for cavity vibrations by averaging over decay curves obtained for a slightly detuned cavity.

As our model confirms, the fast fluorescence decay expected for ions with optimum coupling and maximum Purcell factor, $P_{\mathrm{Er,max}} = 58$, is not directly visible in the ensemble-averaged measurements, because the number of maximally coupled dopants is comparably low.

We attribute the faster decay observed with photo-thermal feedback to a reduced cavity resonance instability (see figure 6.13b). To confirm this hypothesis and exclude any effect from an increased crystal temperature or multi-photon scattering, we also make measurements at higher temperature and for different power levels of the resonant excitation, but see no change in the decay time (see figure 6.14).
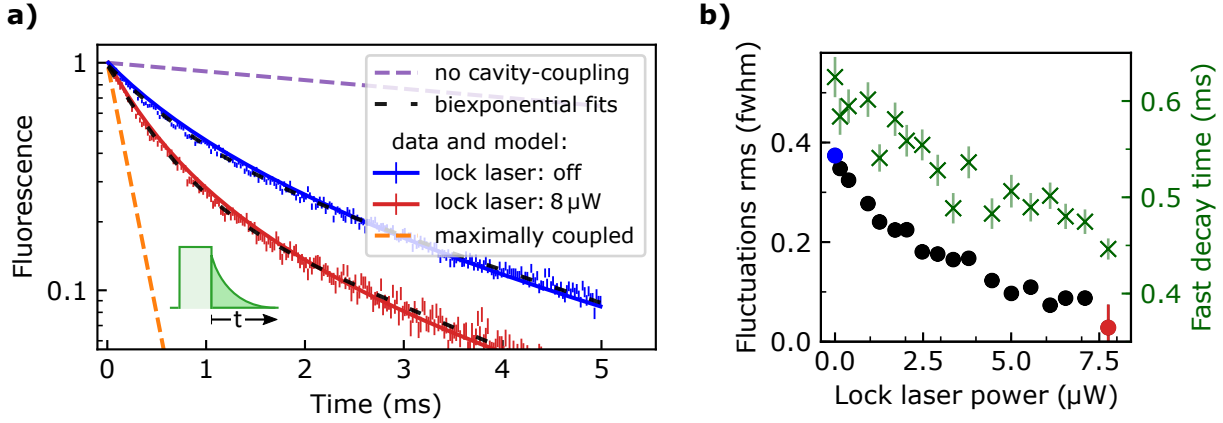
Figure 6.13: **a) Fluorescence curves.** Measurements of the ensemble fluorescence with (red) and without (blue) photo-thermal cavity stabilization show an accelerated decay compared to the situation without cavity-enhancement (purple dashes). Because of the inhomogeneous cavity-coupling, the curves deviate from mono-exponential decay and rather look bi-exponential (fits as black dashes). A complete model with no free parameters can describe both curves excellently (solid lines) and indicates that maximally coupled ions decay faster (orange dashes) than visible in ensemble measurements. **b) Decay time dependence on lock laser power.** When the lock laser power increases, thermo-optic feedback stabilizes the cavity and can be observed as faster decay of the fluorescence, e.g. in the fast time constant of bi-exponential fits (green crosses, right axis). By fitting the measured curves with our model, the remaining rms fluctuations of the cavity resonance can be extracted in units of the cavity linewidth (circles, left axis). The two data points marked in red and blue correspond to the curves in panel (a).
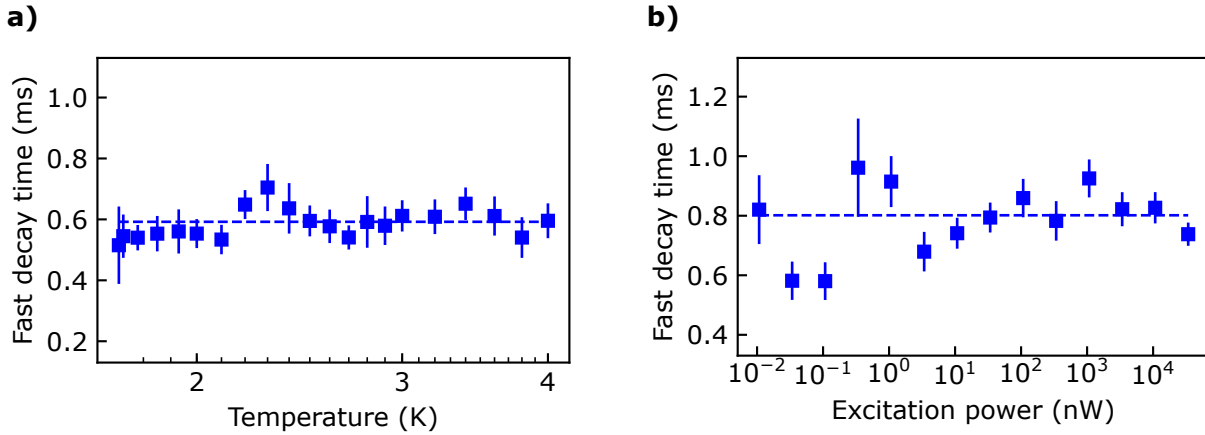
Figure 6.14: **Dependence of the fluorescence decay time on temperature (a) and excitation power (b).** When the crystal temperature is increased up to 4 K, the fluorescence decay does not change its time scale, here represented by the fast time constant of bi-exponential fits (a). Similarly, the fluorescence decay shows no dependence on the resonant excitation power (b). The dashed lines show the respective average value. The excitation pulse length in the temperature scan was 0.5 µs, but 500 µs in the power scan, resulting in slightly different absolute fit parameters. Both data sets were taken without photo-thermal feedback.

94

6.3.2 Modeling the ensemble-averaged fluorescence

In this section, we discuss in detail how we can model the non-exponential fluorescence decay curves that result from an inhomogeneous Purcell-factor distribution in the ensemble measurements.

While the Purcell factor for a single ion positioned at the maximum of the electric field inside the cavity can be calculated from the independently characterized mode volume and dipole moment (see section 6.1.6), the dopants in our crystal are distributed randomly across the cavity mode, at different electric field amplitudes. First, we make a Monte Carlo simulation and derive an analytical formula for the distribution of Purcell factors in our sample, then we discuss how differently coupled ions contribute to the observed fluorescence decay curve due to Purcell-factor-dependent excitation and photon collection efficiencies, and in the end we explain how the effect of cavity vibrations can be included in the model.

Distribution of Purcell factors

We start with the electric field envelope of the fundamental mode, which is approximately a standing wave along the cavity axis, z, with a Gaussian profile along the radial direction ρ:

$$E(\rho, z) = E_{\text{max}} \sin\left(\frac{2\pi n z}{\lambda}\right) \exp\left(-\frac{\rho^2}{w^2}\right) \tag{6.28}$$

Here, n is the refractive index of the crystal, λ the wavelength, w the beam waist, and we neglect that the beam radius increases slightly over the crystal membrane. This is a valid approximation because in our cavity the crystal thickness ($19\,\mu\text{m}$) is much smaller than the Rayleigh length, $\pi w^2 n / \lambda$ ($\sim 120\,\mu\text{m}$).

The Purcell factor P_{Er} of a single emitter scales with the square modulus of the electric field amplitude, and we can write it as fraction of the Purcell factor at a field maximum, $P_{\text{Er,max}}$:

$$P_{\text{Er}} = P_{\text{Er,max}} \underbrace{\sin^2\left(\frac{2\pi n z}{\lambda}\right)}_{u_z(z)} \underbrace{\exp\left(-\frac{2\rho^2}{w^2}\right)}_{u_\rho(\rho)}, \tag{6.29}$$

where the product form of P_{Er} allows us to separate the axial and radial dependencies, $u_z(z)$ and $u_\rho(\rho)$.

By randomly placing $N = 50\,000$ dopants in the modeled cavity mode and calculating their respective Purcell factors with eq. 6.29, we make a Monte Carlo simulation of the probability distribution $p(P_{\text{Er}})$ to find a dopant with Purcell factor P_{Er} (see figure 6.15, grey curve).

In order to derive an analytical expression for $p(P_{\text{Er}})$, we restrict the calculation to ions with $P_{\text{Er}} > 1$, which make up about $36\,\%$ of all dopants in the simulation. This restriction is necessary for convergence reasons, because the radial mode field has no strict bound, and ions with Purcell factors close to zero could as well sit outside the considered volume.

We first need to calculate the probability densities $p(u_z)$ and $p(u_\rho)$ separately. To this end, we start with the probability density $p(x, y, z)$ to find an emitter at Cartesian coordinates x, y, z, which is constant for a homogeneous distribution of dopants in the crystal. Then, we change coordinate systems and transform the probability density function accordingly.

While the probability density $p(x, y, z)$ in Cartesian coordinates is constant, this changes when we switch to cylindrical coordinates ρ, ϕ, z, and after separating axial and radial components again, we have

$$p(\rho) = \frac{\rho}{a_\rho} \quad , \qquad p(z) = \frac{1}{a_z}, \tag{6.30}$$

where the normalization constants $a_\rho = 2w^2$ and $a_z = \pi/2$ are chosen so that

$$\int_0^{2w} \mathrm{d}\rho \, p(\rho) = 1 \quad , \qquad \int_0^{\lambda/4n} \mathrm{d}z \, p(z) = 1. \tag{6.31}$$

The upper limit of integration over ρ is necessary for convergence reasons. Its value of twice the waist seems reasonable because dopants outside of the cavity mode experience no Purcell enhancement and thus radiate predominantly into free space, such that they do not contribute to the measured signal. The validity of this assumption was confirmed by numerical Monte Carlo simulations. In the integral over the axial component we only need to consider the first quarter-wavelength layer of the membrane, as $p(z)$ is constant and values of the light intensity at other positions are related by periodicity and symmetry.

Now we change the coordinates again, from ρ to u_ρ, and from z to u_z. The corresponding transformations of the probability densities are given by the Jacobi determinants

$$p(u_\rho) = p(\rho) \left| \frac{\mathrm{d}\rho}{\mathrm{d}u_\rho} \right| \quad , \qquad p(u_z) = p(z) \left| \frac{\mathrm{d}z}{\mathrm{d}u_z} \right|, \tag{6.32}$$

and we arrive at

$$p(u_\rho) = \frac{1}{8\,u_\rho} \quad , \qquad p(u_z) = \frac{1}{\pi \sqrt{u_z(1 - u_z)}}. \tag{6.33}$$

In the next and final step, we need to find the probability density for any Purcell factor $P_{\mathrm{Er}} \leq P_{\mathrm{Er,max}}$ that depends on the combined probability density, $p(u_\rho u_z)$. To this end, we integrate over the whole parameter space and filter values that match eq. 6.29 using a delta distribution:

$$p(P_{\mathrm{Er}}) = \int \mathrm{d}u_\rho \, p(u_\rho) \int \mathrm{d}u_z \, p(u_z) \, \delta \left(P_{\mathrm{Er}} - P_{\mathrm{Er,max}} \, u_\rho u_z \right) \tag{6.34}$$

By applying the scaling law for the delta distribution, $\delta(ax) = \delta(x)/|a|$, and evaluating first the integral over u_z, we can then solve the integral over u_ρ as well and arrive at

$$p(P_{\mathrm{Er}}) = \frac{\arccos \left(\sqrt{\frac{P_{\mathrm{Er}}}{P_{\mathrm{Er,max}}}} \right)}{4\pi \, P_{\mathrm{Er}}}. \tag{6.35}$$

This result is in agreement with the numerical Monte Carlo simulation for Purcell factors (see figure 6.15, solid grey and dotted blue curves). The divergence of eq. 6.35 at $P_{\mathrm{Er}} \approx 0$ explains, why we needed to assume that $P_{\mathrm{Er}} > 1$ in order to derive this simple expression.

Coupling-dependent excitation and collection efficiency

Not only the decay rate from the excited state depends on the Purcell factor of each individual ion. Also the probability to emit a photon into the cavity mode depends on the Purcell factor, as well as the excitation probability by a laser pulse of certain length and power. Therefore, strongly coupled dopants contribute disproportionately more to the detectable fluorescence signal than weakly coupled ones.
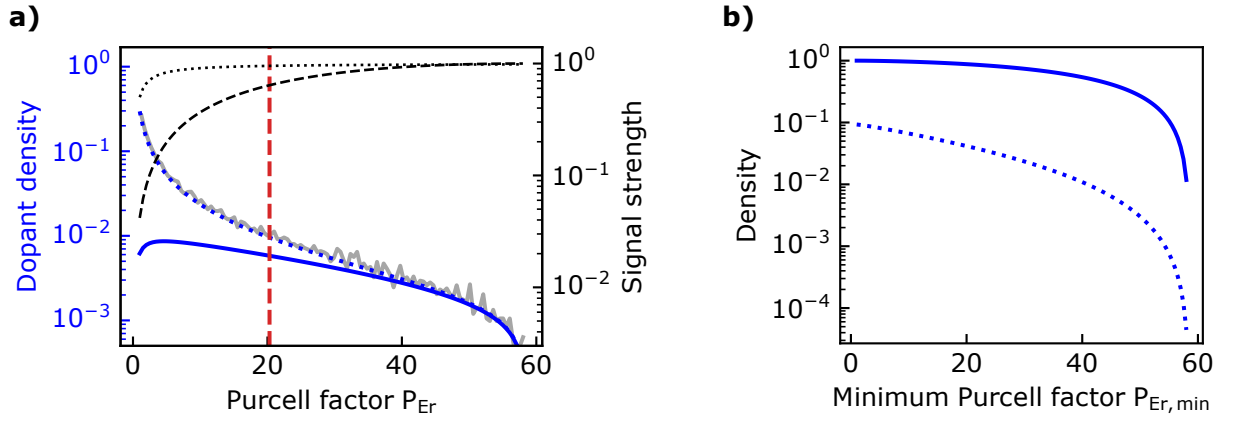
Figure 6.15: **a) Distribution of Purcell factors for cavity-coupled ions.** Because of the Gaussian standing-wave cavity mode profile, most dopants experience reduced Purcell factors, following a distribution $p(P_{\mathrm{Er}})$ that can be calculated analytically (blue dotted curve) or in a Monte Carlo simulation of 50000 ions (grey curve). Weakly coupled ions, however, contribute less to the fluorescence signal, because the probabilities of exciting the ion, η_{exc}, (black dashed curve, assuming a π pulse for maximally coupled dopants) and emitting the photon into the cavity mode, η_{coll}, (black dotted curve) scale with the Purcell factor. The effective weight of each individual Purcell factor in fluorescence measurements, $p(P_{\mathrm{Er}})\,\eta_{\mathrm{coll}}\,\eta_{\mathrm{exc}}$, (solid blue curve) gives an average Purcell factor of ~ 20 (red dashed line). **b) Cumulative density function.** By integrating over the weighted probability density $p(P_{\mathrm{Er}})\,\eta_{\mathrm{coll}}\,\eta_{\mathrm{exc}}$ in (a), we calculate the relative contribution of dopants with Purcell factors greater than some threshold $P_{\mathrm{Er,min}}$, either with respect to all ions in the cavity (dotted blue curve) or only to the ones detected in fluorescence measurements (solid blue curve). For example, ions with Purcell factors $P_{\mathrm{Er}} > 40$ make up $50\,\%$ of the fluorescence signal, but have only a relative density of $1\,\%$ in the cavity mode.

To calculate the collection efficiency via the cavity mode, η_{coll}, we take the ratio of the emission rate into the cavity mode, g^2/κ, to the total decay rate (cf. eq. 6.5):

$$\eta_{\mathrm{coll}} = \frac{\frac{g^2}{\kappa}}{\gamma + \frac{g^2}{\kappa}} = \frac{P_{\mathrm{Er}}}{1 + P_{\mathrm{Er}}} \tag{6.36}$$

The excitation probability η_{exc}, on the other hand, can be modeled by the coherent population transfer at a Rabi frequency $\sqrt{n_{\mathrm{cav}}}g$ after time τ. In this context, the scaling of the Rabi frequency with the electric field amplitude is represented by the square root of the intra-cavity photon number, n_{cav}, and with $P_{\mathrm{Er}} = g^2/\kappa\gamma$ we can write [Kuhn2010]

$$\eta_{\mathrm{exc}} = \sin^2\left(\frac{\sqrt{n_{\mathrm{cav}}P_{\mathrm{Er}}\kappa\gamma}}{2}\tau\right). \tag{6.37}$$

This assumes that the number of photons in the laser pulse is not strongly changed by the ions, i.e., that only a small ensemble is resonant with the laser.

The average intra-cavity photon number for optical driving can be calculated from the photon flux Φ_{in} entering the cavity and the intensity decay rate 2κ:

$$n_{\mathrm{cav}} = \frac{\Phi_{\mathrm{in}}}{2\kappa} \tag{6.38}$$

Here, the photon flux entering the cavity is given by the laser power at the cavity crystal-side mirror, $P_{\text{in}}^{(c)}$, the mode matching efficiency η_{mode} and the transmission of the cavity on resonance (see eq. 6.21):

$$n_{\text{cav}} = \eta_{\text{mode}} \left(1 - R^{(c)} \right) \frac{P_{\text{in}}^{(c)}}{2\kappa \, h\nu} \tag{6.39}$$

Ensemble fluorescence curve

So far, our model considers a cavity with a given maximum Purcell factor, P_{max}, and the different decay rates of dopants homogeneously distributed in the crystal. Then, the observed fluorescence signal $f(t)$ is the sum of all individual decay curves (eq. 6.5) weighted with the probability of the respective Purcell factor and the corresponding collection and excitation efficiencies:

$$f(t) = \int \mathrm{d}P_{\text{Er}} \, p(P_{\text{Er}}) \, \eta_{\text{coll}} \, \eta_{\text{exc}} \, \mathrm{e}^{-(P_{\text{Er}}+1)t/T_1} \tag{6.40}$$

Because the Purcell-factor dependence of excitation and collection efficiency strongly suppress the detection of weakly coupled ions, only a total fraction of $\int \mathrm{d}P_{\text{Er}} \, p(P_{\text{Er}}) \, \eta_{\text{coll}} \, \eta_{\text{exc}} = 25\,\%$ of all dopants with $P_{\text{Er}} > 1$ contribute to the fluorescence at all (see figure 6.15).

Effect of cavity vibrations

For low lock laser power, the cavity stabilization by photo-thermal feedback is not perfect and the resonance frequency fluctuates around its target value. Over a large fraction of the measurement sequence, the cavity is therefore detuned from the dopants, even if – on average – the excitation pulse is applied on resonance. The effect of a cavity detuning $\Delta\nu$ from the ion transition is a reduction in electric field amplitude, thus a lowering of the Purcell factor from its original value P_{Er} to its detuning-corrected value $P_{\text{Er},\Delta\nu}$: [Ruf2020]

$$P_{\text{Er},\Delta\nu} = P_{\text{Er}} \frac{1}{1 + \left(\frac{2\Delta\nu}{\Delta\nu_{\text{fwhm}}} \right)^2}, \tag{6.41}$$

with the cavity resonance fwhm linewidth $\Delta\nu_{\text{fwhm}}$.

Unfortunately, the cavity detuning due to vibrations does not follow a deterministic function but is a stochastic process. Still, for a qualitative understanding of the effect, we can model it as a periodic oscillation around zero, with a root-mean-square detuning of $\Delta\nu_{\text{rms}}$ and a frequency ω. From there, we derive the probability density $p(\Delta\nu)$ to find the cavity detuned by $\Delta\nu$:

$$\Delta\nu(t) = \sqrt{2}\Delta\nu_{\text{rms}} \sin(\omega t) \quad , \qquad p(\Delta\nu) = \frac{2}{\pi} \frac{1}{\sqrt{2\Delta\nu_{\text{rms}}^2 - \Delta\nu^2}} \tag{6.42}$$

Consequently, the fluorescence curve in presence of vibrations is the average of the fluorescence curves for all possible cavity detunings, weighted by the respective probability densities:

$$f(t) = \int \mathrm{d}\Delta\nu \, p(\Delta\nu) \, f(t|P_{\text{Er,max},\Delta\nu}) \tag{6.43}$$

Here, $f(t|P_{\text{Er,max},\Delta\nu})$ is the fluorescence curve as described in eq. 6.40, where the fixed maximum Purcell factor is replaced by its detuning-corrected value, $P_{\text{Er,max},\Delta\nu}$.

Although the assumption of a periodically oscillating detuning is not valid in case of random vibrations, we find good agreement between the simulated fluorescence curves and the measured data. A possible reason is the strong signature of mechanical resonances in the

vibration spectrum (cf. fig. 6.7). Even if oscillations at the cavity's eigenfrequencies are not phase-stable because of stochastic noise, the distribution of resonance detunings is expected to roughly follow eq. 6.42.

6.3.3 Determining the number of dopants

In addition to the relative distribution of ions with different Purcell factors, we are also interested in the absolute number of emitters in the cavity. This helps us to estimate the feasibility of resolving and controlling single dopants in the current setup.

To this end, we are going to analyze the area of the detected fluorescence curves, which is a measure of the number of excitations in the cavity. First, we gauge the number of excited dopants per measurement, then we inspect their spectral distribution and confirm the findings in additional autocorrelation measurements.

Number of excitations per measurement

To estimate the number of excitations inside the cavity, n_{exc}, we start with the number of detected photons in each fluorescence measurement, n_{det}, and divide it by the independently characterized setup detection efficiency, η_{det}, (cf. section 6.2.5):

$$n_{\text{exc}} = \frac{n_{\text{det}}}{\eta_{\text{det}}} \tag{6.44}$$

By scanning the excitation power and analyzing how the number of excitations scales with the number of intra-cavity photons generated by each laser pulse, n_{cav}, (see eq. 6.39), we measure the saturation behavior of the optical transition (see figure 6.16).

At low excitation power, the number of excited ions increases linearly with the average photon number up to a maximum value of about $n_{\text{sat}} \approx 50$ excited dopants, at which the transition saturates. Thus, the number of dopants at a given frequency is on the order of 100. Because of power broadening, higher laser power will still increase the number of excited ions but with a sub-linear scaling law $\sim (n_{\text{cav}})^r$, with $r < 1$. In a phenomenological model, we can fit the data by a modified saturation curve, and find a broadening exponent of about $r \approx 0.3$:

$$n_{\text{exc}}(n_{\text{cav}}) = \frac{\frac{n_{\text{cav}}}{n_{\text{sat}}}}{1 + \left(\frac{n_{\text{cav}}}{n_{\text{sat}}}\right)^{1-r}} \tag{6.45}$$

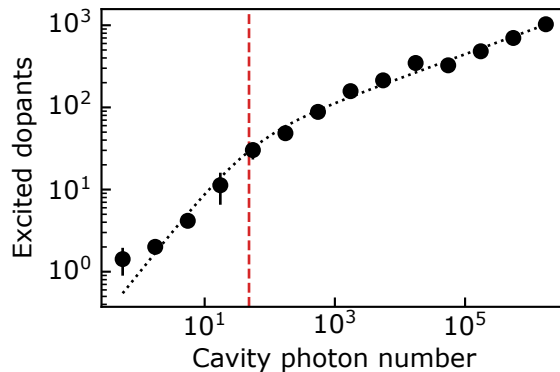
Figure 6.16: **Saturation curve.** The number of excited dopants in the cavity – as calculated from the detected fluorescence signal – increases with the number of intra-cavity photons. The scaling is linear at low excitation power and sub-linear for high power, and by fitting eq. 6.45 to the measured data, we extract a saturation photon number of $n_{\text{sat}} \approx 50$ (red dashed line).

Because of the 500 μs long laser pulses used in these measurements, the excitation bandwidth at saturation was likely not dominated by the Fourier bandwidth but rather by the average Rabi frequency. At saturation level, the Rabi frequency is again calculated by the coupling rate $g = \sqrt{P_{\mathrm{Er}}\kappa\gamma}$, scaled with the electric field amplitude $\sim \sqrt{n_{\mathrm{cav}}}$ (cf. section 6.3.2):

$$\Omega_{\mathrm{avg}} = \langle \sqrt{n_{\mathrm{sat}}}\, g \rangle = \frac{\int \mathrm{d}P_{\mathrm{Er}}\, p(P_{\mathrm{Er}})\, \eta_{\mathrm{coll}}\, \eta_{\mathrm{exc}}\, \sqrt{n_{\mathrm{sat}}P_{\mathrm{Er}}\kappa\gamma}}{\int \mathrm{d}P_{\mathrm{Er}}\, p(P_{\mathrm{Er}})\, \eta_{\mathrm{coll}}\, \eta_{\mathrm{exc}}} \approx 2\pi \cdot 180\,\mathrm{kHz} \tag{6.46}$$

Note that in general, also spectral diffusion processes would add to the effective excitation bandwidth during long laser pulses. In these experiments with low dopant concentrations and the excitation laser locked to the frequency comb, only the interaction of erbium ions with yttrium spins is relevant, but the spectral diffusion due to superhyperfine coupling is smaller than Ω_{avg} and happens on a timescale much longer than the excitation pulse (see section 4.2).

Spectral distribution of dopants

Now we measure the spectral shape and width of the ensemble absorption line by scanning excitation laser and cavity resonance frequency simultaneously and detecting the fluorescence.

At a magnetic field of 3.5 T, we observe separate transition lines of the two magnetic classes and focus on a single class of site 1. We measure a Lorentzian distribution with 414(7) MHz fwhm linewidth (figure 6.17), which is comparable to that of bulk crystals with 10 ppm erbium concentration. Apparently we observe no additional broadening, in contrast to experiments on nano-structured crystals that are prone to increased crystal defects [Dibos2018, Zhong2015b]. At zero magnetic field, however, our measured absorption line peaks at 1536.49 nm, corresponding to a frequency shift by ~ 1.5 GHz compared to large bulk crystals, which could be the result of homogeneous strain in our sample or variations in the crystal purity.
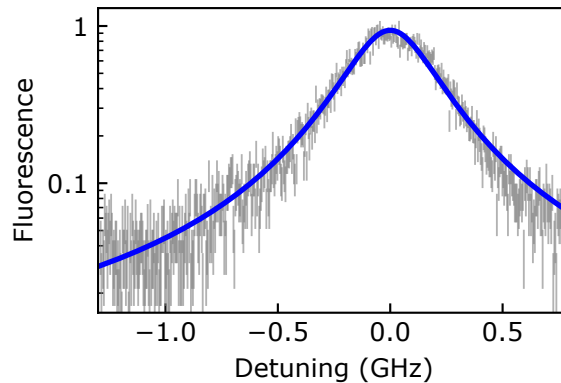

Figure 6.17: **Ensemble absorption line.** In fluorescence measurements at 3.5 T, the ensemble absorption line for a single magnetic class of site-1-dopants has a Lorentzian line shape with a fwhm of 414(7) MHz (grey data and blue fit).

Total number of ions

From the saturation curve measurement, we extracted a number of about 50 excited ions in 180 kHz excitation bandwidth, corresponding to a spectral dopant density of $50/(\Omega_{\mathrm{avg}}/(2\pi))$ = 0.2kHz. To calculate the total number of cavity-coupled ions, we multiply this spectral density with the area of the ensemble absorption line, $(\pi/2) \cdot 414\,\mathrm{MHz}$, and correct for a non-zero population in the high-energy ground state by the Boltzmann factor of about 6 %. We arrive at a number of $\sim 2 \cdot 10^5$ ions of a single magnetic class, or twice that value for all site-1-dopants.

This number does not yet take into account that only 36 % of all dopants in the mode have a Purcell factor $P_{\mathrm{Er}} > 1$ and were considered in the model, and only 25 % of those dopants effectively contribute to the fluorescence measurements because of low excitation and collection efficiencies (see section 6.3.2). Including this correction and all dopants on site 2 as well, we arrive at a total number of $\sim 1 \cdot 10^7$ erbium dopants in the cavity, distributed over the mode volume in the crystal of about $2000\,\mu\mathrm{m}^3$, calculated for a crystal thickness of $19\,\mu\mathrm{m}$ and a beam waist of $5.7\,\mu\mathrm{m}$ (cf. section 6.1.4). Comparing this value with the density of all yttrium sites in the crystal (16 per unit cell volume of $852.658\,\text{Å}^3$), we find a dopant concentration of $\sim 0.2\,\mathrm{ppm}$.

A similar residual erbium dopant concentration of $\sim 0.3\,\mathrm{ppm}$ for nominally undoped YSO crystals has been reported before [Dibos2018]. Contamination of the yttrium precursor with erbium and other rare-earths is common and technically difficult to avoid, which sets a limit to the lowest possible dopant concentration achievable when growing crystals from the melt [Tao1983, Zhang2014].

Autocorrelation measurements

To confirm the spectral density of about 0.2 ions per kHz that we deduced from the saturation curve and our model distribution of coupling strengths, we also make autocorrelation measurements. This time, we choose short pulses of 1 μs length, so that the excitation bandwidth of about 500 kHz now does not depend on the individual Rabi frequencies but on the Fourier-limited time-bandwidth product of about 0.5 for square pulses.

Our experiments consist of a train of excitation pulses with subsequent detection windows. Because of the low photon detection rate of $\sim 1\,\mathrm{kHz}$ compared with the detector dead-time of about 1 μs, we can use a single detector to measure the autocorrelation function $g^{(2)}(\tau)$. This function tells the normalized probability to detect two photons at arrival time difference τ and is defined by [Walls1979, Teich1988]

$$g^{(2)}(\tau) = \frac{\langle I(t)I(t+\tau)\rangle}{\langle I(t)\rangle^2}. \tag{6.47}$$

Here, $I(t)$ is the number of detection events in time bin t, and $\langle\cdot\rangle$ denotes the average over the entire pulse train.

Because of the quantum nature of excitations, the maximum number of detected photons per window is given by the number of excited dopants in the cavity, if the probability of a dark count event is low enough. Therefore, the probability of photons being detected in the same time bin, $g^{(2)}(\tau = 0)$, is reduced with respect to the probability of being detected in neighboring bins, $g^{(2)}(\tau \neq 0)$. This antibunching dip is directly related to the number N of emitters: [Walls1979, Kuhn2010]

$$g^{(2)}(0) = 1 - \frac{1}{N} \tag{6.48}$$

For a more precise analysis, we have to correct for accidental coincidence counts due to detector noise. With a dark count rate D and a total photon detection rate T (including dark counts), the observed autocorrelation $\tilde{g}^{(2)}(\tau)$ has reduced contrast: [Becher2001, Verberk2003]

$$\tilde{g}^{(2)}(\tau) = 1 + \frac{(T-D)^2}{T^2}\left[g^{(2)}(\tau) - 1\right] \tag{6.49}$$

Although our autocorrelation measurements were not yet optimized for a low dark count rate, we measured $D \approx 60\,\text{Hz}$, which is less than $2\,\%$ of the total detection rate $T \approx 3.3\,\text{kHz}$. In the raw data, these accidental coincidences reduce the antibunching dip by $1-(T-D)^2/T^2 \approx 4\,\%$ and let us underestimate the number of emitters.

After correcting for dark counts, we observe an antibunching dip of $g^{(2)}(0) = 0.9907(7)$, corresponding to a number of about $N = 110$ emitters (see figure 6.18). The resulting spectral density of about 0.22kHz is comparable to the value extracted from the saturation measurements.
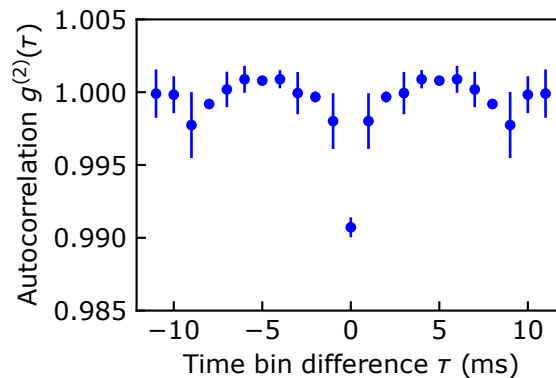
Figure 6.18: **Fluorescence autocorrelation.** In the fluorescence of a train of excitation pulses, the autocorrelation shows an antibunching dip of $g^{(2)}(0) = 0.9907(7)$, corresponding to a number of $N \approx 110$ excited dopants per pulse. Because the detection windows were chosen to be $1\,\text{ms}$ long for fast data acquisition, weakly-coupled dopants could show antibunching in the neighboring bin, at $\tau = 1\,\text{ms}$. The data points were taken at a magnetic field of $6\,\text{T}$ and are already corrected for accidental coincidences from dark counts (eq. 6.49).

6.4 Photon echo measurements

After measuring the excited state lifetime of emitters and their coupling to the cavity, we now study their optical coherence. In this section, we first perform two-pulse photon echo experiments to measure the coherence time. While for maximally-coupled ions the coherence time exceeds the lifetime and three-pulse echo measurements show no significant spectral diffusion, we observe significantly accelerated dephasing at higher crystal temperature as well as for increased lock laser power. Finally, we show the modulation of a photon echo signal by superhyperfine coupling to yttrium spins at lower magnetic field.

6.4.1 Optical coherence time in two-pulse echo measurements

In a two-pulse echo measurement, the first laser pulse with an area of approximately $\pi/2$ prepares the emitters in a superposition between ground and excited state. In the following free-evolution period of length $t/2$ they dephase because of the different transition frequencies in the ensemble. The second pulse of area π inverts the accumulated phases, and after another free-evolution period of length $t/2$, a refocusing of the phases stimulates the collective emission of photons: the echo.

With increasing sequence length t, the echo area $A(t)$ decays exponentially on a timescale set by the coherence time T_2 [Böttger2006b]:

$$A(t) = A_0 \exp\left(-\frac{2t}{T_2}\right) \tag{6.50}$$

First, we determine a pulse length of $0.5\,\mu s$ and power levels of $100\,\text{nW}$ and $25\,\text{nW}$ for π and $\pi/2$ pulses, respectively, to maximize the echo area at constant sequence length. Then, we scan the interpulse delay and derive a coherence time of $0.54(1)\,\text{ms}$ from fitting eq. 6.50 to the echo decay that we measured while the lock laser was turned off (figure 6.19). This value constitutes an improvement by one order of magnitude compared to the coherence time reported recently for bulk crystals without cavity coupling [Car2020], and it is enabled by a strong suppression of ion-ion interactions due to the lower dopant concentration in our crystal.

Apparently, the coherence time obtained for the ensemble of emitters is significantly longer than the expected lifetime of $0.19\,\text{ms}$ for maximally coupled dopants. Assuming they are not subject to stronger dephasing processes than moderately coupled ions, the coherence of dopants with maximum Purcell factor would be lifetime-limited, $T_2 = 2\,T_1$. But even when we compare the ensemble-averaged coherence time with the observable fast decay time of the ensemble-averaged fluorescence in a fully stabilized cavity ($\sim 0.45\,\text{ms}$, see figure 6.13b), most dopants fulfill $T_2 > T_1$, which is a key requirement for having high efficiency in quantum protocols that rely on two-photon interference [Reiserer2015].

We do, however, measure a reduced coherence time of only $0.14(1)\,\text{ms}$ when we turn on the lock laser to about $8\,\mu W$, which we attribute to an increased crystal temperature. In the following, we will investigate more systematically how the coherence time changes with lock laser power and crystal temperature.
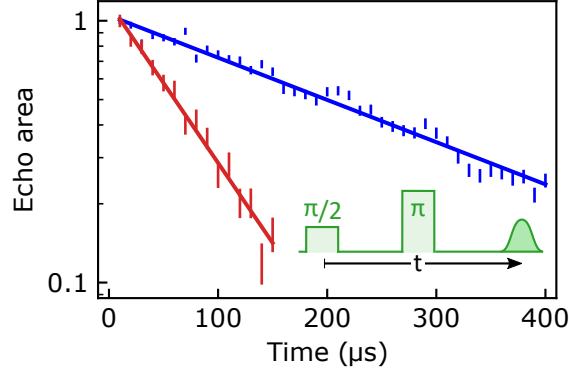
Figure 6.19: **Two-pulse photon echo.** From the decay of the photon echo area over time, we derive a coherence time of $T_2 = 0.54(1)$ ms when the lock laser is turned off (blue curve), which is reduced to $0.14(1)$ ms when photo-thermal feedback is applied (red). All data were taken at a magnetic field of 0.8 T and a cryostat temperature of 1.8 K, and solid curves are exponential fits (see eq. 6.50).

Temperature and power dependence

When we scan the laser power for photo-thermal feedback, we measure a linear increase of the coherence decay rate T_2^{-1} with higher power (see figure 6.20a). While we had also seen a faster population decay in fluorescence measurements with photo-thermal stabilization, the dependence on lock laser power was not as strong, and we could explain it with suppression of cavity vibrations (cf. figure 6.13b). Therefore, we suspect a different mechanism causing the drop in coherence.

Since we know that the absorption of intra-cavity laser light leads to a local temperature increase and thus the photo-thermal effect, we speculate that such temperature increase, induced by the lock laser, induces decoherence. To test this hypothesis, we first confirm that heating by lock laser irradiation increases not only the temperature of the mirrors, but also of the crystal.

To this end, we scan the ensemble absorption lines of both spin-preserving transitions, similar to figure 6.17. The relative height of the two absorption lines reflects their difference in ground state population and is given by the Boltzmann factor $\exp(-\Delta E/k_B T) = 6\%$, where the ground state splitting $\Delta E = \mu_B g_g B \approx h \cdot 112$ GHz can be calculated from the magnetic field $B = 0.8$ T and the effective ground state g-factor $g_g = 10$. Without lock laser irradiation, we measure a Boltzmann factor of 6%, corresponding to 1.91 K and in agreement with the cryostat temperature monitor. When we repeat the scan with a lock laser power of $3\,\mu$W, however, the Boltzmann factor increases to 10%, corresponding to a temperature of 2.33 K.

We have thus confirmed that the crystal temperature increases with lock laser power. In the second step, we turn the lock laser off again and measure the coherence time while we scan the cryostat temperature (see figure 6.20b). Again we observe a linear increase of the coherence decay rate with higher temperature, similar to the lock laser power scan. Importantly, we find about the same coherence decay rate at a temperature of 2.33 K without photo-thermal feedback as for 1.8 K with a lock laser power of $3\,\mu$W, matching our measurements of the Boltzmann factors.

It becomes clear that a low crystal temperature is key to long coherence times. Even without photo-thermal feedback, our experiments were still limited by the temperature control and stability of our cryostat, with a lowest possible temperature of 1.7 K. By extrapolating
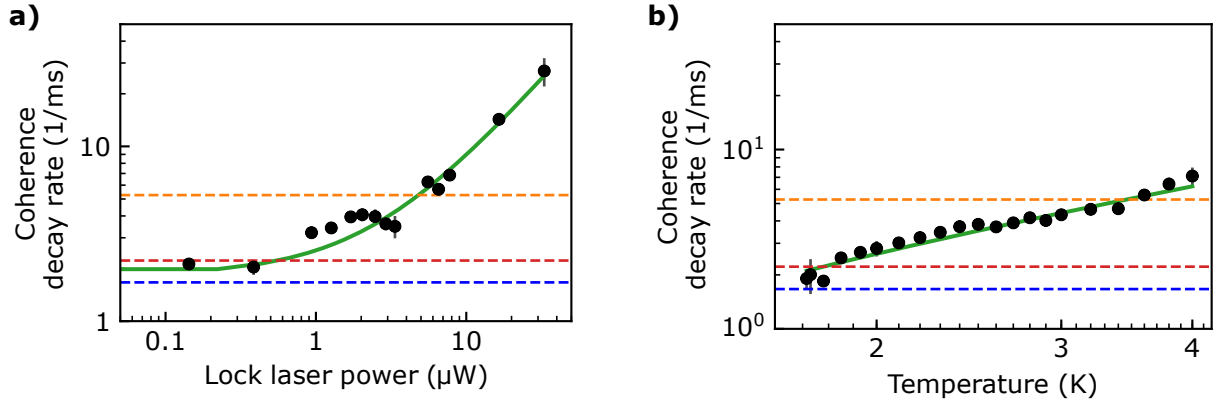
Figure 6.20: **Dependence of the coherence decay rate on lock laser power (a) and temperature (b).** In measurements at 1.8 K, the coherence decay rate (black circles) increases with lock laser power (a). Similarly, the coherence decay rate increases linearly with crystal temperature when no photo-thermal feedback is applied (b). Linear fits are shown as green curves, and the dashed lines indicate the population decay rate of maximally coupled ions in orange, as well as the ensemble-averaged fast fluorescence decay times at 1.8 K with and without photo-thermal stabilization in red and blue, respectively, corresponding to the curves in figure 6.13a.

the linear trend of the decoherence rate, we estimate that a temperature of about 1.5 K would be required in order to achieve coherence time of about 1 ms, which would be the lifetime limit $T_2 = 2 T_1$ for the ensemble-averaged fast fluorescence decay time of about $T_1 = 0.5$ ms (blue dashed curve in fig. 6.20b).

The exact origin of the decoherence process is not clear: a strong temperature dependence typically indicates spin-lattice relaxation processes (see section 4.4). However, we did not observe a significant change in fluorescence decay rate, and the expected ground-state spin-lattice relaxation rate is only ~ 20 Hz. Therefore, it is likely not the resonant erbium dopants interacting with phonons but rather other crystal constituents or defects in their local environments. For example, a linear increase in homogeneous linewidth with temperature is common in disordered systems like glassy host materials, in which defect states modeled as two-level systems couple to phonons [Schmidt1993] and linewidth and temperature dependence can differ between differently grown samples [Flinn1994, Macfarlane2004].

Usually, such processes cause spectral diffusion (see section 4.2), which would be seen as deviation from an exponential photon echo decay closer to a Gaussian decay curve [Böttger2006b, Mims1968]. In the above two-pulse photon echo measurements, we did not observe any signature of spectral diffusion. A possible explanation could be that the diffusion process induces only very small shifts in frequency but happens on a very fast time scale, so that photon echo measurements only see the time-averaged spectral linewidth.

6.4.2 Three-pulse photon echo measurements

To further testify the negligible impact of spectral diffusion on the measured coherence times, we employ stimulated photon echo experiments, consisting of three $\pi/2$ pulses. The first one prepares a superposition state that quickly dephases, similar to the two-pulse echo experiments. After a time $t/2$, the second $\pi/2$ pulse maps the superposition onto the population in ground and excited state, where it is not subject to decoherence anymore. After a waiting time T_w, the third pulse restores the superposition and leads to rephasing and subsequent echo emission after a last free-evolution period of length $t/2$.

Perfect refocusing requires the transition frequencies of all individual ions in the first and last free-evolution period to be equal, which requires that the inhomogeneous linewidth has not changed. The additional waiting time in the qubit eigenstates makes it possible to compare the inhomogeneous linewidths before and after, separated by a time interval not limited by the coherence time. Consequently, any spectral diffusion during the waiting period would increase the apparent decay rate measured over the time t spent in the superposition state.

In general, the echo area for a waiting time T_w spent in the qubit eigenstates and a time t spent in the superposition state decays as follows: [Böttger2006b]

$$A(t, T_w) = A_0 \, \exp\left(-\frac{2T_w}{T_1}\right) \exp\left(-2t \, \pi \Gamma_{\text{eff}}(t, T_w)\right) \tag{6.51}$$

Here, T_1 is the lifetime of the excited state, and Γ_{eff} the effective linewidth. In absence of spectral diffusion, it approaches the homogeneous linewidth, $\Gamma_{\text{eff}} \to \Gamma_{\text{hom}} = 1/(\pi T_2)$, with the coherence time T_2, and in the limit $T_w = 0$ we retrieve the single-exponential decay behavior of a two-pulse echo (eq. 6.50).

Spectral diffusion, however, will lead to an increase of the effective linewidth over time, typically modeled as [Böttger2006b, Thiel2010]

$$\Gamma_{\text{eff}}(t, T_w) = \frac{1}{\pi T_2} + \frac{\Gamma_{\text{SD}}}{2} \left[\frac{Rt}{2} + \left(1 - \exp(-RT_w)\right)\right] \tag{6.52}$$

Here, Γ_{SD} is the spectral width of the diffusion process, and R is the characteristic rate at which it takes place.

In our experiments the shapes of the decay curves do not change with the waiting time and can be fit with exponential functions. Their characteristic decay time, and thus the effective linewidth, stays constant for waiting times up to $200\,\mu\text{s}$ (see figure 6.21), which means we observe no spectral diffusion within the lifetime of the strongest-coupled ions.

Coherence time at high magnetic field

In order to learn more about the microscopic origin of the process that limits the ensemble-averaged coherence time, we also made measurements at higher magnetic fields. Unfortunately, with increasing magnetic field we also observed a worsening of the cavity vibrations and the cryostat temperature stability, which required the heavy use of photo-thermal feedback for active stabilization of the cavity resonance.

In this configuration, we measured a coherence time of about $150\,\mu\text{s}$, which stayed roughly constant over the whole range of magnetic fields up to $6\,\text{T}$. There, we performed another three-pulse echo experiment and again observed no change of the effective linewidth with the waiting time T_w (red circles in figure 6.21b).
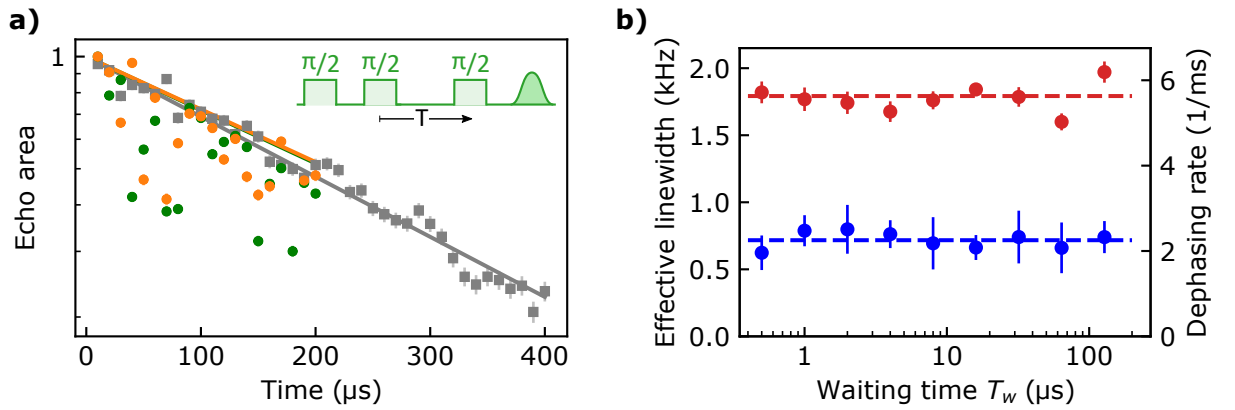
Figure 6.21: **a) Photon echo decay.** In two-pulse photon echo measurements, the echo area decays exponentially (grey data and fit), indicating no spectral diffusion. This is confirmed by three-pulse echo measurements with waiting periods of $T_w = 4\,\mu s$ (green) and $T_w = 128$ (orange) that follow the same envelope curve (exponential fits as solid lines), independent of the waiting period. The apparent modulation in the three-pulse echo is rather indication of coherent interference than presence of diffusive spectral wandering. It was not present in two-pulse echo measurements and could not be reproduced at 6 T, its likely origin could have been light-shift modulation due to insufficiently stabilized laser frequency fluctuations [Chanelière2015]. **b) Effective linewidth.** From the coherence decay rate in three-pulse echo experiments, we can extract the effective linewidth according to eq. 6.51 for measurements at 0.8 T and no lock laser irradiation (blue data and average value) as well as at 6 T and photo-thermal feedback (red data and average value). It stays constant up to waiting times of 0.2 ms, indicating the absence of spectral diffusion during the lifetime of maximally coupled ions.

6.4.3 Photon echo modulation by yttrium spins

In chapter 4.3.3 we had seen that optical excitation can drive not only the spin-preserving transition of erbium but also nuclear spin-flip transitions of superhyperfine-coupled yttrium ions. If the splitting between the superhyperfine states is smaller than the excitation pulse bandwidth and the branching contrast between both optical transitions is high enough, a beating between the two frequencies can be observed as modulation of the photon echo decay.

The measurements at 800 mT were not affected because the magnetic field at each yttrium site was dominated by the external field, and the change caused by excitation of the erbium spins was too small to stimulate nuclear spin-flips. In this section, we apply a field of 350 mT along the D_2-axis and see a clear signature of superhyperfine coupling in the photon echo decay. We show by numerical calculations that in fact a single yttrium site coupled to each erbium ion causes the observed echo modulation.

Photon echo measurements at 350 mT

Figure 6.22 presents the photon echo area as function of the sequence length (from the first $\pi/2$ pulse until the echo detection) for both initial electron spin states, $|\!\uparrow\rangle_g$ and $|\!\downarrow\rangle_g$. While the echo decay for the low-energy spin state $|\!\downarrow\rangle_g$ is exponential with a time constant of $134(2)\,\mu s$, we observe a modulated decay for the high-energy spin state $|\!\uparrow\rangle_g$, with a complete suppression of the echo emission for certain sequence lengths, e.g. at $15\,\mu s$ and $69\,\mu s$.

For given superhyperfine frequency splittings $\Delta\nu_g$ and $\Delta\nu_e$ in ground and excited state, respectively, the decay function of the echo area $A(t)$ can be calculated as follows: [Car2020, Guillot-Noël2007]

$$A(t) = \exp\left(-\frac{2t}{T_2}\right)\left[1 - \frac{\varrho}{2}\big(1 - \cos(2\pi\Delta\nu_g t/2)\big)\big(1 - \cos(2\pi\Delta\nu_e t/2)\big)\right]^2 \qquad (6.53)$$

Here, ϱ is the branching contrast of the yttrium superhyperfine transitions, as defined in chapter 4.3.3. If multiple yttrium spins couple to the same erbium ion, the modulation term in square brackets is replaced by a product over the modulation terms for individual coupling partners [Mims1972].
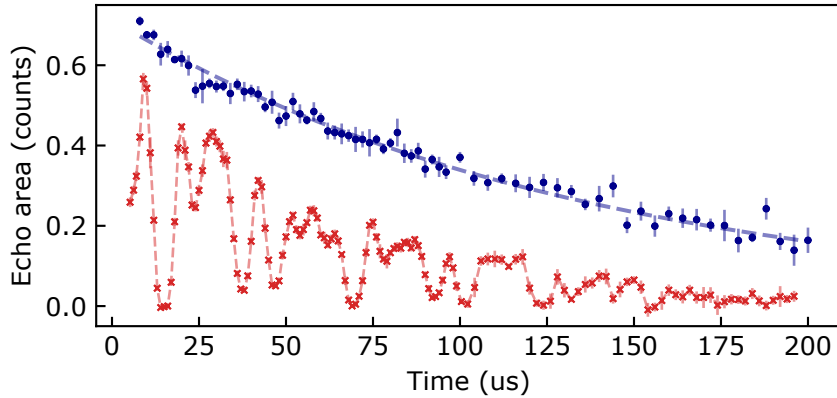
Figure 6.22: **Photon echo modulation by superhyperfine coupling to yttrium nuclear spins.** At a magnetic field of 350 mT along D_2, the photon echo on the high-frequency spin-preserving transition, starting from $|\!\downarrow\rangle_g$, decays exponentially (blue data and fit), while the echo on the low-frequency transition, starting from $|\!\uparrow\rangle_g$, is strongly modulated due to interaction with yttrium spins (red data points, connected for better visibility). Moderate photo-thermal feedback was applied to stabilize the cavity resonance.

Predicted superhyperfine coupling

In figure 6.23a, we plot the branching contrast for the 15 nearest neighbors of an erbium site-1-dopant in the current magnetic field orientation ($\vec{B} \parallel D_2$). Remarkably, we find that only a single yttrium site contributes to superhyperfine branching of the optical transition, which is the nearest neighbor yttrium ion. With eq. 6.53, we can calculate the predicted echo modulation for this yttrium site. By fine-tuning of the assumed magnetic field orientation to $\varphi = 89.5°$ and $\vartheta = 90.7°$, we find good agreement between the prediction and the measurements (fig. 6.23b). In particular, we can reproduce the total suppression of echo emission at 15 µs and 69 µs and the partial suppression at 38 µs and 47 µs. At this magnetic field orientation ($\vartheta \neq 90°$), the crystallographic classes I and II are no longer equivalent and have different superhyperfine coupling, which is accounted for by taking the average of both individual modulation curves.

Still, there are a few differences between theory curve and experiment: at sequence lengths of 24 µs and 54 µs, for example, the observed reduction in echo area does not match quantitatively with the model. While the inclusion of other yttrium sites does not improve the fit quality because their branching contrasts are too low, there is the possibility that strain in the crystal modifies the relative positions of yttrium sites from the erbium ion and thus changes the photon echo modulation. We can exclude inhomogeneities in strain or magnetic field, as the resulting broadband distribution of modulation frequencies would result in a faster envelope decay but not in a distinct modulation pattern. This is in agreement with the observation of a rather narrow ensemble absorption line but a frequency shift with respect to bulk crystal emission (cf. section 6.3.3).
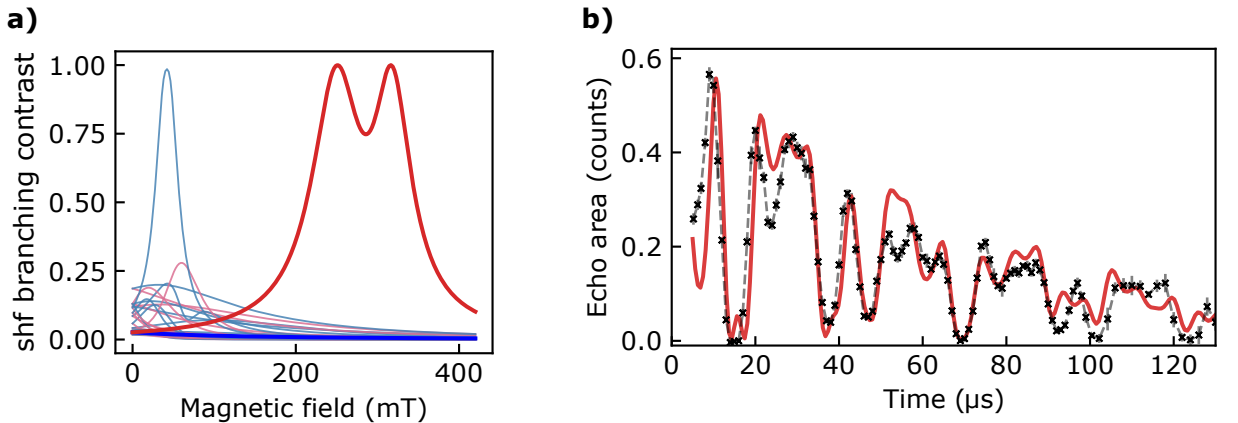

Figure 6.23: **a) Superhyperfine branching contrast.** From the erbium magetic moment and the relative position of an yttrium spin in the crystal, we calculate the superhyperfine branching contrast for each of the 15 closest Y-neighbors (light color). For the high-frequency transition (blue), starting from the $|\downarrow\rangle_g$ ground state, no significant superhyperfine branching occurs at fields > 200 mT, but when we excite the $|\uparrow\rangle_g$ ground state (red), the nearest neighbor couples strongly (highlighted in full color). **b) Echo area modulation.** At a field of 350 mT, the photon echo modulation as calculated from eq. 6.53 for superhyperfine coupling of the $|\uparrow\rangle_g$ spin-preserving transition to a single yttrium site (red line) can explain most features of the measured data (black data points, connected by a dashed line).

Potential for quantum information processing

The high modulation depth of the measured photon echo decay can only be explained by fully coherent interactions. As such, they are not an artifact of ensemble spectroscopy but would also be present in single interacting spin pairs of erbium and yttrium. In this case, an excited dopant could decay via two paths with equal probability into its ground state: either accompanied by a superhyperfine spin flip or not. The emission of a photon is thus entangled with a particular yttrium nuclear spin state. Combined with the expected long coherence times of nuclear spins, single yttrium atoms interfaced optically via erbium dopants have the potential for generation of spin-photon entanglement and long-term storage of quantum bits. [Kornher2020, Zhong2019a, Gao2015].

While addressing yttrium spins optically by their coupling to erbium ions is an attractive prospect, the inhomogeneous broadening of optical transitions precludes its implementation in ensembles of erbium dopants or renders it inefficient.

6.5 Towards spectroscopy and control of single dopants

In the previous sections we demonstrated the coherent and Purcell-enhanced emission of photons from an ensemble of erbium dopants. For applications in quantum information processing, however, the coherent control of single emitters is highly desired [Reiserer2015].

Here, we show the full potential of cavity-enhanced spectroscopy by resolving spectral lines of single or few emitters. To this end, we detune the cavity and the excitation laser by about 6.5 GHz from the absorption line center, where the spectral density of dopants is reduced by several orders of magnitude. In each measurement, we excite the dopants by a narrow-band laser pulse and collect their emission within a 0.3 ms time window to maximize the signal-to-noise ratio.

When we scan the excitation frequency, we observe several lines, which we attribute to single or few emitters (figure 6.24a). Their widths of a few 100 kHz are increased due to spectral diffusion over the total experiment duration of about 1 hour per scan. In these first measurements, the exact line positions differ slightly from scan to scan, and they seem to follow a very slow drift of roughly 1 MHz/hour. Later we find out that air slowly diffuses out of the compressed-air dampers, which slightly shifts the cavity position inside the cryostat and thus the magnetic field at the sample.

In order to confirm that these spectral lines belong to single or few emitters, we analyze the autocorrelation of the detected photons (fig. 6.24b). For these measurements, we sweep the laser frequency in each pulse by 0.5 MHz to ensure excitation of the spectral line despite its slow drift. We suppress the dark count rate to 2 Hz at the price of a reduced detection efficiency, leading to a total detection rate of 22 Hz. After correcting for the resulting reduction in contrast due to accidental coincidences (eq. 6.49), we find $g^{(2)}(0) = 0.40(7)$. This value is lower than the theoretical minimum value of 0.5 for the fluorescence from two emitters, but still far from the absolute minimum value of 0 for the signal from a single emitter. A possible reason could be the contribution of a second dopant or several others with weaker coupling to the cavity.

For the next experiments, we deflate the compressed-air dampers and optimize the cavity stability as well as the detection efficiency again. By increasing the magnetic field to 2 T and the detuning from the ensemble center to ~ 16 GHz, we reduce the spectral density of dopants further in order to achieve better separation of different emitters.

In a fluorescence scan, we find a pair of two narrow lines with widths of 0.20(2) MHz and 0.43(5) MHz (figure 6.25a). These linewidth already approach the inhomogeneous linewidth set by the superhyperfine coupling to the bath of yttrium nuclear spins of about 0.20(1) MHz (cf. section 4.2.4 and figure A.2b). The emission frequencies now stay stable over several hours (fig. 6.25b), confirming the mechanical drift as origin for the previously observed spectral wandering. Both emission lines decay with a lifetime of 0.25(4) ms (fig. 6.25c), corresponding to a Purcell factor of 45(7).

Our measurements demonstrate that cavity-enhanced spectroscopy of dilute rare-earth ensembles can resolve narrow spectral lines of few dopants and that single-emitter experiments are within reach. The observed optical linewidths can be as narrow as 0.20(2) MHz, only limited by the nuclear spin bath. This is in stark contrast to experiments with nano-photonic cavities, in which an inhomogeneous broadening of the emission lines up to ~ 10 MHz was observed [Dibos2018]. Even narrower lines could possibly be observed in host materials with no nuclear spins, like silicon [Weiss2021] or TiO_2 [Phenicie2019].
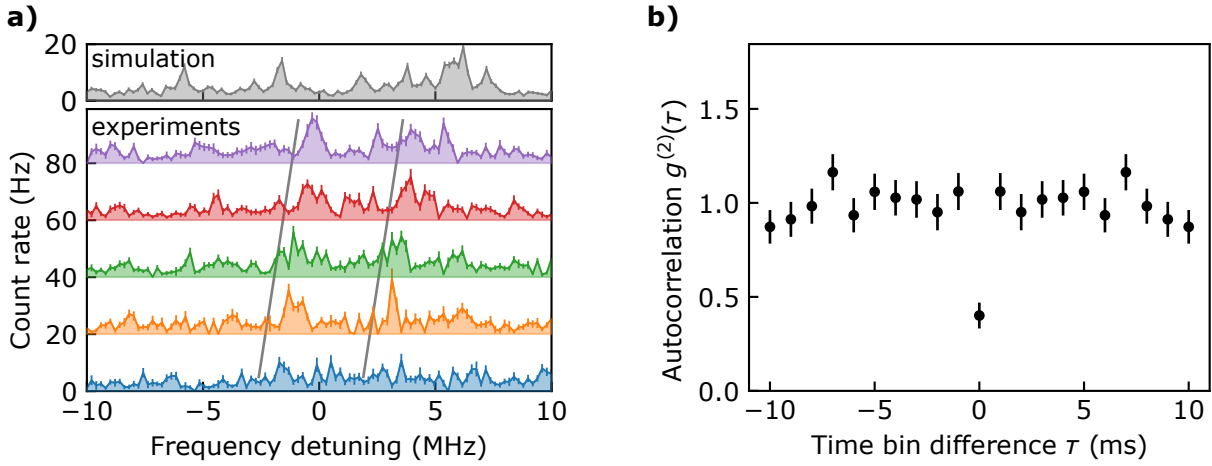
Figure 6.24: **a) Fluorescence measurement (bottom panel) and Monte Carlo simulation (top) of few dopants.** At a detuning of $\sim 6.5\,\text{GHz}$ from the center of the ensemble absorption line, we observe narrow fluorescence lines, which are reproducible in repeated scans over several hours (differently colored rows). We also observe a slow drift of the emission lines, which was later identified as shift of the sample position in the magnetic field of the cryostat due to diffusion of air out of the compressed-air dampers. These experiments were made after a re-assembly of the cavity, with a different polarization $\vec{E} \parallel D_2$ but a similar Purcell factor of ~ 60, and with a magnetic field of $0.95\,\text{T}$ applied along the b-axis. The observed fluorescence pattern is consistent with a Monte Carlo simulation for our cavity parameters (top row). **b) Autocorrelation measurement.** To measure the fluorescence autocorrelation despite the drift, we sweep the excitation pulse over $0.5\,\text{MHz}$ and obtain an antibunching dip of $g^{(2)}(0) = 0.40(7)$ after correcting for dark counts (cf. eq. 6.49). A value < 0.5 indicates that most detected photons originate from a single quantum emitter.
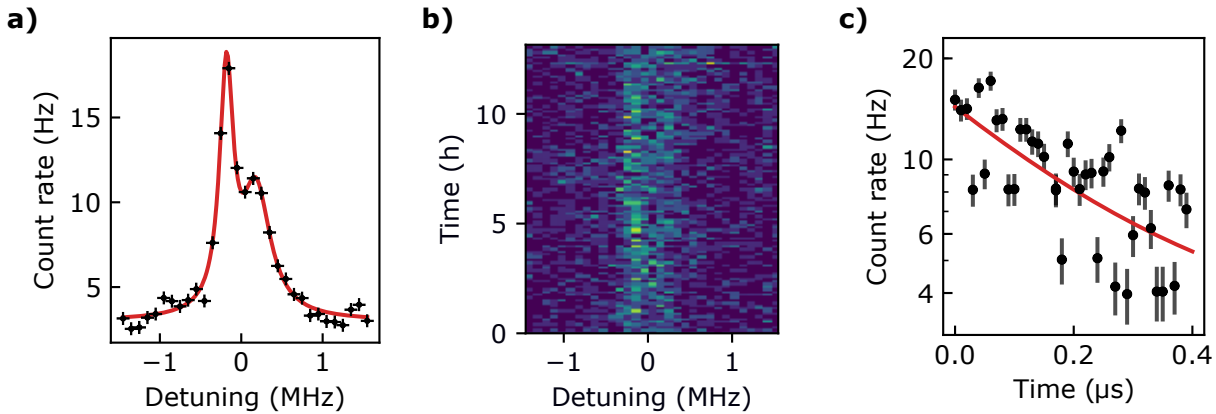
Figure 6.25: **a) Fluorescence scan.** After stabilizing the cavity at $2\,\text{T}$ and increasing the detuning from the ensemble center to $16\,\text{GHz}$, we observe narrow fluorescence lines on a vanishing background, here fitted with two Lorentzians. Their widths can be as narrow as $0.20(2)\,\text{MHz}$ (left peak), which precisely matches the expected diffusion width due to coupling to the nuclear spin bath of $0.20(1)\,\text{MHz}$ (cf. section 4.2.4). **b) Long-term stability.** With improved position stability of the cavity inside the cryostat, we can suppress the slow drift of the emission frequency that we had seen in fig. 6.24. Each row is a fluorescence scan as in panel (a). **c) Fluorescence decay.** By measuring the fluorescence decay over time, we find an emitter lifetime of $0.25(4)\,\text{ms}$ (exponential fit), corresponding to a Purcell factor of $45(7)$.

7 Summary and outlook

In this work, we have investigated erbium dopants in YSO as a promising platform for future applications in distributed quantum information processing. In particular, we discussed the role of dipolar interactions among erbium dopants and their superhyperfine coupling to yttrium nuclear spins in the context of holeburning spectroscopy as well as their implication for the coherent control of erbium spins.

After presenting two schemes for optical spin initialization and readout, we studied the spin coherence in the densely populated ground level and the selectively initialized excited level, which allowed us to distinguish interactions with resonant spins from coupling to an off-resonant spin bath. Supported by theoretical modeling, we demonstrated that effective dynamical decoupling from off-resonant spins in the excited state is possible, while the ground-state spin coherence is limited by instantaneous spectral diffusion.

Although dipolar coupling in ensembles of interacting spins is a common phenomenon, previous studies have focused on isotropic systems. In contrast, in this work we presented a comprehensive analytical approach to describe magnetic interactions in the Zeeman eigenbasis, which enabled us to construct the average Hamiltonian for an optimum decoupling sequence. As important result, we derived that in systems with highly prolate g-tensors (like Er:YSO) conventional decoupling sequences are not effective, and even optimized, asymmetric sequences can not completely counteract instantaneous diffusion. This limitation is even more severe in systems with highly oblate g-tensors (like Er:CaWO$_4$), where asymmetric sequences provide no improvement as compared to conventional decoupling sequences. While our analysis was based on the effective spin-1/2 level structure as found in Er:YSO, it is not restricted to this particular material system and can be applied to many other combinations of dopants and hosts [Venet2019, Tiranov2018, Bertaina2007, Thiel2012b] and even to quantum dots [vanBree2016].

Since interactions in dense ensembles of erbium dopants set an ultimate limit to the achievable electron spin coherence time, alternative systems need to be advanced: either nuclear spins that are effectively not susceptible to instantaneous diffusion, or extremely dilute ensembles that require optical resonators for efficient readout and control.

In this work, we built a Fabry-Perot cavity to study a nominally undoped YSO crystal. By combining good passive vibration isolation with active feedback, we achieved a relative stability of $\sim 1 \cdot 10^{-8}$ at cryogenic temperature, which is about two orders of magnitude better than previously reported for cryogenic Fabry-Perot fiber cavities [Salz2020].

In ensemble measurements we observed a lifetime reduction from a bulk value of 11.4 ms [Böttger2006a] to 0.45 ms, while maintaining a good optical coherence time of up to 0.54 ms. The observed multi-exponential fluorescence curve shape and time constant is in excellent agreement with a theoretical modeling based on independently measured parameters. For optimally coupled emitters, this model predicts a 530(50)-fold enhancement of the telecom transition at 1536 nm, resulting in a lifetime reduction factor of 59(6). This value is comparable to the Purcell factor realized in nanophotonic resonators, despite the vastly different mode volumes [Miyazono2016].

In the end, we demonstrate the capability to resolve single ions in the tail of the ensemble distribution, where the spectral density is lower. So far, the number of resolvable ions is small because only a small fraction of all dopants is located at an antinode of the cavity mode and exhibits sufficiently strong Purcell enhancement. At the same time, a large number of those strongly coupled dopants can not be addressed individually because their emission

frequencies are too close, within the inhomogeneous linewidth. In future experiments, the inhomogeneity and thus the number of individually addressable ions could potentially be increased by strain engineering. For example, other rare-earth impurities like europium or scandium are known to induce strain that shifts the optical transition frequencies of erbium dopants [Welinski2017, Thiel2012a]. Small amounts of these and other rare earths are expected to be found in undoped YSO, similar to erbium, but deliberate co-doping would also be possible. Such co-doping with other rare-earths also increases the inhomogeneous linewidth of the erbium spin transition [Welinski2017] and effectively lowers the concentration of resonant spins, which reduces the impact of instantaneous diffusion. Since the trivalent ions Sc^{3+} and Eu^{3+} have no electron magnetic moment, their proximity would cause only little perturbation to the erbium spins. At best, their nuclear spins could even be used as a resource, like a quantum register [KimiaeeAsadi2018]. Similarly, the nuclear spins of yttrium can provide a long-term quantum memory that can be interfaced via the optical transition of erbium. In particular, we observed coherent interaction with yttrium spins both in spectral holeburning experiments and as photon echo envelope modulation. Modeling such superhyperfine coupling showed good agreement with measurements and suggests that in certain magnetic field configurations only single yttrium sites couple efficiently to the optical transition of erbium spins.

As an alternative to the mentioned use of nuclear spins, crystals without rare-earth contamination could be employed, such as TiO_2 [Phenicie2019], $CaWO_4$ [Bertaina2007], or silicon [Weiss2021]. The latter has the additional advantage of established fabrication of thin membranes [McCann2001, Shchepetov2013], as well as ultrapure growth of even-isotopically purified and thus nuclear-spin free material [Chartrand2018, Itoh2014].

Our cryogenic Fabry-Perot cavity design will also work for other hosts of erbium dopants, such as silicon, but can also be adopted to study different emitters, like color centers in diamond or silicon carbide [Awschalom2018] or the recently discovered silicon defects at telecom wavelengths [Bergeron2020]. While the presented cavity design allows for frequency multiplexing and therefore is already useful for quantum information processing, there is still room for improvement: by using a thinner crystal membrane and reducing the width of the air gap, a smaller mode volume could be achieved, resulting in higher coupling strengths. Alternatively, this would allow for an increase in the cavity linewidth while maintaining the high Purcell factor, so that a larger bandwidth is available for frequency multiplexing. Furthermore, the effort of stabilizing the cavity is still quite high, and resonator designs with a better passive stability should be considered. For example, a fiber cavity aligned and stabilized in a glass ferrule has shown great intrinsic stability but has not yet been adapted to cryogenic environment [Saavedra2021, Gallego2016]. Such a design would not only allow for miniaturization of the setup but also greatly improve the scalability due to a completely fiber-coupled setup.

In the context of scalability and mass production, also silicon as host for erbium dopants and material with highly optimized fabrication techniques for nanophotonic structures should be considered [Yin2013]. Although the integration of erbium ions in silicon is not trivial because of the large size mismatch and the required charge compensation, we could measure narrow spectral lines in first experiments with resonant excitation [Weiss2021], which is promising for the integration into nanophotonic resonators.

A Appendix

A.1 Dipolar broadening

As can be seen in eq. 2.17, the dipole-dipole interaction shifts the energies of interacting spin pairs. To calculate the total energy shift for a single ion in an ensemble of many, we have to integrate over the entire crystal. The result will depend on the exact positions of dopants and their respective spin orientations, and averaging over all possible configurations leads to spectral broadening of the level energy.

In this section, we derive an analytical expression for the dipolar broadening. In contrast to derivations in [Mims1968, Baibekov2014, Maryasov1982] we use SI units where relevant and start with the most general form of the dipole-dipole interaction (cf. section 2.4.1):

$$\langle \uparrow\uparrow | \, \mathcal{H}_{\text{dd}} \, | \uparrow\uparrow \rangle = \frac{A \, \xi(\Omega)}{r^3} \tag{A.1}$$

Here, we separated the scaling with the distance between the interacting spins, r, and the dependence on the solid angle, Ω. A is the remaining prefactor.

For the coupling between two similar erbium dopants, for example, we find (see eq. 2.18)

$$A = \frac{\mu_0}{4\pi} \frac{h^2 \gamma_{\text{eff}}^2}{4} \quad , \qquad \xi(\Omega) = 1 - 3\cos^2\alpha, \tag{A.2}$$

where α is the angle between the precession axis of the magnetic moment and the vector that connects the spins. We note that the most general form in eq. A.1 also applies to the effective dipolar coupling Hamiltonian under the influence of dynamical decoupling, as discussed in section 5.2.3.

In the following, we consider an ensemble of N interaction partners at positions $\vec{r}_j$ relative to a central spin, whose transition broadening we analyze. To derive the distribution of the energy shifts, $I(\epsilon)$, we follow the approach in [Mims1968] and start by summing over all configurations $(\vec{r}_1, \ldots, \vec{r}_j, \ldots, \vec{r}_N)$, weighted with their probabilities $P_{\text{config}}^{(j)}$:

$$I(\epsilon) = \sum_{\text{configurations } (\vec{r}_j)} P_{\text{config}}^{(j)} \, \delta\left(\epsilon - \sum_j^N \frac{A\xi(\Omega)}{r_j^3}\right) \tag{A.3}$$

For low dopant concentrations, we can assume a continuous, uniform distribution of spin positions in the crystal, and the probability of an interaction partner to occupy the volume element $\mathrm{d}V_j$ is simply $P_{\text{config}}^{(j)} = \mathrm{d}V_j/V$. We also express the delta function by its Fourier transform and then recognize that the integrals over individual dopants are all the same:

$$I(\epsilon) = \int \cdots \int \prod_j^N \left(\frac{\mathrm{d}V_j}{V}\right) \frac{1}{2\pi} \int_{-\infty}^{+\infty} \mathrm{d}\rho \exp\left(-i\rho\epsilon + \sum_j^N i\rho\frac{A\xi(\Omega)}{r_j^3}\right) \tag{A.4}$$

$$= \frac{1}{2\pi} \int_{-\infty}^{+\infty} \mathrm{d}\rho \, e^{-i\rho\epsilon} \left[\frac{1}{V} \underbrace{\int \mathrm{d}V \exp\left(\rho\frac{A\xi(\Omega)}{r^3}\right)}_{V'}\right]^N \tag{A.5}$$

To study the limit $N \to \infty$ while keeping the dopant concentration $n = N/V$ constant, we rewrite

$$\left[\frac{V'}{V}\right]^N = \left[1 - \left(\frac{\tilde{V}}{V}\right)\right]^N = \left[1 - \left(\frac{n\tilde{V}}{N}\right)\right]^N \to \exp(-n\tilde{V}) \tag{A.6}$$

with

$$\tilde{V} = V - V' = \int_0^\infty dr\, r^2 \int d\Omega \left(1 - e^{i\rho A\xi(\Omega)/r^3}\right) = \frac{\pi}{6}|\rho|A \int d\Omega\, |\xi(\Omega)|. \tag{A.7}$$

After inserting eq. A.7 into eq. A.5, we recognize that the expression for $I(\epsilon)$ is the Fourier transform of a Lorentzian with a fwhm linewidth $\Delta\epsilon$:

$$I(\epsilon) = \frac{1}{2\pi} \int_{-\infty}^{+\infty} d\rho\, e^{-i\rho\epsilon}\, e^{-\Delta\epsilon|\rho|/2}, \tag{A.8}$$

with

$$\Delta\epsilon = \frac{2n\tilde{V}}{|\rho|} = \frac{\pi}{3}nA \int d\Omega\, |\xi(\Omega)| \tag{A.9}$$

After inserting the expression from eq. A.2, we can solve the integral over the solid angle and find the linewidth

$$\Delta\epsilon = \frac{\pi}{3}nA \int d\Omega\, |1 - 3\cos^2\alpha| = \frac{16\pi^2}{9\sqrt{3}}\, A\, n \tag{A.10}$$

$$= \frac{\pi}{9\sqrt{3}}\, \mu_0 h^2 \gamma_{\text{eff}}^2\, n \tag{A.11}$$

In our derivation, $\Delta\epsilon$ is the linewidth of the energy distribution of a single state and related to the fwhm linewidth of the ground level spin transition, $\Delta\nu$, by $h\Delta\nu = 2\Delta\epsilon$. The resulting dipolar transition linewidth is in agreement with derivations in [Mims1968, Baibekov2014, Maryasov1982] which were using cgs units and therefore differ by a factor $\mu_0/4\pi$:

$$h\Delta\nu = \frac{2\pi}{9\sqrt{3}}\, \mu_0 h^2 \gamma_{\text{eff}}^2\, n \tag{A.12}$$

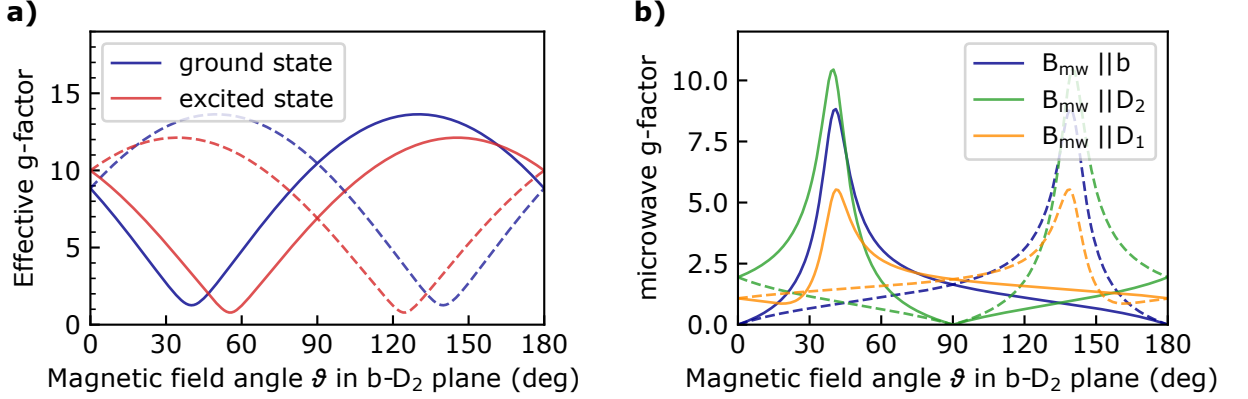# A.2 Plots for a magnetic field orientation in the b-D2 plane

a)

b)

Figure A.1: **a) Effective g-values for ground and excited state.** When the external magnetic field is varied in the b-D2 plane, the effective g-values for ground and excited state are different for magnetic class I (solid lines) and II (dashed), except for $\vartheta = 0°$ (along the b-axis) and $\vartheta = 90°$ (along the D_2-axis). [cf. figure 2.2b] **b) Ground state microwave g-factors.** The effective g-factor for microwave fields, $\sqrt{g_{mw,x}^2 + g_{mw,y}^2}$ as calculated with eq. 5.2, does not only depend on the orientation of the static magnetic field in the b-D2 plane, but also on the orientation of the microwave field, here shown for along b (blue), along D_2 (green) and along D_1 (yellow). Again, the values differ between magnetic class I (solid) and II (dashed). [cf. figure 5.1]

a)

b)
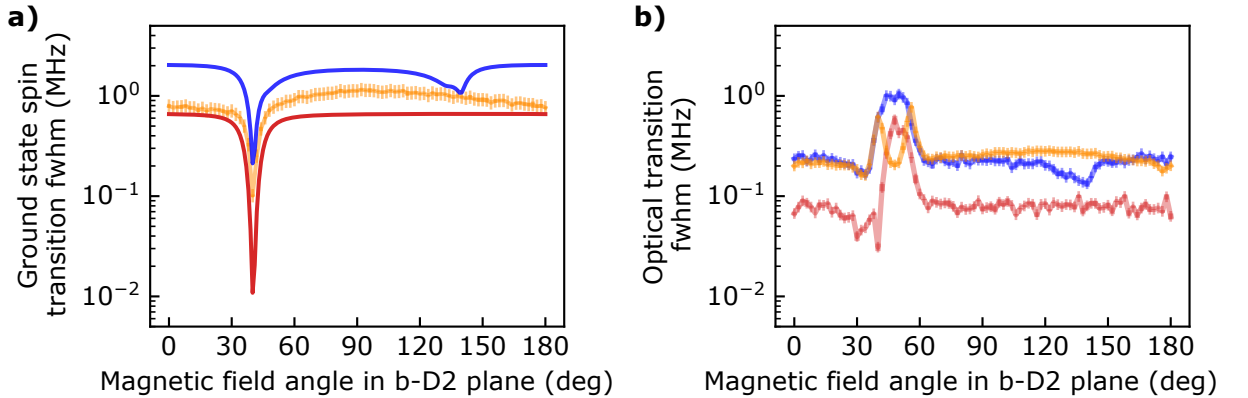
Figure A.2: **Spectral diffusion linewidth of the spin (a) and optical (b) transition.** Dipolar interactions with similar (red) and dissimilar (blue) spins as well as with yttrium nuclear spins (yellow) lead to a broadening of the erbium transitions (here shown for site 1, class I-dopants). The dipolar linewidth of the spin transition due to interaction erbium spins can be calculated analytically with eq. 4.3 and 4.4. All other curves are calculated in 2000 runs of a Monte Carlo simulation for 100 interacting erbium ions and the 550 closest yttrium sites. All calculations were performed for a total erbium concentration of 10 ppm, distributed equally on sites 1 and 2 and on magnetic classes I and II. [cf. figures 4.4 and 4.5]
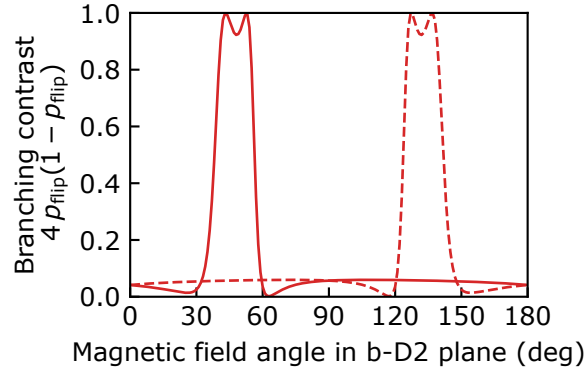
Figure A.3: **Branching contrast for the optical spin-flip transition.** At a magnetic field oriented along $\vartheta = 45°$ in the b-D2 plane, the optical spin-flip transition is favored for magnetic class I (solid) but not for class II (dashed). The branching contrast is calculated with eq. 4.6 and 4.7. [cf. figure 4.8]
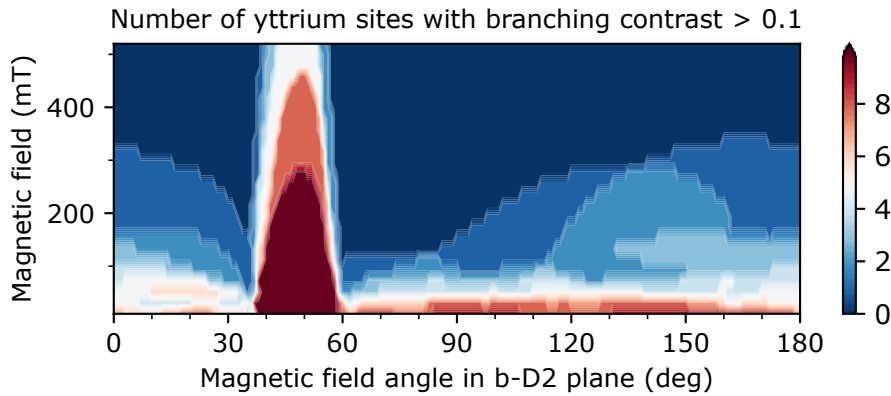
Figure A.4: **Number of yttrium sites with significant branching contrast of their optical superhyperfine transitions.** For a given external magnetic field orientation and amplitude, we calculate the superhyperfine branching contrast via eq. 4.14 for the 36 nearest yttrium neighbors. The plot assumes a class I erbium dopant; the results for the magnetic class II are related by mirror symmetry around $\vartheta = 90°$. [cf. figure 4.12a]

B Bibliography

[Abragam2012]   A. Abragam and B. Bleaney. *Electron Paramagnetic Resonance of Transition Ions*. Oxford Classic Texts in the Physical Sciences. Oxford University Press, Incorporated, 2012. ISBN: 9780191023002.

[Acosta2012]   V. M. Acosta, C. Santori, A. Faraon, Z. Huang, K.-M. C. Fu, A. Stacey, D. A. Simpson, K. Ganesan, S. Tomljenovic-Hanic, A. D. Greentree, S. Prawer, and R. G. Beausoleil. *Dynamic Stabilization of the Optical Resonances of Single Nitrogen-Vacancy Centers in Diamond*. Phys. Rev. Lett. **108**, 20 (2012).

[Acquaroli2018]   L. N. Acquaroli. *Matrix method for thin film optics*. 2018. arXiv:1809.07708.

[Afzelius2009]   M. Afzelius, C. Simon, H. de Riedmatten, and N. Gisin. *Multimode quantum memory based on atomic frequency combs*. Phys. Rev. A **79**, 5 (2009).

[Afzelius2010]   M. Afzelius, I. Usmani, A. Amari, B. Lauritzen, A. Walther, C. Simon, N. Sangouard, J. Minář, H. de Riedmatten, N. Gisin, and S. Kröll. *Demonstration of Atomic Frequency Comb Memory for Light with Spin-Wave Storage*. Phys. Rev. Lett. **104**, 4 (2010).

[Agnello2001]   S. Agnello, R. Boscaino, M. Cannas, and F. M. Gelardi. *Instantaneous diffusion effect on spin-echo decay: Experimental investigation by spectral selective excitation*. Phys. Rev. B **64**, 17 (2001).

[Agrawal2010]   G. Agrawal. *Fiber-Optic Communication Systems*. Wiley Series in Microwave and Optical Engineering. Wiley, 2010. ISBN: 9780470918517.

[Aharonovich2012]   I. Aharonovich, J. C. Lee, A. P. Magyar, B. B. Buckley, C. G. Yale, D. D. Awschalom, and E. L. Hu. *Homoepitaxial Growth of Single Crystal Diamond Membranes for Quantum Information Processing*. Advanced Materials **24**, 10 (2012).

[Ambrose1991]   W. P. Ambrose and W. E. Moerner. *Fluorescence spectroscopy and spectral diffusion of single impurity molecules in a crystal*. Nature **349**, 6306 (1991).

[Arcangeli2014]   A. Arcangeli, M. Lovrić, B. Tumino, A. Ferrier, and P. Goldner. *Spectroscopy and coherence lifetime extension of hyperfine transitions in $^{151}Eu^{3+}$:Y_2SiO_5*. Phys. Rev. B **89**, 18 (2014).

[Arcizet2009]   O. Arcizet, R. Rivière, A. Schliesser, G. Anetsberger, and T. J. Kippenberg. *Cryogenic properties of optomechanical silica microcavities*. Phys. Rev. A **80**, 2 (2009).

[Askarani2019]   M. F. Askarani, M. G. Puigibert, T. Lutz, V. B. Verma, M. D. Shaw, S. W. Nam, N. Sinclair, D. Oblak, and W. Tittel. *Storage and Reemission of Heralded Telecommunication-Wavelength Photons Using a Crystal Waveguide*. Phys. Rev. Applied **11**, 5 (2019).

[Åström2010]   K. Åström and R. Murray. *Feedback Systems: An Introduction for Scientists and Engineers*. Princeton University Press, 2010. ISBN: 9781400828739.

[Atatüre2018]   M. Atatüre, D. Englund, N. Vamivakas, S.-Y. Lee, and J. Wrachtrup. *Material platforms for spin-based photonic quantum technologies*. Nature Reviews Materials **3**, 5 (2018).

[Awschalom2018]   D. D. Awschalom, R. Hanson, J. Wrachtrup, and B. B. Zhou. *Quantum technologies with optically interfaced solid-state spins*. Nature Photonics **12**, 9 (2018).

[Baibekov2014] E. I. Baibekov, M. R. Gafurov, D. G. Zverev, I. N. Kurkin, B. Z. Malkin, and B. Barbara. *Coherent manipulation of dipolar coupled spins in an anisotropic environment.* Phys. Rev. B **90**, 17 (2014).

[Baldit2010] E. Baldit, K. Bencheikh, P. Monnier, S. Briaudeau, J. A. Levenson, V. Crozatier, I. Lorgeré, F. Bretenaker, J. L. Le Gouët, O. Guillot-Noël, and P. Goldner. *Identification of Λ-like systems in $Er^{3+}{:}Y_2SiO_5$ and observation of electromagnetically induced transparency.* Phys. Rev. B **81**, 14 (2010).

[Bar-Gill2012] N. Bar-Gill, L. M. Pham, C. Belthangady, D. Le Sage, P. Cappellaro, J. R. Maze, M. D. Lukin, A. Yacoby, and R. Walsworth. *Suppression of spin-bath dynamics for improved coherence of multi-spin-qubit systems.* Nature Communications **3**, 1 (2012).

[Baranov2017] D. G. Baranov, R. S. Savelev, S. V. Li, A. E. Krasnok, and A. Alù. *Modifying magnetic dipole spontaneous emission with nanophotonic structures.* Laser & Photonics Reviews **11**, 3 (2017).

[Bartholomew2017] J. G. Bartholomew, K. de Oliveira Lima, A. Ferrier, and P. Goldner. *Optical Line Width Broadening Mechanisms at the $10\,kHz$ Level in $Eu^{3+}{:}Y_2O_3$ Nanoparticles.* Nano Letters **17**, 2 (2017).

[Bartholomew2018] J. G. Bartholomew, T. Zhong, J. M. Kindem, R. Lopez-Rios, J. Rochman, I. Craiciu, E. Miyazono, and A. Faraon. *Controlling rare-earth ions in a nanophotonic resonator using the ac Stark shift.* Phys. Rev. A **97**, 6 (2018).

[Bartholomew2020] J. G. Bartholomew, J. Rochman, T. Xie, J. M. Kindem, A. Ruskuc, I. Craiciu, M. Lei, and A. Faraon. *On-chip coherent microwave-to-optical transduction mediated by ytterbium in YVO_4.* Nature Communications **11**, 1 (2020).

[Bauch2020] E. Bauch, S. Singh, J. Lee, C. A. Hart, J. M. Schloss, M. J. Turner, J. F. Barry, L. M. Pham, N. Bar-Gill, S. F. Yelin, and R. L. Walsworth. *Decoherence of ensembles of nitrogen-vacancy centers in diamond.* Phys. Rev. B **102**, 13 (2020).

[Baumann1996] I. Baumann, S. Bosso, R. Brinkmann, R. Corsini, M. Dinand, A. Greiner, K. Schafer, J. Sochtig, W. Sohler, H. Suche, and R. Wessel. *Er-doped integrated optical devices in $LiNbO_3$.* IEEE Journal of Selected Topics in Quantum Electronics **2**, 2 (1996).

[Bayat2014] K. Bayat, J. Choy, M. Farrokh Baroughi, S. Meesala, and M. Loncar. *Efficient, Uniform, and Large Area Microwave Magnetic Coupling to NV Centers in Diamond Using Double Split-Ring Resonators.* Nano Letters **14**, 3 (2014).

[Beach1990] R. Beach, M. D. Shinn, L. Davis, R. W. Solarz, and W. F. Krupke. *Optical absorption and stimulated emission of neodymium in yttrium orthosilicate.* IEEE Journal of Quantum Electronics **26**, 8 (1990).

[Becerro2004] A. Becerro and A. Escudero. *Revision of the crystallographic data of polymorphic $Y_2Si_2O_7$ and Y_2SiO_5 compounds.* Phase Transitions **77**, 12 (2004).

[Becher2001] C. Becher, A. Kiraz, P. Michler, A. Imamoğlu, W. V. Schoenfeld, P. M. Petroff, L. Zhang, and E. Hu. *Nonclassical radiation from a single self-assembled InAs quantum dot.* Phys. Rev. B **63**, 12 (2001).

[BenAttar2020] K. I. O. Ben 'Attar, D. Farfurnik, and N. Bar-Gill. *Hamiltonian engineering of general two-body spin-1/2 interactions.* Phys. Rev. Research **2**, 1 (2020).

[Benedikter2015] J. Benedikter, T. Hümmer, M. Mader, B. Schlederer, J. Reichel, T. W. Hänsch, and D. Hunger. *Transverse-mode coupling and diffraction loss in tunable Fabry–Pérot microcavities.* New Journal of Physics **17**, 5 (2015).

[Bergeron2020]   L. Bergeron, C. Chartrand, A. T. K. Kurkjian, K. J. Morse, H. Riemann, N. V. Abrosimov, P. Becker, H.-J. Pohl, M. L. W. Thewalt, and S. Simmons. *Silicon-Integrated Telecommunications Photon-Spin Interface.* PRX Quantum **1**, 2 (2020).

[Bertaina2007]   S. Bertaina, S. Gambarelli, A. Tkachuk, I. N. Kurkin, B. Malkin, A. Stepanov, and B. Barbara. *Rare-earth solid-state qubits.* Nature Nanotechnology **2**, 1 (2007).

[Biercuk2011]   M. J. Biercuk, A. C. Doherty, and H. Uys. *Dynamical decoupling sequence construction as a filter-design problem.* Journal of Physics B: Atomic, Molecular and Optical Physics **44**, 15 (2011).

[Black2001]   E. D. Black. *An introduction to Pound–Drever–Hall laser frequency stabilization.* American Journal of Physics **69**, 1 (2001).

[Bloch2012]   I. Bloch, J. Dalibard, and S. Nascimbène. *Quantum simulations with ultracold quantum gases.* Nature Physics **8**, 4 (2012).

[Bogdanović2017]   S. Bogdanović, S. B. van Dam, C. Bonato, L. C. Coenen, A.-M. J. Zwerver, B. Hensen, M. S. Z. Liddy, T. Fink, A. Reiserer, M. Lončar, and R. Hanson. *Design and low-temperature characterization of a tunable microcavity for diamond-based quantum networks.* Applied Physics Letters **110**, 17 (2017).

[Böttger2003]   T. Böttger, Y. Sun, C. W. Thiel, and R. L. Cone. *Material optimization of Er^{3+}:Y_2SiO_5 at 1.5 μm for optical processing, memory, and laser frequency stabilization applications.* Proc. SPIE **4988**, Advanced Optical Data Storage (2003).

[Böttger2006a]   T. Böttger, Y. Sun, C. W. Thiel, and R. L. Cone. *Spectroscopy and dynamics of Er^{3+}:Y_2SiO_5 at 1.5 μm.* Phys. Rev. B **74**, 7 (2006).

[Böttger2006b]   T. Böttger, C. W. Thiel, Y. Sun, and R. L. Cone. *Optical decoherence and spectral diffusion at 1.5 μm in Er^{3+}:Y_2SiO_5 versus magnetic field, temperature, and Er^{3+} concentration.* Phys. Rev. B **73**, 7 (2006).

[Böttger2008]   T. Böttger, C. W. Thiel, R. L. Cone, and Y. Sun. *Controlled compositional disorder in Er^{3+}:Y_2SiO_5 provides a wide-bandwidth spectral hole burning material at 1.5 μm.* Phys. Rev. B **77**, 15 (2008).

[Böttger2009]   T. Böttger, C. W. Thiel, R. L. Cone, and Y. Sun. *Effects of magnetic field orientation on optical decoherence in Er^{3+}:Y_2SiO_5.* Phys. Rev. B **79**, 11 (2009).

[Brachmann2016]   J. F. S. Brachmann, H. Kaupp, T. W. Hänsch, and D. Hunger. *Photothermal effects in ultra-precisely stabilized tunable microcavities.* Opt. Express **24**, 18 (2016).

[Bradley2019]   C. E. Bradley, J. Randall, M. H. Abobeih, R. C. Berrevoets, M. J. Degen, M. A. Bakker, M. Markham, D. J. Twitchen, and T. H. Taminiau. *A Ten-Qubit Solid-State Spin Register with Quantum Memory up to One Minute.* Phys. Rev. X **9**, 3 (2019).

[Briegel1998]   H.-J. Briegel, W. Dür, J. I. Cirac, and P. Zoller. *Quantum Repeaters: The Role of Imperfect Local Operations in Quantum Communication.* Phys. Rev. Lett. **81**, 26 (1998).

[Brinkmann2016]   A. Brinkmann. *Introduction to average Hamiltonian theory. I. Basics.* Concepts in Magnetic Resonance Part A **45A**, 6 (2016).

[Bruzewicz2019]   C. D. Bruzewicz, J. Chiaverini, R. McConnell, and J. M. Sage. *Trapped-ion quantum computing: Progress and challenges.* Applied Physics Reviews **6**, 2 (2019).

[Canuel2018]   B. Canuel et al. *Exploring gravity with the MIGA large scale atom interferometer.* Scientific Reports **8**, 1 (2018).

[Car2018]   B. Car, L. Veissier, A. Louchet-Chauvet, J.-L. Le Gouët, and T. Chanelière. *Selective Optical Addressing of Nuclear Spins through Superhyperfine Interaction in Rare-Earth Doped Solids.* Phys. Rev. Lett. **120**, 19 (2018).

[Car2019]   B. Car, L. Veissier, A. Louchet-Chauvet, J.-L. Le Gouët, and T. Chanelière. *Optical study of the anisotropic erbium spin flip-flop dynamics.* Phys. Rev. B **100**, 16 (2019).

[Car2020]   B. Car, J.-L. Le Gouët, and T. Chanelière. *Superhyperfine induced photon-echo collapse of erbium in Y_2SiO_5.* Phys. Rev. B **102**, 11 (2020).

[Casabone2020]   B. Casabone, C. Deshmukh, S. Liu, D. Serrano, A. Ferrier, T. Hümmer, P. Goldner, D. Hunger, and H. de Riedmatten. *Dynamic control of Purcell enhanced emission of erbium ions in nanoparticles.* 2020. arXiv:2001.08532.

[Chambers2000]   S. A. Chambers. *Epitaxial growth and properties of thin film oxides.* Surface Science Reports **39**, 5 (2000).

[Chambers2001]   J. Chambers, B. Busch, W. Schulte, T. Gustafsson, E. Garfunkel, S. Wang, D. Maher, T. Klein, and G. Parsons. *Effects of surface pretreatments on interface structure during formation of ultra-thin yttrium silicate dielectric films on silicon.* Applied Surface Science **181**, 1 (2001).

[Chanelière2015]   T. Chanelière and G. Hétet. *Light-shift-modulated photon-echo.* Opt. Lett. **40**, 7 (2015).

[Chartrand2018]   C. Chartrand, L. Bergeron, K. J. Morse, H. Riemann, N. V. Abrosimov, P. Becker, H.-J. Pohl, S. Simmons, and M. L. W. Thewalt. *Highly enriched ^{28}Si reveals remarkable optical linewidths and fine structure for well-known damage centers.* Phys. Rev. B **98**, 19 (2018).

[Chen2020]   S. Chen, M. Raha, C. M. Phenicie, S. Ourari, and J. D. Thompson. *Parallel single-shot measurement and coherent control of solid-state spins below the diffraction limit.* Science **370**, 6516 (2020).

[Childress2006]   L. Childress, M. V. Gurudev Dutt, J. M. Taylor, A. S. Zibrov, F. Jelezko, J. Wrachtrup, P. R. Hemmer, and M. D. Lukin. *Coherent Dynamics of Coupled Electron and Nuclear Spin Qubits in Diamond.* Science **314**, 5797 (2006).

[Choi2017]   S. Choi, N. Y. Yao, and M. D. Lukin. *Dynamical Engineering of Interactions in Qudit Ensembles.* Phys. Rev. Lett. **119**, 18 (2017).

[Choi2020]   J. Choi, H. Zhou, H. S. Knowles, R. Landig, S. Choi, and M. D. Lukin. *Robust Dynamic Hamiltonian Engineering of Many-Body Spin Systems.* Phys. Rev. X **10**, 3 (2020).

[Citron1977]   M. L. Citron, H. R. Gray, C. W. Gabel, and C. R. Stroud. *Experimental study of power broadening in a two-level atom.* Phys. Rev. A **16**, 4 (1977).

[Cook2015]   S. Cook, T. Rosenband, and D. R. Leibrandt. *Laser-Frequency Stabilization Based on Steady-State Spectral-Hole Burning in Eu3+Y2SiO5.* Phys. Rev. Lett. **114**, 25 (2015).

[Cruzeiro2017]   E. Z. Cruzeiro, A. Tiranov, I. Usmani, C. Laplane, J. Lavoie, A. Ferrier, P. Goldner, N. Gisin, and M. Afzelius. *Spectral hole lifetimes and spin population relaxation dynamics in neodymium-doped yttrium orthosilicate.* Phys. Rev. B **95**, 20 (2017).

[Degen2017]   C. L. Degen, F. Reinhard, and P. Cappellaro. *Quantum sensing.* Rev. Mod. Phys. **89**, 3 (2017).

[Derevianko2014] A. Derevianko and M. Pospelov. *Hunting for topological dark matter with atomic clocks.* Nat. Phys. **10**, 12 (2014).

[Dibos2018]   A. M. Dibos, M. Raha, C. M. Phenicie, and J. D. Thompson. *Atomic Source of Single Photons in the Telecom Band.* Phys. Rev. Lett. **120**, 24 (2018).

[DiVincenzo2000] D. P. DiVincenzo. *The Physical Implementation of Quantum Computation.* Fortschritte der Physik **48**, 9-11 (2000).

[Dodson2012]   C. M. Dodson and R. Zia. *Magnetic dipole and electric quadrupole transitions in the trivalent lanthanide series: Calculated emission rates and oscillator strengths.* Phys. Rev. B **86**, 12 (2012).

[Dong2015]   J. Dong, Y. Hu, J. Huang, M. Ye, Q. Qu, T. Li, and L. Liu. *Subhertz linewidth laser by locking to a fiber delay line.* Appl. Opt. **54**, 5 (2015).

[Dong2016]   J. Dong, J. Huang, T. Li, and L. Liu. *Observation of fundamental thermal noise in optical fibers down to infrasonic frequencies.* Appl. Phys. Lett. **108**, 2 (2016).

[Doualan1995]   J. L. Doualan, C. Labbe, P. L. Boulanger, J. Margerie, R. Moncorge, and H. Timonen. *Energy levels of the laser active Er^{3+} ion in each of the two crystallographic sites of yttrium orthosilicate.* Journal of Physics: Condensed Matter **7**, 26 (1995).

[Duan2010]   L. Z. Duan. *Intrinsic thermal noise of optical fibres due to mechanical dissipation.* Electronics Letters **46**, 22 (2010).

[Dutt2007]   M. V. G. Dutt, L. Childress, L. Jiang, E. Togan, J. Maze, F. Jelezko, A. S. Zibrov, P. R. Hemmer, and M. D. Lukin. *Quantum Register Based on Individual Electronic and Nuclear Spin Qubits in Diamond.* Science **316**, 5829 (2007).

[Edén2014]   M. Edén. *Zeeman truncation in NMR. I. The role of operator commutation.* Concepts in Magnetic Resonance Part A **43**, 4 (2014).

[Egan2015]   P. F. Egan, J. A. Stone, J. H. Hendricks, J. E. Ricker, G. E. Scace, and G. F. Strouse. *Performance of a dual Fabry-Perot cavity refractometer.* Opt. Lett. **40**, 17 (2015).

[Farfurnik2018]   D. Farfurnik, Y. Horowicz, and N. Bar-Gill. *Identifying and decoupling many-body interactions in spin ensembles in diamond.* Phys. Rev. A **98**, 3 (2018).

[Fernandez-Gonzalvo2015] X. Fernandez-Gonzalvo, Y.-H. Chen, C. Yin, S. Rogge, and J. J. Longdell. *Coherent frequency up-conversion of microwaves to the optical telecommunications band in an Er:YSO crystal.* Phys. Rev. A **92**, 6 (2015).

[Fleming2008]   A. J. Fleming. *Techniques and considerations for driving piezoelectric actuators at high speed.* Proc. SPIE **6926**, Modeling, Signal Processing, and Control for Smart Structures (2008).

[Flinn1994]   G. P. Flinn, K. W. Jang, J. Ganem, M. L. Jones, R. S. Meltzer, and R. M. Macfarlane. *Sample-dependent optical dephasing in bulk crystalline samples of Y_2O_3:Eu^{3+}.* Phys. Rev. B **49**, 9 (1994).

[Freeman1962]   A. J. Freeman and R. E. Watson. *Theoretical Investigation of Some Magnetic and Spectroscopic Properties of Rare-Earth Ions.* Phys. Rev. **127**, 6 (1962).

[Freeman1998]   R. Freeman. *Shaped radiofrequency pulses in high resolution NMR.* Progress in Nuclear Magnetic Resonance Spectroscopy **32**, 1 (1998).

[Frydrych2015] H. Frydrych. *Advanced dynamical decoupling strategies for simulating Hamiltonian interactions.* PhD thesis. Technische Universität Darmstadt, 2015. URL: https://tuprints.ulb.tu-darmstadt.de/5233/1/dissertation_frydrych_2016.pdf.

[Gallego2016] J. Gallego, S. Ghosh, S. K. Alavi, W. Alt, M. Martinez-Dorantes, D. Meschede, and L. Ratschbacher. *High-finesse fiber Fabry–Perot cavities: stabilization and mode matching analysis.* Applied Physics B **122**, 3 (2016).

[Gao2015] W. B. Gao, A. Imamoglu, H. Bernien, and R. Hanson. *Coherent manipulation, measurement and entanglement of individual solid-state spins using optical fields.* Nature Photonics **9**, 6 (2015).

[Genov2020] G. T. Genov, M. Hain, N. V. Vitanov, and T. Halfmann. *Universal composite pulses for efficient population inversion with an arbitrary excitation profile.* Phys. Rev. A **101**, 1 (2020).

[Ghelfi2014] P. Ghelfi, F. Laghezza, F. Scotti, G. Serafino, A. Capria, S. Pinna, D. Onori, C. Porzi, M. Scaffardi, A. Malacarne, V. Vercesi, E. Lazzeri, F. Berizzi, and A. Bogoni. *A fully photonics-based coherent radar system.* Nature **507**, 7492 (2014).

[Gisin2007] N. Gisin and R. Thew. *Quantum communication.* Nature Photonics **1**, 3 (2007).

[Gong2017] B. Gong, T. Tu, Z.-Q. Zhou, X.-Y. Zhu, C.-F. Li, and G.-C. Guo. *Environment spectrum and coherence behaviours in a rare-earth doped crystal for quantum memory.* Scientific Reports **7**, 1 (2017).

[Guenot2003] P. Guenot. *Material Aspects of Standard Transmission Optical Fibers.* MRS Bulletin **28**, 5 (2003).

[Guillot-Noël2007] O. Guillot-Noël, H. Vezin, P. Goldner, F. Beaudoux, J. Vincent, J. Lejay, and I. Lorgeré. *Direct observation of rare-earth-host interactions in Er:Y_2SiO_5.* Phys. Rev. B **76**, 18 (2007).

[Gullion1990] T. Gullion, D. B. Baker, and M. S. Conradi. *New, compensated Carr-Purcell sequences.* Journal of Magnetic Resonance (1969) **89**, 3 (1990).

[Haeberlen1968] U. Haeberlen and J. S. Waugh. *Coherent Averaging Effects in Magnetic Resonance.* Phys. Rev. **175**, 2 (1968).

[Hartmann1968] S. Hartmann. *Photon, spin, and Raman echoes.* IEEE Journal of Quantum Electronics **4**, 11 (1968).

[Harty2014] T. P. Harty, D. T. C. Allcock, C. J. Ballance, L. Guidoni, H. A. Janacek, N. M. Linke, D. N. Stacey, and D. M. Lucas. *High-Fidelity Preparation, Gates, Memory, and Readout of a Trapped-Ion Quantum Bit.* Phys. Rev. Lett. **113**, 22 (2014).

[Hastings-Simon2008] S. R. Hastings-Simon, B. Lauritzen, M. U. Staudt, J. L. M. van Mechelen, C. Simon, H. de Riedmatten, M. Afzelius, and N. Gisin. *Zeeman-level lifetimes in Er^{3+}:Y_2SiO_5.* Phys. Rev. B **78**, 8 (2008).

[Hennel2005] J. W. Hennel and J. Klinowski. *Magic-Angle Spinning: a Historical Perspective.* In: *New Techniques in Solid-State NMR.* Ed. by J. Klinowski. Springer Berlin Heidelberg, 2005, pp. 1–14. ISBN: 978-3-540-31473-8.

[Hogan2016] J. M. Hogan and M. A. Kasevich. *Atom-interferometric gravitational-wave detection using heterodyne laser links.* Phys. Rev. A **94**, 3 (2016).

[Horvath2019] S. P. Horvath, J. V. Rakonjac, Y.-H. Chen, J. J. Longdell, P. Goldner, J.-P. R. Wells, and M. F. Reid. *Extending Phenomenological Crystal-Field Methods to C_1 Point-Group Symmetry: Characterization of the Optically Excited Hyperfine Structure of $^{167}Er^{3+}$:Y_2SiO_5.* Phys. Rev. Lett. **123**, 5 (2019).

[Huang2019]   J. Huang, L. Wang, Y. Duan, Y. Huang, M. Ye, L. Liu, and T. Li. *Optical Fiber Spool with Ultralow Acceleration Sensitivity*. In: *2019 Joint Conference of EFTF/IFC*. 2019. DOI: 10.1109/FCS.2019.8856066.

[Hunger2012]   D. Hunger, C. Deutsch, R. J. Barbour, R. J. Warburton, and J. Reichel. *Laser micro-fabrication of concave, low-roughness features in silica*. AIP Advances **2**, 1 (2012).

[Itoh2014]   K. M. Itoh and H. Watanabe. *Isotope engineering of silicon and diamond for quantum computing and sensing applications*. MRS Communications **4**, 4 (2014).

[Jang1995]   K. W. Jang and R. S. Meltzer. *Homogeneous and inhomogeneous linewidths of Eu^{3+} in disordered crystalline systems*. Phys. Rev. B **52**, 9 (1995).

[Janitz2015]   E. Janitz, M. Ruf, M. Dimock, A. Bourassa, J. Sankey, and L. Childress. *Fabry-Perot microcavity for diamond-based photonics*. Phys. Rev. A **92**, 4 (2015).

[Jelezko2004]   F. Jelezko, T. Gaebel, I. Popa, M. Domhan, A. Gruber, and J. Wrachtrup. *Observation of Coherent Oscillation of a Single Nuclear Spin and Realization of a Two-Qubit Conditional Quantum Gate*. Phys. Rev. Lett. **93**, 13 (2004).

[Jensen2020]   R. H. Jensen, E. Janitz, Y. Fontana, Y. He, O. Gobron, I. P. Radko, M. Bhaskar, R. Evans, C. D. Rodríguez Rosenblueth, L. Childress, A. Huck, and U. Lund Andersen. *Cavity-Enhanced Photon Emission from a Single Germanium-Vacancy Center in a Diamond Membrane*. Phys. Rev. Applied **13**, 6 (2020).

[Karr2019]   J.-P. Karr and D. Marchand. *Progress on the proton-radius puzzle*. Nature **575**, 7781 (2019).

[Katsidis2002]   C. C. Katsidis and D. I. Siapkas. *General transfer-matrix method for optical multilayer systems with coherent, partially coherent, and incoherent interference*. Appl. Opt. **41**, 19 (2002).

[Kawakami2016]   E. Kawakami, T. Jullien, P. Scarlino, D. R. Ward, D. E. Savage, M. G. Lagally, V. V. Dobrovitski, M. Friesen, S. N. Coppersmith, M. A. Eriksson, and L. M. K. Vandersypen. *Gate fidelity and coherence of an electron spin in an Si/SiGe quantum dot with micromagnet*. Proceedings of the National Academy of Sciences **113**, 42 (2016).

[Kéfélian2009]   F. Kéfélian, H. Jiang, P. Lemonde, and G. Santarelli. *Ultralow-frequency-noise stabilization of a laser by locking to an optical fiber-delay line*. Optics Letters **34**, 7 (2009).

[Kessler2012]   T. Kessler, C. Hagemann, C. Grebing, T. Legero, U. Sterr, F. Riehle, M. J. Martin, L. Chen, and J. Ye. *A sub-40-mHz-linewidth laser based on a silicon single-crystal optical cavity*. Nature Photonics **6**, 10 (2012).

[KimiaeeAsadi2018]   F. Kimiaee Asadi, N. Lauk, S. Wein, N. Sinclair, C. O'Brien, and C. Simon. *Quantum repeaters with individual rare-earth ions at telecommunication wavelengths*. Quantum **2** (2018).

[Kindem2018]   J. M. Kindem, J. G. Bartholomew, P. J. T. Woodburn, T. Zhong, I. Craiciu, R. L. Cone, C. W. Thiel, and A. Faraon. *Characterization of $^{171}Yb^{3+}$:YVO_4 for photonic quantum technologies*. Phys. Rev. B **98**, 2 (2018).

[Kindem2020]   J. M. Kindem, A. Ruskuc, J. G. Bartholomew, J. Rochman, Y. Q. Huan, and A. Faraon. *Control and single-shot readout of an ion embedded in a nanophotonic cavity*. Nature **580**, 7802 (2020).

[Konthasinghe2017]   K. Konthasinghe, J. G. Velez, A. J. Hopkins, M. Peiris, L. T. M. Profeta, Y. Nieves, and A. Muller. *Self-sustained photothermal oscillations in high-finesse Fabry-Perot microcavities*. Phys. Rev. A **95**, 1 (2017).

[Kornher2020]   T. Kornher, D.-W. Xiao, K. Xia, F. Sardi, N. Zhao, R. Kolesov, and J. Wrachtrup. *Sensing Individual Nuclear Spins with a Single Rare-Earth Electron Spin*. Phys. Rev. Lett. **124**, 17 (2020).

[Krenn2016]   M. Krenn, M. Malik, T. Scheidl, R. Ursin, and A. Zeilinger. *Quantum Communication with Photons*. In: *Optics in Our Time*. Ed. by M. D. Al-Amri, M. El-Gomati, and M. S. Zubairy. Springer International Publishing, 2016, pp. 455–482. ISBN: 978-3-319-31903-2.

[Krohn2014]   D. A. Krohn, T. W. MacDougall, and A. Mendez. *Fiber Optic Sensors: Fundamentals and Applications*. SPIE, 2014. ISBN: 978-1-62841-180-5.

[Kuhlmann2013]   A. V. Kuhlmann, J. Houel, A. Ludwig, L. Greuter, D. Reuter, A. D. Wieck, M. Poggio, and R. J. Warburton. *Charge noise and spin noise in a semiconductor quantum device*. Nature Physics **9**, 9 (2013).

[Kuhn2010]   A. Kuhn and D. Ljunggren. *Cavity-based single-photon sources*. Contemporary Physics **51**, 4 (2010).

[Kunkel2016]   N. Kunkel, J. Bartholomew, L. Binet, A. Ikesue, and P. Goldner. *High-Resolution Optical Line Width Measurements as a Material Characterization Tool*. The Journal of Physical Chemistry C **120**, 25 (2016).

[Kurkin1980]   I. Kurkin and K. Chernov. *EPR and spin-lattice relaxation of rare-earth activated centres in Y_2SiO_5 single crystals*. Physica B+C **101**, 2 (1980).

[Lauritzen2008]   B. Lauritzen, S. R. Hastings-Simon, H. de Riedmatten, M. Afzelius, and N. Gisin. *State preparation by optical pumping in erbium-doped solids using stimulated emission and spin mixing*. Phys. Rev. A **78**, 4 (2008).

[Laws2002]   D. D. Laws, H.-M. L. Bitter, and A. Jerschow. *Solid-State NMR Spectroscopic Methods in Chemistry*. Angewandte Chemie International Edition **41**, 17 (2002).

[Leibrandt2011]   D. R. Leibrandt, M. J. Thorpe, M. Notcutt, R. E. Drullinger, T. Rosenband, and J. C. Bergquist. *Spherical reference cavities for frequency stabilization of lasers in non-laboratory environments*. Opt. Express **19**, 4 (2011).

[Leibrandt2015]   D. R. Leibrandt and J. Heidecker. *An open source digital servo for atomic, molecular, and optical physics experiments*. Review of Scientific Instruments **86**, 12 (2015).

[Li1992]   C. Li, C. Wyon, and R. Moncorge. *Spectroscopic properties and fluorescence dynamics of Er^{3+} and Yb^{3+} in Y_2SiO_5*. IEEE Journal of Quantum Electronics **28**, 4 (1992).

[Lim2017]   J. Lim, A. A. Savchenkov, E. Dale, W. Liang, D. Eliyahu, V. Ilchenko, A. B. Matsko, L. Maleki, and C. W. Wong. *Chasing the thermodynamical noise limit in whispering-gallery-mode resonators for ultrastable laser frequency stabilization*. Nature Communications **8**, 1 (2017).

[Lim2018]   H.-J. Lim, S. Welinski, A. Ferrier, P. Goldner, and J. J. L. Morton. *Coherent spin dynamics of ytterbium ions in yttrium orthosilicate*. Phys. Rev. B **97**, 6 (2018).

[Ludlow2015]   A. D. Ludlow, M. M. Boyd, J. Ye, E. Peik, and P. O. Schmidt. *Optical atomic clocks*. Rev. Mod. Phys. **87**, 2 (2015).

[Macfarlane1997]   R. M. Macfarlane, T. L. Harris, Y. Sun, R. L. Cone, and R. W. Equall. *Measurement of photon echoes in $Er:Y_2SiO_5$ at $1.5\,\mu m$ with a diode laser and an amplifier*. Opt. Lett. **22**, 12 (1997).

[Macfarlane1998]   R. M. Macfarlane, R. S. Meltzer, and B. Z. Malkin. *Optical measurement of the isotope shifts and hyperfine and superhyperfine interactions of Nd in the solid state.* Phys. Rev. B **58**, 9 (1998).

[Macfarlane2002]   R. M. Macfarlane. *High-resolution laser spectroscopy of rare-earth doped insulators: a personal perspective.* Journal of Luminescence **100**, 1 (2002).

[Macfarlane2004]   R. Macfarlane, Y. Sun, R. Cone, C. Thiel, and R. Equall. *Optical dephasing by disorder modes in yttrium orthosilicate (Y_2SiO_5) doped with Eu^{3+}.* Journal of Luminescence **107**, 1 (2004).

[Macfarlane2007]   R. M. Macfarlane. *Optical Stark spectroscopy of solids.* Journal of Luminescence **125**, 1 (2007).

[Maksimov1970]   B. A. Maksimov, V. V. Ilyukhin, Y. A. Kharitonov, and N. V. Belov. Kristallografiya **15**, 5 (1970).

[Maniloff1999]   E. S. Maniloff, A. E. Johnson, and T. W. Mossberg. *Spectral Data Storage Using Rare-Earth-Doped Crystals.* MRS Bulletin **24**, 9 (1999).

[Mansfield1971]   P. Mansfield. *Symmetrized pulse sequences in high resolution NMR in solids.* Journal of Physics C: Solid State Physics **4**, 11 (1971).

[Mansfield1981]   P. Mansfield and J. G. Powles. *Multiple-Pulse n.m.r. Experiments in Solids: An Introduction to Symmetrized Pulse Sequences [and Discussion].* Philosophical Transactions of the Royal Society of London. Series A, Mathematical and Physical Sciences **299**, 1452 (1981).

[Maryasov1982]   A. Maryasov, S. Dzuba, and K. Salikhov. *Spin-polarization effects on the phase relaxation induced by dipole-dipole interactions.* Journal of Magnetic Resonance (1969) **50**, 3 (1982).

[Maryasov2012]   A. G. Maryasov and M. K. Bowman. *Spin dynamics of paramagnetic centers with anisotropic g tensor and spin of 1/2.* Journal of Magnetic Resonance **221** (2012).

[Maryasov2013]   A. G. Maryasov and M. K. Bowman. *Bloch equations for anisotropic paramagnetic centers with spin of 1/2.* Journal of Magnetic Resonance **233** (2013).

[Maryasov2020]   A. G. Maryasov and M. K. Bowman. *Anisotropic S = 1/2 Kramers Doublets: g-Matrix, the Tensor G, and Dynamics of the Spin and Magnetic Moment.* Applied Magnetic Resonance **51**, 9 (2020).

[Matei2016]   D. G. Matei, T. Legero, C. Grebing, S. Häfner, C. Lisdat, R. Weyrich, W. Zhang, L. Sonderhouse, J. M. Robinson, F. Riehle, J. Ye, and U. Sterr. *A second generation of low thermal noise cryogenic silicon resonators.* J. Phys.: Conf. Ser. **723** (2016).

[Matei2017]   D. G. Matei, T. Legero, S. Häfner, C. Grebing, R. Weyrich, W. Zhang, L. Sonderhouse, J. M. Robinson, J. Ye, F. Riehle, and U. Sterr. *1.5 μm Lasers with Sub-10 mHz Linewidth.* Phys. Rev. Lett. **118**, 26 (2017).

[McAuslan2009]   D. L. McAuslan, J. J. Longdell, and M. J. Sellars. *Strong-coupling cavity QED using rare-earth-metal-ion dopants in monolithic resonators: What you can do with a weak oscillator.* Phys. Rev. A **80**, 6 (2009).

[McAuslan2012]   D. L. McAuslan, J. G. Bartholomew, M. J. Sellars, and J. J. Longdell. *Reducing decoherence in optical and spin transitions in rare-earth-metal-ion–doped materials.* Phys. Rev. A **85**, 3 (2012).

[McCann2001]   M. J. McCann, K. R. Catchpole, K. J. Weber, and A. W. Blakers. *A review of thin-film crystalline silicon for solar cell applications. Part 1: Native substrates.* Solar Energy Materials and Solar Cells **68**, 2 (2001).

[McDonald1991]   S. McDonald and W. S. Warren. *Uses of shaped pulses in NMR: A primer.* Concepts in Magnetic Resonance **3**, 2 (1991).

[McRae2013]   T. G. McRae, S. Ngo, D. A. Shaddock, M. T. L. Hsu, and M. B. Gray. *Frequency stabilization for space-based missions using optical fiber interferometry.* Opt. Lett. **38**, 3 (2013).

[Medford2012]   J. Medford, Ł. Cywiński, C. Barthel, C. M. Marcus, M. P. Hanson, and A. C. Gossard. *Scaling of Dynamical Decoupling for Spin Qubits.* Phys. Rev. Lett. **108**, 8 (2012).

[Meija2016]   J. Meija, T. B. Coplen, M. Berglund, W. A. Brand, P. D. Bièvre, M. Gröning, N. E. Holden, J. Irrgeher, R. D. Loss, T. Walczyk, and T. Prohaska. *Isotopic compositions of the elements 2013 (IUPAC Technical Report).* Pure and Applied Chemistry **88**, 3 (2016).

[Merkel2020]   B. Merkel, A. Ulanowski, and A. Reiserer. *Coherent and Purcell-Enhanced Emission from Erbium Dopants in a Cryogenic High-Q Resonator.* Phys. Rev. X **10**, 4 (2020).

[Mims1968]   W. B. Mims. *Phase Memory in Electron Spin Echoes, Lattice Relaxation Effects in $CaWO_4$: Er, Ce, Mn.* Phys. Rev. **168**, 2 (1968).

[Mims1972]   W. B. Mims. *Envelope Modulation in Spin-Echo Experiments.* Phys. Rev. B **5**, 7 (1972).

[Minář2009]   J. Minář, B. Lauritzen, H. de Riedmatten, M. Afzelius, C. Simon, and N. Gisin. *Electric control of collective atomic coherence in an erbium-doped solid.* New Journal of Physics **11**, 11 (2009).

[Miyazono2016]   E. Miyazono, T. Zhong, I. Craiciu, J. M. Kindem, and A. Faraon. *Coupling of erbium dopants to yttrium orthosilicate photonic crystal cavities for on-chip optical quantum memories.* Applied Physics Letters **108**, 1 (2016).

[Mohammady2018]   M. H. Mohammady, H. Choi, M. E. Trusheim, A. Bayat, D. Englund, and Y. Omar. *Low-control and robust quantum refrigerator and applications with electronic spins in diamond.* Phys. Rev. A **97**, 4 (2018).

[Moncorgé2005]   R. Moncorgé. *Current Topics in Rare-earth Lasers.* In: *Spectroscopic Properties of Rare Earths in Optical Materials.* Ed. by R. Hull, J. Parisi, R. M. Osgood, H. Warlimont, G. Liu, and B. Jacquier. Springer Berlin Heidelberg, 2005, pp. 320–378. ISBN: 978-3-540-28209-9.

[Morss1976]   L. R. Morss. *Thermochemical properties of yttrium, lanthanum, and the lanthanide elements and ions.* Chemical Reviews **76**, 6 (1976).

[Navarro-Urrios2014]   D. Navarro-Urrios, J. Gomis-Bresco, N. E. Capuj, F. Alzina, A. Griol, D. Puerto, A. Martínez, and C. M. Sotomayor-Torres. *Optical and mechanical mode tuning in an optomechanical crystal with light-induced thermal effects.* Journal of Applied Physics **116**, 9 (2014).

[Norambuena2018]   A. Norambuena, E. Muñoz, H. T. Dinani, A. Jarmola, P. Maletinsky, D. Budker, and J. R. Maze. *Spin-lattice relaxation of individual solid-state spins.* Phys. Rev. B **97**, 9 (2018).

[Norcia2018]   M. A. Norcia, J. R. K. Cline, J. A. Muniz, J. M. Robinson, R. B. Hutson, A. Goban, G. E. Marti, J. Ye, and J. K. Thompson. *Frequency Measurements of Superradiance from the Strontium Clock Transition.* Phys. Rev. X **8**, 2 (2018).

[Numata2004]   K. Numata, A. Kemery, and J. Camp. *Thermal-Noise Limit in the Frequency Stabilization of Lasers with Rigid Cavities.* Phys. Rev. Lett. **93**, 25 (2004).

[Ortu2018]   A. Ortu, A. Tiranov, S. Welinski, F. Fröwis, N. Gisin, A. Ferrier, P. Goldner, and M. Afzelius. *Simultaneous coherence enhancement of optical and microwave transitions in solid-state electronic spins*. Nature Materials **17**, 8 (2018).

[Pang2005]   H. Pang, G. Zhao, M. Jie, J. Xu, and X. He. *Study on the growth, etch morphology and spectra of Y_2SiO_5 crystal*. Materials Letters **59**, 28 (2005).

[Petersen2018] E. S. Petersen, A. M. Tyryshkin, K. M. Itoh, J. W. Ager, H. Riemann, N. V. Abrosimov, P. Becker, H. .-. Pohl, M. L. W. Thewalt, and S. A. Lyon. *Dynamical decoupling of interacting dipolar spin ensembles*. 2018. arXiv:1807.04908.

[Petit2020]   Y. Petit, B. Boulanger, J. Debray, and T. Chanelière. *Demonstration of site-selective angular-resolved absorption spectroscopy of the $^4I_{15/2} \to {}^4I_{13/2}$ erbium transition in the monoclinic crystal Y_2SiO_5"*. Optical Materials: X" **8** (2020).

[Phenicie2019] C. M. Phenicie, P. Stevenson, S. Welinski, B. C. Rose, A. T. Asfaw, R. J. Cava, S. A. Lyon, N. P. de Leon, and J. D. Thompson. *Narrow Optical Line Widths in Erbium Implanted in TiO_2*. Nano Letters **19**, 12 (2019).

[Pisenti2016]   N. C. Pisenti, A. Restelli, B. J. Reschovsky, D. S. Barker, and G. K. Campbell. *An ultra-low noise, high-voltage piezo-driver*. Review of Scientific Instruments **87**, 12 (2016).

[Probst2013]   S. Probst, H. Rotzinger, S. Wünsch, P. Jung, M. Jerger, M. Siegel, A. V. Ustinov, and P. A. Bushev. *Anisotropic Rare-Earth Spin Ensemble Strongly Coupled to a Superconducting Resonator*. Phys. Rev. Lett. **110**, 15 (2013).

[Probst2015]   S. Probst, H. Rotzinger, A. V. Ustinov, and P. A. Bushev. *Microwave multimode memory with an erbium spin ensemble*. Phys. Rev. B **92**, 1 (2015).

[Raha2020]   M. Raha, S. Chen, C. M. Phenicie, S. Ourari, A. M. Dibos, and J. D. Thompson. *Optical quantum nondemolition measurement of a single rare earth ion qubit*. Nature Communications **11**, 1 (2020).

[Rančić2018]   M. Rančić, M. P. Hedges, R. L. Ahlefeldt, and M. J. Sellars. *Coherence time of over a second in a telecom-compatible quantum memory storage material*. Nature Physics **14**, 1 (2018).

[Rebane2002]   K. K. Rebane. *Purely electronic zero-phonon line as the foundation stone for high resolution matrix spectroscopy, single impurity molecule spectroscopy, persistent spectral hole burning*. Journal of Luminescence **100**, 1 (2002).

[Reed1973]   E. D. Reed and H. W. Moos. *Multiphonon Relaxation of Excited States of Rare-Earth Ions in YVO_4, $YAsO_4$, and YPO_4*. Phys. Rev. B **8**, 3 (1973).

[Reid2005]   M. F. Reid. *Transition Intensities*. In: *Spectroscopic Properties of Rare Earths in Optical Materials*. Ed. by R. Hull, J. Parisi, R. M. Osgood, H. Warlimont, G. Liu, and B. Jacquier. Springer Berlin Heidelberg, 2005, pp. 95–129. ISBN: 978-3-540-28209-9.

[Reiserer2015] A. Reiserer and G. Rempe. *Cavity-based quantum networks with single atoms and optical photons*. Rev. Mod. Phys. **87**, 4 (2015).

[Richter2009]   B. Richter, J. Twiefel, and J. Wallaschek. *Piezoelectric Equivalent Circuit Models*. In: *Energy Harvesting Technologies*. Ed. by S. Priya and D. J. Inman. Springer US, 2009, pp. 107–128. ISBN: 978-0-387-76464-1.

[Riedmatten2008] H. de Riedmatten, M. Afzelius, M. U. Staudt, C. Simon, and N. Gisin. *A solid-state light–matter interface at the single-photon level*. Nature **456**, 7223 (2008).

129

[Robinson2019]   J. M. Robinson, E. Oelker, W. R. Milner, W. Zhang, T. Legero, D. G. Matei, F. Riehle, U. Sterr, and J. Ye. *Crystalline optical cavity at 4K with thermal-noise-limited instability and ultralow drift.* Optica, OPTICA **6**, 2 (2019).

[Rodríguez-deMarcos2016]   L. V. Rodríguez-de Marcos, J. I. Larruquert, J. A. Méndez, and J. A. Aznárez. *Self-consistent optical constants of SiO_2 and Ta_2O_5 films.* Opt. Mater. Express **6**, 11 (2016).

[Ruf2020]   M. Ruf, M. J. Weaver, S. B. van Dam, and R. Hanson. *Resonant Excitation and Purcell Enhancement of Coherent Nitrogen-Vacancy Centers Coupled to a Fabry-Pérot Micro-Cavity.* 2020. arXiv:2009.08204.

[Saavedra2021]   C. Saavedra, D. Pandey, W. Alt, H. Pfeifer, and D. Meschede. *Tunable fiber Fabry-Perot cavities with high passive stability.* Opt. Express **29**, 2 (2021).

[Sabooni2016]   M. Sabooni, A. N. Nilsson, G. Kristensson, and L. Rippe. *Wave propagation in birefringent materials with off-axis absorption or gain.* Phys. Rev. A **93**, 1 (2016).

[Salomon1988]   C. Salomon, D. Hils, and J. L. Hall. *Laser stabilization at the millihertz level.* J. Opt. Soc. Am. B **5**, 8 (1988).

[Salz2020]   M. Salz, Y. Herrmann, A. Nadarajah, A. Stahl, M. Hettrich, A. Stacey, S. Prawer, D. Hunger, and F. Schmidt-Kaler. *Cryogenic platform for coupling color centers in diamond membranes to a fiber-based microcavity.* Applied Physics B **126**, 8 (2020).

[Schmidt1993]   T. Schmidt, J. Baak, D. A. van de Straat, H. B. Brom, and S. Völker. *Temperature dependence of optical linewidths and specific heat of rare-earth-doped silicate glasses.* Phys. Rev. Lett. **71**, 18 (1993).

[Schmitt2017]   S. Schmitt, T. Gefen, F. M. Stürner, T. Unden, G. Wolff, C. Müller, J. Scheuer, B. Naydenov, M. Markham, S. Pezzagna, J. Meijer, I. Schwarz, M. Plenio, A. Retzker, L. P. McGuinness, and F. Jelezko. *Submillihertz magnetic spectroscopy performed with a nanoscale quantum sensor.* Science **356**, 6340 (2017).

[Serrano2018]   D. Serrano, J. Karlsson, A. Fossati, A. Ferrier, and P. Goldner. *All-optical control of long-lived nuclear spins in rare-earth doped nanoparticles.* Nature Communications **9**, 1 (2018).

[Shannon1976]   R. D. Shannon. *Revised effective ionic radii and systematic studies of interatomic distances in halides and chalcogenides.* Acta Crystallographica Section A **32**, 5 (1976).

[Shchepetov2013]   A. Shchepetov, M. Prunnila, F. Alzina, L. Schneider, J. Cuffe, H. Jiang, E. I. Kauppinen, C. M. Sotomayor Torres, and J. Ahopelto. *Ultra-thin free-standing single crystalline silicon membranes with strain control.* Applied Physics Letters **102**, 19 (2013).

[Shrivastava1983]   K. N. Shrivastava. *Theory of Spin–Lattice Relaxation.* physica status solidi (b) **117**, 2 (1983).

[Siyushev2014]   P. Siyushev, K. Xia, R. Reuter, M. Jamali, N. Zhao, N. Yang, C. Duan, N. Kukharchyk, A. D. Wieck, R. Kolesov, and J. Wrachtrup. *Coherent properties of single rare-earth spin qubits.* Nature Communications **5**, 1 (2014).

[Smith1992]   S. A. Smith, W. E. Palke, and J. T. Gerig. *The Hamiltonians of NMR. Part II.* Concepts in Magnetic Resonance **4**, 3 (1992).

[Sousa2009]   R. de Sousa. *Electron Spin as a Spectrometer of Nuclear-Spin Noise and Other Fluctuations*. In: *Electron Spin Resonance and Related Phenomena in Low-Dimensional Structures*. Ed. by M. Fanciulli. Springer Berlin Heidelberg, 2009, pp. 183–220. ISBN: 978-3-540-79365-6.

[Souza2012]   A. M. Souza, G. A. Álvarez, and D. Suter. *Robust dynamical decoupling*. Philosophical Transactions of the Royal Society A **370**, 1976 (2012).

[Stone2005]   N. Stone. *Table of nuclear magnetic dipole and electric quadrupole moments*. Atomic Data and Nuclear Data Tables **90**, 1 (2005).

[Sun2008]   Y. Sun, T. Böttger, C. W. Thiel, and R. L. Cone. *Magnetic g tensors for the $^4I_{15/2}$ and $^4I_{13/2}$ states of $Er^{3+} : Y_2SiO_5$*. Phys. Rev. B **77**, 8 (2008).

[Suzuki1992]   H. Suzuki, T. Tombrello, C. Melcher, and J. Schweitzer. *UV and gamma-ray excited luminescence of cerium-doped rare-earth oxyorthosilicates*. Nuclear Instruments and Methods in Physics Research Section A **320**, 1 (1992).

[Szczyrbowski1977]   J. Szczyrbowski and A. Czapla. *Optical absorption in D.C. sputtered InAs films*. Thin Solid Films **46**, 2 (1977).

[Tamarat2006]   P. Tamarat, T. Gaebel, J. R. Rabeau, M. Khan, A. D. Greentree, H. Wilson, L. C. L. Hollenberg, S. Prawer, P. Hemmer, F. Jelezko, and J. Wrachtrup. *Stark Shift Control of Single Optical Centers in Diamond*. Phys. Rev. Lett. **97**, 8 (2006).

[Tao1983]   Z. Tao. *Concentration of yttrium subgroup impurities in high-purity yttrium oxide by TBP-NH4SCN extraction chromatography*. Talanta **30**, 11 (1983).

[Teich1988]   M. C. Teich and B. E. Saleh. *I Photon Bunching and Antibunching*. In: ed. by E. Wolf. Vol. 26. Progress in Optics. Elsevier, 1988.

[Terblanche2001]   C. J. Terblanche, E. C. Reynhardt, S. A. Rakitianski, and J. A. Van Wyk. *^{13}C Spin–Lattice Relaxation in Natural Diamond: Zeeman Relaxation in Fields of 500 to 5000 G at 300 K Due to Fixed Paramagnetic Nitrogen Defects*. Solid State Nuclear Magnetic Resonance **19**, 3 (2001).

[Thiel1999]   C. Thiel. *A Discussion of Oscillator Strengths and Related Issues*. Tech. rep. 1999.

[Thiel2010]   C. Thiel, R. Macfarlane, T. Böttger, Y. Sun, R. Cone, and W. Babbitt. *Optical decoherence and persistent spectral hole burning in Er^{3+}:$LiNbO_3$*. Journal of Luminescence **130**, 9 (2010).

[Thiel2011]   C. Thiel, T. Böttger, and R. Cone. *Rare-earth-doped materials for applications in quantum information storage and signal processing*. Journal of Luminescence **131**, 3 (2011).

[Thiel2012a]   C. W. Thiel, W. R. Babbitt, and R. L. Cone. *Optical decoherence studies of yttrium oxyorthosilicate Y2SiO5 codoped with Er^{3+} and Eu^{3+} for optical signal processing and quantum information applications at 1.5 microns*. Phys. Rev. B **85**, 17 (2012).

[Thiel2012b]   C. W. Thiel, Y. Sun, R. M. Macfarlane, T. Böttger, and R. L. Cone. *Rare-earth-doped $LiNbO_3$ and $KTiOPO_4$ (KTP) for waveguide quantum memories*. Journal of Physics B: Atomic, Molecular and Optical Physics **45**, 12 (2012).

[Thomas2000]   G. A. Thomas, B. I. Shraiman, P. F. Glodis, and M. J. Stephen. *Towards the clarity limit in optical fibre*. Nature **404**, 6775 (2000).

[Thorpe2011]   M. J. Thorpe, L. Rippe, T. M. Fortier, M. S. Kirchner, and T. Rosenband. *Frequency stabilization to 6×10^{-16} via spectral-hole burning*. Nat. Photonics **5**, 11 (2011).

[Tiranov2018]   A. Tiranov, A. Ortu, S. Welinski, A. Ferrier, P. Goldner, N. Gisin, and M. Afzelius. *Spectroscopic study of hyperfine properties in $^{171}Yb^{3+} : Y_2SiO_5$*. Phys. Rev. B **98**, 19 (2018).

[Tyryshkin2012]   A. M. Tyryshkin, S. Tojo, J. J. L. Morton, H. Riemann, N. V. Abrosimov, P. Becker, H.-J. Pohl, T. Schenkel, M. L. W. Thewalt, K. M. Itoh, and S. A. Lyon. *Electron spin coherence exceeding seconds in high-purity silicon*. Nature Materials **11**, 2 (2012).

[Ulanowski2020]   A. Ulanowski. *Erbium ions in cryogenic high-finesse Fabry-Perot resonators*. MA thesis. Technical University of Munich and Max Planck Institute of Quantum Optics, Garching, 2020.

[Upadhyay2019]   K. Upadhyay, S. Thomas, N. Kalarikkal, and R. K. Tamrakar. *Effect of synthesis process on particle size and band gap of Er^{3+} doped Y_2SiO_5*. AIP Conference Proceedings **2104**, 1 (2019).

[Uphoff2015]   M. Uphoff, M. Brekenfeld, G. Rempe, and S. Ritter. *Frequency splitting of polarization eigenmodes in microscopic Fabry–Perot cavities*. New Journal of Physics **17**, 1 (2015).

[Utikal2014]   T. Utikal, E. Eichhammer, L. Petersen, A. Renn, S. Götzinger, and V. Sandoghdar. *Spectroscopic detection and state preparation of a single praseodymium ion in a crystal*. Nature Communications **5**, 1 (2014).

[vanBree2016]   J. van Bree, A. Y. Silov, M. L. van Maasakkers, C. E. Pryor, M. E. Flatté, and P. M. Koenraad. *Anisotropy of electron and hole g tensors of quantum dots: An intuitive picture based on spin-correlated orbital currents*. Phys. Rev. B **93**, 3 (2016).

[vanDam2018]   S. B. van Dam, M. Ruf, and R. Hanson. *Optimal design of diamond-air microcavities for quantum networks using an analytical approach*. New Journal of Physics **20**, 11 (2018).

[Vandersypen2005]   L. M. K. Vandersypen and I. L. Chuang. *NMR techniques for quantum control and computation*. Rev. Mod. Phys. **76**, 4 (2005).

[Venet2019]   C. Venet, B. Car, L. Veissier, F. Ramaz, and A. Louchet-Chauvet. *Deep and persistent spectral holes in thulium-doped yttrium orthosilicate for imaging applications*. Phys. Rev. B **99**, 11 (2019).

[Verberk2003]   R. Verberk and M. Orrit. *Photon statistics in the fluorescence of single molecules and nanocrystals: Correlation functions versus distributions of on- and off-times*. The Journal of Chemical Physics **119**, 4 (2003).

[Vuckovic2014]   J. Vuckovic. *Quantum optics and cavity QED with quantum dots in photonic crystals*. to be published by Oxford University Press. 2014. arXiv:1402.2541.

[Waeber2019]   A. M. Waeber, G. Gillard, G. Ragunathan, M. Hopkinson, P. Spencer, D. A. Ritchie, M. S. Skolnick, and E. A. Chekhovich. *Pulse control protocols for preserving coherence in dipolar-coupled nuclear spin baths*. Nature Communications **10**, 1 (2019).

[Walls1979]   D. F. Walls. *Evidence for the quantum nature of light*. Nature **280**, 5722 (1979).

[Wanser1992]   K. H. Wanser. *Fundamental phase noise limit in optical fibres due to temperature fluctuations*. Electronics Letters **28**, 1 (1992).

[Webster2008]   S. A. Webster, M. Oxborrow, S. Pugla, J. Millo, and P. Gill. *Thermal-noise-limited optical cavity*. Phys. Rev. A **77**, 3 (2008).

[Weil2006]   J. Weil and J. Bolton. *Appendix B: Quantum Mechanics of Angular Momentum.* In: *Electron Paramagnetic Resonance.* Ed. by J. Weil and J. Bolton. John Wiley & Sons, Ltd, 2006, pp. 455–483. ISBN: 9780470084984.

[Weiss2021]   L. Weiss, A. Gritsch, B. Merkel, and A. Reiserer. *Erbium dopants in nanophotonic silicon waveguides.* Optica **8**, 1 (2021).

[Welinski2017] S. Welinski, C. Thiel, J. Dajczgewand, A. Ferrier, R. Cone, R. Macfarlane, T. Chanelière, A. Louchet-Chauvet, and P. Goldner. *Effects of disorder on optical and electron spin linewidths in $Er^{3+},Sc^{3+}:Y_2SiO_5$.* Optical Materials **63** (2017).

[Welinski2020] S. Welinski, A. Tiranov, M. Businger, A. Ferrier, M. Afzelius, and P. Goldner. *Coherence Time Extension by Large-Scale Optical Spin Polarization in a Rare-Earth Doped Crystal.* Phys. Rev. X **10**, 3 (2020).

[White1975]   G. K. White. *Thermal Expansion of Vitreous Silica at Low Temperatures.* Phys. Rev. Lett. **34**, 4 (1975).

[Williamson2014]   L. A. Williamson, Y.-H. Chen, and J. J. Longdell. *Magneto-Optic Modulator with Unit Quantum Efficiency.* Phys. Rev. Lett. **113**, 20 (2014).

[Wolfowicz2020] G. Wolfowicz, C. P. Anderson, B. Diler, O. G. Poluektov, F. J. Heremans, and D. D. Awschalom. *Vanadium spin qubits as telecom quantum emitters in silicon carbide.* Science Advances **6**, 18 (2020).

[Yin2013]   C. Yin, M. Rancic, G. G. de Boo, N. Stavrias, J. C. McCallum, M. J. Sellars, and S. Rogge. *Optical addressing of an individual erbium ion in silicon.* Nature **497**, 7447 (2013).

[Zhang2014]   Z. Zhang, Z. Wang, R. Miao, Q. Zhu, D. Chen, X. Zhang, L. Zhou, Z. Li, and S. Yan. *Purification of yttrium to 4N5+ purity.* Vacuum **107** (2014).

[Zhang2017]   W. Zhang, J. M. Robinson, L. Sonderhouse, E. Oelker, C. Benko, J. L. Hall, T. Legero, D. G. Matei, F. Riehle, U. Sterr, and J. Ye. *Ultrastable Silicon Cavity in a Continuously Operating Closed-Cycle Cryostat at 4 K.* Phys. Rev. Lett. **119**, 24 (2017).

[Zhang2020]   S. Zhang, N. Galland, N. Lučić, R. Le Targat, A. Ferrier, P. Goldner, B. Fang, Y. Le Coq, and S. Seidelin. *Inhomogeneous response of an ion ensemble from mechanical stress.* Phys. Rev. Research **2**, 1 (2020).

[Zhong2015a]   M. Zhong, M. P. Hedges, R. L. Ahlefeldt, J. G. Bartholomew, S. E. Beavan, S. M. Wittig, J. J. Longdell, and M. J. Sellars. *Optically addressable nuclear spins in a solid with a six-hour coherence time.* Nature **517**, 7533 (2015).

[Zhong2015b]   T. Zhong, J. M. Kindem, E. Miyazono, and A. Faraon. *Nanophotonic coherent light–matter interfaces based on rare-earth-doped crystals.* Nature Communications **6**, 1 (2015).

[Zhong2018]   T. Zhong, J. M. Kindem, J. G. Bartholomew, J. Rochman, I. Craiciu, V. Verma, S. W. Nam, F. Marsili, M. D. Shaw, A. D. Beyer, and A. Faraon. *Optically Addressing Single Rare-Earth Ions in a Nanophotonic Cavity.* Phys. Rev. Lett. **121**, 18 (2018).

[Zhong2019a]   M. Zhong, R. L. Ahlefeldt, and M. J. Sellars. *Quantum information processing using frozen core Y^{3+} spins in $Eu^{3+}:Y_2SiO_5$.* New Journal of Physics **21**, 3 (2019).

[Zhong2019b]   T. Zhong and P. Goldner. *Emerging rare-earth doped material platforms for quantum nanophotonics.* Nanophotonics **8**, 11 (2019).

[Zhu2020]   W. Zhu, E. R. N. Fokoua, A. A. Taranta, Y. Chen, T. Bradley, M. N. Petrovich, F. Poletti, M. Zhao, D. J. Richardson, and R. Slavík. *The Thermal Phase Sensitivity of Both Coated and Uncoated Standard and Hollow Core Fibers Down to Cryogenic Temperatures.* Journal of Lightwave Technology **38**, 8 (2020).

C   Acknowledgments

The research presented in this thesis was conducted in the Quantum Networks group at the Max Planck Institute of Quantum Optics, and I am grateful for the opportunity to work under excellent conditions in such a stimulating environment.

First, I want to express my deep gratitude to Andreas Reiserer, who leads the Quantum Networks group and who supported me on my path as a PhD student from the very beginning. He managed to ignite my enthusiasm for erbium dopants before I even started my work, and he always encouraged me and showed impressive optimism through all ups and downs. I am very thankful that he was always very constructive in his feedback and made an effort to make the work enjoyable.

I also want to thank Gerhard Rempe for being my doctoral supervisor and for integrating the Quantum Networks group in the Quantum Dynamics division and sharing the resources. I still remember the joint group retreat in my first year and appreciate his encouragement to be curious and ask questions.

When I started my work at MPQ, I was the first PhD student of the Quantum Networks group, and our lab was an empty room. I am still amazed how quickly we filled the space and how many people joined and left over the years. I would like to thank all my colleagues for the great time we had together in the lab.

My first office mate was Natalie Wilson, who I thank for operating the laser-ablation setup for the mirror fabrication. At this point, I also want to thank the CavityX team who built and maintained the CO_2 laser setup, in particular Manuel Uphoff, Manuel Brekenfeld and Dominik Niemitz.

I also enjoyed the company of Valentin Crépel, who I had joyful discussions with about heterodyning, stability and noise levels, as well as general physics and its applications outside the laboratory. Speaking of joy, I want to thank our Master's students Natalia Herrera Valencia and Pablo Cova Fariña for teaching us the 'southern way' of expressing happiness in the lab. Both students also contributed to the coherent control of erbium spin ensembles with microwaves, together with Kutlu Kutluer, Penghong Yu, and Alexander Ulanoswki. I want to thank Alexander Ulanowski in particular, for his modeling of the cavity mode spectrum, the programming of the lockbox FPGA and improvements to the laser stabilization system. His participation gave the cavity project a significant boost during the last year and I am very happy that he now takes over and continues the Fabry-Perot cavity project in his PhD.

I want to thank my fellow PhD student colleagues Lorenz Weiss and Andreas Gritsch, who I shared the lab with for several years. It was always a very relaxed and friendly atmosphere; and I enjoyed working with both of them and wish them good luck with their experiments on erbium dopants in silicon! Also, I thank Samarth Chawla and Daniel Repp for their contributions to the laser stabilization to a fiber resonator, and Maximilian Löw from the Quantum Dynamics division for his maintenance work on the frequency comb that was also made available to our group.

Many thanks to all technicians in our division. In particular, I want to thank Johannes Siegl for enduring our continuously updated requests for new designs and modifications of cryostat and cavity parts.

I am very grateful for the education, love and support that my family gave me while I grew up, which laid the foundations for my scientific studies as an adult and eventually allowed me to pursue a PhD. I also thank all my friends for their emotional support.